**Distribution Agreement**

Signature:

__________________________________ ________________

Meghan Kohne Date

# Characterizing the Configurational Fluctuations that Contribute to Enzyme Catalysis for Ethanolamine Ammonia Lyase

By

Meghan Kohne
Doctor of Philosophy
Physics

Dr. Kurt Warncke
Advisor

Dr. Stefan Boettcher
Committee Member

Dr. Laura Finzi
Committee Member

Dr. Connie Roth
Committee Member

Dr. Emily Weinert
Committee Member

Accepted:

Lisa A. Tedesco, Ph.D.
Dean of the James T. Laney School of Graduate Studies

Date

# Characterizing the Configurational Fluctuations that Contribute to Enzyme Catalysis for Ethanolamine Ammonia Lyase

By

Meghan Kohne

B.A., DePauw University, 2010

Advisor:

Kurt Warncke, PhD.

An abstract of

A Dissertation Submitted to the Faculty of the

James T. Laney Graduate School of Emory University

In Partial Fulfillment of the Requirements for the Degree of

Doctor of Philosophy

in Physics

2018

## Abstract

# Characterizing the Configurational Fluctuations that Contribute to Enzyme Catalysis for Ethanolamine Ammonia-Lyase

By

Meghan Kohne

Ethanolamine Ammonia Lyase (EAL) is a coenzyme-$B_{12}$ dependent enzyme found in *Salmolella typhimurium* that converts the substrate ethanolamine into two products: acetaldehyde and ammonia. This process is utilized by the bacterium to produce adenosine triphosphate (ATP) and is the sole source of carbon and nitrogen. The minimalistic mechanism for EAL catalysis consists of six steps. First-order rate constants of the rate limiting chemical reaction step (radical rearrangement) are determined by using temperature-step-triggered decay of the cryotrapped substrate radical intermediate, and time-resolved, full-spectrum electron paramagnetic resonance (EPR) spectroscopy over a wide temperature range. The piecewise-linear Arrhenius dependence shows a kinetic bifurcation (220 K) and kinks (217 K) in the decay components, which arise from the effective quenching of collective configurational fluctuations that are coupled to the radical rearrangement reaction. Below the temperature transition, the reaction persists by local protein fluctuations. The origins of the dynamical transitions are described by using a temperature-dependent free energy landscape (FEL) model. Experiments using deuterated ethanolamine and utilizing these same methods account for the kinetic isotope effects (KIE), determine the origin of the microscopic states from the FEL model, and reveal a distinct set of specific collective-atom protein motions that contribute to an additional step in the EAL catalytic cycle. These dynamical temperature transitions are shifted to higher temperatures through the introduction of varying sucrose concentrations, which quantify the influence of the solvent on the dynamics of the protein and protein function. The results and analysis established here reveal key insights in enzymology, specifically the role of configurational protein fluctuations in catalysis.

# Characterizing the Configurational Fluctuations that Contribute to Enzyme Catalysis for Ethanolamine Ammonia Lyase

By

Meghan Kohne

B.A., DePauw University, 2010

Advisor:

Kurt Warncke, PhD.

A Dissertation Submitted to the Faculty of the

James T. Laney Graduate School of Emory University

In Partial Fulfillment of the Requirements for the Degree of

Doctor of Philosophy

in Physics

2018

# Acknowledgements

I am indebted to my advisor, Dr. Kurt Warncke, who provided guidance and support throughout my time at Emory University. His assistance allowed me to grow and develop as a scientist. I also owe thanks to members of my committee, Dr. Laura Finzi, Dr. Stefan Boettcher, Dr. Connie Roth, and Dr. Emily Weinert for their time and guidance throughout the completion of my dissertation research. Also want to thank all members of the Warncke Lab group, both past and present.

I'm also deeply indebted to my family, especially my parents, Janean Lanham, David Lanham, and Edward Kohne, for their love and support. Thank you.

Table of Contents

# List of Tables and Figures

## Chapter 1

### Figures

## Chapter 2

### Tables

## Figures

# Chapter 3

## Tables

## Figures

## Chapter 4

### Tables

### Figures

## Chapter 5

### Tables

### Figures

# Chapter 1

# Introduction

## 1.1 Enzyme Catalysis and Dynamics

In general, protein dynamics refers to configurational fluctuations in the protein. One of the challenges in the explication of enzyme catalysis today is how dynamics affect chemical reactions. The enzyme's main function is to lower the energy required to form the product(s) (Figure 1.1).

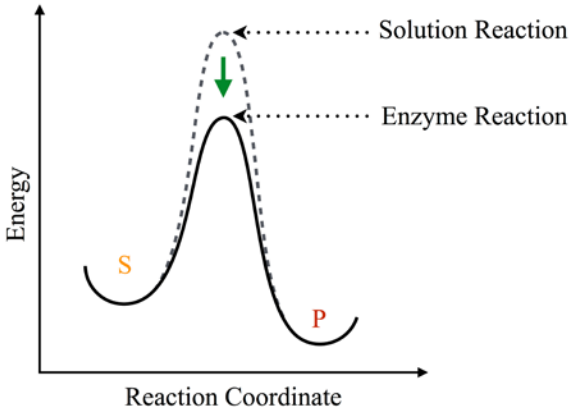

**Figure 1.1**. **Qualitative energy diagram** showing the energy barrier difference between a solution reaction (gray dashed) and an enzyme reaction (solid black) when the substrate (S) forms the product (P).

This lowering of energy barriers results in higher enzymatic rates of several orders of magnitude compared to the solution reaction. [1] To accomplish this, the enzyme must undergo specific configurational changes throughout the reaction (Scheme 1.1).

$$E + S \leftrightarrow ES \rightarrow P + S \qquad \text{Scheme 1.1}$$

The enzyme (E) must bind and position the substrate (S) inside the active site to form the enzyme substrate complex (ES). The substrate then undergoes a chemical transformation to form the enzyme product complex (EP) then the product (P) is released.[2] The ability of the enzyme to achieve such high reaction rates lies in the lowering of the free energy barrier of the transition state (TS). The transition state is represented as the peak of the barrier in Figure 1.1 between the substrate (S) and the product (P) states. There are multiple mechanisms and combinations enzymes utilize to stabilize the transition state including manipulating charge dispersal and electrostatic interactions.[3]

### 1.1.1 Timescale of Enzyme Fluctuations

In addition to transition state stabilization, the catalyst must turnover through several cycles. To achieve this, the enzyme must effectively access many configurational sub-states rapidly throughout the catalytic cycle over a wide range of timescales.[4]

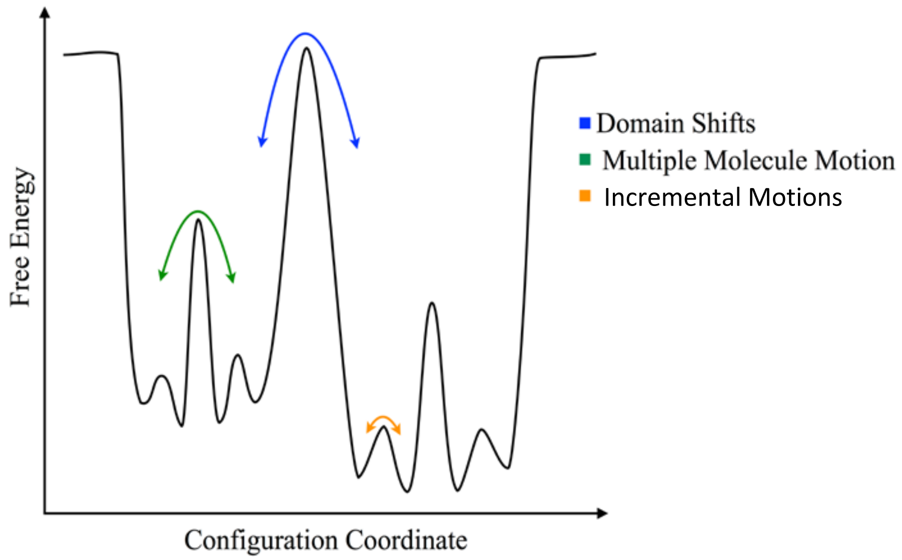

**Figure 1.2**. **Hierarchies of protein fluctuations** along a configuration coordinate. Coordinated, large-scale (blue) and molecule (green) fluctuations as well as localized, incremental motions (yellow).

Figure 1.2 depicts the hierarchy of fluctuations represented in an energy diagram of the protein. Unlike Figure 1.1, the topography of the enzyme energy landscape is roughened, representing the energy required by the enzyme to execute different categorized motions to move through the configuration space. Collective domain shifts occur on the μs–ms timescale (at ~ 297 K) and are instrumental in product release and substrate binding. Many biological processes occur on this timescale, including catalysis.[5-6] Faster motions, on the ns-ps timescale allow for conformational sampling within the substates,[7] depicted in Figure 1.2 as the yellow arrow. These motions are usually contributed by individual atom motions.

### 1.1.2 Dielectric Relaxation Studies of Protein Fluctuations

Dielectric spectroscopic studies have become a prominent tool used to study global dynamics of enzymes over the past few decades.[5, 8-15] Dielectric spectroscopy measures the permittivity ($\epsilon^*$) of the enzyme as a function of frequency (*f*), described in Equation 1.2.

$$\epsilon^* = \epsilon'(f) - i\epsilon''(f) \tag{1.1}$$

The permittivity is described by a real ($\epsilon'(f)$) and imaginary part ($i\epsilon''(f)$). Permittivity is the reduction of the applied electric field caused by the electric dipoles of the sample. The electric dipoles of the sample interact with the applied voltage causing an impedance and therefore a change in permittivity. Different molecular processes will affect the permittivity at different frequencies, creating different absorption peaks in the dielectric permittivity.[12] In complex protein systems, there are several absorbance peaks over a wide range of frequencies. These absorbance peaks often overlap each other. Therefore, the imaginary part of the permittivity ($i\epsilon''(f)$) is fit to the Cole-Cole function to deconvolute the different absorbance populations found in Equation 1.2:

$$\epsilon_j^*(f,T) = \frac{\Delta\epsilon_j(T)}{1+(2\pi i f \tau_j(T))^{\beta_j(T)}} \tag{1.2}$$

where the permittivity ( $\epsilon_j^*(f,T)$) is dependent on the dielectric strength ($\Delta\epsilon_j(T)$), relaxation time ($\tau_j(T)$), and fractional exponent ($\beta$) (which are functions of temperature (*T*)). Each dynamical process ($j$) corresponds to an absorbance population and $\tau_j(T)$ corresponds to its peak frequency.

### 1.1.3 Categories of Protein Fluctuations

Dielectric studies have identified several different populations of fluctuations and categorize them by timescales. However, many types of motions can overlap in timescales. [6, 15] For determining global behavior of fluctuations, protein motions generally fall into two categories: collective or localized. Collective motion describes atoms fluctuating concertedly, these types of motions are generally referred to as α-fluctuations. Localized motions describe individual atoms fluctuating independently and are commonly referred to as β-fluctuations. There is another classification of protein fluctuation or sub-classification. Johari-Goldstein (JG) fluctuations are a type of β-fluctuation that manifest collective motion on a smaller scale than the α fluctuations.[16-18]

### 1.1.4 Temperature Dependence on Protein Fluctuations

The most definitive way to identify the distinct types of configurational fluctuations is to determine their temperature dependence. For dielectric studies the relaxation time ($\tau$) is determined by the Cole-Cole function (Equation 1.3). The α-type fluctuations follow the Vogel-Tammann-Fulcher (VTF) approximation[19-22]:

$$k_\alpha(T) = A_\alpha e^{-DT_0/(T-T_0)} \qquad (1.3)$$

where $k_\alpha(T)$ is the rate constant and $A_\alpha$, $D$, and $T_0$ are experimentally determined coefficients. In contrast, β-fluctuations follow an Arrhenius dependence:

$$k_\beta(T) = A_\beta e^{-E_a/(RT)} \tag{1.4}$$

Where the rate ($k_\beta(T)$) is dependent on the activation energy ($E_a$) and the pre-exponential factor ($A_\beta$) which are experimentally determined. $R$ is the gas constant. The different behavior of these two processes becomes obvious when depicted on an Arrhenius plot.

The β-fluctuations, persist with a linear dependence throughout the temperature scope of the experiment. In contrast, the magnitude of the slope of the α-fluctuation curve increases as the temperature decreases to the point where the population is no longer detectable in the dielectric spectra. This freezing-out of collective motion is generally considered as the glass (dynamical) transition. [5-6, 9-15, 22]

### 1.1.5 Solvent Contributions to Protein Dynamics

The environment of the protein can dramatically influence its dynamics, both in frequency and dynamical transitions, specifically the temperature at which collective motions are quenched.[22] The localized environment of the protein is comprised of water molecules that hydrogen bond to the polar surface of the protein, called the hydration shell. In a completely hydrated system, the hydration shell consists of approximately two layers of water molecules[14-15] covering the surface area of a protein.

Several studies have shown the dramatic effect the hydration shell has on the fluctuations of the protein.[22] Specifically the mobility of the enzyme decreases with less of a hydration layer, leading to the conclusion that solvent and protein dynamics are coupled. [22-24]

The global fluctuations observed in these studies have provided a definitive quantification of protein motions, yet lack specificity in determining how these motions affect enzyme catalysis. Specific configurational changes have been proven to affect certain steps in the catalytic process such as substrate binding and positioning as well as product release.[25] However, in terms of the transition state step, the role of protein dynamics remains elusive.

## 1.2 Ethanolamine Ammonia-Lyase

Ethanolamine ammonia-lyase (EAL) is an enzyme found in *Salmonella typhimurium* (and other bacterial species) that converts the substrate ethanolamine into two products: acetaldehyde and ammonia.[26-28] This process is utilized by for bacterium to produce adenosine triphosphate (ATP) and is the sole source of carbon and nitrogen. [29] Over the course of five decades, EAL's structure and function have been studied at length, [30] which makes the enzyme a perfect vessel to study protein dynamics.

### 1.2.1 $B_{12}$-Dependent Superfamily

EAL belongs to the $B_{12}$-dependent superfamily[31], which utilizes a $B_{12}$ cobalamin coenzyme. Two forms of the coenzyme can undergo catalysis: adenosylcobalamin (AdoCbl) and methylcobalamin (MeCbl). [32]

Cobalamin is one of the most complex cofactors in biology. At the center of both forms is the cobalt ion. It is bonded to four nitrogens on the corrin ring and one nitrogen from the 5,6-dimethylbenzimidazole group (DMB), which forms an axial bond. The difference between the two types of cobalamin lies with the group that forms the cobalt-carbon bond above the corrin ring. In adenosylcobalamin, the cobalt-carbon bond is formed with a 5'-deoxyadenosyl group which is used to form both reduced and oxidized states of cobalt during the enzyme catalytic cycle. In methylcobalamin the cobalt-carbon bond is formed with a methyl group.

EAL belongs to a $B_{12}$ dependent subfamily (class), that catalyzes a 1,2 rearrangement reaction: adenosylcobalamin-dependent isomerase, which facilitate a hydrogen exchange between two carbons. [33] The other subcategories are methylcobalamin-dependent methyltransferases that involve methyl group transfers, and dehalogenases, which are involved in dehalogenation. [27] AdoCl-dependent isomerases are further delineated with respect to the binding AdoCl to the enzyme, generally described as either base-on or base-off. For base-off configurations, a histidine is embedded in the tail of AdoCl, resulting in the DMB group being less than 10 Å from the cobalt center. For base-on configurations this does not occur, therefore the DMB group is farther away from the cobalt center. [34]

### 1.2.2 Ethanolamine Catabolism Pathway

The *eut* operon expresses EutB, EutE, EutD, and EutG responsible for ethanolamine catalysis.[35] Other proteins that are expressed on the *eut* gene are microcompartment shell proteins that help house the reactions and isolate the volatile acetaldehyde. Ethanolamine is an organic compound derived from phosphatidylethanolamine, which is found in abundance in both mammalian and bacterial cell membranes. [36]

Ethanolamine is first converted into acetaldehyde and ammonia by EutBC (EAL) and adocobalamin ($B_{12}$). Acetaldehyde is catalyzed by the EutE enzyme along with nicotinamide adenine dinucleotide ($NAD^+$) and coenzyme A (CoA). EutE oxidizes acetaldehyde to form acetyl coenzyme A (acetyl-CoA) and reduces $NAD^+$ to NADH. At this point acetyl-CoA can be passed directly into the citric acid cycle that culminates in the formation of ATP and GTP, which the bacterium utilizes for energy transfer. EutD and EutG are utilized in auxiliary processes used to balance redox reactions and fermentation growth. [35]

### 1.2.3 Structure of EAL

EAL[37-39] is a large globular protein (489 kDa) consisting of two subunits: EutB and EutC. Adensoylcobalamin is located in the interior of EutB. In *S. typhimurium*, EutB is the larger subunit, consisting of 453 residues and has a molecular mass of 49.4 kDa and EutC has a molecular mass of 32.1 kDa comprised of 286 residues (Figure 1.8)

Both subunits are expressed by the *eutB* and *eutC* genes found on the *eut* operon along with several other *eut* operon used throughout the bacterium. [40] EAL is organized as a trimer of dimers (Figure 1.3) with each dimer with a mass of 163 kDa.

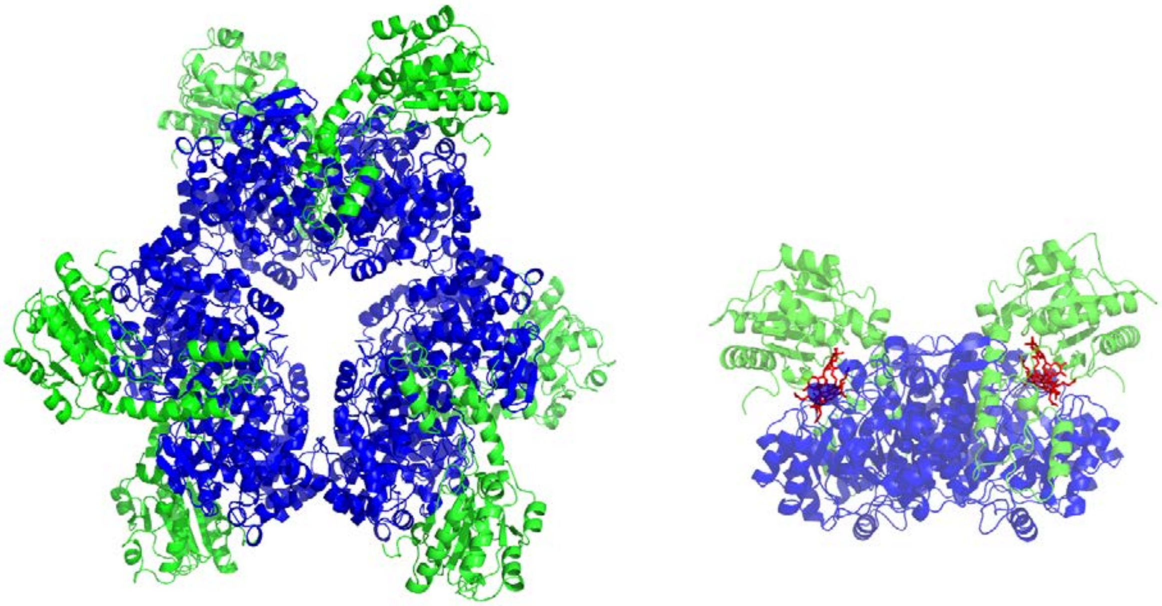

**Figure 1.3**. **Representation of the EAL hexamer** (left) and dimer (right) from the homology model, based on the X-ray crystal structure.[37] EutB subunit is represented in blue, EutC in green, and the coenzyme adocobalamin in red. The image was rendered using Pymol.

### 1.2.4 Minimal Catalytic Mechanism for EAL

EAL and other AdoCl-dependent isomerases utilize the cobalt-carbon bond between the corrin ring and the dimethyl-benzimidazole group to aid in catalysis. This bond is very weak for a covalent bond, requiring approximately 30 kcal mol$^{-1}$ to break.[40] Figure 1.4 shows the minimalistic mechanism for EAL catalysis. In brief, after the substrate binds to the $B_{12}$-EAL complex the cobalt-carbon bond on the corrin ring of AdoCl cleaves homiletically, leaving the unpaired electron on the 5’-deoxyandenosyl group. The Co(III) becomes low-spin Co(II) with an unpaired electron in the d$^2$ orbital.[41] The deoxyadensyl radical[42] migrates to the C1 carbon of the substrate where it extracts a hydrogen from the C1 carbon, creating a Co(II)-substrate radical pair. This is the first hydrogen transfer (HT1) in the catalytic cycle. The radical migrates to the C2 carbon coincidently with the amine group migration to the C1 carbon, forming the product radical (rearrangement step).[43-44] The hydrogen on the deoxyadenosyl group migrates back to the product radical, forming the two products: acetaldehyde and ammonia and completes the second hydrogen transfer (HT2). The deoxyadenosyl radical migrates back to the vicinity of the corrin ring and reforms the cobalt-carbon bond, reforming the cofactor and releasing the two products.

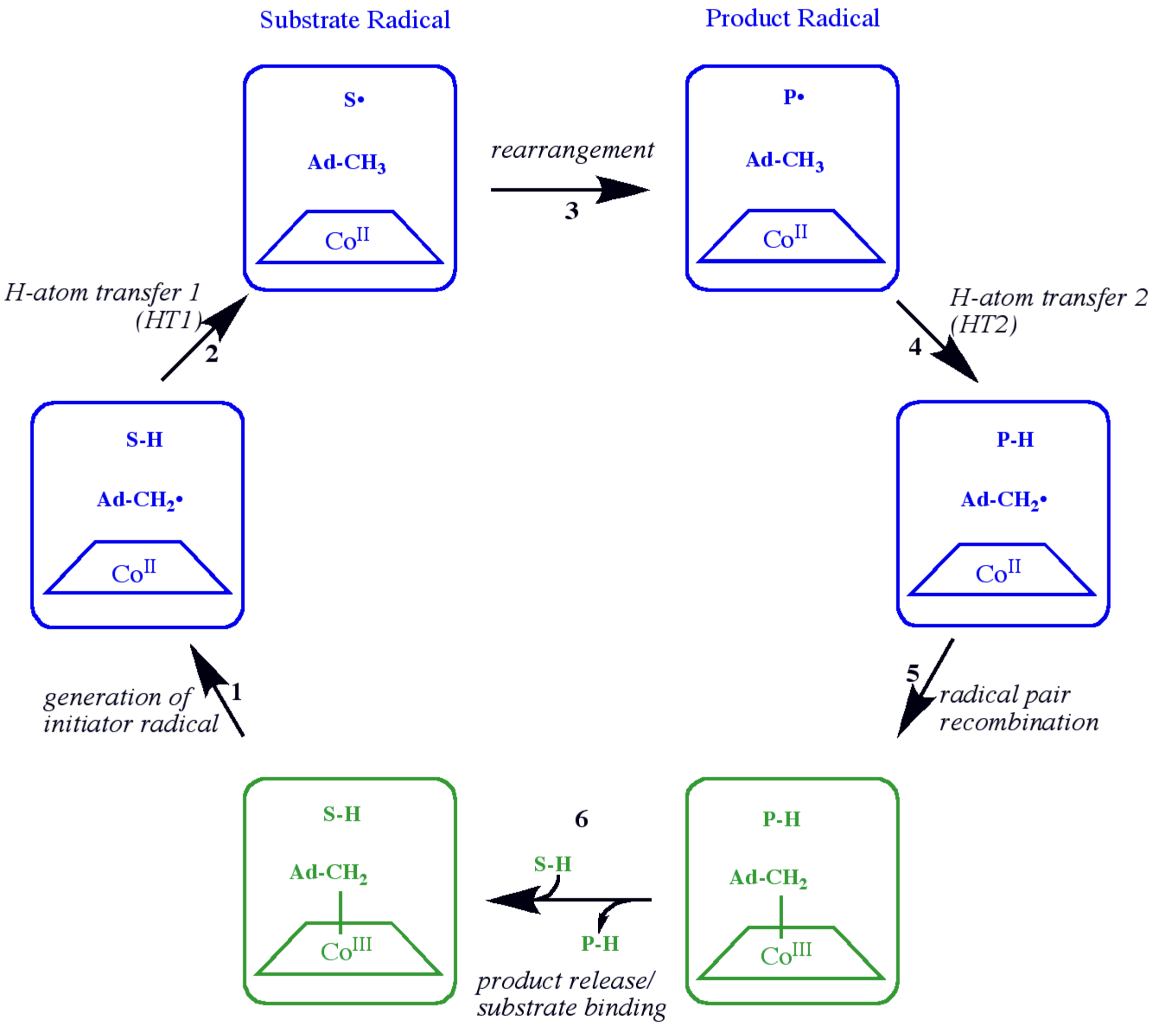

**Figure 1.4 Minimal mechanism for the catalytic cycle of EAL**. The process begins with the binding of the substrate, ethanolamine. The binding causes hemolytic cleavage of the cobalt carbon bond (1) which generates the first radical species. The unpaired electron migrates to the substrate and removes a hydrogen atom from the C1 carbon (2) forming the substrate radical. The amine group on the substrate migrates from C2 to C1 (3), forming the product radical state. The second hydrogen transfer occurs, (4) where a hydrogen atom is removed from the 5’-

deoxyadenosine group and binds to the product, reforming the 5'-deoxyadenosyl radical. The cobalt-carbon bond is reformed (5) then the product is released (6). The states that produce paramagnetic species are in blue, diamagnetic species are in green.

### 1.2.5 EAL Active Site

EAL's active site is located on the interface of the two subunits (EutB and EutC) and projected into EutB. The substrate resides in a small pocket (Figure 1.5) The substrate radical interacts directly with side chains of Asp362, Arg160, Asn162, Asn193, and Glu287 of the large, EutB subunit. The polypeptide structure surrounding the active site is comprised of unstructured, α-helix, and β-sheet formations.

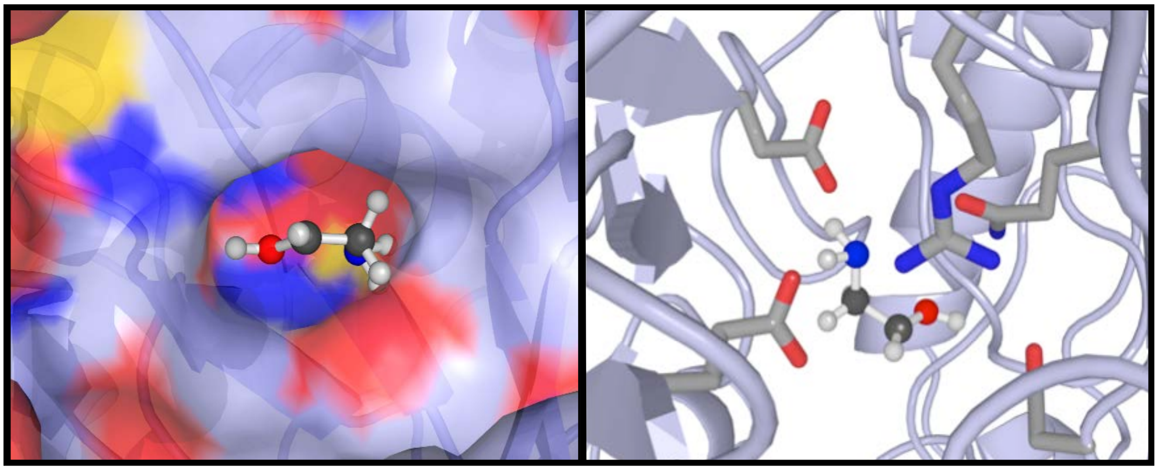

**Figure 1.5**. **Pymol representation of the EAL active site**. The left panel depicts the substrate radical (ball and stick) semi-enclosed in EutB.[37] The substrate radical interacts directly with side chains (stick) of Asp362, Arg160, Asn162, Asn193, and Glu287 of the large, EutB (subunit right panel clockwise, from top left).

### 1.2.6 Paramagnetic Species in the EAL Catalytic Cycle

There are four states in EAL's catalytic cycle that include paramagnetic species (Figure 1.4, blue states). The removal of the hydrogen atom from the substrate creates two paramagnetic species: the substrate radical and the low spin Co(II) radical pair. Both have a net electron spin angular momentum, meaning they are detectable by using electron paramagnetic resonance techniques. [5, 11] The radical rearrangement that follows produces the product radical. This radical has never been directly observed in EAL or other Class II enzymes, and its existence is only theorized.

## 1.3 Electron Paramagnetic Resonance

Electron Paramagnetic Resonance (EPR) is a technique, first discovered by Yevgeny Zavoisky in 1946, that detects unpaired electrons in chemical species. [45-47] In EPR, electron spin transitions are measured, allowing for the study of biological, chemical and physical systems with Ångstrom level resolution.[48-52] Quantum mechanically, the fundamental principle of EPR, is the electron Zeeman effect. The Zeeman effect occurs when the electron spin aligns parallel ($m_s$ = -½) or antiparallel ($m_s$ = +½) in the presence of an external magnetic field, where the energy of the electron expressed in Equation 1.5.

$$H = g\mu_B B m_s \tag{1.5}$$

where $g$ is the electron g-factor, $\mu_\beta$ is the Bohr magneton, and $m_s$ is the spin state of the system and $B$ is the magnetic field. In an external magnetic field, the degeneracy of the two electron states ($m_s$ = ±½) is lifted (Figure 1.6) and the energy difference between the two states is:

$$\Delta E = g\mu_B B \tag{1.6}$$

When the energy of the applied electromagnetic radiation, with a frequency $v$, satisfies the equation:

$$hv = g\mu_B B_r \quad (1.7)$$

where $h$ is the Planck constant and $B_r$ is the resonant magnetic field, the applied radiation is equal to the energy separation between the two electron states (Zeeman manifolds), which is determined by the strength of the applied magnetic field.

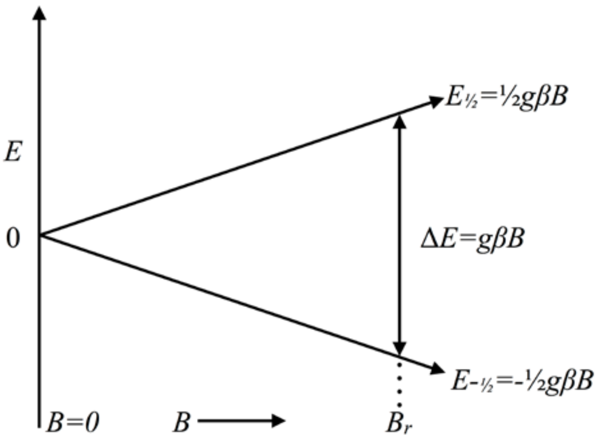

**Figure 1.6. Energy level diagram for a free electron showing resonance absorption**. Where $E_{+½}$ and $E_{-½}$ represent the upper ($m_s = +½$) and lower ($m_s = -½$) energy levels respectively and $B_r$ is the magnetic field where the condition $hv=g\beta B_r$ is met.[53]

At thermodynamic equilibrium, the population ratio between the two electron states is determined by the Boltzmann distribution:

$$\frac{N_{+½}}{N_{-½}} = e^{-\frac{\Delta E}{RT}} \quad (1.8)$$

Where $N_{+1/2}$ and $N_{-1/2}$ are the number of spins in the upper and lower manifolds, respectively. $\Delta E$ is the energy level separation of each state (Equation 1.6), $R$ is the gas constant and $T$ is the temperature.

To achieve resonance, the microwave frequency or the magnetic field is varied. Due to the experimental difficulty in sweeping the microwave frequency over a significant range, the magnetic field is varied, and the microwave frequency remains fixed. This method is called continuous-wave (CW) EPR. CW EPR utilizes phase-sensitive detection, by varying the magnetic field.[53-54] The field is varied at a set modulation frequency (usually 100 kHz). At resonance, the microwaves are reflected from the cavity and amplified. Any signals that are not modulated at this frequency are suppressed and not detectable. Over the modulation frequency, the signal should be approximately linear, outputting a sinusoidal wave with an amplitude equal to the slope of the signal, therefore the first derivative of the signal is measured.[54]

CW EPR usually utilizes magnetic fields around 0.3 T ($B$). Therefore, at room temperature ($T$ = 298 K), with the gas constant ($R$) ≈ 2, the populations are approximately equal ($\frac{N_{+½}}{N_{-½}}$= 0.998). However, by lowering the temperature, the population difference increases (with a greater population in the lower state) and the signal intensity is increased. The intensity of the EPR signal is dependent on the net population difference between the ground and excited states.

Most systems studied by EPR do not have a single isolated radical, but rather the electron interacts with other magnetic nuclei and unpaired electrons in their local vicinity. The Hamiltonian then becomes:

$$H = H_{EZ} + H_{NZ} + H_{HF} + H_{NQ} + H_{NN} + H_{EE} \tag{1.7}$$

Where $H_{EZ}$, $H_{NZ}$, $H_{HF}$, $H_{NQ}$, $H_{NN}$ and $H_{EE}$ are the electron Zeeman (Equation 1.5) term, nuclear Zeeman term, hyperfine coupling term, nuclear quadrupole, nuclear-nuclear, and electron-electron interactions respectively.[45, 53, 55]

### 1.3.1 Paramagnetic States of EAL

There are three possible paramagnetic states in the minimal mechanistic catalytic cycle for the coenzyme $B_{12}$-dependent EAL (Figure 1.9). These states are the Co(II)-5’-deoxyadenosyl radical pair, Co(II)-substrate radical pair, and the Co(II)-product radical pair. During steady-state turnover, in the presence of excess substrate, the system accumulates in the $Co^{II}$-substrate radical state and is the only EPR detectable paramagnetic species.[39, 49, 56-58] CW-EPR simulations show the separation for Co(II)- C1 and separation for (S)-2-aminopropanol-genertated Co(II)-substrate radical pair is 11± 1 Å. The Co(II)-C1 separation for aminoethanol-generated Co(II)-substrate radical pair is 9.3± 1 Å.[59-61] This approximate 2 Å separation difference is proposed to arise from steric interaction of the extra methol group on (S)-2-aminopropanol with the enzyme.

### 1.3.2 CW-EPR Spectral of the Substrate Radical State

Low temperature CW-EPR studies show a spectrum consistent with the Co(II)-substrate radical pair intermediate. The spectrum consists of Co(II) located at the magnetic field associated with the perpendicular component of the $g$-tensor ($g_{\perp}$ ~ 2.3) at 290 mT.[43, 62-63] The substrate radical is located at approximately $g$ ~ 2.003 corresponding to the magnetic field value of 337 mT, derived from Equation 1.7, with a microwave frequency $v$ of ~9.45 GHz. Both the Co(II) and substrate radical are coupled, resulting in perturbations in the signals for each paramagnetic species, leading to unresolved doublet splitting and inhomogeneous line broadening in the CW-EPR spectrum.[62]

## 1.4 Outline of Dissertation

This dissertation identifies the underlying protein dynamics that drive the substrate radical rearrangement reaction. This is an isolated chemical step in B12-dependent Ethanolamine Ammonia-lyase catalytic cycle, through time-resolved EPR spectroscopy experiments of the decay of the cryotrappped Co(II)-substrate radical pair.

Chapter 2 introduces the low temperature kinetic experiments from 203-230 K $^1H_4$-aminoethanol-derived Co(II)-substrate radical pair decay. Low temperature measurements reveal a dynamical transition in the form of a bifurcation and kink that signal the effective quenching of two specific sets of native collective protein configurational fluctuations that drive the chemical step. Below 217 K, local, incremental fluctuations drive the substrate radical decay reaction through a non-native reaction coordinate.

Chapter 3 identifies the rate-limiting steps for the EAL catalysis with $^2H_4$-ethanolamine-derived Co(II) substrate radical pair decay from 203-230 K. These results, along with electron spin echo envelope modulation (ESEEM) experiments, reveal the dynamic temperature transition and $S_1^\bullet \leftrightarrow S_2^\bullet$ process is a manifestation in the change of protein dynamics from collective to incremental fluctuations that drive the radical rearrangement step.

Chapter 4 reveals the effect of solvent mobility on the substrate radical decay for both $^1H_4$- and $^2H4$-ethanolamine-derived Co(II) substrate radical pair at 217 K, by utilizing varying concentrations of sucrose (0-30% (w/v)).

Chapter 5 characterizes the sets of distinctive collective motions driving the chemical reaction through $^{1}H_{4}$-ethanolamine-derived Co(II) substrate radical pair decays with low sucrose concentrations (0-2% (w/v)) from 232-203 K.

# Chapter 2

## Two Dynamical Regimes of the Substrate Radical Rearrangement Reaction in B12 Dependent Ethanolamine Ammonia-Lyase Resolve Contributions of Native Protein Configurations and Collective Configurational Fluctuations to Catalysis

The work presented in this chapter is available at:

Kohne, M.; Zhu, C.; Warncke, K., Two dynamical regimes of the substrate radical rearrangement reaction in B-12-dependent Ethanolamine Ammonia-Lyase resolve contributions of native protein configurations and collective configurational fluctuations to catalysis. *Biochemistry* **2017,** *56* (25), 3257-3264.

https://pubs.acs.org/doi/abs/10.1021/acs.biochem.7b00294

## 2.1 Introduction

An enduring challenge to the comprehensive microscopic description of enzyme-catalyzed reactions has been the identification of the contribution of an evolved choreography of particular protein configurational fluctuations, or “protein dynamics,” to the chemical step of substrate-to-product transformation.[1-3, 64-67] Adjustments in the protein structure by configurational changes are an integral part of substrate binding, intermediate poising, and product release steps,[25] as described in molecular detail by spectroscopic, scattering, and theoretical techniques.[5, 9-11, 68] However, experimental evidence for specific configurational transitions, that conduct the chemical step of the reaction over the free energetically biased reaction coordinate, has proven elusive. Proposals have been criticized, on the basis that they are incompletely formulated, or lie outside the realm of Boltzmann equilibrium statistics.[64] Here, we show that specific collective-atom protein motions define the native reaction coordinate for the radical rearrangement step in the adenosylcobalamin (coenzyme $B_{12}$)-dependent ethanolamine ammonia-lyase [EAL; EC 4.3.1.7; cobalamin (vitamin $B_{12}$)-dependent enzyme superfamily] from Salmonella typhimurium.[69-70] These collective motions are stochastic and involve the thermalized configurational states of the system. The motions are not intra-configurational vibrations, as in models proposed for protein contributions to nonadiabatic electron[71] and light-atom[72-76] (e.g., H) transfers. Rather, the motions are inter-configurational transitions, that are mediated by a subset of the broad spectrum of fluctuations characteristic of protein as a condensed-phase system.[20, 77]

### 2.1.1 Configurational Protein Fluctuations

The effects of protein fluctuations, and the configurational states that they connect, on reactions are typically not detected in room-temperature (T) enzyme steady-state or transient kinetics studies,[3] because their rates ($>10^6$ $s^{-1}$, with the main density in the range of $10^9-10^{12}$ $s^{-1}$) far exceed those of chemical steps.[77] Thus, to reveal the effects of native protein inter-configurational motions on reaction chemistry, the configurational transition rates, displacement amplitudes (extents), or both, of these motions must be perturbed selectively, so that the reaction rate is impacted. In EAL, this condition is realized by studying an isolated, single reaction step in the catalytic sequence, the substrate radical rearrangement, over the cryogenic *T* range of 190−230 K.[49, 78]

### 2.1.2 Substrate Radical Step in EAL

The substrate radical intermediate state in EAL, $S^{\bullet}$ (Figure 2.1), [37-38] is first accumulated in the steady-state at room temperature and then cryotrapped at 140 K.[51] Subsequently, *T*-step to ≥ 190 K triggers first-order decay of the substrate radical to the diamagnetic products state, P, (Figure 1) which is monitored by using time-resolved, full-spectrum electron paramagnetic resonance (EPR) spectroscopy of the decay of $S^{\bullet}$.[51] The $P^{\bullet}$ state is not detected by EPR, [49] consistent with the calculated 5−9 kcal/mol higher energy of $P^{\bullet}$[79-81] and rapid depletion by the subsequent $P^{\bullet} \rightarrow P$ step.

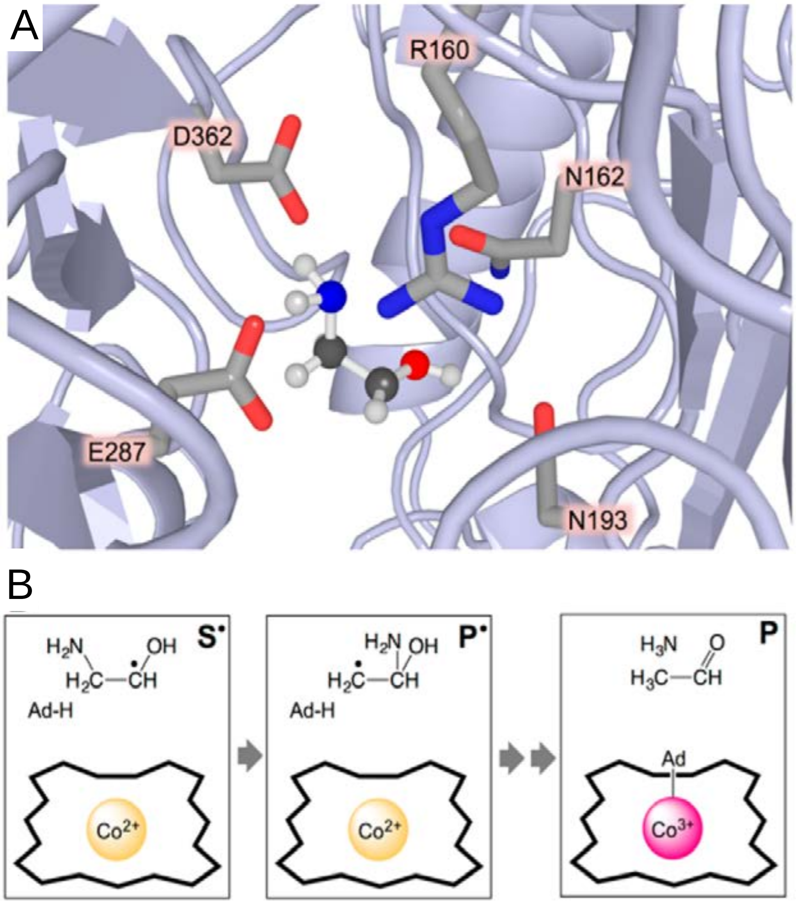

**Figure 2.1. Structure of the aminoethanol substrate radical and EAL protein in the active site region and substrate radical decay reaction sequence**. (A) The substrate radical (ball and stick) interacts directly with the annotated side chains (stick) of the large, EutB subunit (clockwise, from top left). The polypeptide secondary structure surrounding the active site (blue-gray) is depicted as loop, α-helix (coil), and β-sheet (flat arrow). (B) The decay reaction sequence depicts canonical states: substrate radical ($S^{\bullet}$), product radical ($P^{\bullet}$), diamagnetic product (P). Formal cobalt ion redox state in cobalamin and the 5′-deoxyadenosyl moiety (Ad−) are shown.

Rate limitation of $S^{\bullet}$ decay by the chemical rearrangement step in the low T range is indicated by a substrate $^{1}H/^{2}H$ secondary isotope effect,[78] which is consistent with steady-state accumulation of $S^{\bullet}$ as the only paramagnetic intermediate, [51] the substrate-nitrogen, $^{14}N/^{15}N$

steady-state isotope effect that arises from the C2−N bond cleavage microstep in the rearrangement,[82-83] and theory-based calculations.[79-81]

### 2.1.3 Protein Fluctuation Classification

A framework for interpretation of the T-dependence of the decay kinetics is provided by analogy to canonical classes of motions in supercooled molecular fluids and glasses:[20] Larger-scale, collective-particle motions ($\alpha$-fluctuations; rate constants, $k_\alpha$) display non-Arrhenius $T$-dependence ( $\frac{d^2 \ln k_\alpha}{d(1/T)^2} < 0$; Vogel−Fulcher−Tamman law), with $k_\alpha$ defined as $10^{-2}$ $s^{-1}$ at the glass transition ($T = T_g$), below which collective motions are effectively quenched. Localized, “caged” motions of single particles ($\beta$-fluctuations; rate constants, $k_\beta$) generally display linear Arrhenius dependence over a wide $T$ range.[21, 84-85] The Johari−Goldstein class of $\beta$-fluctuations ($k_{JG\beta}$) display a transition at a characteristic $T$ from localized collective to incremental displacements of the same particle cluster.[17-18] These fundamental classes of fluctuations have been recognized in proteins.[15, 77] Probe techniques provide a partial resolution of the structural origins of these motions.

A multisite nuclear magnetic resonance (NMR) study of a fully hydrated nanocrystalline protein identified three transitions in the onset of amplitude increases in amino acid side chains, the peptide backbone, and coupled solvent motions with increasing $T$, at 195 (TI), 220 (TII), 250 (TIII) K.[86] Together, the preceding results establish the following tenets for interpretation of the low-$T$ studies of protein-reaction dynamical coupling in enzymes: (1) Stochastic collective ($\alpha$-type) and localized ($\beta$-type) fluctuations among configurational states combine to create the complex motions at different temporal and spatial scales, that reconfigure the protein shape and modulate electrostatics in parallel with reaction progress. (2) The net direction of protein structural and chemical change (the reaction coordinate) follows the path of decreasing free energy of the configurations. A description of these effects is provided by the free energy landscape (FEL), which portrays the free energy of the system as a function of the configurations.[87-88]

The low-*T* kinetics of the $S^\bullet$ decay process in EAL over 203−230 K are marked by two abrupt changes in Arrhenius dependence with descending *T*, at 220 K (bifurcation) and 217 K (kinks). This behavior shows that the free energy landscape (FEL), itself, is *T*-dependent. The changes in the FEL indicate a transformation, over 219 → 217 K, from a dependence of the reaction on collective fluctuations in the native reaction regime (220−295 K), to a dependence on local protein fluctuations in the regime below the transition (203-214 K). Two different dynamical paradigms for catalysis of the radical rearrangement reaction are thus revealed. The bifurcation and kink transitions are proposed to represent the effective quenching of two distinct sets of native protein collective configurational fluctuations, that (1) reconfigure the $S^\bullet$ state and enable it for reaction, and (2) execute the chemical step of rearrangement.

## 2.2 Materials and Methods

### 2.2.1 Enzyme Preparation

Enzyme was purified from the *Escherichia coli* overexpression system incorporating the cloned S. typhimurium EAL coding sequence[89] as described,[90] with modifications.[37] The specific activity of purified EAL with aminoethanol as substrate was 20 μmol/min/mg (T = 298 K, *P* = 1 atm), as determined by using the coupled assay with alcohol dehydrogenase and NADH.[30]

### 2.2.2 Standard EPR Sample Preparation for Low-T Decay Measurements

All chemicals were purchased from commercial sources. Reactions were performed in aerobic buffer containing 10 mM potassium phosphate (pH 7.5). Kinetic parameters were identical in anaerobic samples. Manipulations were carried out on ice under dim red safe-lighting. No photodegradation of the coenzyme $B_{12}$ (adenosylcobalamin, AdoCbl) cofactor was detected under any of the conditions. AdoCbl was added to 2-fold molar excess over active sites. The final concentration of enzyme in EPR samples was 10−15 mg/ mL, which is equivalent to 20−30 μM for a holoenzyme molecular mass of 500 000 g/mol,[90] and an active site concentration of 120−180 μM, based on an active site/ holoenzyme stoichiometry of 6:1.[91-92] The procedure for cryotrapping of the $Co^{2+}$-substrate radical pair samples has been described in detail.[51] In brief, holoenzyme and substrate solutions were manually mixed and loaded into a 4 mm outer diameter EPR tube, and the tube was immersed in isopentane ($T$ = 140 K; elapsed time, ∼10 s).

### 2.2.3 Time-Resolved, Full Spectrum EPR Measurements of Substrate Radical Decay at Low-*T*

EPR spectra were collected by using a Bruker E500 ElexSys EPR spectrometer equipped with a Bruker ER4123 SHQE cavity. Instrumentation and methods for measurements of the substrate radical decay kinetics by EPR have been described in detail.[51] Briefly, EPR samples were held at a staging temperature of 160−180 K in the ER4131VT cryostat system in the spectrometer, and temperature was step-increased to decay measurement values of 203−230 K. The time from initiation of the temperature step to the start of acquisition of the first spectrum was 30−60 s. Repetitive acquisition of EPR spectra (24 s sweep time; 2.56 ms time constant) proceeded for the duration of the decay. The temperature at the sample was determined by using an Oxford Instruments ITC503 temperature controller with a calibrated model 19180 4-wire RTD probe, which has ±0.3 K accuracy over the range of decay measurements. The ER4131VT cryostat/controller system provided a temperature stability of ±0.5 K over the length of the EPR sample cavity. The temperature was therefore stable to ±0.5 K during each run.

### 2.2.4 Steady-State Kinetics Measurements

The $k_{\mathrm{cat}}$ values were determined from the measured rate of steady-state turnover at saturating substrate concentrations by using the coupled assay with alcohol dehydrogenase and NADH.[30]

### 2.2.5 Transient Kinetics Analysis: Empirical Fitting of the Observed Substrate Radical Decay

EPR spectra were acquired continuously during the decay. For each EPR spectrum in the decay time series, the amplitude of the substrate radical signal was obtained from the difference between peak and trough amplitudes of the derivative feature around g ≈ 2.0, with baseline correction. All data processing programs were written in Matlab (Mathworks, Natick, MA). The observed decays were fitted to monoexponential (eq S1, N = 1) or biexponential (eq S1, N = 2) functions by using the following expression,[93]

$$\frac{A(t)}{A(0)} = \sum_{i=1}^{N} A_i exp[-k_i t] \qquad (2.1)$$

where $\frac{A(t)}{A(0)}$ is the normalized total amplitude, $A_{\mathrm{i}}$ is the normalized component amplitude ($\sum_{i=1}^{N} A_i = 1$ at t = 0), and $k_{\mathrm{i}}$ is the first-order rate constant. The best-fit rate constant and amplitude parameters of the biexponential fits were independent of the initial parameters. Additional data collection and averaging has led to slight changes in the mean and standard deviation of k values at some temperatures, relative to earlier reports.[49, 78]

### 2.2.6 Numerical Simulation and Fitting to the Microscopic Model

The observed decays for the *T*-range, 203-219 K, were fitted to the 3-state, 2-step microscopic kinetic model (Scheme 2.1), where $S_1^{\bullet}$ , $S_2^{\bullet}$ and $P$ are states, and $k_{12}$, $k_{21}$ and $k_P$ are first-order rate constants. The fitting was performed by using programs written in Matlab.

$$S_1^{\bullet} \underset{k_{21}}{\overset{k_{12}}{\rightleftarrows}} S_2^{\bullet} \xrightarrow{k_P} P \qquad \text{Scheme 2.1}$$

The 3-state, 2-step model was solved symbolically by using the *dsolve* function in the Matlab suite. The following set of ordinary differential equations describe the time dependence of $S_1^{\bullet}$ , $S_2^{\bullet}$ and $P$:

$$dS_1^{\bullet}/_{dt} = -S_1^{\bullet}\ k_{12} + S_2^{\bullet}\ k_{21} \qquad (2.2)$$

$$dS_2^{\bullet}/_{dt} = S_1^{\bullet}\ k_{12} - S_2^{\bullet}\ k_{21} - S_2^{\bullet}\ k_P \qquad (2.3)$$

$$dP/_{dt} = S_2^{\bullet}\ k_P \qquad (2.4)$$

The equations were solved explicitly, under the initial conditions, $S_1^{\bullet} = A_1$, $S_2^{\bullet} = 1\text{-}A_1$ and $P = 0$, where $A_1$ is the initial concentration of the $S_1^{\bullet}$ state. The substrate radical signal decays to zero and concomitantly forms diamagnetic products. Therefore, the solution for $P$(t) was fit to the inverse of the substrate radical decay curve by using the least squares regression analysis equation:

$$\underset{x}{min} \|F(x, xdata) - ydata\|_2^2 = \sum_i (F(x, xdata\ a_i) - ydata\ a_i)^2 \tag{2.5}$$

In Equation 2.5, $x$ is the set of variables $k_{12}$, $k_{21}$, $k_P$ and $A_1$. The *xdata* and *ydata* are the time and substrate radical amplitude matricies for the decay curve, respectively. The *lsqcurvefit* function in Matlab was used to find the numerical solution for P(t) for each decay. Trust-region-reflective and Levenberg-Marquardt algorithms were used. Both algorithms were shown to have no significant difference between results, with the lower bounds of the step size and the function set to $10^{-10}$.

### 2.2.7 Transient Kinetics Analysis: Numerical Simulation and Fitting to the Microscopic Model

The observed decays for the *T*-range, 203−219 K, were fitted to a three-state, two-step microscopic kinetic model (Scheme 2.1), by symbolic solution of the coupled differential equations (Equations 2.2-2.4).

### 2.2.8 Temperature-Dependence of First-Order Rate Constants

The temperature dependence of the first-order microscopic rate constants were fitted to the expression from Arrhenius reaction rate theory: [93]

$$k(T) = A\exp[-\frac{E_a}{RT}] \tag{2.6}$$

where $A$, $E_a$, and $R$ are the Arrhenius prefactor (units, $s^{-1}$ ), the activation energy and the gas constant, respectively. The activation enthalpy, $\Delta H^{\dagger}$ , and activation entropy, $\Delta S^{\dagger}$ , were obtained by fitting the temperature dependence of the firstorder, microscopic rate constants to the expression from Eyring theory:[93]

$$\frac{k(T)}{T} = \frac{k_B}{h}\, exp\left[\frac{\Delta S^{\ddagger}}{R}\right] exp\left[\frac{\Delta H^{\ddagger}}{RT}\right] \tag{2.7}$$

where $k_B$ and $h$ are Boltzmann's constant and Planck's constant, respectively. The activation free energy is obtained from $\Delta G^{\ddagger} = \Delta H^{\ddagger} - T\Delta S^{\ddagger}$.

## 2.3 Results

### 2.3.1 Time-Resolved, Full-Spectrum EPR Measurements of the Co$^{2+}$-Substrate Radical Pair Decay

EPR spectra (Figure 2.2) of the substrate radical component were acquired continuously as the decay of the Co$^{2+}$-substrate radical pair progressed, following $T$-step to temperatures of 203−230 K (Figure 2.3).

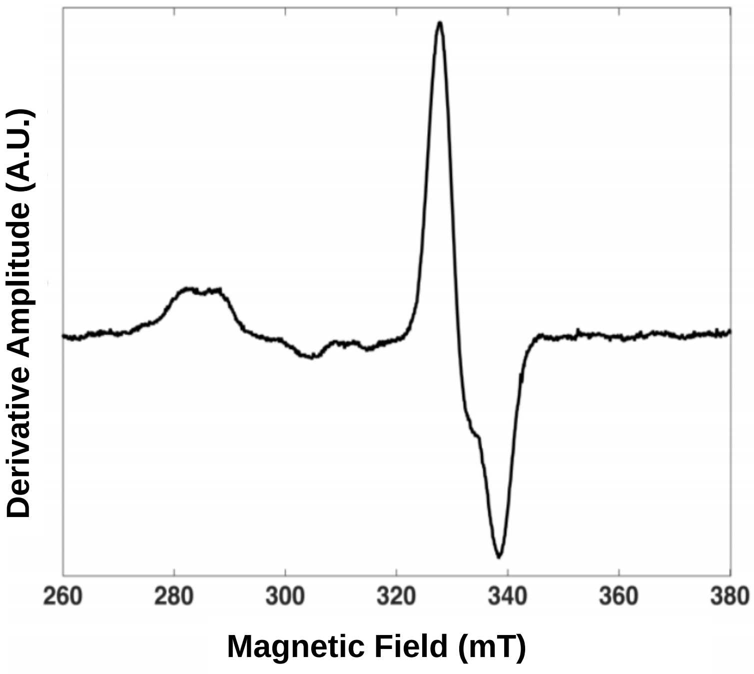

**Figure 2.2. Electron paramagnetic resonance spectrum of the aminoethanol-generated Co(II)-substrate radical pair EPR spectrum in EAL**. EPR conditions: microwave frequency, 9.3405 GHz; microwave power, 20 mW; magnetic field modulation, 1.0 mT; modulation frequency, 100 kHz; temperature, 207 K; single scan.

The experimental decays were performed to a level of ≤10% of the initial amplitude, to identify the possible presence of multiple components and to obtain reliable rate constants and amplitudes from fits to theoretical decay functions.

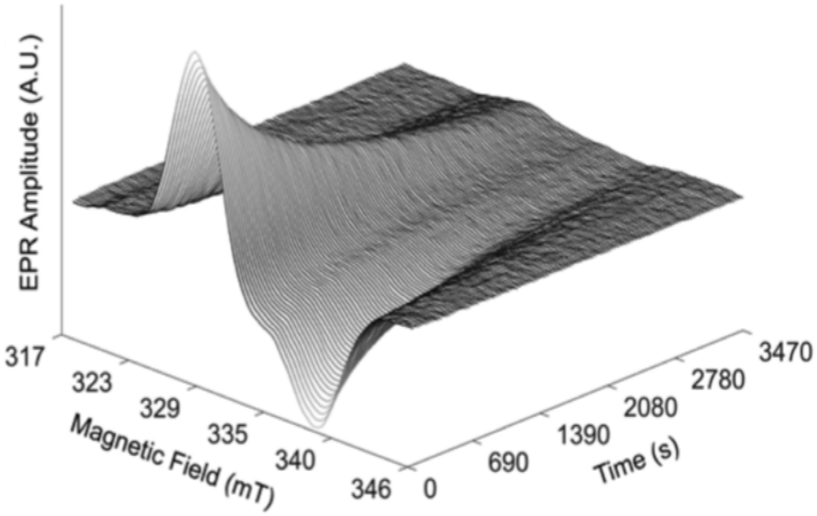

**Figure 2.3. EPR spectrum**: Amplitudes represent a moving average over 5 spectra for 600 total spectra. EPR conditions: microwave frequency, 9.3337 GHz; microwave power, 20 mW; magnetic field modulation, 1.0 mT; modulation frequency, 100 kHz.

The decay curves were well-fit by a monoexponential function (observed rate constant, kobs,n) over the range, 220−230 K, and by a biexponential function over 203−214 K (observed slow- and fast-phase rate constants, $k_{obs,s}$, $k_{obs,f}$ and corresponding normalized amplitudes $A_{obs,s}$, $A_{obs,f}$) and 217−219 K ($k'_{obs,s}$, $k'_{obs,f}$; $A'_{obs,s}$, $A'_{obs,f}$) (Figure 2.4 and Table 2.1).

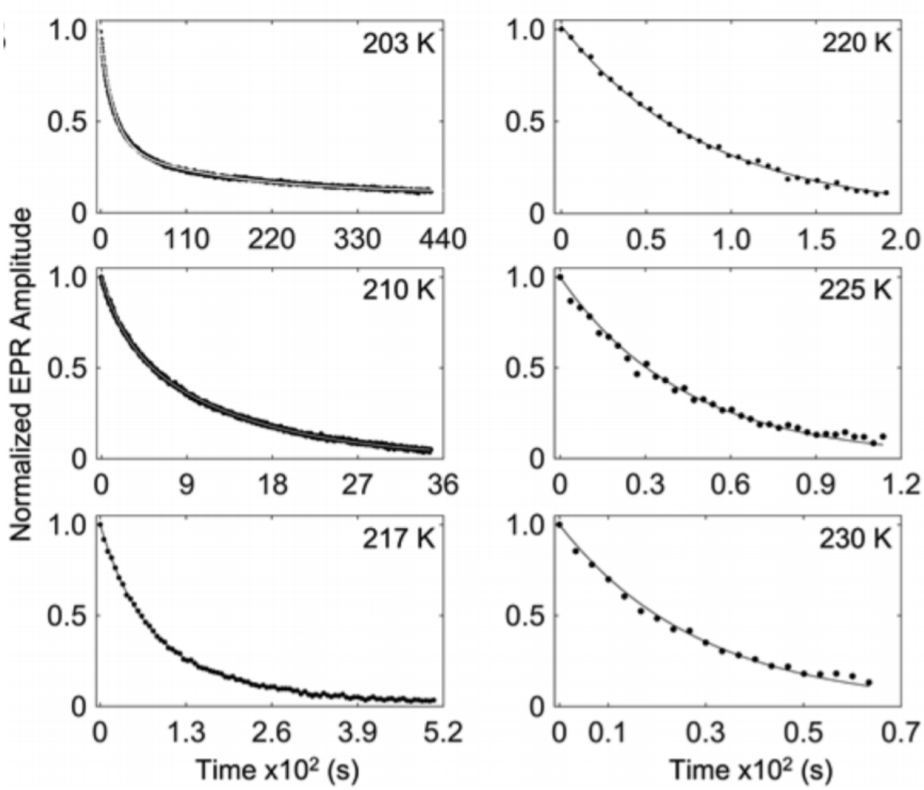

**Figure 2.4. Time-dependence of the EPR amplitude of the substrate radical. Decays** at selected *T* values and overlaid best-fit mono- or biexponential functions (line). EPR amplitudes are normalized to the zero-time value.

### 2.3.2 Steady-State Measurements of the Co$^{2+}$-Substrate Radical Pair Decay

Substrate depletion following steady-state turnover of EAL under solution conditions leads to the decay of the accumulated Co$^{2+}$-substrate radical pair state to the holoenzyme resting state (Figure 2.1). The rate of the Co$^{2+}$- substrate radical pair state decay under these conditions has been measured by using rapid-mixing methods and optical detection, and the measured substrate radical decay rate constants are comparable to the steady-state turnover number, $k_{\text{cat}}$. [94-95] The equivalence of $k_{\text{cat}}$ and the substrate radical decay rate constant is congruent with rearrangement as the dominant internal step in rate determination of turnover.[82-83] Therefore, we measured $k_{cat}$ values of EAL for aminoethanol at 277 K [5.7 (±0.4) × $10^0$ $s^{-1}$ ] and 295 K [2.9 (±0.2) × $10^1$ $s^{-1}$ ] (mean value, ± standard deviation, n = 3).

### 2.3.3 Temperature-Dependence of the Observed Rate Constants

The Arrhenius plot (ln $k_{obs}$ versus $T^{-1}$ ) of $k_{obs,s}$ and $k_{obs,f}$ from the empirical fits to the decay of the $Co^{2+}$- substrate radical pair state in EAL from 203 to 230 K, and the $k_{cat}$ values show a piecewise-linear pattern over the wide *T* range (Figure 2.5), characterized by three regions: (1) $220 \leq T \leq 295$ K; $k_{obs,n}$: This region represents the native reaction, because the lower-*T* data at 220−230 K and the higher-*T* data at 277 and 295 K adhere to the same linear relation. (2) $217 \leq T \leq 219$ K; $k'_{obs,s}$ and $k'_{obs,f}$: There is a bifurcation of the decay process into fast and slow components with descending *T*. The values of $k'_{obs,s}$ and $k'_{obs,f}$ at the measurement *T* values of 217, 218, and 219 K remain constant to within one standard deviation. (3) $T < 217$ K; $k_{obs,s}$ and $k_{obs,f}$: Linear Arrhenius dependences are displayed by the fast and slow decay components, and $A_{obs,s}$ and $A_{obs,f}$ are constant for $T < 217$ K (Table 2.1). There are kinks at the $k'_{obs,s}/k_{obs,s}$ and $k'_{obs,f}/k_{obs,f}$ boundaries.

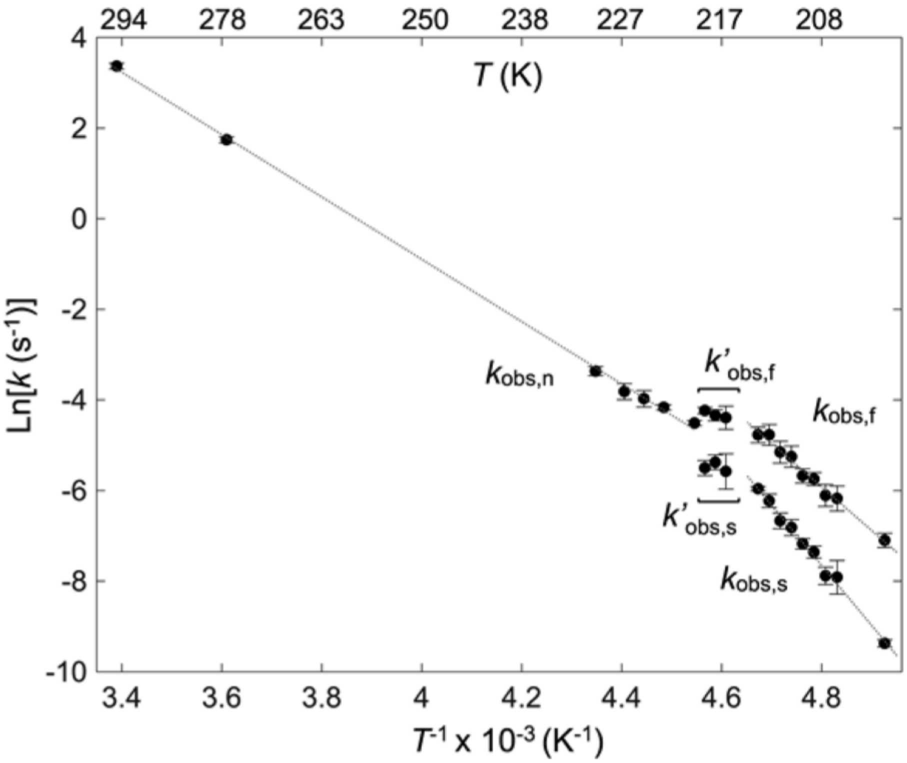

**Figure 2.5. Arrhenius plot of observed first-order rate constants**. The mean $k_{obs}$ value for each temperature is shown, with standard deviation representing at least three separate decay measurements. Values of $k_{cat}$ (277, 295 K) are also shown. Dashed lines represent the best linear fit to the data for $k_{obs,n}$ (220−295 K), $k_{obs,s}$, and $k_{obs,f}$ (203−214 K).

**Table 2.1. Observed first-order rate constant and normalized amplitude parameters** for the fit of the mono- and biexponential functions to the Co$^{2+}$-substrate radical pair decay kinetics at different temperatures.

| $T$(K) | $k_{obs,n}$ (s$^{-1}$) | $A_{obs,n}$ | $k_{obs,f}$ (s$^{-1}$) | $A_{obs,f}$ | $k_{obs,s}$ (s$^{-1}$) | $A_{obs,s}$ | R$^2$ |
|---|---|---|---|---|---|---|---|
| 203 | -- | -- | 8.3(±1.4) ×10$^{-4}$ | 0.60±0.03 | 8.5(±0.07) ×10$^{-5}$ | 0.40±0.03 | 0.9978 |
| 207 | -- | -- | 2.1(±0.7) ×10$^{-3}$ | 0.46±0.16 | 3.7(±1.6) ×10$^{-4}$ | 0.54±0.16 | 0.9993 |
| 208 | -- | -- | 2.2(±0.6) ×10$^{-3}$ | 0.49±0.12 | 3.8(±0.8) ×10$^{-4}$ | 0.51±0.12 | 0.9988 |
| *209* | -- | -- | 3.2(±0.5) ×10$^{-3}$ | 0.38±0.08 | 6.4(±0.1) ×10$^{-4}$ | 0.62±0.08 | 0.9992 |
| *210* | -- | -- | 3.4(±0.6) ×10$^{-3}$ | 0.39±0.07 | 7.6(±0.1) ×10$^{-4}$ | 0.61±0.07 | 0.9992 |

| | | | | | | | | |
|---|---|---|---|---|---|---|---|---|
| *211* | -- | -- | $5.2(\pm0.5)\times10^{-3}$ | 0.30±0.15 | $1.1(\pm0.2)\times10^{-3}$ | 0.70±0.15 | 0.9986 |
| *212* | -- | -- | $5.8(\pm1.6)\times10^{-3}$ | 0.33±0.13 | $1.3(\pm0.2)\times10^{-3}$ | 0.67±0.13 | 0.9993 |
| *213* | -- | -- | $8.5(\pm2.2)\times10^{-3}$ | 0.30±0.13 | $2.0(\pm0.3)\times10^{-3}$ | 0.70±0.13 | 0.9992 |
| *214* | -- | -- | $8.5(\pm1.6)\times10^{-3}$ | 0.32±0.10 | $2.6(\pm0.1)\times10^{-3}$ | 0.68±0.10 | 0.9993 |
| *217* | -- | -- | $1.2(\pm0.4)\times10^{-2}$ | 0.63±0.09 | $3.8(\pm1.8)\times10^{-3}$ | 0.37±0.09 | 0.9990 |
| *218* | -- | -- | $1.3(\pm0.2)\times10^{-2}$ | 0.56±0.09 | $4.6(\pm0.8)\times10^{-3}$ | 0.44±0.09 | 0.9953 |
| *219* | -- | -- | $1.4(\pm0.1)\times10^{-2}$ | 0.62±0.12 | $4.1(\pm0.7)\times10^{-3}$ | 0.38±0.12 | 0.9945 |
| *220* | $1.1(\pm0.1)\times10^{-2}$ | 1.00±0.00 | -- | -- | -- | -- | 0.9978 |
| *223* | $1.6(\pm0.1)\times10^{-2}$ | 1.00±0.00 | -- | -- | -- | -- | 0.9982 |
| *225* | $1.9(\pm0.4)\times10^{-2}$ | 1.00±0.00 | -- | -- | -- | -- | 0.9748 |
| *227* | $2.2(\pm0.4)\times10^{-2}$ | 1.00±0.00 | -- | -- | -- | -- | 0.9450 |
| *230* | $3.5(\pm0.4)\times10^{-2}$ | 1.00±0.00 | -- | -- | -- | -- | 0.9460 |

### 2.3.4 Homogeneity of the $Co^{2+}$-Substrate Radical Pair Decay Population

A three-temperature annealing protocol was used to address whether the observed slow and fast kinetic components originate from a single, homogeneous active site population, or a heterogeneous population, composed of two kinetically distinct classes of active site. The decay of the $Co^{2+}$- substrate radical pair intermediate at low *T* values, at which the separation in fast and slow rates is greatest, leads to enrichment in the slow component. Decay at 193 K produces a sample composed of >99% slow phase component. The sample temperature was then raised to a set-point at 223 K (20−35 s residence time at *T* > 220 K) and thereafter decreased to a decay measurement temperature of 210 K. The decay at 210 K was found to be biexponential, with $k_{obs,s}$, $A_{obs,s}$ (5.0 ± 1.0 × 10−4 s −1 , 0.58) and $k_{obs,f}$, $A_{obs,f}$ (2.6 ± 0.2 × $10^{-3}$ $s^{-1}$ , 0.42) values that are comparable to the values from the single temperature annealing experiment (Table 2.1). These results show that the observed slow and fast decay populations are in equilibrium, and accessible to each EAL active site, in the temperature range of the monoexponential decay (≥ 220 K). Therefore, the EAL protein is homogeneous (single type of active site), with respect to the origin of the two decay populations. The populations do not arise from a static heterogeneity in EAL, present in the room-temperature solution state of the protein, or caused by conditions during cryotrapping.

## 2.4 Discussion

### 2.4.1 Temperature-Dependent Free Energy Landscape Model

A *T*-dependent FEL is required to explain the origins of the piecewise-continuous Arrhenius dependences for the observed rate constants (Figure 2.6). The bifurcation and kink features are proposed to arise from *T*-dependent contributions of the protein to the FEL, because the intrinsic chemistry of the rearrangement reaction is not expected to introduce the abrupt changes in Arrhenius behavior.

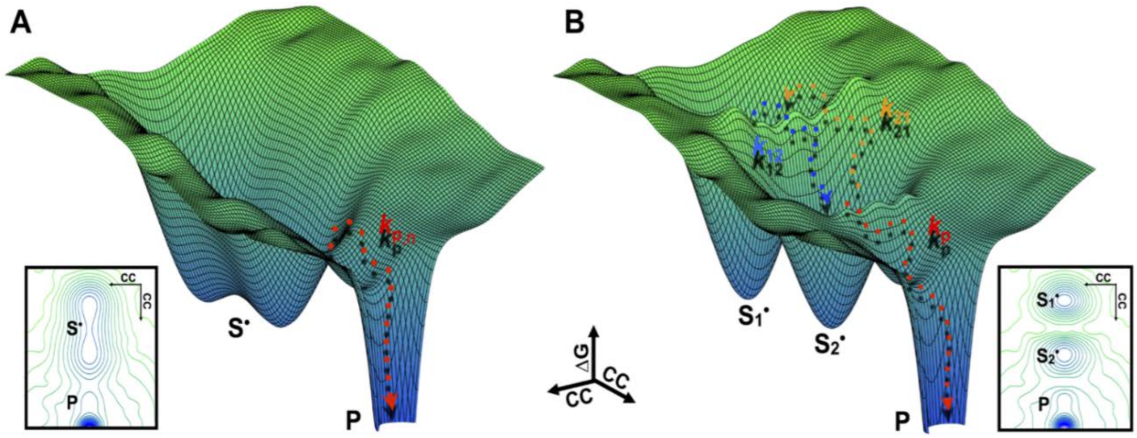

**Figure 2.6. Free energy landscape representations of the substrate radical rearrangement process in EAL**. (A) $T \geq 220$ K. (B) $T < 217$ K. The vertical axis represents the intrinsic free energy of the reactants-protein system, and the horizontal axes are a two-dimensional representation of the multidimensional configuration coordinate (CC). One of many possible trajectories is depicted for steps that correspond to the microscopic rate constants. For clarity, only the principal barriers corresponding to the microscopic rate constants are portrayed, along with an illustrative number of minor minima and maxima, that represent roughness of the FEL topography on free energy scales smaller than the measured

barrier heights. The minima, maxima, and intervening regions represent collections of protein configurational states. At the resolution of the surface mesh, for example, each grid point can be regarded as a different protein configuration. Therefore, multiple protein configurational states, and fluctuations among them, compose an individual trajectory along the reaction coordinate.

The *T*-dependence of the FEL (Figure 2.6) is described with descending *T*, as follows:

Region 1, $T \geq 220$ K: In the native FEL (Figure 2.6A), the $S^{\bullet}$ state encompasses a broad minimum, with many thermally accessible configurational states. This is consistent with the high entropy of the $\mathbf{S}^{\bullet}$ state, relative to the EAL ternary complex ($\Delta S = 45 \pm 3$ cal/mol/K), which was interpreted as caused by an increase in protein configurations.[50] A relatively large entropy for the $\mathbf{S}^{\bullet}$ state in EAL was also found by computational methods.[96] The observed decay of the native $\mathbf{S}^{\bullet}$ state is governed by the single rate constant, $k_{\mathrm{obs,n}}$.

Region 2, $217 \leq T \leq 219$ K: The origin of the bifurcation of $k_{\mathrm{obs,n}}$, leading to $k'_{\mathrm{obs,s}}$ and $k'_{\mathrm{obs,f}}$, is an abrupt transition in the FEL, which gives rise to a barrier (Figure 6B), that partitions the broad $\mathbf{S}^{\bullet}$ minimum into two sequential microstates, $\mathbf{S}_1^{\bullet}$ and $\mathbf{S}_2^{\bullet}$, that differ in protein configuration. This leads to two components of decay: (1) The population in $\mathbf{S}_1^{\bullet}$ follows a sequential path from $\mathbf{S}_1^{\bullet}$ to $\mathbf{S}_2^{\bullet}$, and then $\mathbf{S}_2^{\bullet}$ to **P**. (2) The population in $\mathbf{S}_2^{\bullet}$ decays directly to **P** ($\mathbf{S}_2^{\bullet}$ can also convert to $\mathbf{S}_1^{\bullet}$ and return, prior to decay). The values of $k'_{\mathrm{obs,s}}$ and $k'_{\mathrm{obs,f}}$ display apparent *T*-independence over this relatively narrow range of *T* values, to within one standard deviation (Figure 5). Although the biexponential function provides a good fit, the decays over 217−219 K can also be fitted by a power-law function, which suggests a distribution in the decay rates.[22, 97-98] We attribute this, and the apparent *T*-independence of $k'_{\mathrm{obs,s}}$ and $k'_{\mathrm{obs,f}}$, to protein configurational relaxation that occurs in parallel with the substrate rearrangement process in the transition region, 217−219 K. The kinetics in the 217−219 K region will be addressed by using a coupled reaction-relaxation formalism, in a separate work.

Region 3, $T < 217$ K: The origin of the kinks in the $k'_{\mathrm{obs,s}}$ and $k'_{\mathrm{obs,f}}$ relations at a $T$ value just below 217 K (Figure 5) is represented as a change in the FEL that increases the barrier of the $\mathbf{S_2^{\bullet}} \rightarrow \mathbf{P}$ step (Figure 2.6B). The linear Arrhenius dependence of both $k'_{\mathrm{obs,s}}$ and $k'_{\mathrm{obs,f}}$ at $T < 217$ K indicates that the FEL is $T$-independent on the time scale of the substrate radical decay.

### 2.4.2 Microscopic Kinetic Mechanism

The $T$-dependent FEL model implies a minimal two-step/three-state kinetic mechanism for $T < 217$ K (Figure 2.7-8). Numerical simulations of the amplitude versus time data at the different $T$ values, based on the set of coupled differential equations for the time dependence of the $\mathbf{S_1^{\bullet}}$ , $\mathbf{S_2^{\bullet}}$ , and **P** populations (Equations 2.2-4), provided an excellent match to the data (Figure 2.9). The best-fit microscopic rate constants, $k_{12}$, $k_{21}$, and $k_{\mathrm{P}}$, (Table 2.2) display Arrhenius T-dependence (Figure 2.7 and Table 2.3).

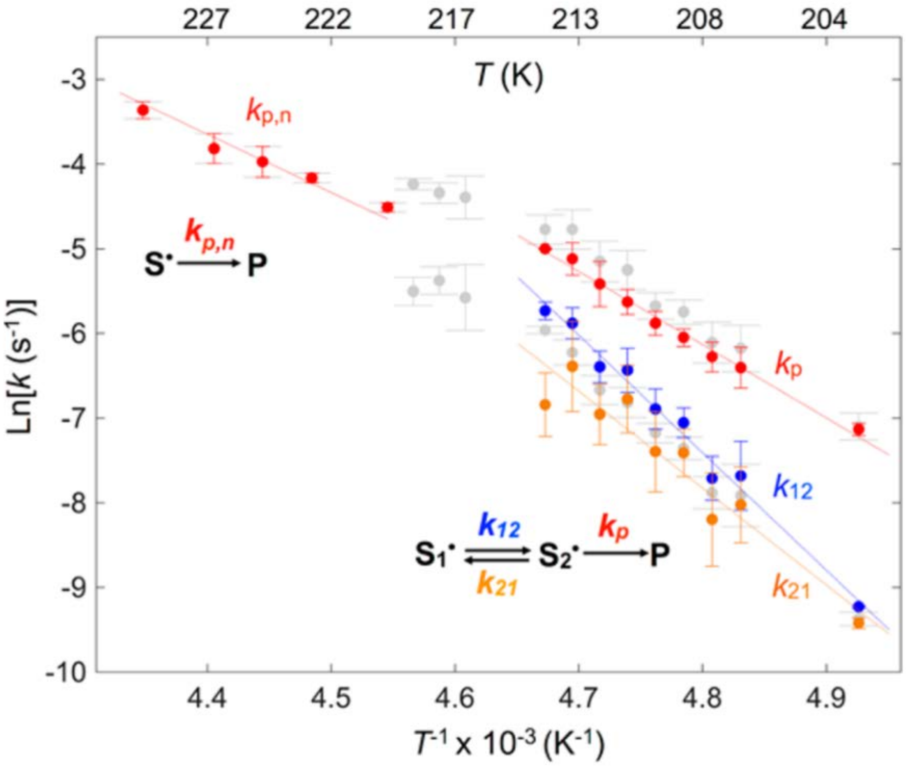

**Figure 2.7. Arrhenius plot of the microscopic rate constants**. The microscopic *k*-values are overlaid on the observed mono- and biexponential rate constants (light gray circles). The mean *k* values for each temperature are shown, and error bars represent the standard deviation for simulations of at least three separate decay measurements.

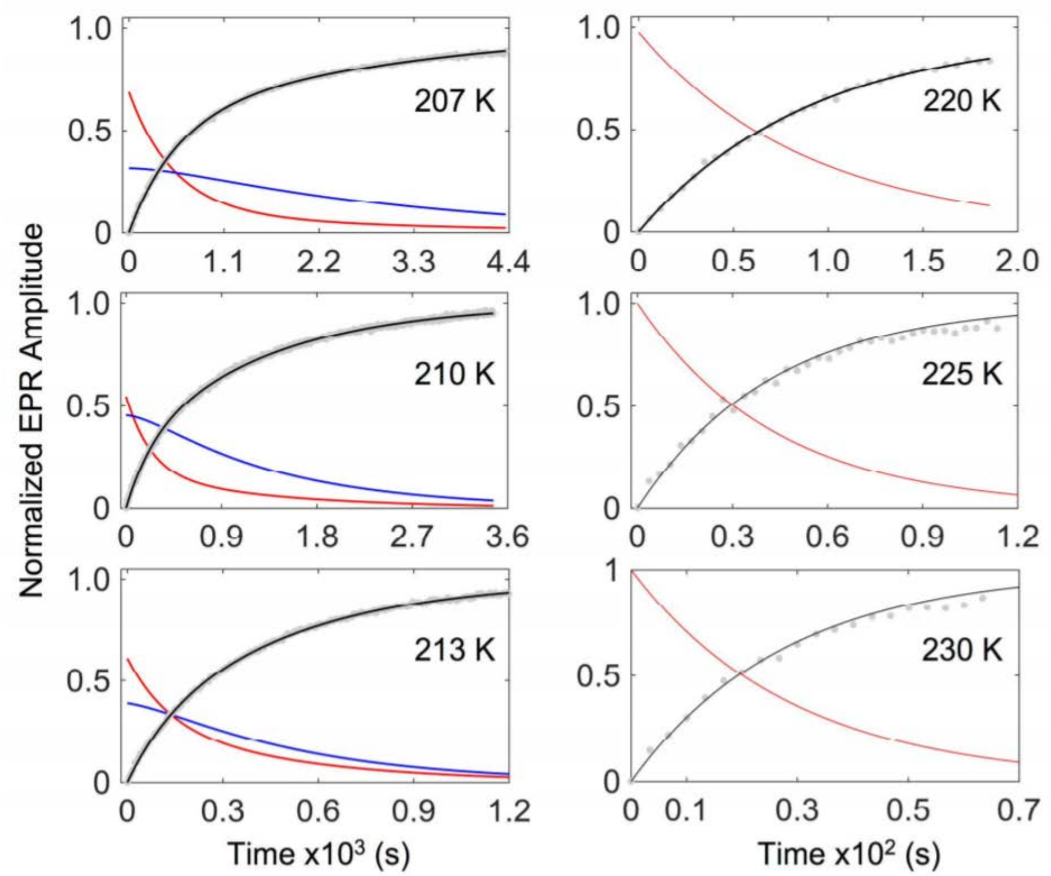

**Figure 2.8. Numerical simulations of the amplitude versus time data at different T values**. Simulations are based on the 3-state, 2-step mechanism and the set of coupled differential equations for the time-dependence of the $\mathbf{S}_1^\bullet$ , $\mathbf{S}_2^\bullet$ , and **P** populations. The time-dependence of the product (**P**) growth represents unity minus the normalized, measured substrate radical decay, as obtained from the EPR amplitudes, and is shown as light grey circles. The simulated **P** growth curve is shown as a black line. The decay of the $\mathbf{S}_1^\bullet$ and $\mathbf{S}_2^\bullet$ states is shown by the red and blue curves, respectively. At $T \geq 220$ K, the single $\mathbf{S}^\bullet$ state decays with first-order kinetics to **P** (red curve only).

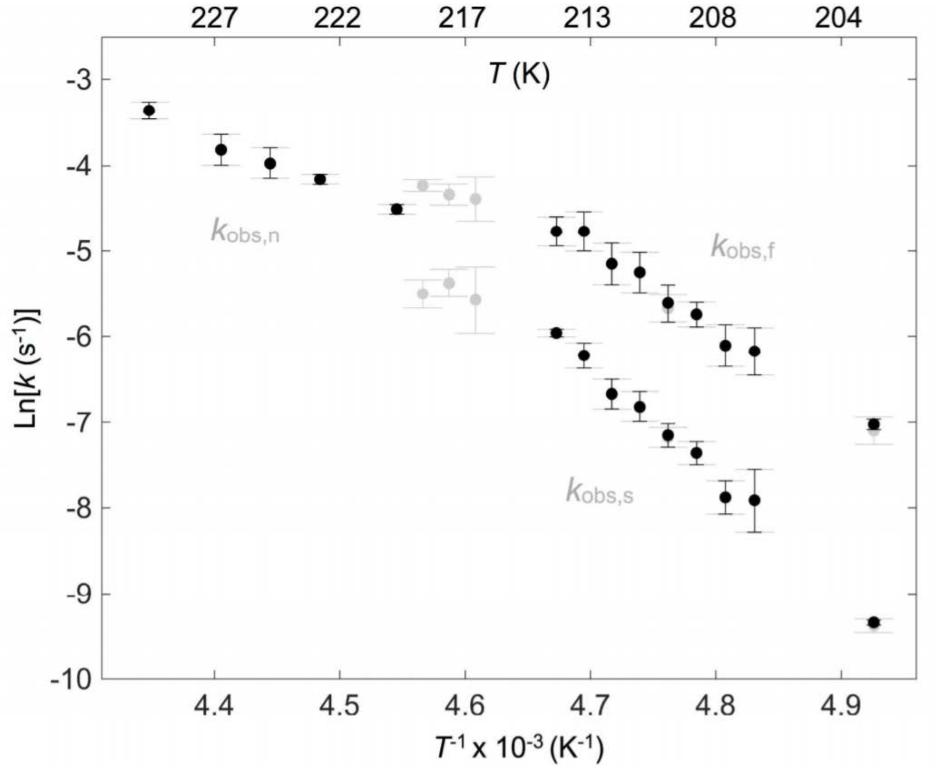

**Figure 2.9. Comparison of the rate constants from the empirical fitting of the substrate radical decay data (grey circles, grey labels) with the rate constants obtained by fitting the numerical simulation** of the time-dependence of the substrate radical decay. Empirical mono- and biexponential fitting of the substrate radical decay data (grey circles, grey labels); mono- and biexponential rate constants obtained by fitting the numerical simulation (black circles). The numerical simulation was based on the model in Scheme 1. The error bars represent the standard deviation for simulations of at least three separate decay measurements.

**Table 2.2. First-order microscopic rate constant and amplitude parameters for the Co2+ - substrate radical pair decay kinetics** at different temperatures, obtained by simulation by using the 3-state, 2-step model.

| $T$ (K) | $[S\bullet]_0$ | $[S\bullet_1]_0$ | $k_{21}$ ($s^{-1}$) | $k_{12}$ ($s^{-1}$) | $[S\bullet_2]_0$ | $k_p$ ($s^{-1}$) | $R^{2\,a}$ |
|---|---|---|---|---|---|---|---|
| 203 | -- | 0.28±0.04 | $8.1(\pm0.5)\times10^{-5}$ | $9.8(\pm0.01)\times10^{-5}$ | 0.72±0.04 | $8.0(\pm0.6)\times10^{-4}$ | 0.9630 |
| 207 | -- | 0.31±0.13 | $3.3(\pm1.8)\times10^{-4}$ | $4.6(\pm2.3)\times10^{-4}$ | 0.69±0.13 | $1.7(\pm0.5)\times10^{-3}$ | 0.9884 |
| 208 | -- | 0.33±0.07 | $2.8(\pm2.0)\times10^{-4}$ | $4.5(\pm1.3)\times10^{-4}$ | 0.67±0.07 | $1.9(\pm0.4)\times10^{-3}$ | 0.9644 |
| 209 | -- | 0.33±0.04 | $6.0(\pm2.0)\times10^{-4}$ | $8.6(\pm1.6)\times10^{-4}$ | 0.67±0.04 | $2.4(\pm0.3)\times10^{-3}$ | 0.9790 |

| | | | | | | | |
|---|---|---|---|---|---|---|---|
| 210 | -- | 0.35±0.06 | 6.1(±3.7) ×$10^{-4}$ | 1.0(±0.3) ×$10^{-3}$ | 0.65±0.06 | 2.8(±0.4) ×$10^{-3}$ | 0.9512 |
| 211 | -- | 0.37±0.10 | 1.1(±0.6) ×$10^{-3}$ | 1.6(±0.5) ×$10^{-3}$ | 0.63±0.10 | 3.6(±0.6) ×$10^{-3}$ | 0.9742 |
| 212 | -- | 0.37±0.13 | 9.5(±4.0) ×$10^{-4}$ | 1.7(±0.3) ×$10^{-3}$ | 0.63±0.13 | 4.4(±1.4) ×$10^{-3}$ | 0.9899 |
| 213 | -- | 0.36±0.07 | 1.7(±1.2) ×$10^{-3}$ | 2.8(±0.6) ×$10^{-3}$ | 0.64±0.07 | 6.0(±1.3) ×$10^{-3}$ | 0.9906 |
| 214 | -- | 0.33±0.06 | 1.1(±0.5) ×$10^{-3}$ | 3.2(±0.4) ×$10^{-3}$ | 0.67±0.06 | 6.7(±0.04) ×$10^{-3}$ | 0.9950 |
| 220 | 1.00±0.00 | -- | -- | -- | -- | 1.1(±0.1) ×$10^{-2}$ | 0.9978 |
| 223 | 1.00±0.00 | -- | -- | -- | -- | 1.6(±0.1) ×$10^{-2}$ | 0.9982 |
| 225 | 1.00±0.00 | -- | -- | -- | -- | 1.9(±0.4) ×$10^{-2}$ | 0.9748 |
| 227 | 1.00±0.00 | -- | -- | -- | -- | 2.2(±0.4) ×$10^{-2}$ | 0.9450 |
| 230 | 1.00±0.00 | -- | -- | -- | -- | 3.5(±0.4) ×$10^{-2}$ | 0.9460 |

**Table 2.3. Arrhenius reaction rate parameters for the microscopic rate constants of the Co2+-substrate radical pair decay.**

| Component | ln[$A_{\mathrm{app}}$ ($s^{-1}$)] | $E_{\mathrm{a,app}}$ (kcal $mol^{-1}$) | $R^2$ [a] |
|---|---|---|---|
| $k_{21}$ | 47.1 (±6.8) | 22.7 (±2.8) | 0.9148 |
| $k_{12}$ | 59.2 (±3.3) | 27.6 (±1.4) | 0.9855 |
| $k_{p,}$ | 35.4 (±1.6) | 17.2 (±0.7) | 0.9906 |
| $k_{p,n}$ | 26.6 (±0.4) | 13.7 (±0.2) | 0.9992 |

### 2.4.3 Specific Native Collective Protein Configurational Fluctuations Guide the Substrate Radical Rearrangement Reaction in EAL

In Figure 2.10, the *T*-dependence of the S• decay rate constants is compared with the NMR-derived motional regimes for a fully hydrated, nanocrystalline protein (protein G, B1 domain),[86] and with the *T*-dependence of the rates at peak amplitude of the *α*-, *β*-, and JG-*β*-fluctuations, measured by dielectric resonance spectroscopy, in two representative globular proteins at defined hydration levels (bovine serum albumin,[15] 0.40 g of $H_2O$/g of protein; lysozyme,[77] 0.36 g of $H_2O$/g of protein).

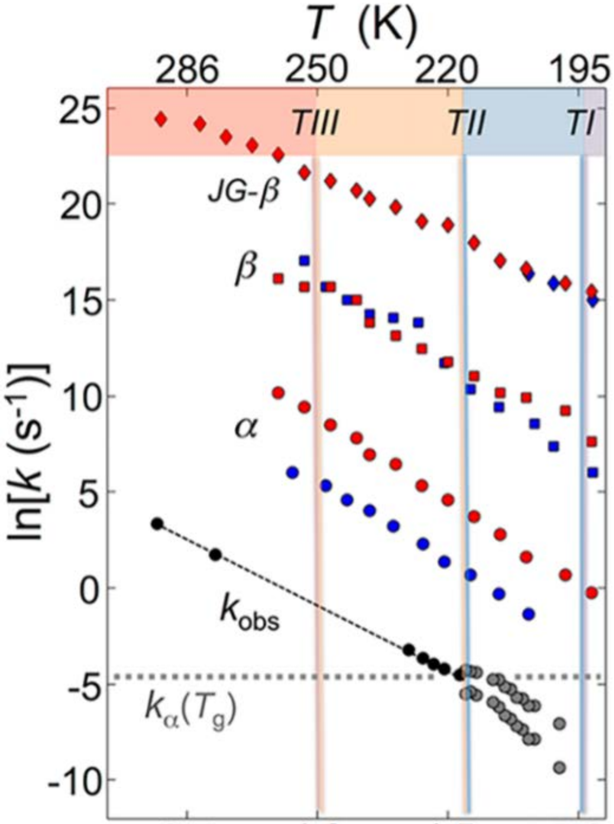

**Figure 2.10. Arrhenius plot of observed rate constants for substrate radical decay in EAL and dynamical parameters from other protein systems**. Data sets: EAL: $k_{obs}$ (black), with linear best-fit of $k_{obs,n}$ (black dashed line), and biexponential decay components (gray). Partially hydrated bovine serum albumin[15] (blue; 0.40 g of $H_2O$/g of protein) and lysozyme[77] (red; 0.36 g of $H_2O$/g of protein): Frequencies corresponding to *α*- (circles), *β*- (squares), and JG-*β*- (diamonds) fluctuations at peak

amplitudes of dielectric loss, measured by broadband dielectric spectroscopy. Hydrated crystalline GB1 protein: TI, TII, TIII, transitions between dominant dynamical regimes, measured by suite of multinuclear NMR relaxation methods.40 The defined value of $k_\alpha = 10^{-2}$ $s^{-1}$ at the glass transition ($T_g$) in fluids[20] is represented (gray dashed line).

The bifurcation and kink temperatures in EAL occur near TII (220 K). The TII transition was interpreted to arise primarily from an increase in amplitude of collective, anisotropic motions of the peptide backbone and multiple amino acid side chains.[86] The $k_{obs,s}$ and $k_{obs,f}$ values for $T < 217$ K fall in the region from TI (195 K) to TII, in which side chain and backbone motions are activated, but restricted to lower amplitudes (localized fluctuations).[86] For the proteins at defined hydration levels (Figure 10), the collective motion (glass) transition in α-fluctuations is shifted to the lower end of the 180−220 K range reported for different proteins[99] by the decrease in hydration level.[15, 100] The calorimetric $T_g$ for bovine serum albumin at 0.40 g of $H_2O$/g of protein is 193 K.[101] This coincides with the intersection of the extrapolated *α*-fluctuation Arrhenius relation for bovine serum albumin and the value of $k_\alpha = 10^{-2}$ $s^{-1}$ , which characterizes the effective quenching of collective fluctuations at the glass transition.[20] The $k_\alpha = 10^{-2}$ $s^{-1}$ criterion for the glass transition is denoted by the dashed line at $\ln k_\alpha = -4.6$ in Figure 9. The *T*-dependence of the EAL kinetics, and comparison with the protein dynamical behaviors, provides the following three insights into coupling of the rearrangement reaction to protein configurations and configurational fluctuations in EAL:

(1). The bifurcation and kink *T* values correspond to TII, and the $k_{obs}$ values in the transition region coincide with the $10^{-2}$ $s^{-1}$ value of $k_\alpha$. Therefore, the results show that the native protein configurational changes, that correspond to the traverse from the $\mathbf{S_1^\bullet}$ to $\mathbf{S_2^\bullet}$ regions of the $\mathbf{S^\bullet}$ minimum, and reaction from the $\mathbf{S_2^\bullet}$ region to form **P**, depend on collective motions (*α*-fluctuations). A primary dependence of the $\mathbf{S_1^\bullet} \rightarrow \mathbf{S_2^\bullet}$ and $\mathbf{S_2^\bullet} \rightarrow \mathbf{P}$ processes on localized (*β*-)

fluctuations would not cause the bifurcation and kinks, because the high rates ($k_{\beta} \gg k_{\mathrm{obs}}$) and Arrhenius dependence of protein $\beta$-fluctuations are maintained across the full $T$ range of the EAL experiments.[22-23]

(2). The presence of two distinct Arrhenius plot slope changes (bifurcation, kinks), with separate effects on the reaction mechanism (rise of the barrier that partitions $\mathbf{S}^{\bullet}$ into $\mathbf{S_1}^{\bullet}$ and $\mathbf{S_2}^{\bullet}$ ; increase in barrier to $\mathbf{S_2}^{\bullet} \rightarrow \mathbf{P}$) indicates that two distinct sets of collective configurational fluctuations have been resolved. These collective fluctuations, and the configurations that they connect, are therefore specific (distinguished from the generic distribution of collective fluctuations in the protein medium) in providing the path for the native rearrangement process (at $T \geq 220$ K) through the multidimensional configuration space.

(3). A remarkable feature is that the bifurcation, defined by the boundary of the $k_{\mathrm{obs,n}}$ and $k'_{\mathrm{obs,s}}$, $k'_{\mathrm{obs,f}}$ dependences, and the kinks at the $k'_{\mathrm{obs,s}}/k_{\mathrm{obs,s}}$, and $k'_{\mathrm{obs,f}}/k_{\mathrm{obs,f}}$ boundaries, occur without a significant discontinuity in the ln $k$ dimension of the Arrhenius plot (Figure 10). Large discontinuities would be expected in the case of a change in the underlying mechanism of the protein structural and dynamical contributions to the reaction (e.g., different protein−substrate interactions). This leads us to conclude that the molecular origin of the bifurcation and kinks is a change from dependence on collective motions to localized, incremental motions, that involve the same sets of protein groups.

### 2.4.4 Correspondence to EAL Protein Structure

Direct (contact) and longer-range favorable and unfavorable electrostatic interactions of the substrate with the surrounding EAL protein structure [37-38] (Figure 2.1) form the underpinning of the FEL (Figure 6). Native collective configuration changes alter the multiple contact and noncontact protein−substrate interactions that minimize free energy barriers involved in the interconversion of $\mathbf{S_1^\bullet}$ and $\mathbf{S_2^\bullet}$ within the $\mathbf{S^\bullet}$ minimum, and reaction from the $\mathbf{S_2^\bullet}$ region to form **P**. Below 217 K, the suppression of collective motions restricts the ability of individual protein−substrate interactions to access the mutual optimal distances and orientations, that provide the pathway of lowest free energy through configuration space, on the decay time scale. This is the microscopic origin of the emergence of the $k_{12}$, $k_{21}$ barrier, and the increase in activation energy $\Delta E_a$ (or $\Delta\Delta H^\dagger$ ) values for $k_P$ at $T < 217$ K, relative to the values for $k_{P,n}$ at $T \geq 220$ K (Tables 3 and 4).

**Table 2.4. Activation enthalpy and entropy values obtained from Eyring analysis of the microscopic rate constants**.

| Component | $\Delta S^\ddagger$ (cal mol$^{-1}$ K$^{-1}$ ) | $\Delta H^\ddagger$ (kcal mol$^{-1}$) |
|---|---|---|
| $k_{21}$ | 33.6 (±13.6) | 22.3 (±2.9) |
| $k_{12}$ | 57.6 (±6.6) | 27.1 (±1.4) |
| $k_{p,}$ | 10.2 (±3.1) | 16.7 (±0.6) |
| $k_{p,n}$ | -7.3 (±0.8) | 13.2 (±0.2) |

Concomitantly, the increase in number of microstates for the pathway of incremental, *β*-fluctuation-associated configuration changes at $T < 217$ K relative to $T \geq 220$ K is the origin of the increase in the A-prefactor (corresponding to $\Delta\Delta S^\dagger > 0$) for $k_P$ at $T < 217$ K, and the relatively large $\Delta S^\dagger$ values for $k_{12}$, $k_{21}$. The changes in $E_a$ ($\Delta H^\dagger$) and *A*-prefactor ($\Delta S^\dagger$ ) with decreasing $T$ correspond to a transition in the FEL topography[88] from “smooth” (collective motions, fewer microstates at $T \geq 220$ K) to “rough” (incremental motions, greater number of microstates at $T <$

217 K) over the $\mathbf{S_1^\bullet} \rightarrow \mathbf{S_2^\bullet} \rightarrow \mathbf{P}$ path, depicted as an increased dimension, or number of grid points, along and transverse to, the reaction coordinate, in Figure 2.6B relative to 2.6A.

## 2.5 Conclusion

The experimental features of first-order kinetic measurement, and a room-to-cryogenic temperature range of 92 K, provide conditions for the direct manifestation of protein dynamical effects on the rate of the core adiabatic, bond-making/bond breaking, chemical step in EAL. The linear Arrhenius relation from 295 to 220 K demonstrates that the native reaction mechanism prevails over this range, connecting the physiological and cryogenic regimes. Over 219 to 217 K, bifurcation and kink transitions in the Arrhenius dependence signal that two distinct sets of collective protein configurational fluctuations become effectively “quenched” on the time scale of the rearrangement process. This reveals two specific sets of native collective protein configurational fluctuations that (1) reconfigure the protein in the substrate radical state, in a reaction enabling step, and (2) provide the adjustments in the protein structure associated with the chemical step. Below 217 K, the substrate radical decay reaction persists, but increases in activation enthalpy and entropy of both the enabling and reaction steps indicate that the non-native reaction coordinate involves local, incremental fluctuations. Continuity in the Arrhenius relations indicates that the same sets of protein groups and interactions mediate the rearrangement over the 295 to 203 K range. However, below 217 K, the suppression of collective motions restricts the ability of individual protein− substrate interactions to access the mutual optimal distances and orientations, that provide the pathway of lowest free energy through configuration space, on the decay time scale.

# Chapter 3

# Characterization of the Kinetic Isotope Effects on the Radical Rearrangement and Second Hydrogen Transfer Step

## 3.1 Introduction

The radical rearrangement step in the catalytic cycle of EAL[27, 57, 102] remains kinetically viable at low temperatures and can be measured using CW-EPR as the substrate radical decays into diamagnetic products.[49, 103] Analysis of the substrate radical decays over a 92 K range revealed two specific sets of native collective protein configurational fluctuations. These fluctuations reconfigure the protein in the substrate radical state through the native reaction coordinate and provide the adjustments in the protein structure associated with the chemical step.[103] Transitions over 219 to 217 K demonstrate the effective quenching of these collective motions and the persistence of the reaction driven by local, incremental fluctuations along the non-native reaction coordinate. In this chapter, we present results for the $Co^{2+}$-substrate radical pair decay kinetics generated from $^2H_4$-aminoethanol from 203- 230 K. Through these experiments we fully account for all the kinetic isotope effects from 203-295, determine the origin of the $S_1^\bullet$ and $S_2^\bullet$ states, and reveal a distinct set of specific collective-atom protein motions that contribute to a different step in the catalytic cycle of EAL: HT2.

### 3.1.1 Kinetic Isotope Effects (KIE)

Specific collective-atom protein motions define the native reaction coordinate for the radical rearrangement step.[103] As the only EPR detectable paramagnetic intermediate during steady-state turnover (for $^1H_4$-aminoethanol substrate samples)[39, 49, 59], the radical rearrangement step is significantly rate determining for the reaction overall. This is consistent with $^{14}N/^{15}N$ steady-state kinetic isotope effect on $V/K_M$, where $V$ is the maximum velocity and $K_M$ is Michaelis constant. These effects contribute to the migration of the amine group on C2 of the substrate radical. [59, 82, 104] (Figure 1). The nitrogen isotope effect detected (1.0017) is less than predicted (1.03), [59, 82] which led to the proposal that at least one of the hydrogen atom transfer steps was rate limiting.[83]

During the first hydrogen transfer step (HT1), the C5′ radical center of the 5’-deoxyadenosyl extracts a hydrogen atom from the C1 carbon of the substrate, which becomes the substrate radical.[43, 105-106] For the second hydrogen transfer step (HT2), a hydrogen migrates from the C5′ to the C2 carbon of the product radical. Both steps exhibit a hydrogen isotope effect (IE): HT2 has a $^{1}H/^{2}H$ IE of 7.4 and a $^{1}H/^{3}H$ IE of 160, HT1 has an $^{1}H/^{3}H$ IE of 4.7.[57, 95, 107] Additionally, the steady-state $^{1}H/^{2}H$ IE of 7.5 was observed on $k_{cat}$, leading to the conclusion that HT2 contributes to the rate determination for steady-state turnover at room temperature.[107]

### 3.1.2 Low Temperature Kinetic Isotope Effects (KIE)

In this chapter, we examine $^{1}H/^{2}H$ IE in the low temperature regime (203- 230 K), where kinetic rates have slowed enough to be EPR detectable and absent of any enzyme turnover. Previous low temperature studies of transient kinetics (fast phase) have attributed any isotope effects to secondary KIEs.[78] The secondary isotope effects arise from the rehybridization of the C1 carbon atom from $sp^3$ to $sp^2$ during the substrate radical step due to force constant changes of the C-H bonds.[108-109] The secondary $^{1}H/^{2}H$ KIE typically range 1.1-1.2, and the theoretical maximum value has been calculated to be 1.4.[110]

### 3.1.3 Microscopic Model Implications

As stated previously, analysis of the substrate radical decays over a 92 K range revealed the contributions of collective configurational fluctuations to the native chemical reaction.[103] These fluctuations are not detectable at room-temperature during steady state kinetic studies[3] because their rates (>$10^6$ $s^{-1}$) are much greater than any chemical reaction rates.[77] However, kinetic studies at low temperatures ($T$< 220K) revealed a bifurcation into two distinct microstates ($S_1^\bullet$ and $S_2^\bullet$) with corresponding rates ($k_{21}$, $k_{12}$, and $k_p$) within the radical rearrangement step. These microscopic parameters manifest from the effective quenching of collective protein configurational fluctuations that reconfigure the native $S^\bullet$ state for reaction. Below this transition, the radical rearrangement step persists and is mediated by local, protein incremental fluctuations along the non-native coordinate. Because the radical rearrangement step is driven by fluctuations in the protein, certain microscopic rates, specifically $k_{12}$, and $k_{21}$, do not have any primary or secondary KIEs. The microscopic rate, $k_p$, is the rate most closely related to the chemical transformation of the $S^\bullet$ to the $P^\bullet$ state. This could involve the C1 rehybridization of the substrate radical state, therefore, it is unclear if $k_p$ exhibits a secondary isotope effect at this time. This chapter shows, through analysis of the $^2H_4$-aminoethanol substrate radical decays over a 92 K range and structural analysis of the two microstates ($S_1^\bullet$ and $S_2^\bullet$), using both CW-EPR and ESEEM paramagnetic techniques, that the radical rearrangement step is driven by protein configurational fluctuations. It also shows any ambient $^1H/^2H$ KIE on the radical rearrangement step is due to HT2 step being partially rate limiting.

## 3.2 Materials and Methods

### 3.2.1 Enzyme Preparation

Enzyme purification and preparation was conducted using the same procedure outlined in previously.[89-90] Briefly, the enzyme was purified from the *Escherichia coli* overexpression system. Reactions were performed in aerobic buffer containing 10 mM potassium phosphate (pH 7.5). Samples were prepared on ice under dim red safe-lighting. The final concentration of enzyme in EPR samples was 10−15 mg/mL. Samples were manually mixed and loaded into a 4 mm outer diameter EPR tube, and the tube was immersed in isopentane ($T$ = 140 K; elapsed time, ~10 s).[51]

### 3.2.2 Time-Resolved, Full Spectrum EPR Measurements of Substrate Radical Decay at Low-T

EPR spectra were collected by the same procedure outlined previously,[51, 103] using the same EPR spectrometer. EPR samples were held at a staging temperature of 160−180 K and temperature was step-increased to decay measurement values of 203−230 K. The time from initiation of the temperature step to the start of acquisition of the first spectrum was 30−60 s.

### 3.2.3 Steady-State Kinetics Measurements

The $k_{cat}$ values were determined from the measured rate of steady-state turnover at saturating substrate concentrations by using the coupled assay with alcohol dehydrogenase and NADH.[30]

### 3.2.4 Transient Kinetics Analysis

EPR spectra were collected between every 5-60 seconds depending on the experimental temperature. The amplitude decay of the derivative feature around g≈2.0 (substrate radical) was fit using a monoexponential ($N$=1) or biexponential ($N$=2) equation (Equation 2.1). The amplitude of the substrate radical is the peak-to-trough difference, with the trough corresponding to the high field trough located at ~338 mT.

### 3.2.5 Numerical simulation and fitting to the microscopic model

The observed decays for the T-range, 203-217 K, were fitted to the 3-state, 2-step microscopic kinetic model (Scheme 2.1), where $S_1^{\bullet}$, $S_2^{\bullet}$ and P are states, and $k_{12}$, $k_{21}$ and $k_P$ are first-order rate constants. The fitting was performed by using programs written in Matlab. The set of ordinary differential equations that describe the time dependence of $S_1^{\bullet}$, $S_2^{\bullet}$ and P (Equations 2.2-4) were solved symbolically by using the *dsolve* function in the Matlab suite. The equations were solved explicitly, under the initial conditions, $S_1^{\bullet} = A_1$, $S_2^{\bullet} = 1\text{-}A_1$ and P = 0, where A1 is the initial concentration of the S1 state. The substrate radical signal decays to zero and forms diamagnetic products. Therefore, the solution for P(t) was fit to the inverse of the substrate radical decay curve by using least squares regression analysis (Equation 2.5). The lsqcurvefit function in

Matlab was used to find the numerical solution for P(t) for each decay. Trust-region-reflective and Levenberg-Marquardt algorithms were used. Both algorithms were shown to have no significant difference between results, with the lower bounds of the step size and the function set to $10^{-10}$.

### 3.2.6 Controlled Sample Decay to Detect Differences in Microscopic States

A controlled sample decay was used to identify structural differences between the two substrate radical microstates ($S_1^\bullet$ and $S_2^\bullet$). The decay amplitude was monitored at $T = 197$ K using the same procedure as the other experimental decays with CW-EPR. The sample was quenched in liquid nitrogen ($T = 77$ K) at 50% and 30% of the initial amplitude the decay was subsequently resumed until the sample reached ~15% of its initial amplitude. The 3-state/2-step kinetic model was applied to the decay and the $S_1^\bullet$ and $S_2^\bullet$ population ratios were determined at 100%, 50%, and 30% of initial amplitude.

### 3.2.7 Pulsed EPR

After the sample was quenched, Electron spin-echo envelope modulation (ESEEM) studies were performed at 50% and 30% of the initial amplitude. ESEEM was also performed on the sample before the decay. ESEEM studies were conducted by Dr. Umar Twahir.

ESEEM spectroscopy was used to identify structural differences in samples where the two substrate radical microstates ($\mathrm{S}_1^\bullet$ and $\mathrm{S}_2^\bullet$) that lead to the kinetic components are varied by using controlled decays. ESEEM experiments were carried out on a home-built spectrometer that operates over a frequency range of 8.2 to 12.4 GHz. The spectrometer is equipped with a FPGApulse programmer, HP83572A MW Synthesizer, Applied Systems Engineering 1 kW pulsed TWT amplifier, and Tektronix TDS 620B digital oscilloscope for signal acquisition. Primary resonator design was a folded strip-line, half-wave resonator. Instrumentation is controlled by software developed and controlled by MATLAB Instrument Control Toolbox.[111-112]

### 3.2.8 Incorporation of the HT2 step into the Microscopic Model

The HT2 step was incorporated into the microscopic model for the temperature ranges 220-230 K and 203-214 K. The microscopic model for the temperature region: $230 \geq T \geq 220$ K was derived from the coupled differential equations associated with a three state/two step kinetic mechanism:

$$S^{\bullet} \underset{k_{PS}}{\overset{k_{P,N}}{\rightleftarrows}} P^{\bullet} \xrightarrow{k_{HT}} PH \qquad \text{Scheme 3.1}$$

where the parameters $S^{\bullet}$ and $k_{\mathrm{P,N}}$ correspond to the same microscopic parameters in the previous kinetic mechanism[103] that describes the radical rearrangement. $P$ has been replaced with $P^{\bullet}$ to represent the product radical and $PH$ represents the diamagnetic product. The microscopic rate $k_{\mathrm{PS}}$ is the back rate, from $P^{\bullet}$ to $S_2^{\bullet}$, and $k_{\mathrm{HT}}$ are associated with the HT2 step. The corresponding differential equations for Scheme 3.1 are as follows:

$$^{dS^\bullet}/_{dt} = -S^\bullet\ k_{P,N} + P^\bullet\ k_{PS} \tag{3.1}$$

$$^{dP^\bullet}/_{dt} = S^\bullet\ k_{P,N} - P^\bullet\ k_{PS} - P^\bullet\ k_{HT} \tag{3.2}$$

$$^{dPH}/_{dt} = P^\bullet\ k_{HT} \tag{3.3}$$

The microscopic model for the temperature region: 214 ≥ $T$ ≥ 203 K was derived from the coupled differential equations associated with a four state/three step kinetic mechanism:

$$S_1^\bullet \underset{k_{21}}{\overset{k_{12}}{\rightleftarrows}} S_2^\bullet \underset{k_{PS}}{\overset{k_P}{\rightleftarrows}} P^\bullet \xrightarrow{k_{HT}} PH \qquad \text{Scheme 3.2}$$

where the decay was the summation of the $S_1^\bullet$ and $S_2^\bullet$ concentrations as a function of time for $T < 217$ K. The parameters $S^\bullet$, $S_1^\bullet$, $S_2^\bullet$, $k_{12}$, $k_P$, and $k_{21}$ correspond to the same microscopic parameters in the previous kinetic mechanism and are associated with the radical rearrangement.[103] $P$ has been replaced with $P^\bullet$ to represent the product radical and $PH$ represents the diamagnetic product. The microscopic rate $k_{PS}$ is the back rate, from $P^\bullet$ to $S_2^\bullet$, and $k_{HT}$ are associated with the HT2 step. The corresponding differential equations to the microscopic model (Scheme 3.2):

$$dS_1^{\bullet}/_{dt} = S_2^{\bullet}\ k_{21} - S_1^{\bullet}\ k_{12} \tag{3.4}$$

$$dS_2^{\bullet}/_{dt} = S_1^{\bullet}\ k_{12} - S_2^{\bullet}\ k_{21} - S_2^{\bullet}\ k_{P} + P^{\bullet}\ k_{PS} \tag{3.5}$$

$$dP^{\bullet}/_{dt} = S_2^{\bullet}\ k_P - P^{\bullet}\ k_{PS} - P^{\bullet}\ k_{HT} \tag{3.6}$$

$$dPH/_{dt} = P^{\bullet}\ k_{HT} \tag{3.7}$$

### 3.2.9 Numerical simulation and fitting to the HT2 Incorporated Microscopic Model

The observed decays for the T-range, 230-220 K, were fitted to the 3-state, 2-step microscopic kinetic model (Scheme 3.1), where $S^{\bullet}$, $P^{\bullet}$ and PH are states, and $k_{P,N}$, $k_{PS}$ and $k_{HT}$ are first-order rate constants. The fitting was performed by using programs written in Matlab. The set of ordinary differential equations that describe the time dependence of $S^{\bullet}$, $P^{\bullet}$ and PH (Equations 3.1-3) were solved symbolically by using the *dsolve* function in the Matlab suite. The equations were solved explicitly, under the initial conditions, $S^{\bullet} = 1$, $P^{\bullet} = 0$ and PH = 0. The substrate radical signal decays to zero and forms diamagnetic products. Therefore, the solution for S(t) was to fit to the substrate radical decay curve by using least squares regression analysis (Equation 2.5). The lsqcurvefit function in Matlab was used to find the numerical solution for P(t) for each decay. Trust-region-reflective and Levenberg-Marquardt algorithms were used. Both algorithms were shown to have no significant difference between results, with the lower bounds of the step size and the function set to $10^{-10}$. The first order rate constant, $k_{P,N}$ ,was fixed to the corresponding average value $^1H_4$ radical pair decays (Table 2.3). This was based on the conclusion from other experiments [57, 95, 107, 110] (Figure 3.7-8) that HT2 is the only detectable rate-limiting step exhibiting a hydrogen IE and rate constants associated with the substrate radical step that are unaffected by the change in substrate from $^1H_4$-aminoethanol to $^2H_4$-aminoethanol.

The observed decays, for the T-range, 214-203 K, were fitted to the 4-state, 3-step microscopic kinetic model (Scheme 3.2), where $S_1^•$, $S_2^•$, $P^•$ and PH are states, and $k_{12}$, $k_{21}$, $k_{P,N}$, $k_{PS}$ and $k_{HT}$ are first-order rate constants. The fitting was performed by using programs written in Matlab. The set of ordinary differential equations that describe the time dependence $S_1^•$, $S_2^•$, $P^•$ and PH (Equations 3.4-7) were solved symbolically by using the *dsolve* function in the Matlab suite. The equations were solved explicitly, under the initial conditions, $S_1^• = 0.33$, $S_2^• = 0.67$, $P^• = 0$, and PH = 0. The first order rate constants, $k_{12}$, $k_{21}$, and $k_{P,N}$, and the initial concentrations of the $S_1^•$ and $S_2^•$ states were fixed to the corresponding average value $^1H_4$ radical pair decays (Table 2.3). This was based on the conclusion from other experiments [57, 95, 107, 110] (Figure 3.7-8) that the substrate radical step is unaffected by the change in substrate from $^1H_4$-aminoethanol to $^2H_4$-aminoethanol. Because both $S_1^•$ and $S_2^•$ states describe the substrate radical state, and are not distinguishable by CW-EPR spectroscopy, the substrate radical decay was fit to the summation of solutions for $S_1^•(t)$ and $S_2^•(t)$.

### 3.2.10 Construction of Simulated Decays

The fitting of the microscopic model that incorporates the HT2 step to the experimental substrate radical decays were not well constrained, exhibiting large 95% confidence intervals, and results were dependent on the initial conditions (see Discussion). Therefore, the microscopic rate constants $k_{PS}$ and $k_{HT}$ could not be determined explicitly. To remedy this, the value of $k_{PS}$ is fixed and the value of $k_{HT}$ is varied in order to determine the ratio: $\frac{k_{HT}}{k_{PS}}$. These “simulated” decays are then directly compared to the observed $^2H_4$-aminoethanol experimental decays to gain further insight into the apparent IEs of the observed rate constants $k_{obs,f}$ and $k_{obs,s}$.

These simulated decays were generated from the solutions to Equations 3.1-3, for the three-state, two-step model, under the initial conditions, $S^\bullet = 1$, $P^\bullet = 0$ and PH = 0 for $295 \geq T \geq 220$ K. The rate constant, $k_{P,N}$, was fixed to the corresponding average value $^1H_4$ radical pair decays(Table 2.3).[103] For $213 \geq T \geq 207$ K, the simulated decays were generated from the solutions to Equations 3.4-7 under the initial conditions, $S_1^\bullet = 0.33$, $S_2^\bullet = 0.67$, $P^\bullet = 0$, and PH = 0, for the simulated decays. The first order rate constants $k_{12}$, $k_{21}$, and $k_{P,N}$, and the initial concentrations of the $S_1^\bullet$ and $S_2^\bullet$ states were fixed to the corresponding average value $^1H_4$ radical pair decays (Table 2.3). [103] Another set of simulated decays were generated under the same initial conditions, however the rate constant, $k_{P,N}$, was fixed 1.4x slower than the corresponding average value $^1H_4$ radical pair decays (Table 2.3). This represented the theoretical limit of a secondary isotope effect on $k_{P,N}$ for both temperature regions ($295 \geq T \geq 220$ K and $213 \geq T \geq 207$).

The simulated decays had two strict criteria. (1) The product radical concentration ($[P^\bullet]$) must remain less than 0.001 (for aminopropanol substrate)[113] relative to $[S^\bullet]$ throughout the decay (the product radical has never been observed in any CW EPR experiments even though it is paramagnetic), and (2) the simulated decays must exhibit the same transient kinetic behavior as the experimental decays: for $230 \geq T \geq 220$ K the decay is monoexponential and for $T < 217$ K the decay is biexponential. To fulfill the first criteria, the rate constant, $k_{PS}$, was set 1000-fold faster than $k_{P,N}$ ($T \geq 220$ K) and $k_P$ (for $T \leq 214$ K). The microscopic rate parameter $k_{HT}$ was then varied from 0.1 – 7 x the value of $k_{PS}$.

The simulated decays were fit to either a monoexponential ($T \geq 220$ K) or biexponential ($T \leq 214$ K), to determine the relationship between the transient IE and the $\frac{k_{HT}}{k_{PS}}$ ratio. The observed rate constants from these fits to the simulated decays were compared to the observed rate constants from $^1H_4$ radical pair decays (Table 2.3). An IE (for observed rate constants) vs $\frac{k_{HT}}{k_{PS}}$ plot was generated for both temperature regimes based on the simulated results and the observed rate constants from $^1H_4$ radical pair decays. The $\frac{k_{HT}}{k_{PS}}$ ratio for the experimental $^2H_4$ radical pair decays were calculated using these results.

## 3.3 Results

### 3.3.1 Full-Spectrum EPR Measurements of the Co(II)-Substrate Radical Pair

Figure 3.1 shows the initial EPR spectral scan collected during the signal decay of the of the $^2H_4$-aminoethanol generated Co(II)- substrate radical pair at 207 K.

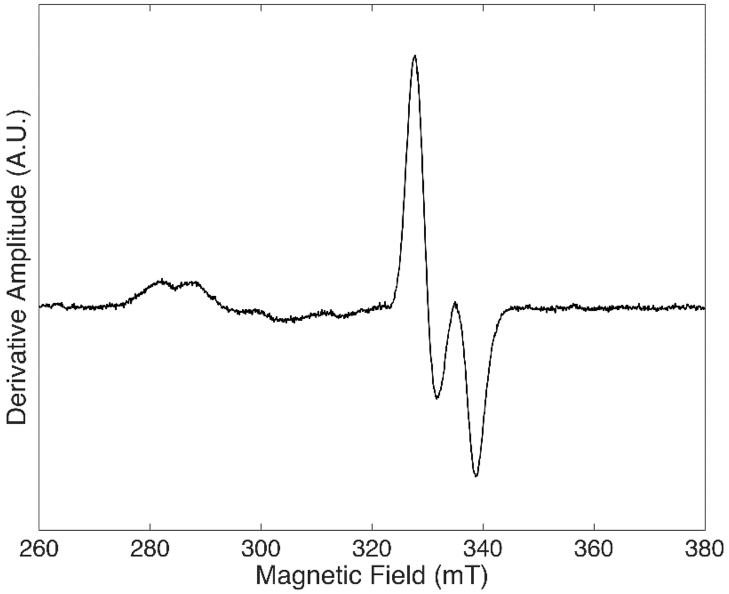

**Figure 3.1 Electron paramagnetic resonance spectrum of the aminoethanol-generated Co(II)-substrate radical pair EPR spectrum for deuterated substrate**. *EPR conditions*: microwave frequency: 9.3427 GHz; microwave power, 20 mW; magnetic field modulation, 1.0 mT; modulation frequency, 100 kHz; temperature 207 K; single scan.

The unpaired electron spins give rise to two major features at 285 mT and 345 mT. Inhomogeneous broadening of the Co(II) feature, relative to isolated cob(II)alamin, because of its interaction with the unpaired electron on C1 of the substrate radical.[63] The substrate radical feature (325 to 345 mT) is split into a doublet and broadened by the interaction with the Co(II) unpaired electron spin.[39, 63] These features of the CoII-substrate radical pair spectrum can be accounted for by EPR simulations.[60-61]

EPR spectra were collected during the decay of the substrate radical for temperatures 203-230 K**.** Figure 3.2 is an example of such a decay at 210 K (substrate radical), both the substrate -radical and Co(II) decay simultaneously[78], here, only the substrate radical signal was collected to increase time resolution. No other paramagnetic species was detected, which is consistent with $^1H_4$-aminoethanol substrate samples.

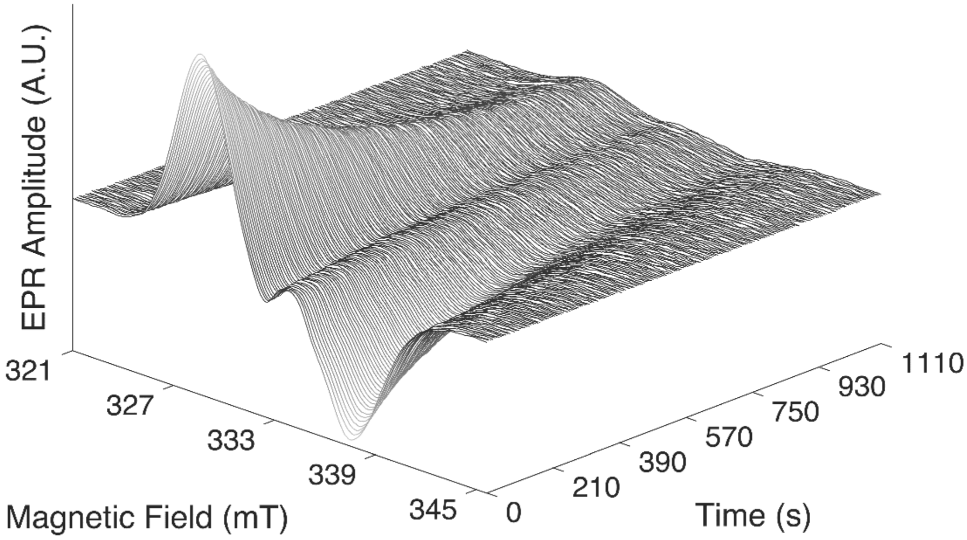

**Figure 3.2 EPR spectral time series.** Amplitudes represent a moving average over 5 spectra for 410 total spectra. EPR conditions: microwave frequency, 9.3381GHz; microwave power, 20 mW; magnetic field modulation, 1.0 mT; modulation frequency, 100 kHz

### 3.3.2 Characterization of the Substrate Radical Rearrangement Step

Figure 3.3 shows the amplitude decay of the substrate radical feature. The observed decays exhibited monoexponential decay behavior for $T \geq 220$ K and biexponential decay behavior for $T < 220$ K.

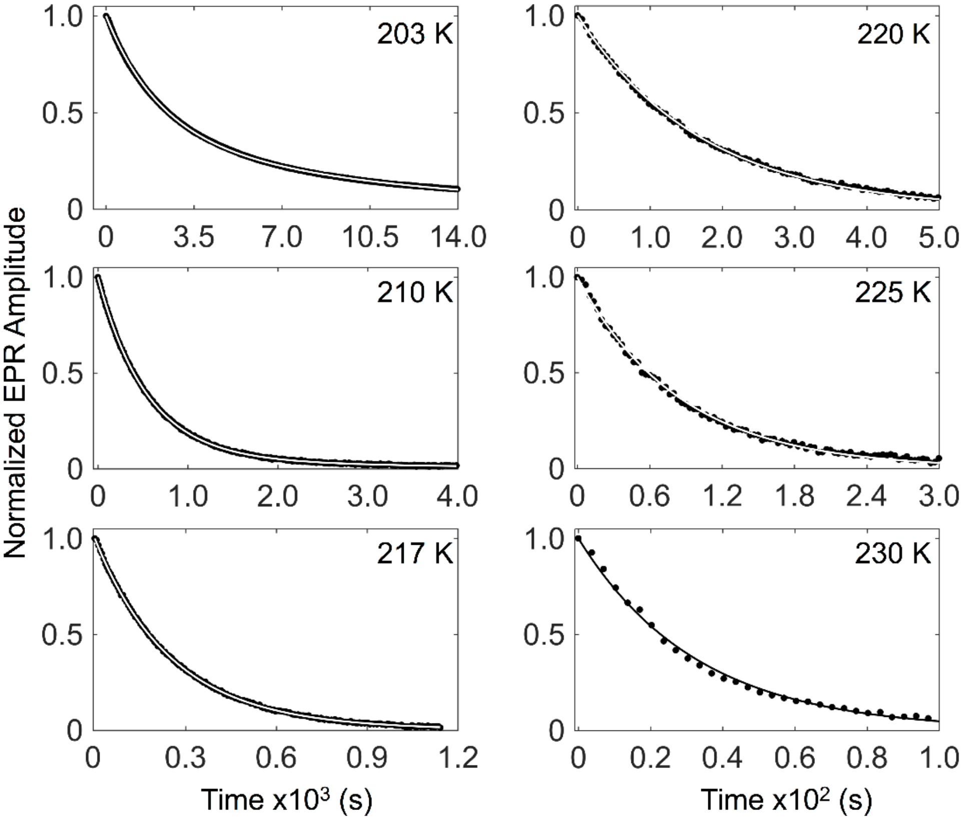

**Figure 3.3. The time-dependent decay of the EPR amplitude of the substrate radical at selected T values.** The decays are overlaid with the best-fit monoexponential ($T \geq 220$ K) or biexponential functions ($T < 220$ K), represented as a line. EPR amplitudes are normalized to the zero-time value.

Figure 3.4 depicts the Arrhenius behavior of the observed rate constants: $k_{\text{obs,f}}$ and $k_{\text{obs,s}}$ over a wide range of temperatures for $^2H_4$-aminoethanol (black) and $^1H_4$-aminoethanol (gray) generated substrate radical amplitude decay. Each point represents the observed rate constant averaged over three samples. The observed rate constants along with their respective standard deviations and $R^2$ vales are recorded in Table 3.1 along with the apparent IEs (Table 3.2).

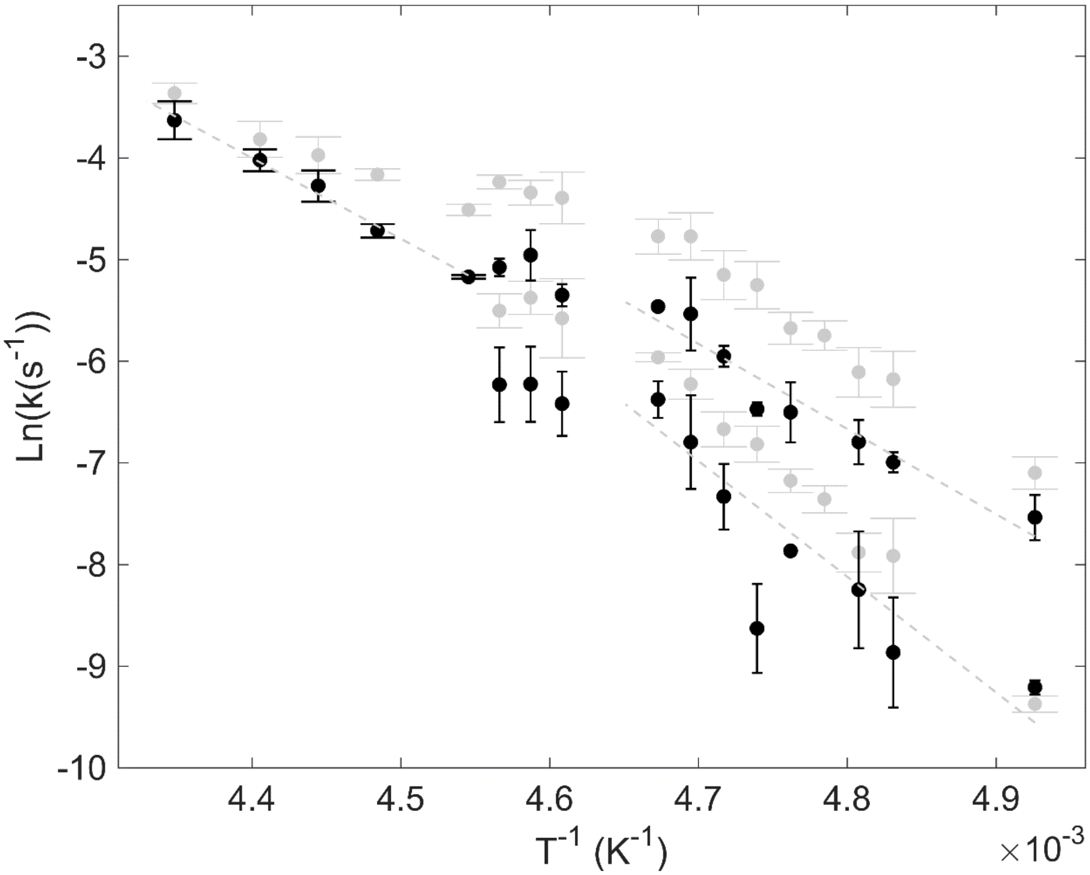

**Figure 3.4**. **Arrhenius plot of observed first-order rate constants for deuterated (black) and protiated (gray)**. The mean $k_{obs}$ value for each temperature is shown, with standard deviation representing at least three separate decay measurements. Dashed lines represent the best linear fit to the data for $k_{obs,n}$ (220−295 K), $k_{obs,s}$, and $k_{obs,f}$ (203−214 K). The error bars represent the standard deviation of at least three samples.

The Arrhenius behavior of the observed rate constants from the substrate radical decay can be characterized into linear dependencies (Figure 3.4, dashed lines). The *native* dependency describes those samples that were monoexponential from 230 ≤ $T$ ≤ 220 K). The *fast* and *slow* dependencies arise from the bi-phasic decays from 217 < $T$ ≤ 203 K.  There is also a region between 220 < $T$ ≤ 217 K, where the kinetic rate displays no significant temperature dependence.

**Table 3.1 First-order rate constant and amplitude parameters** for the fit of the biexponential function to the $\mathrm{Co^{II}}$-substrate radical pair decay kinetics at different temperatures for deuterated substrate with $^{1}H$ / $^{2}H$ isotope effect in bold for each kinetic rates.

| $T$ (K) | $k_{\mathrm{obs,n}}$ ($\mathrm{s^{-1}}$) | $k_{\mathrm{obs,f}}$ ($\mathrm{s^{-1}}$) | $A_{\mathrm{obs,f}}$ | $k_{\mathrm{obs,s}}$ ($\mathrm{s^{-1}}$) | $A_{\mathrm{obs,s}}$ [a] | $R^2$ [b] |
|---|---|---|---|---|---|---|
| 203 | -- | $5.3(\pm1.3)\times10^{-4}$ | 0.52±0.11 | $1.0(\pm0.07)\times10^{-4}$ | 0.48±0.11 | 0.9997 |
| 207 | -- | $9.1(\pm0.1)\times10^{-4}$ | 0.71±0.16 | $1.4(\pm1.0)\times10^{-4}$ | 0.29±0.16 | 0.9707 |
| 208 | -- | $1.1(\pm0.3)\times10^{-3}$ | 0.64±0.10 | $2.6(\pm0.2)\times10^{-4}$ | 0.36±0.10 | 0.9991 |
| 210 | -- | $1.5(\pm0.5)\times10^{-3}$ | 0.67±0.39 | $3.8(\pm0.1)\times10^{-4}$ | 0.33±0.39 | 0.9999 |
| 211 | -- | $1.5(\pm0.1)\times10^{-3}$ | 0.81±0.01 | $1.8(\pm1.0)\times10^{-4}$ | 0.19±0.01 | 0.9980 |
| 212 | -- | $2.6(\pm0.2)\times10^{-3}$ | 0.71±0.05 | $6.5(\pm2.5)\times10^{-4}$ | 0.29±0.05 | 0.9987 |
| 213 | -- | $3.9(\pm1.6)\times10^{-3}$ | 0.52±0.36 | $1.1(\pm0.7)\times10^{-3}$ | 0.48±0.36 | 0.9988 |
| 214 | -- | $4.2(\pm0.1)\times10^{-3}$ | 0.31±0.23 | $1.7(\pm0.3)\times10^{-3}$ | 0.69±0.23 | 0.9997 |
| 217 | -- | $4.7(\pm0.5)\times10^{-3}$ | 0.80±0.04 | $1.6(\pm0.6)\times10^{-3}$ | 0.20±0.04 | 0.9992 |
| 218 | -- | $7.0(\pm1.9)\times10^{-3}$ | 0.70±0.25 | $2.0(\pm0.9)\times10^{-3}$ | 0.30±0.25 | 0.9988 |
| 219 | -- | $6.2(\pm0.6)\times10^{-3}$ | 0.81±0.04 | $2.0(\pm0.9)\times10^{-3}$ | 0.19±0.04 | 0.9984 |
| 220 | $5.7(\pm0.1)\times10^{-3}$ | -- | -- | -- | -- | 0.9988 |
| 223 | $8.9(\pm0.6)\times10^{-3}$ | -- | -- | -- | -- | 0.9983 |
| 225 | $1.4(\pm0.2)\times10^{-2}$ | -- | -- | -- | -- | 0.9971 |
| 227 | $1.8(\pm0.2)\times10^{-2}$ | -- | -- | -- | -- | 0.9899 |
| 230 | $2.6(\pm0.5)\times10^{-2}$ | -- | -- | -- | -- | 0.9867 |

**Table 3.2 Apparent $^1H$ / $^2H$ Kinetic Isotope Effect (KIE) for the first-order rate constant and amplitude parameters** for the fit of the biexponential ($T < 220$ K) or monoexponential function ($T \geq 220$ K) to the Co$^{II}$-substrate radical pair decay kinetics at different temperatures for deuterated substrate.

| $T$ (K) | *KIE* [$k_{obs,N}$] | *KIE* [$k_{obs,f}$] | *KIE* [$k_{obs,s}$] |
|---|---|---|---|
| 203 | -- | 1.6 ± 0.5 | 0.9 ± .01 |
| 207 | -- | 2.3 ± 0.8 | 2.6 ± 1.2 |
| 208 | -- | 2.0 ± 0.8 | 1.5 ± 0.3 |
| 210 | -- | 2.3 ± 0.8 | 2.0 ± 0.1 |
| 211 | -- | 3.5 ± 0.5 | 6.1 ± 3.6 |
| 212 | -- | 2.2 ± 0.3 | 2.0 ± 0.8 |
| 213 | -- | 2.2 ± 1.0 | 1.8 ± 1.2 |
| 214 | -- | 2.0 ± 0.5 | 1.5 ± 0.3 |
| 217 | -- | 2.6 ± 0.4 | 2.4 ± 1.4 |
| 218 | -- | 1.9 ± 0.8 | 2.3 ± 1.1 |
| 219 | -- | 2.3 ± 0.3 | 2.1 ± 1.0 |
| 220 | 1.9 ± 0.2 | -- | -- |
| 223 | 1.8 ± 0.2 | -- | -- |
| 225 | 1.4 ± 0.3 | -- | -- |
| 227 | 1.2 ± 0.2 | -- | -- |
| 230 | 1.3 ± 0.2 | -- | -- |

### 3.3.3 ESEEM and Controlled Decays

Pulsed-EPR experiments are to detect any geometric structural differences between the $S_1^\bullet$ and $S_2^\bullet$ microstates, manifested in the substrate radical and its direct interactions with the protein. These states are predicted from the 3-state, 2-step kinetic model (Scheme 2.1), as the source of the kinetic bifurcation (Figure 3.4). Figure 3.5 shows the EPR peak-to-trough amplitude of the Co(II)-substrate radical decay at 197 K and corresponding fit to the 3-state, 2-step kinetic model. The KIE for slow and fast phases were calculated (0.6 ± 0.2 and 1.3 ± 0.3 respectively), therefore the 3-state, 2-step kinetic model is adequate to estimate the $S_1^\bullet$ and $S_2^\bullet$ microstate populations.

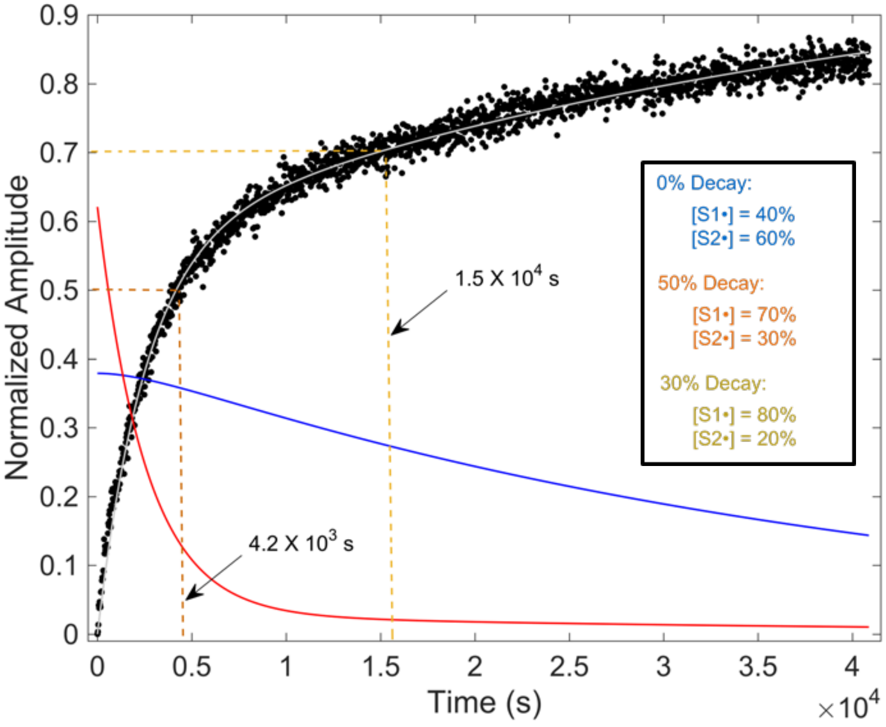

**Figure 3.5 Model fit of the amplitude versus time data at 197 K.** Simulations are based on the 3-state, 2-step kinetic model and the corresponding set of coupled differential equations that describe the time-dependence of the $S_1^\bullet$ (blue), $S_2^\bullet$ (red), and *P* (gray). The product growth is represented as the difference between the initial normalized amplitude and the substrate radical decay from the experiment (black). The yellow and orange dashed lines represent the time points and corresponding amplitudes the decay

measurement was stopped and the sample was quenched to preform ESEEM experiments. The inset describes the overall decay and the recalculated $S_1^{\bullet}$ and $S_2^{\bullet}$ concentration percentages.

The corresponding set of coupled differential equations associated with the 3-state, 2-step kinetic model (Scheme 2.1) describe the time-dependence of the $S_1^{\bullet}$ (blue), $S_2^{\bullet}$ (red), and *PH* (gray). The product growth is represented as the difference between the initial normalized amplitude and the substrate radical decay. The yellow and orange dashed lines represent the time points and corresponding amplitudes at which the decay measurement was stopped and the sample was quenched to preform ESEEM experiments. The inset shows the overall decay and the recalculated $S_1^{\bullet}$ and $S_2^{\bullet}$ concentration percentages.

Figure 3.6.A shows the three-pulse ESEEM waveforms of the Co(II)-substrate radical intermediate at 100%, 50%, and 30% of the initial amplitude.

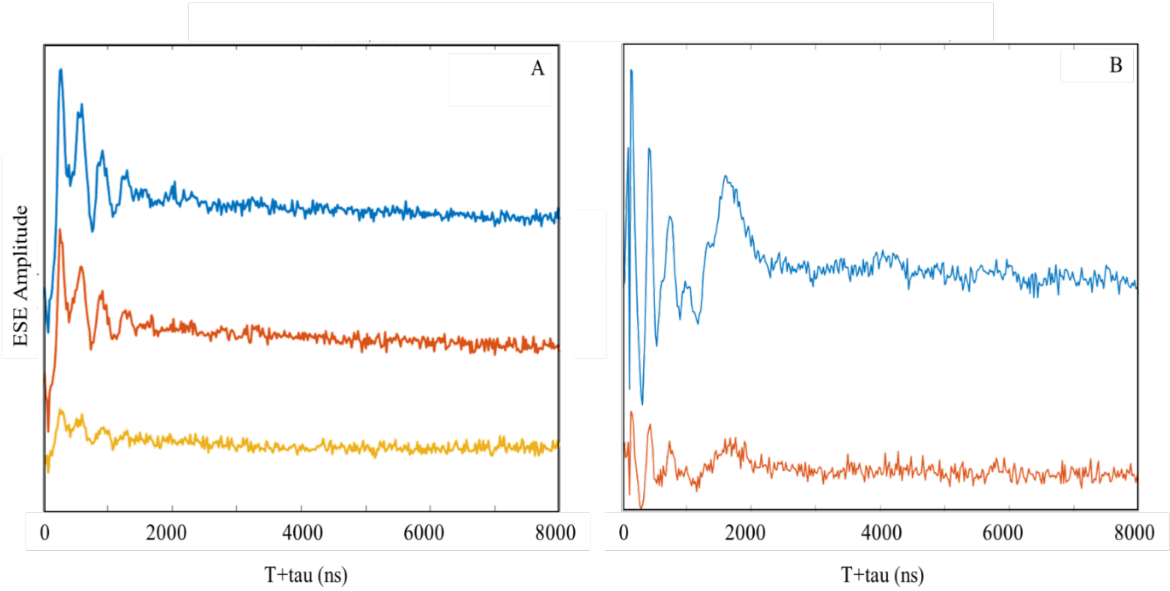

**Figure 3.6. Three-pulse ESEEM waveforms**. (A) the Co(II)-substrate radical intermediate for the un-decayed (blue), 50% decayed (red) and 30% decayed (orange) samples collected at 8.703 GHz, 3109 Gauss (A) and at 10.770 GHz, 3847 Gauss (B). Un-decayed, 50% and 30% decayed samples contain 40:60, 67:33 and 80:20 of $S_1^{\bullet}$:$S_2^{\bullet}$, respectively.

Figure 3.6.B depicts the Three-pulse ESEEM waveforms of the Co(II)-substrate radical intermediate 100% and 50% of the initial amplitude.

Cosine Fourier transforms of the 3-pulsed wave forms collected at 8.703 GHz, 3109 Gauss for 100%, 50%, and 30% of initial amplitude (Figure 3.8.A) reveal three groups of couplings: (1) strongly coupled $^2H_s$ and (2) weakly coupled $^2H_w$ from the C5’ methyl group of 5’-deoxyadenosine moiety, and (3) strongly coupled $^2H_{\beta a}$ from the C2 of the substrate radical of $^2H$ hyperfine of couplings. Cosine Fourier transforms of the 3-pulsed wave forms collected at 10.770 GHz, 3847 Gauss for 100% and 50% of initial amplitude (Figure 3.8.B) reveal a fourth strong coupling that corresponds to the strongly coupled $^2H_{\beta b}$ from the C2 of the substrate radical.

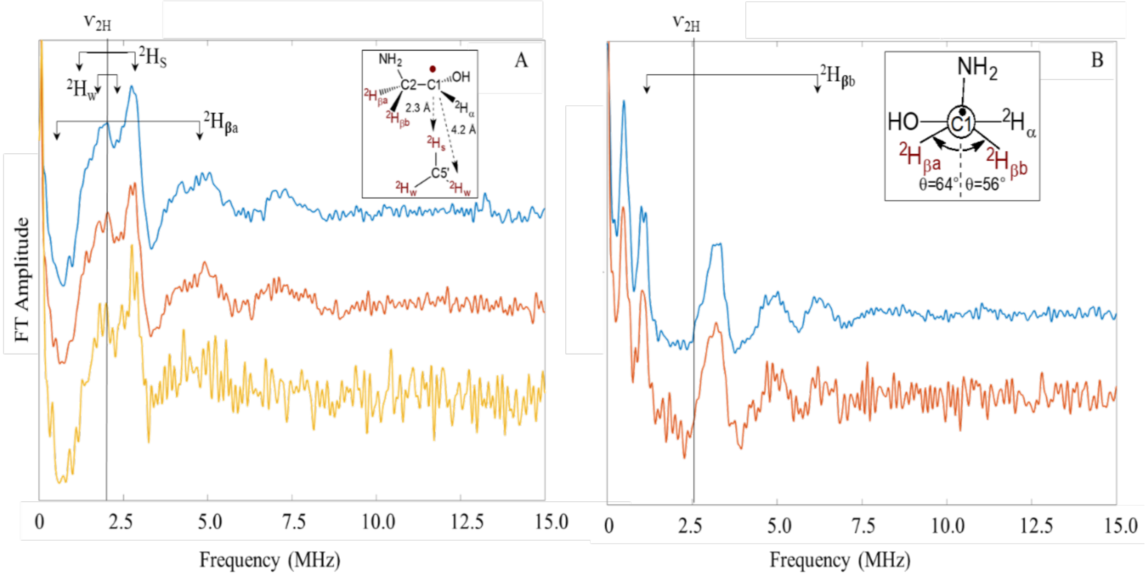

**Figure 3.7. Cosine Fourier transform of the waveforms.** Three groups of couplings are observed in A: (1) strongly coupled $^2H_s$ and (2) weakly coupled $^2H_w$ from the C5’ methyl group of 5’-deoxyadenosine moiety, and (3) strongly coupled $^2H_{\beta a}$ from the C2 of the substrate radical. In B, a fourth strong coupling is observed in Figure 6B, corresponding to the strongly coupled $^2H_{\beta b}$ from the C2 of the substrate radical. The structure, angles, and distances for $^2H$’s are illustrated in the insets.

## 3.4 Discussion

### 3.4.1 Temperature-Dependent Free Energy Landscape and Microscopic Model

The observed kinetics from the $^2H_4$-aminoethanol generated Co(II)- substrate radical pair decays (Figure 3.4) exhibit the same features as $^1H_4$-aminoethanol generated Co(II)- substrate radical pair decays. This can be described by a temperature-dependent FEL with three distinct temperature regimes outlined in Chapter 2. In brief, for Region 1 ($T \geq 220$ K), the FEL contains a broad minimum ($S^\bullet$ state) that directly feeds into the $P$ state. Region 2 ($217 \leq T \leq 219$ K) contains the bifurcation, which describes a temperature dependent barrier that separates the $S^\bullet$ state into two separate microstates: $S_1^\bullet$ and $S_2^\bullet$, which follows a sequential path to the $P$ state. In Region 3 ($T < 217$ K), the FEL is temperature independent and the observed kinetics express linear Arrhenius dependencies.

### 3.4.2 Applying the Minimal 3-State/2-Step Microscopic Model (Unincorporated HT2)

The results of the transient kinetics (Figure 3.4, Table 3.1) imply a kinetic isotope effect (Table 3.2) on at least one of the microscopic rates associated with the microscopic model (Scheme 2.1). In order to determine the IE on the microscopic rates, a minimal 3-state/2-step kinetic model (The implied by the FEL) was applied to experimental decays for $T < 217$ K. Simulations are based on the corresponding set of coupled differential equations that describe the time-dependence of the $S_1^\bullet$ , $S_2^\bullet$, and $P$. The resulting P($t$) function was fit to the difference between the initial amplitude (normalized to 1) and the substrate radical decay (Figure 3.8).

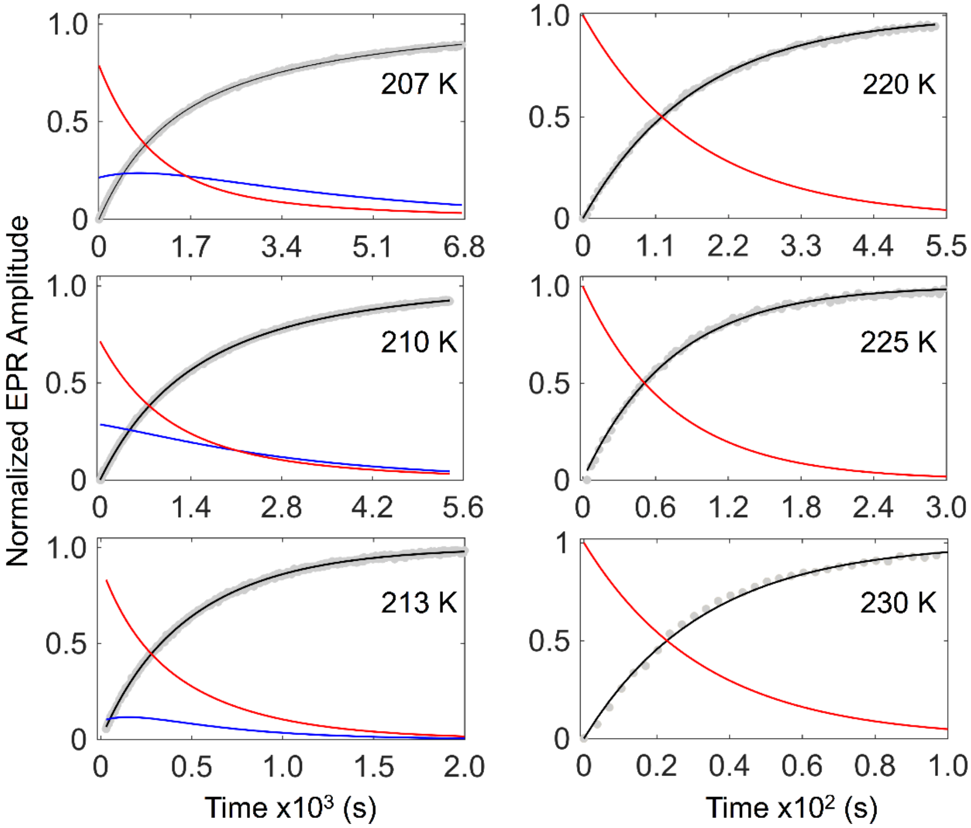

**Figure 3.8. Numerical simulations of the amplitude versus time data at different *T* values.** Simulations are based on the 3-state, 2-step kinetic model and the corresponding set of coupled differential equations that describe the time-dependence of the $S_1^{\bullet}$ (blue), $S_2^{\bullet}$ (red), and $P$ (black) for decays at $T$< 217 K. The product growth is represented as the difference between the initial normalized amplitude and the substrate radical decay. At $T \geq 220$ K the $S^{\bullet}$ state decays with first-order kinetics to $P$ (red curve only)

The model was applied to all samples for $T < 217$ K, the best-fit microscopic parameters are recorded in Table 3.3 and Arrhenius dependencies in Figure 3.9 and Table 3.4.

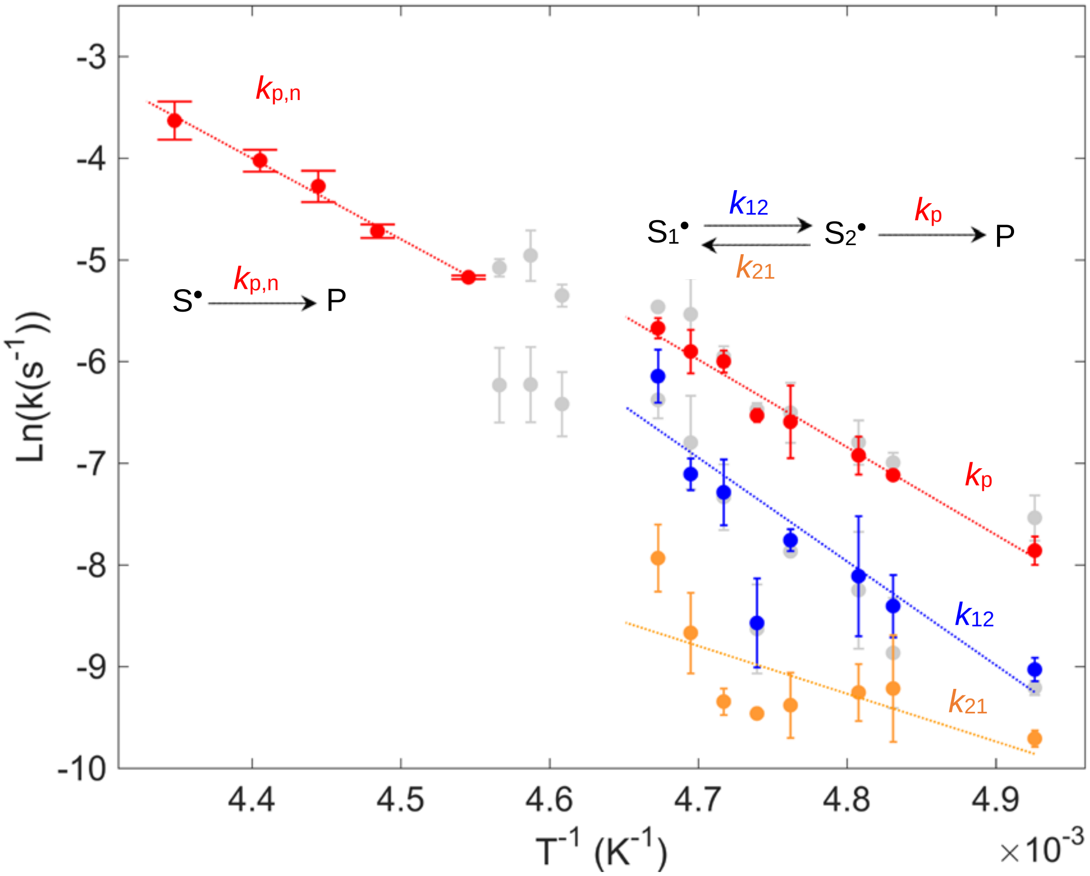

**Figure 3.9. Arrhenius plot of the microscopic rate constants resulting from the fit of the 2-step, 3-state microscopic model (Scheme 2.1) to the $^2H_4$-aminoethanol generated Co(II)- substrate radical pair decays**. The microscopic *k*-values are overlaid with the observed rate constants (light gray) for each temperature is shown, with standard deviation representing at least three separate decay measurements. Dashed lines represent the best linear fit to the data for $k_{p,n}$ (220−295 K); $k_p$, $k_{12}$, $k_{21}$ (203−214 K).

**Table 3.3. First-order microscopic rate constant and amplitude parameters** for the fit of the 3-state, 2-step microscopic model to the Co$^{II}$-substrate radical pair decay kinetics at different temperatures. Values in the $k_p$, $k_{p,N}$ column are $k_p$ for $T < 217$ K and $k_{p,N}$ for $T \geq 220$ K.

| $T$ (K) | $[S\bullet_1]_0$ | $k_{21}$ (s$^{1}$) | $k_{12}$ (s$^{-1}$) | $[S\bullet_2]_0$ | $k_p$, $k_{p,N}$ (s$^{-1}$) | $R^2$ |
|---|---|---|---|---|---|---|
| 203 | 0.20±0.01 | 6.1(±0.5) ×10$^{-5}$ | 1.2(±0.1) ×10$^{-4}$ | 0.80±0.01 | 3.9(±0.6) ×10$^{-4}$ | 0.9997 |
| 207 | 0.14±0.07 | 1.0(±0.7) ×10$^{-4}$ | 2.2(±0.8) ×10$^{-4}$ | 0.86±0.07 | 8.1(±0.2) ×10$^{-4}$ | 0.9990 |

| | | | | | | |
|---|---|---|---|---|---|---|
| 208 | 0.18±0.01 | $9.6(\pm3.0)\times10^{-5}$ | $3.0(\pm2.4)\times10^{-4}$ | 0.82±0.01 | $9.8(\pm2.0)\times10^{-4}$ | 0.9875 |
| 210 | 0.15±0.19 | $8.5(\pm3.2)\times10^{-5}$ | $4.3(\pm0.5)\times10^{-4}$ | 0.85±0.19 | $1.4(\pm0.6)\times10^{-3}$ | 0.9999 |
| 211 | 0.12±0.01 | $7.8(\pm0.01)\times10^{-5}$ | $1.9(\pm1.0)\times10^{-4}$ | 0.88±0.12 | $1.2(\pm0.01)\times10^{-3}$ | 0.9767 |
| 212 | 0.18±0.02 | $8.7(\pm1.2)\times10^{-5}$ | $6.9(\pm2.6)\times10^{-4}$ | 0.82±0.02 | $2.5(\pm0.3)\times10^{-3}$ | 0.9957 |
| 213 | 0.12±0.06 | $1.7(\pm0.8)\times10^{-4}$ | $8.2(\pm1.4)\times10^{-4}$ | 0.88±0.06 | $2.7(\pm0.07)\times10^{-3}$ | 0.9937 |
| 214 | 0.26±0.03 | $3.6(\pm1.4)\times10^{-4}$ | $2.1(\pm0.6)\times10^{-3}$ | 0.74±0.03 | $3.4(\pm0.4)\times10^{-3}$ | 0.9958 |
| 220 | -- | -- | -- | -- | $5.7(\pm0.1)\times10^{-3}$ | 0.9988 |
| 223 | -- | -- | -- | -- | $8.9(\pm0.6)\times10^{-3}$ | 0.9983 |
| 225 | -- | -- | -- | -- | $1.4(\pm0.2)\times10^{-2}$ | 0.9971 |
| 227 | -- | -- | -- | -- | $1.8(\pm0.2)\times10^{-2}$ | 0.9899 |
| 230 | -- | -- | -- | -- | $2.6(\pm0.5)\times10^{-2}$ | 0.9867 |

**Table 3.4 Apparent Arrhenius reaction rate parameters for the microscopic rate components of the Co$^{II}$-product radical pair decay.**

| Component | $\ln[A_{\mathrm{app}}\ (\mathrm{s}^{-1})]$ | $E_{\mathrm{a,app}}$ (kcal mol$^{-1}$) | $R^2$ |
|---|---|---|---|
| $k_{21}$ | 13.3 (±10.0) | 9.4 (±4.2) | 0.4810 |
| $k_{12}$ | 41.0 (±7.1) | 20.4 (±3.0) | 0.9159 |
| $k_p$ | 34.5 (±2.6) | 17.2 (±1.1) | 0.9784 |
| $k_{p,N}$ | 30.9 (±2.0) | 15.9 (±0.9) | 0.9926 |

**Table 3.5 Apparent $^1H$ / $^2H$ Kinetic Isotope Effect (KIE) for the first-order microscopic rate constants** for the fit of the 3-state, 2-step microscopic model to the $Co^{II}$-substrate radical pair decay kinetics at different temperatures. Values in the $k_p$ , $k_{p,N}$ column are $k_p$ for $T < 217$ K and $k_{p,N}$ for $T \geq 220$ K. Standard deviations were calculated using $\frac{\sigma_{IE}}{IE} = \sqrt{\left(\frac{\sigma_{k_1}}{k_1}\right)^2 + \left(\frac{\sigma_{k_2}}{k_2}\right)^2}$ .

| $T$ (K) | $KIE$ [$k_{p,N}$] | $KIE$ [$k_{21}$] | $KIE$ [$k_{12}$] | $KIE$ [$k_p$] |
|---|---|---|---|---|
| 203 | -- | 1.2 ± 0.1 | 0.8 ± 0.07 | 2.1 ± 0.4 |
| 207 | -- | 3.3 ± 2.9 | 2.1 ± 1.1 | 2.1 ± 0.6 |
| 208 | -- | 2.9 ± 2.3 | 1.5 ± 1.2 | 1.9 ± 0.6 |
| 210 | -- | 7.2 ± 5.1 | 2.3 ± 0.3 | 2.0 ± 0.9 |
| 211 | -- | 14.1 ± 7.7 | 8.4 ± 4.6 | 3.0 ± 0.5 |
| 212 | -- | 10.9 ± 4.8 | 2.5 ± 1.0 | 1.8 ± 0.6 |
| 213 | -- | 10.0 ± 8.5 | 3.4 ± 0.7 | 2.2 ± 0.5 |
| 214 | -- | 3.1 ± 1.8 | 1.5 ± 0.4 | 2.0 ± 0.2 |
| 220 | 1.9 ± 0.2 | -- | -- | -- |
| 223 | 1.8 ± 0.2 | -- | -- | -- |
| 225 | 1.4 ± 0.3 | -- | -- | -- |
| 227 | 1.2 ± 0.2 | -- | -- | -- |
| 230 | 1.3 ± 0.2 | -- | -- | -- |

The rate constants in both the observables and the microscopic kinetic model contain a kinetic isotope effect (Table 3.1 and 3.2). The $^1H/^2H$ kinetic isotope effects were calculated from both the observed and microscopic rates from the $^1H_4$-aminoethanol generated Co(II)- substrate radical pair decays recorded in Ch 2 (Table 2.2). The IE remains approximately constant for $k_{\mathrm{obs,n}}$, $k_{\mathrm{obs,f}}$, and $k_{\mathrm{obs,s}}$, which are 1.5 (±0.3), 2.3 (±0.5), and 1.8 (±0.5) respectively for $230 \leq T \leq 203$ K. The IE for the microscopic rate parameters $k_{12}$, $k_{\mathrm{p}}$, and $k_{\mathrm{p,n}}$ also remain approximately constant (2.0 (±0.8), 2.1 (±0.4), and 1.5 (±0.3) respectively). However, the microscopic rate parameter $k_{21}$ is much larger with high variance (8.9 (±4.0)) for $210 \leq T \leq 214$ K and for $T<210$, $k_{21}$ IE decreases to 2.5 (±1.1) which is consistent with the other microscopic IEs (Table 3.5). This IE is larger than previously reported[78]. The kinetic IEs on all microscopic rate constants are inconsistent with any secondary kinetic IE arising from the rehybridization of carbon from $sp^3$ to $sp^2$ where the theoretical maximum IE $^1H/^2H$ value is 1.4.[110] Therefore, the primary kinetic IE from the second hydrogen transfer (HT2) step is partially rate-determining and must be incorporated into the microscopic model.

### 3.4.3 Fitting Inconsistencies in HT2 step Incorporated Microscopic Model

The experimental $^2H$ -substrate radical decays were fit to HT2 incorporated microscopic model (Scheme 3.1 for 230-220 K and Scheme 3.2 for 214-203 K) in order to determine the rate constants, $k_{\mathrm{PS}}$ and $k_{\mathrm{HT}}$. However, the fits produced large confidence intervals and standard deviations throughout the temperature range. The average 95% confidence interval for each fit was approximately $\pm\ 10^7\ \mathrm{s^{-1}}$ for rate constants ($k_{\mathrm{PS}}$ and $k_{\mathrm{HT}}$) ranging from $10^{-1}$ to $10^3\ \mathrm{s^{-1}}$. Standard deviations for $k_{\mathrm{PS}}$ and $k_{\mathrm{HT}}$ were on the same order of magnitude as the rate constants themselves or one order of magnitude greater. In contrast, fits to the unincorporated HT2 microscopic model produced standard deviations averaging one to two orders of magnitude less for each microscopic rate constant (Table 3.2).

Additionally, the value of each rate constant $k_{PS}$ and $k_{HT}$, determined by the fit of the HT2 incorporated microscopic model to the experimental $^{2}H$ -substrate radical decays, were dependent on the initial conditions of each fit. The initial values of $k_{PS}$ and $k_{HT}$ were varied between 100 to 1000x larger than the corresponding $k_{P}$ (Table 2.2) for each sample at the given temperature. The resulting fits produced $k_{PS}$ and $k_{HT}$ values that varied over one to two orders of magnitude on average. In contrast, when the initial values for the microscopic parameters were varied for the HT2 unincorporated microscopic model or the transient kinetics (Tables 3.1 and 3.2) and fit to the experimental decays, the values microscopic parameters remained constant.

The large confidence intervals and standard deviations, coupled with dependence of the initial conditions on the fitting results, indicates that the specific values of $k_{PS}$ and $k_{HT}$ cannot be determined by fitting the HT2 incorporated microscopic model to the experimental $^{2}H$ -substrate radical decays. However, the specific ratio: $\frac{k_{HT}}{k_{PS}}$ can be determined and used to provide insights into the kinetic mechanism.

### 3.4.4 Determining the $k_{PS}$ : $k_{HT}$ Ratio for $^{2}H_{4}$-Substrate Radical Decays

The apparent IE on the microscopic rate constants associated with substrate radical step for the experimental $^{2}H_{4}$-aminoethanol generated Co(II)- substrate radical pair decays when fitted to the microscopic model (Scheme 2.1, Equations 2.2-4) are a result of HT2 becoming partially rate-limiting for $^{2}H_{4}$-aminoethanol generated decays. Meaning, the condition $k_{HT} >> k_{PS}$, (which is true for experimental $^{1}H_{4}$-aminoethanol generated Co(II)- substrate radical pair decays[103]) is not true for experimental $^{2}H_{4}$-aminoethanol generated Co(II)- substrate radical pair decays. Where $k_{HT}$ is the rate associated with the removal of a hydrogen atom from the 5'-

deoxyadenosine group and binds to the product (reforming the 5’-deoxyadenosyl radical), and $k_{PS}$ is the reverse reaction. Therefore, HT2 must be incorporated into the microscopic model.

One hundred simulations of the $^2H_4$-substrate radical decays were generated for each temperature for both temperature regimes using microscopic parameters from $^1H_4$-substrate radical pair rate constants (Table 2.2) for $k_{12}$, $k_{21}$, and $k_P$ as well as amplitude parameters $[S\bullet_1]_0$ and $[S\bullet_2]_0$. Additionally another set of simulations were generated with $k_{P,N}$ and $k_P$ 1.4x slower than the corresponding $^1H_4$-substrate radical pair rate constants to simulate a secondary IE on $k_{P,N}$ and $k_P$. The rate constant $k_{PS}$ was set to 1000x the value of $k_P$ and $k_{HT}$ was varied. Each simulated decay was fit to either a monoexponential ($T \geq 220$ K) or biexponential ($T < 214$ K) and the rate constants ($k_{obs,sim}$) were determined. The ratios of simulated rate constants to the experimental observed rate constants from the $^1H_4$-substrate radical pair (Table 2.1) were ($\frac{k_{obs,sim}}{k_{obs,1H}}$) calculated. The fraction $\frac{k_{obs,sim}}{k_{obs,1H}}$ was plotted against the corresponding $\frac{k_{HT}}{k_{PS}}$ fraction from the simulated decays (Figures 3.10-11). The $\frac{k_{obs,sim}}{k_{obs,1H}}$ fractions were compared to the corresponding apparent observed KIEs from the monoexponential or biexponential fits to the $^2H_4$-substrate radical decays (Table 3.2) for each temperature. The $\frac{k_{HT}}{k_{PS}}$ fraction was then estimated for each temperature Table 3.6-7.

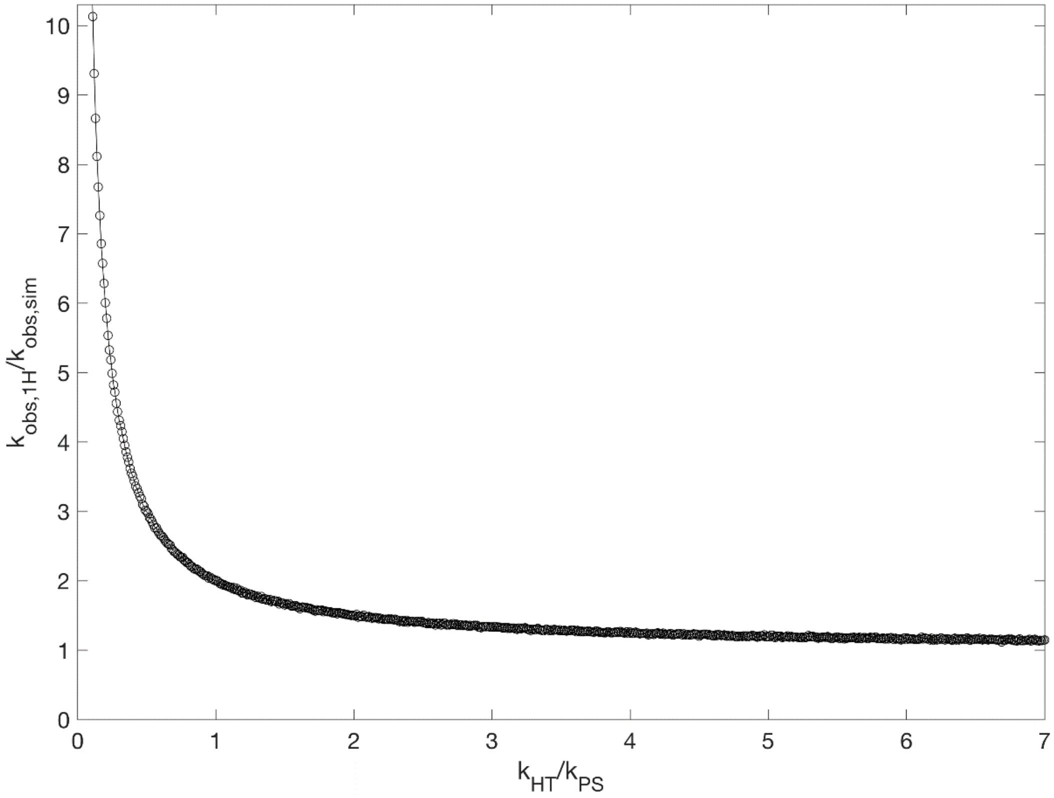

**Figure 3.10 IE vs $k_{HT}$ / $k_{PS}$ plot based on the HT2 incorporated microscopic model for the high temperature regime.** The solid black line corresponds to the results of the simulated decays generated by varying $k_{HT}$ then fitting those simulations to a monoexponential equation. The solid black circles represent the location of the IE calculated from the experimental $^{2}H_{4}$-radical decays and corresponding temperatures (K).

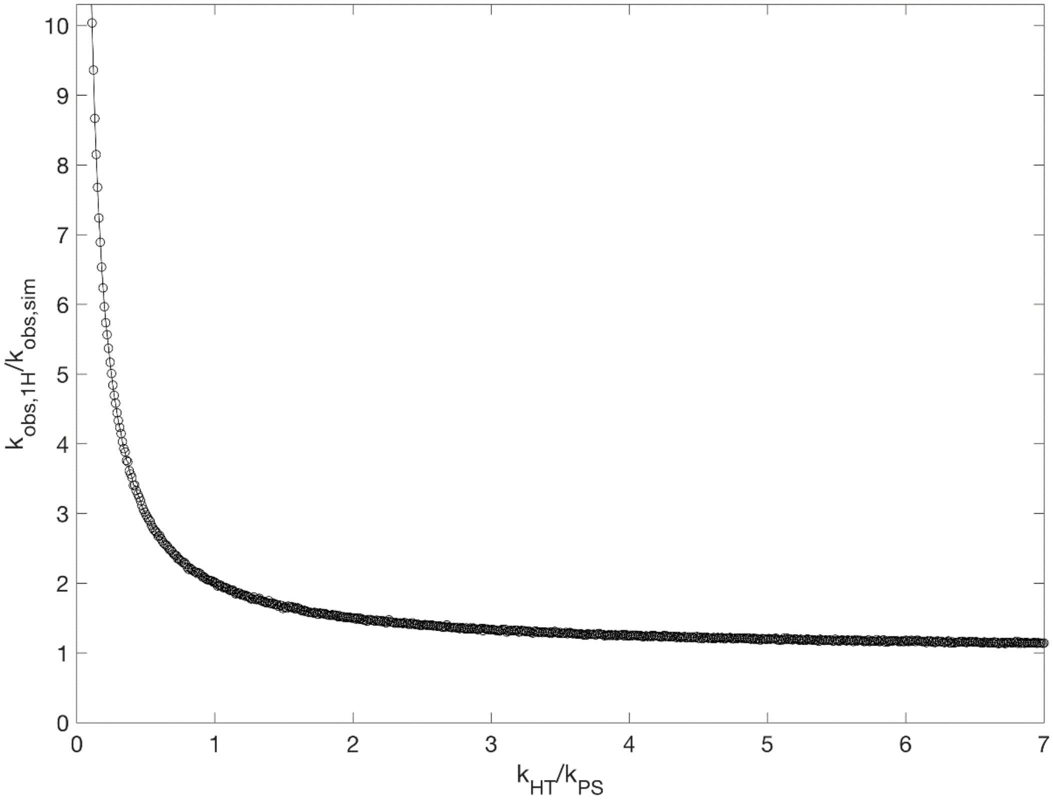

**Figure 3.11 IE vs $k_{HT}$ / $k_{PS}$ plot based on the HT2 incorporated microscopic model for the high temperature regime where the simulated $k_{P,N}$ is 1.4x slower than 1H experimental value for $k_{P,N}$.** The solid black line corresponds to the results of the simulated decays generated by varying $k_{HT}$ then fitting those simulations to a monoexponential equation. The solid black circles represent the location of the IE calculated from the experimental $^2H_4$-radical decays and corresponding temperatures (K).

Additionally, the solid black dots represent the experimental $^2H_4$-radical decays and the corresponding $k_{HT}/k_{PS}$ values based on the decay simulations. Figure 3.12 shows $\frac{k_{obs,sim}}{k_{obs,1H}}$ vs $\frac{k_{HT}}{k_{PS}}$ plot for the microscopic model corresponding to Scheme 3.2, where $T < 214$ K (low temperature regime).

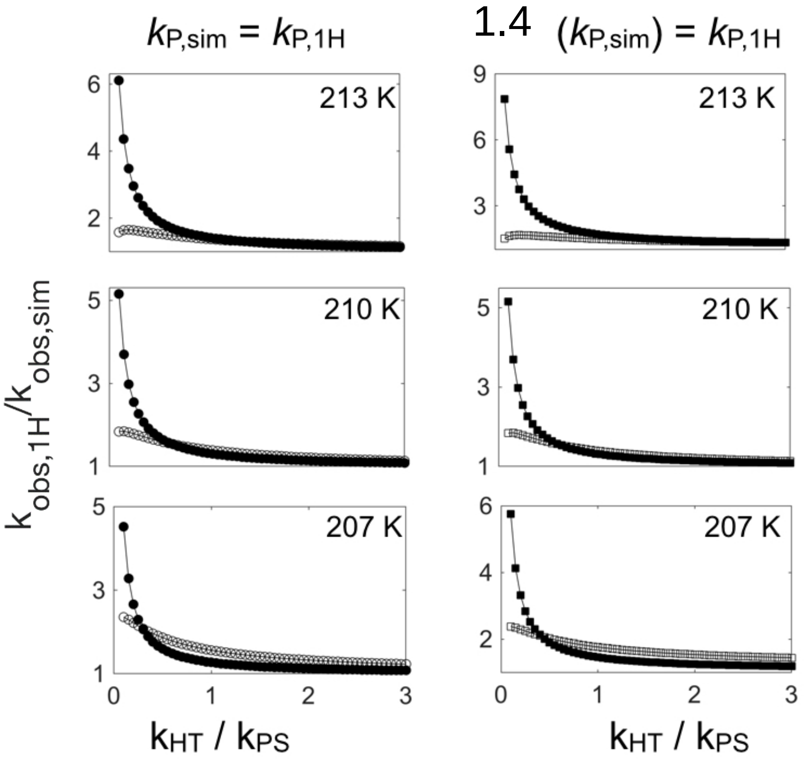

**Figure 3.12 IE vs $k_{HT}$ / $k_{PS}$ plot based on the HT2 incorporated microscopic model for the low temperature regime.** The open black shapes ($k_{obs,f}$ ) and solid black shapes ($k_{obs,s}$) corresponds to the results of the simulated decays generated by varying $k_{HT}$ then fitting those simulations to a biexponential equation.

All IEs for the experimental $^2H_4$-radical decays correspond to $\frac{k_{HT}}{k_{PS}}$ values between 0.2 and 1. All $\frac{k_{HT}}{k_{PS}}$ values with their corresponding IE and temperatures are recorded in Tables 3.6-7

**Table 3.6. $k_{\mathrm{PS}}$ / $k_{\mathrm{HT}}$ ratio for 295 ≤ $T$ ≤ 203 K.** The ratio was determined by the bi- exponential ($T <$ 214 K) or monoexponential ($T \geq 220$ K) fit the the simulated decays. $\mathrm{KIE}_{k\mathrm{obs,f,n,calc}}$ and $\mathrm{KIE}_{k\mathrm{obs,s,calc}}$ represent the $\frac{k_{obs,sim}}{k_{obs,1H}}$ fraction that most closely corresponds with the experimental KIEs in Table 3.2. Standard deviations were calculated using $\frac{\sigma_{IE}}{IE} = \sqrt{\left(\frac{\sigma_{k_1}}{k_1}\right)^2 + \left(\frac{\sigma_{k_2}}{k_2}\right)^2}$ from the experimental protiated ($k_1$) and deuterated samples ($k_2$).

| $T$ (K) | $\mathrm{KIE}_{k\mathrm{obs,f,n,calc}}$ | $\mathrm{KIE}_{k\mathrm{obs,s,calc}}$ | $k_{\mathrm{PS}}$ / $k_{\mathrm{HT}}$[a] |
|---|---|---|---|
| 207 | 2.2± 0.8 | 2.6± 1.2 | 0.2 |
| 208 | 2.0 ± 0.8 | 1.5± 0.3 | 0.5 |
| 210 | 1.7 ± 0.8 | 2.1± 0.1 | 0.4 |
| 213 | 1.5 ± 1.0 | 1.8± 1.2 | 0.6 |
| 220 | 1.9 ± 0.2 | -- | 1.1 |
| 223 | 1.8 ± 0.2 | -- | 1.3 |
| 225 | 1.4 ± 0.3 | -- | 2.9 |
| 227 | 1.2 ± 0.2 | -- | 4.8 |
| 230 | 1.3 ± 0.2 | -- | 2.9 |
| 277 | 5.7 ± 0.7 | -- | 0.2 |
| 295 | 7.4 ± 0.9 | -- | 0.1 |

[a] Ratio was determined from $k_{\mathrm{obs,f}}$ curves represented in Figure 3.11 ($T \geq 220$ K) or Figure 3.13, left column ($T \leq 213$ K).

**TABLE 3.7. $k_{PS}$ / $k_{HT}$ ratio for 295 ≤ $T$ ≤ 203 K where the simulated $k_{P,N}$ is 1.4x slower than 1H experimental value for $k_{P,N}$ .** The ratio was determined by the bi- exponential ($T$ < 214 K) or monoexponential ($T \geq 220$ K) fit the the simulated decays. $\mathrm{KIE}_{k\mathrm{obs,f,n,calc}}$ and $\mathrm{KIE}_{k\mathrm{obs,s,calc}}$ represent the $\frac{k_{obs,sim}}{k_{obs,1H}}$ fraction that most closely corresponds with the experimental KIEs in Table 3.2 Standard deviations were calculated using $\frac{\sigma_{IE}}{IE}=\sqrt{\left(\frac{\sigma_{k_1}}{k_1}\right)^2+\left(\frac{\sigma_{k_2}}{k_2}\right)^2}$ from the experimental protiated ($k_1$) and deuterated samples ($k_2$).

| $T$ (K) | $KIE_{kobs,f,n,calc}$ | $KIE_{kobs,s,calc}$ | $k_{PS}$ / $k_{HT}$[a] |
|---|---|---|---|
| 207 | 2.2 ± 0.8 | 2.5± 1.2 | 0.3 |
| 208 | 2.1 ± 0.8 | 1.5± 0.3 | 0.7 |
| 210 | 1.7 ± 0.8 | 2.1± 0.1 | 0.4 |
| 213 | 1.5 ± 1.0 | 1.8± 1.2 | 0.9 |
| 220 | 1.9 ± 0.2 | -- | 1.1 |
| 223 | 1.8 ± 0.2 | -- | 1.3 |
| 225 | 1.4 ± 0.3 | -- | 2.5 |
| 227 | 1.2 ± 0.2 | -- | 4.8 |
| 230 | 1.3 ± 0.2 | -- | 3.4 |
| 277 | 5.7 ± 0.7 | -- | 0.2 |
| 295 | 7.3± 0.8 | -- | 0.2 |

[a] Ratio was determined from $k_{\mathrm{obs,f}}$ curves from Figure 3.12 ($T$ ≥ 220 K) or Figure 3.13, right column ($T$ ≤ 213 K

The both $\mathrm{KIE}_{k\mathrm{obs,f,n,calc}}$ and $\mathrm{KIE}_{k\mathrm{obs,s,calc}}$ fall within one standard deviation of $\mathrm{KIE}_{k\mathrm{obs,f,n,}}$ and $\mathrm{KIE}_{k\mathrm{obs,s}}$ determined by comparing the observed rate constants from $^1$H and $^2$H (Table 3.2) for both sets of simulations ($k_{P,sim} = k_{P,1H}$, $k_{P,N,sim} = k_{P,N,1H}$ and $1.4(k_{P,sim}) = k_{P,1H}$, $1.4(k_{P,N,sim}) = k_{P,N,1H}$ ), although the corresponding $\frac{k_{HT}}{k_{PS}}$ fractions differ (Tables 3.6-7) . Both fast and slow phase $\mathrm{KIE}_{k\mathrm{obs,f,n,calc}}$ and $\mathrm{KIE}_{k\mathrm{obs,s,calc}}$ correspond to the same $\frac{k_{HT}}{k_{PS}}$ fraction within one decimal place.

### 3.4.5 Four Temperature Regimes for $k_{\mathrm{HT}}$ and $k_{\mathrm{PS}}$

Both sets of Simulated $^{2}H_{4}$-radical decays reveal four temperature regimes that describe the relationship between $k_{\mathrm{HT}}$ and $k_{\mathrm{PS}}$. (1) $T$ = 295 – 277 K : The $\frac{k_{HT}}{k_{PS}}$ ratio is less than one, therefore $k_{\mathrm{HT}} < k_{\mathrm{PS}}$. The $\frac{k_{HT}}{k_{PS}}$ ratio at 295 K is less than the ratio at 277 K, meaning the Arrhenius dependencies for $k_{\mathrm{HT}}$ and $k_{\mathrm{PS}}$ are converging. (2) $T$ = 230 –227 K : The $\frac{k_{HT}}{k_{PS}}$ ratio is greater than one, therefore $k_{\mathrm{HT}} > k_{\mathrm{PS}}$. The $\frac{k_{HT}}{k_{PS}}$ ratio at 230 K is less than the ratio at 227 K, indicating that the Arrhenius dependencies for $k_{\mathrm{HT}}$ and $k_{\mathrm{PS}}$ are diverging. (3) $T$ = 227 – 220 K : The $\frac{k_{HT}}{k_{PS}}$ ratio is greater than one, therefore $k_{\mathrm{HT}} > k_{\mathrm{PS}}$. The $\frac{k_{HT}}{k_{PS}}$ ratio decreases sequentially with decreasing temperature, meaning the Arrhenius dependencies for $k_{\mathrm{HT}}$ and $k_{\mathrm{PS}}$ are converging. (4) $T$ = 213 – 207 K : The $\frac{k_{HT}}{k_{PS}}$ ratio is less than one, therefore $k_{\mathrm{HT}} > k_{\mathrm{PS}}$. The $\frac{k_{HT}}{k_{PS}}$ ratio overall slightly decreases with decreasing temperature from 213-207 K, indicating that the slopes for $k_{\mathrm{HT}}$ and $k_{\mathrm{PS}}$ Arrhenius dependencies are diverging.

### 3.4.6 Arrhenius Dependencies of $k_{\mathrm{HT}}$ and $k_{\mathrm{PS}}$

Although specific Arrhenius parameters for $k_{\mathrm{HT}}$ and $k_{\mathrm{PS}}$ cannot be determined with simulations, certain Arrhenius behaviors can be determined, specifically the Arrhenius behavior of $k_{\mathrm{HT}}$. According to the microscopic models used to construct the simulated decays (Scheme 3.1-2), $k_{\mathrm{PS}}$ and $k_{\mathrm{P}}$ share an energy barrier. Therefore, $k_{\mathrm{PS}}$ should express the same Arrhenius behavior, in the form activation energy changes (slope changes), as $k_{\mathrm{P}}$. The rate constant $k_{\mathrm{P}}$, maintains a linear dependence for $T$ = 295-220 K, from 220 > $T \geq$ 217 K $k_P$ becomes temperature independent, and for $T$ < 217 K maintains a linear dependence. This behavior is consistent for both experimental $^1H_4$ and $^2H_4$-radical decays (Figure 2.7 and 3.9). Figure 3.13-14 shows a hypothetical Arrhenius plot for $k_{HT}$ and $k_{PS}$ , where the Arrhenius parameters for $k_{PS}$ at $T$ = 295-220 K are as follows: $E_{a,app}$ = 12 kcal mol$^{-1}$ and ln[$A_{app}$ (s$^{-1}$)] = 40.

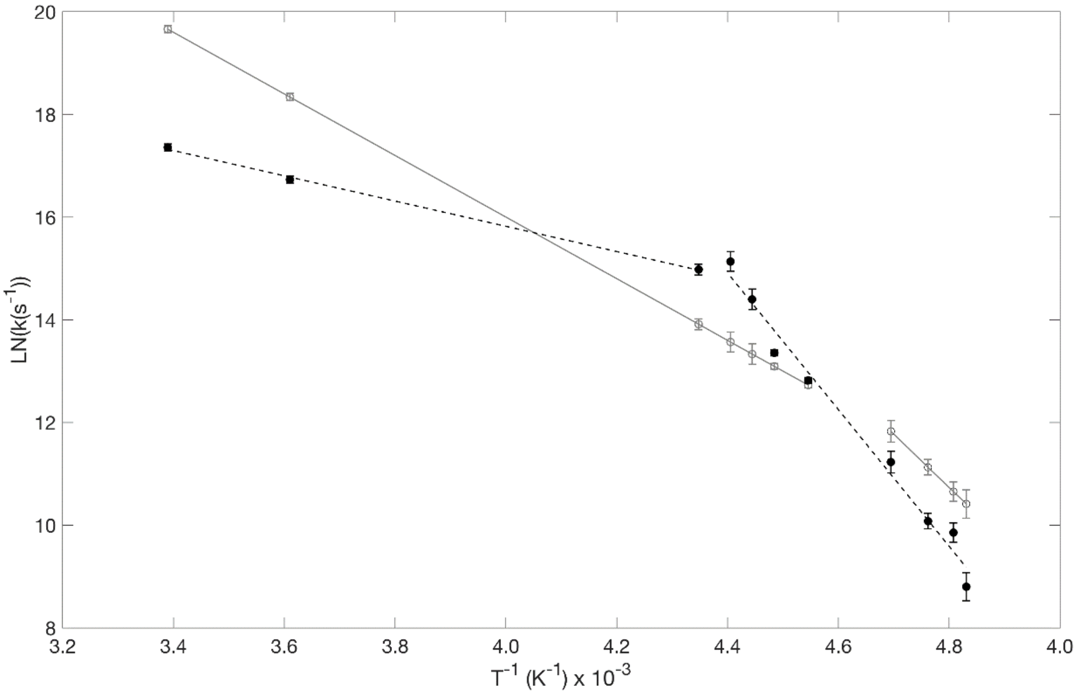

**Figure 3.13. Arrhenius Plot of $k_{HT}$ (black) and $k_{PS}$ (gray).** Dashed lines represent the best linear fit to the data for $k_{HT}$ at $T$ =295−230 K and $T$ =227−207 K. Standard deviations were calculated using $\sigma_x$= ($\sigma_u$ /u) where u and $\sigma_u$ is *k*P,N ($T$ =295−220) or kP ($T$ =213−207) and the corresponding standard deviation.

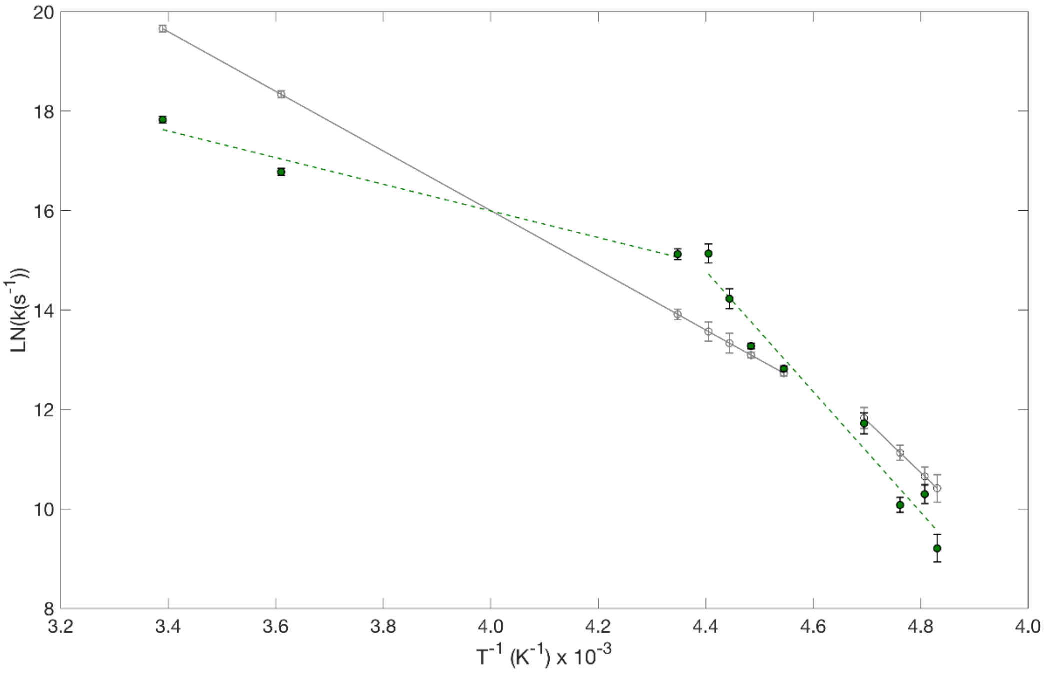

**Figure 3.14. Arrhenius Plot of $k_{HT}$ (green) and $k_{PS}$ (gray) where the simulated $k_{P,N}$ is 1.4x slower than 1H experimental value for $k_{P,N}$.** Dashed lines represent the best linear fit to the data for $k_{HT}$ at $T$ =295−230 K and $T$ =227−207 K. Standard deviations were calculated using $\sigma_x$= ($\sigma_u$ /u) where u and $\sigma_u$ is *k*P,N ($T$ =295−220) or kP ($T$ =213−207) and the corresponding standard deviation.

### 3.4.7 Temperature Transition of $k_{HT}$ at 227 K

Decay simulations reveal two Arrhenius dependencies for $k_{HT}$, with an abrupt increase in both activation energy and Arrhenius intercept parameters at $T$ = 227 K. This Arrhenius behavior for $k_{HT}$ is persistent for a range of $E_{a,app}$ values between 6-60 kcal mol$^{-1}$ any value of ln[$A_{app}$ (s$^{-1}$)] for $k_{PS}$ (at $T$ = 295-220 K). This transition is consistent with a dynamical transition, where the alpha fluctuations associated with the HT2 step are quenched (at $T$ = 227), yet the reaction persists through a non-native pathway. This transition is similar to the dynamical transitions found in the radical rearrangement step.[103] However, this transition occurs at a higher temperature and does not exhibit a bifurcation or plateau. This indicates that the energy well associated with product radical state remains unaffected and the energy barrier associated with

$k_{HT}$ has increased. Another remarkable result of the decay simulations is the consistency between both high (Scheme 3.1) and low (Scheme 3.2) temperature models. The high temperature model demonstrates the same linear dependency (from $T \leq 227$ K) as the low temperature model for $k_{HT}$ ($R^2 = 0.9741$). These features reveal a quenching of a set of $\alpha$ fluctuations that another chemical step, HT2 and these collective motions are distinct from those associated with the radical rearrangement.

### 3.4.8 (Lack of) Structural Difference in $S_1^\bullet$ and $S_2^\bullet$ States

There was no significant difference observed from the ESEEM analysis between the un-decayed and decayed samples. Meaning, there are no significant structural differences in the C1-C2 rotameric states of the substrate radical, or in the interaction of the substrate radical with the C5'-methyl group of deoxyadenosine, between the $S_1^\bullet$ and $S_2^\bullet$ states. Therefore, the $S_1^\bullet$ and $S_2^\bullet$ microstates, that enable the rearrangement reaction step, arise from changes in the configuration of the protein.

### 3.4.9 Possible I.E. on $k_{P,N}$ and $k_P$

Two sets of simulations were created to explore the possibility of an IE on the microscopic rate parameter(s) most closely related to the chemical step of the substrate radical rearrangement: $k_{P,N}$ ($T \geq 220$ K) and $k_P$ ($T < 217$ K). These microscopic rate parameters were set to either corresponding 1H value for $k_{P,N}$ and $k_P$ or 1.4x slower (to represent the theoretical limit of the secondary isotope effect). Results of both simulations were effectively identical. Both sets of KIE$_{k\text{obs,,calc}}$'s (Tables 3.6-7) fell within one standard deviation of the KIE's calculated from the corresponding observed rate constants from the experimental decays (Table 3.2). However, the $\frac{k_{obs,sim}}{k_{obs,1H}}$ vs $\frac{k_{HT}}{k_{PS}}$ curves (Figures 3.10-12) produced different $\frac{k_{HT}}{k_{PS}}$ fractions throughout the temperature range (Tables 3.6-7). This difference becomes more evident in the Arrhenius dependencies of $k_{\text{HT}}$ and $k_{\text{PS}}$ (Figures 3.12-13). Although the parameters ($E_{\text{a,app}}$ and ln $A_{\text{a,app}}$) of the linear fits to both Arrhenius dependences ($T$ =295−230 K and $T$ =227−207 K) overlap (within one standard deviation), the $R^2$ values differ. The $R^2$ values corresponding to simulations generated with $\text{k}_{\text{P,N}}$ and $\text{k}_{\text{P}}$ values that matched $^1$H values were better (0.9974 for $T$ =295−230 K and 0.9800 for $T$ =227−207 K) than the $R^2$ values corresponding to simulations generated with $\text{k}_{\text{P,N}}$ and $\text{k}_{\text{P}}$ values that were 1.4x slower than $^1$H values (0.9403 for $T$ =295−230 K and 0.9577 for $T$ =227−207 K). These $R^2$ values indicate that the simulations run with parameters that match $^1$H experimental values are more consistent with the $^2$H experimental results. However, these results are insufficient in determining whether there is an IE on $\text{k}_{\text{P,N}}$ and $\text{k}_{\text{P}}$ for $^2$H substrate radical decays.

## 3.5 Conclusions

Incorporation of the HT2 step into the microscopic model is necessary to fully describe the rate limiting steps that drive the chemical reaction in EAL for $^2H_4$-aminoethanol radical pair decays. When the microscopic model introduced in Chapter 2 (Scheme 2.1) (HT2 is not incorporated) is applied to $^2H_4$-aminoethanol radical pair decays, the results exhibit the same Arrhenius characteristics, i.e. temperature transitions and bifurcations as well as similar activation energies to the $^1H_4$-aminoethanol radical pair decays. These results indicate that the radical rearrangement is the step being observed and the bifurcation is caused by the quenching of two distinct sets of specific collective motions in the protein for the rearrangement step.[103] However, the IE on the microscopic rate constants are inconsistent with secondary isotope effects.[110] Further, ESEEM experiments revealed no significant structural difference between the microstates $S_1^{\bullet}$ and $S_2^{\bullet}$, showing no evidence of hydrogen rearrangement on the substrate structure that would cause a primary or secondary IE for the microscopic rate constants: $k_{21}$ and $k_{12}$. However application of the microscopic model (introduced in Ch 2) revealed secondary IE on microscopic rate constants $k_{PN}$ and $k_P$. Yet analysis of the $^2H_4$-radical decays revealed IE effects greater than the theoretical limit. Both the application of the unincorporated HT2 model to the experimental data and the results of the ESEEM experiments prove that the HT2 step is partially rate limiting, along with the RR step, and must be incorporated into the model.

Based on this conclusion, simulated decays were constructed in order to account for these IEs and gain further insights into the underlying kinetic mechanism of HT2 step. The simulated results determined the specific relationship between the observed IE and the $\frac{k_{HT}}{k_{PS}}$ fraction for two senarios: with or without a secondary IE on $k_{PN}$ and $k_P$. Applying the transient kinetic results (Figure 3.4 and Table 3.1) to the simulation results reveal three insights into the RR and HT2 steps. (1) The transient IEs are explained solely by HT2 or a combination of HT2 and a secondary IE on $k_{PN}$ and $k_P$. (2) The rate constant ($k_{HT}$) associated with HT2 undergoes a dynamical temperature transition at 227 K for either case (secondary IE or not). (3) This temperature transition is distinct from the temperature transitions associated with the RR step, indicating that the set collective motions associated with HT2 step are different than the set of collective motions associated with the RR. Additionally, the microscopic model for both regimes (Scheme 3.1-2) express the same linear Arrhenius dependence for $k$HT at $T \leq 227$ K, further solidifying both RR and HT2 microscopic models. The methods and models in this chapter deconvolute the rate limiting steps for EAL catalysis and reveal the contributions of native protein configurations and specific fluctuations to multiple chemical steps of enzyme catalyzes.

# Chapter 4

# Protein and Coupled Solvent Dynamic Contributions to the Radical Rearrangement Step in a $B_{12}$-Dependent Enzyme Addressed by Sucrose Effects on Reaction Kinetics at 217 K

## 4.1 Introduction

The radical rearrangement step in the catalytic cycle of EAL[27, 57, 102] is influenced by fluctuations of the protein.[103] This is evident through the abrupt change in the temperature dependencies of the substrate radical decay, associated with the substrate radical rearrangement step, when studied over a large temperature range (92 K). The kinetic transition at $T$ = 219 K is a bifurcation of $k_{\mathrm{obs,n}}$ into two distinct temperature independent rates: $k'_{\mathrm{obs,f}}$ and $k'_{\mathrm{obs,s}}$, that represent an abrupt transition in the FEL (Figure 2.6) where the broad $S^{\bullet}$ minimum is partitioned into two sequential microstates: $S_1^{\bullet}$ and $S_2^{\bullet}$. The second transition occurs at $T$ = 217 K in the form of a “kink”[103], where $k'_{\mathrm{obs,f}}$ and $k'_{\mathrm{obs,s}}$ become temperature dependent ($k_{\mathrm{obs,f}}$ and $k_{\mathrm{obs,s}}$), with distinct Arrhenius dependencies for $T < 217$ K (Figure 2.5) indicating that the FEL becomes temperature independent. This temperature region (219-217 K) marks the transition of a collective protein motion -driven reaction to the reaction driven by localized, incremental motions, involving the same sets of protein groups.[103]

The bifurcation and kink are present in both $^{1}H_4$-aminoethanol and $^{2}H_4$-aminoethanol generated Co(II)- substrate radical pair decays[49, 78, 103] (Figure 2. 5 and 3.5) and occur within the same temperature region (219-217 K). This indicates that the transitions do not originate from a chemical process associated with the rehybridization of the C1 carbon atom from $sp^3$ to $sp^2$ or partial rate dependence from the second hydrogen transfer step.[57-58, 95, 103, 107-110] In this chapter, we demonstrate the sensitivity of the transient kinetics to the protein dynamics by shifting the dynamical temperature transition to higher temperatures.

### 4.1.1 The Role of Solvent in Protein Dynamics

To demonstrate the effect of protein dynamics on the kinetics associated with the radical rearrangement step, the dynamics of the protein must be varied without changing the structure of the protein. To do this, the solvent surrounding the enzyme is used. Protein dynamics are highly influenced by the solvent[114] and have been studied intensively.[23, 115-117] Specifically, protein dynamics are affected by the formation of ice or glass in the bulk solvent as the solution freezes.[118] Cryoprotectants, such as sucrose, are used to decrease ice formation.[119]

CW-EPR spectral studies for TEMPOL spin probe in water and varying concentrations of sucrose reveal a dramatic change in solvent dynamics.[117] TEMPOL is a paramagnetic nitroxide ($S = {}^{1}/_{2}$) and is relatively small in size (effective diameter, approximately 7 Å). The probe is used to probe dynamics because its CW-EPR spectral line shape is sensitive to the tumbling motions of the probe on the same time scales as protein motions in solutions.[117, 120-122] In addition, TEMPOL resides in the same vicinity as the protein, between ice crystals that form during quenching of frozen aqueous solutions.[117] Therefore, TEMPOL provides a metric for the dynamics of the solvent surrounding the protein. Studies have shown that TEMPOL undergoes a mobility transition (from rigid to mobile) at a specific temperature, $T_t$ and $T_t$ increases with increasing sucrose concentrations.[117]

TEMPOL experiments established the effect of sucrose on the dynamics of aqueous solutions, specifically the mobility transitions in the solvent surrounding the protein. This chapter reveals unique effects increased sucrose concentrations have on both observed kinetic phases associated with the $^{1}H_4$-aminoethanol and $^{2}H_4$-aminoethanol generated Co(II)- substrate radical pair decays in EAL. Specifically, these experiments reveal two characteristics: (1) The diminishing fast phase population with higher sucrose concentrations, caused by the shift of the dynamical transition temperature region to higher temperatures; (2) The distributive property associated with the slow phase rate(s), caused by the roughening of the FEL.

## 4.2 Materials and Methods

### 4.2.1 Sucrose Sample Preparation

Sucrose solutions were prepared using the USDA Brix conversion tables[123] to calculate the weight per volume (w/v) percentage of sucrose in 10mM KPi solution. A 10% (w/v) stock solution was prepared and used to create 1%, 2%, 4%, and 5% sucrose samples. A 50% (w/v) stock was used to prepare the 10%, 20%, and 30% sucrose samples. Equation 4.1 was used to calculate the % (w/v) of the stock solution:

$$\%(w/v) = \frac{m_S}{\frac{m_S}{SG_{Apparent}} + V_{H_2O}} \tag{4.1}$$

where $m_s$ is the mass of sucrose, $V_{H_20}$ is the volume of water, and $SG_{\text{Apparent}}$ is the apparent specific gravity of sucrose at 20° C outlined in USDA Brix conversion tables.[123]

### 4.2.2 Enzyme Purification and Sample Preparation

Enzyme was purified from the *Escherichia coli* overexpression system incorporating the cloned S. typhimurium EAL coding sequence[89] as described,[90] with modifications.[37] The specific activity of purified EAL with aminoethanol as substrate was 20 μmol/min/mg ($T$ = 298 K, $P$ = 1 atm), as determined by using the coupled assay with alcohol dehydrogenase and NADH.[30]

Reactions were performed in aerobic buffer containing 10 mM potassium phosphate (pH 7.5). Manipulations were carried out on ice under dim red safe-lighting. No photodegradation of the coenzyme $B_{12}$ (adenosylcobalamin, AdoCbl) cofactor was detected under any of the conditions. An EAL-10 mM KPi solution was centrifuged in (Centrifuge Name) with ~ 70% efficiency to isolate pure EAL for sample preparation. EAL was resuspended in 10mM KPi, varying % (w/v) sucrose, B12, and $^{1}H_4$-aminoethanol or $^{2}H_4$-aminoethanol substrate solutions. Final concentration of EAL was 15mg/mL which is equivalent to 20−30 μM for a holoenzyme molecular mass of 500 000 g/mol,[90] and an active site concentration of 120−180 μM, based on an active site/ holoenzyme stoichiometry of 6:1.[91-92] AdoCbl was added to the sample at a ratio of 2:1 to EAL active site. $^{1}H_4$-aminoethanol or $^{2}H_4$-aminoethanol substrate concentrations were both 100mM. Background samples were prepared using EAL and B12 suspended in 10 mM KPi solution with the same EAL and B12 concentrations. Neither substrate nor sucrose solutions were present in the background samples. All samples were manually mixed and loaded into a 4 mm outer diameter EPR tube, and the tube was immersed in isopentane (T = 140 K; elapsed time, ∼10 s). The procedure for cryotrapping of the $Co^{2+}$-substrate radical pair samples has been described in detail.[51]

### 4.2.3 Full Spectrum EPR Measurements the Substrate Radical Decay at 120 K

EPR spectra were collected by using a Bruker E500 ElexSys EPR spectrometer equipped with a Bruker ER4123 SHQE cavity. Instrumentation and methods for measurements of the substrate radical decay kinetics by EPR have been described in detail.[51] EPR spectra were collected for samples with sucrose concentrations of 0-30% (w/v) for both $^{1}H_4$-aminoethanol and $^{2}H_4$-aminoethanol substrates held at 120 K. The spectra were averaged over at least 10 scans.

Background spectra were collected using the samples prepared without $^1H_4$-aminoethanol or $^2H_4$-aminoethanol substrate. Background spectra were averaged over 100 scans.

### 4.2.4 Time-Resolved, Full Spectrum EPR Measurements of Substrate Radical Decay at Low-*T*

EPR spectra were collected by using a Bruker E500 ElexSys EPR spectrometer equipped with a Bruker ER4123 SHQE cavity. EPR samples were held at a staging temperature of 160−180 K and temperature was step-increased to decay measurement value of 217 K for samples with sucrose concentrations of 0-30% (w/v) for both $^1H_4$-aminoethanol and $^2H_4$-aminoethanol substrates. The time from initiation of the temperature step to the start of acquisition of the first spectrum was 30−60 s.

### 4.2.5 Transient Kinetics Analysis

EPR spectra were collected every 5 seconds. For each EPR spectrum in the decay time series, the amplitude of the substrate radical signal was obtained from the difference between peak and trough amplitudes of the derivative feature around g ≈ 2.0, with baseline correction. The decay curves were fit with either a biexponential (*N*=2, equation (Equation 2.1 ), power law, or a combination of a monoexponential (*N*=1, equation (Equation 2.1) and power law fit. The power law is represented by the following equation:

$$A(t) = (1 + \frac{t}{t_0})^{-n} \tag{4.2}$$

where the amplitude ($A$) is related to the parameters $t_0$ and $n$, where the most probable rate constant ($k$) is equal to $\frac{n}{t_0}$. In a log($A$($t$)) vs log($t$) plot the parameter $t_0$ gives the approximate time when $A$($t$) breaks from the horizontal axis and $n$ gives the slope of the $A$($t$) line after the break.[124]

## 4.3 Results

### 4.3.1 Full-Spectrum EPR Measurements of Co(II)-Substrate Radical Pair at 120 K

Figure 4.1 shows the EPR spectral scans collected at 120 K for $^1H_4$-aminoethanol (A) and $^2H_4$-aminoethanol (B) substrate samples with sucrose concentrations between 0 and 30% (w/v).

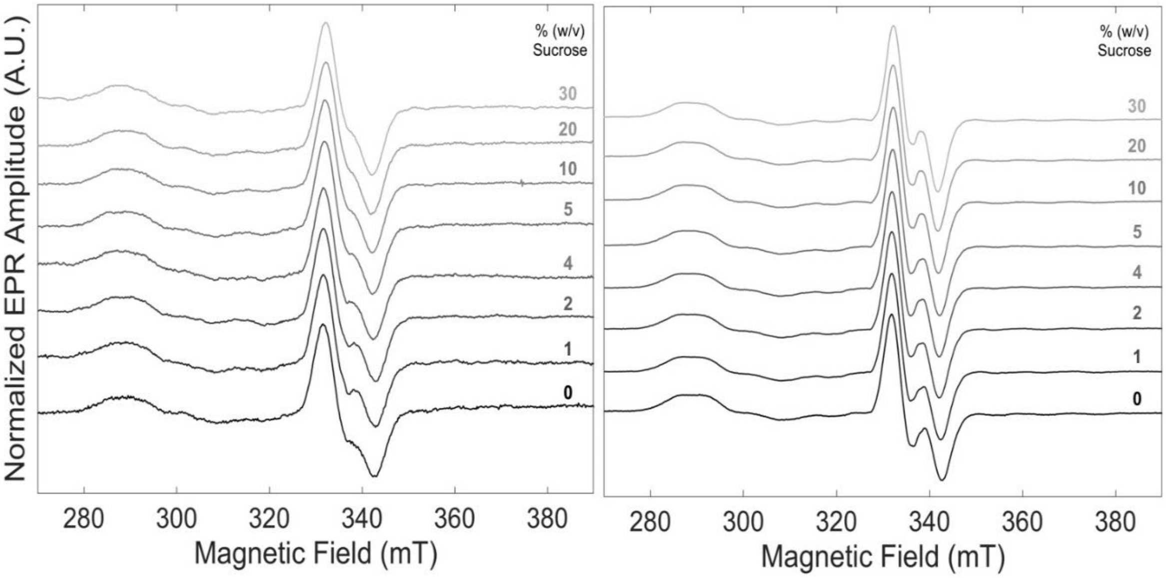

**Figure 4.1. EPR Spectra at 120 K** for $^1H_4$-aminoethanol (A) and $^2H_4$-aminoethanol (B) with sucrose concentrations between 0 and 30% (w/v).

All spectra contain the Co(II)-substrate radical pair with the same features as 0% (w/v) sucrose concentrations for both $^1H_4$-aminoethanol and $^2H_4$-aminoethanol substrate samples. There is a slight narrowing of the substrate radical width from 11.4 mT at 0% to 10.0 mT at 30% for $^1H_4$-

aminoethanol and 10.8 mT at 0% to 9.6 mT at 30% for $^2H_4$-aminoethanol substrate samples. However, low concentrations of sucrose < 4% have the same width as 0% for $^1H_4$-aminoethanol substrate samples. The central feature of $^2H_4$-aminoethanol substrate radical for sucrose concentrations > 4% narrow with increasing sucrose concentrations. The maximum sucrose concertation measured by these experiments: 30% (w/v) narrows by 0.2 mT.

### 4.3.2 Decay of Co(II)-Substrate Radical Amplitude at 217 K for 0-30% Sucrose Concentrations

$^1H_4$-aminoethanol and $^2H_4$-aminoethanol substrate radical decay samples with sucrose concentrations between 0 and 30% (w/v) were fit to a biexponential, monoexponential + power law, and a power law. The best fit was determined by comparing the $R^2$ values and 95% confidence intervals. For sucrose concentrations between 1 and 4% (w/v) for $^1H_4$ decay samples and 1 and 30% (w/v) for $^2H_4$ decay samples the monoexponential + power law expression was determined to be the best fit. Both biexponential and power law expressions failed to capture all the features of the decays, with $R^2 < 0.97$. Figure 4.2 shows the peak-to-trough amplitude decay for both $^1H_4$-aminoethanol (top) and $^2H_4$-aminoethanol (bottom) substrate samples at sucrose concentrations 2% (w/v). Both decays shown are fitted to a biexponential and a monoexponential+ power law as a representation of the fits for sucrose concentrations between 1 and 4% (w/v) for $^1H_4$ decay samples and 1 and 30% (w/v) for $^2H_4$ decay samples. Figure 4.3 shows the power law fits for these samples failed to capture key features of the decays, similar to the biexponential fits.

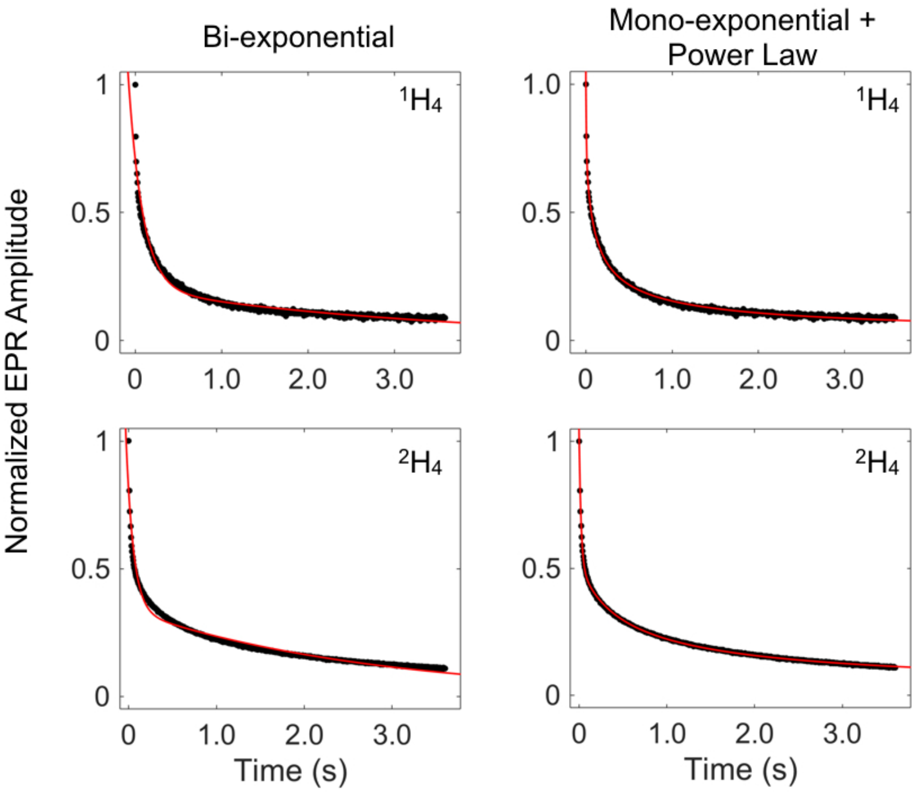

**Figure 4.2. Substrate radical amplitude decay at 217 K** for $^1H_4$-aminoethanol (top) and $^2H_4$-aminoethanol (bottom) with sucrose concentration of 2% (w/v). Samples were fit to either a biexponential (left) or monoexponential + power law (right).

For $^1H_4$-substrate radical decays with sucrose concentrations between 5-30 % (w/v), the best fit was a single power law (Equation 4.2) with $R^2 > 0.98$. Both the biexponential and monoexponential + power law fits expressed similar $R^2$ values, however, they also expressed large confidence intervals (over multiple orders of magnitude in most cases). Therefore, the power law expression was determined to be the best fit. For 0% sucrose concentrations, the biexponential was determined to be the best fit, previously established in chapters 2 and 3.

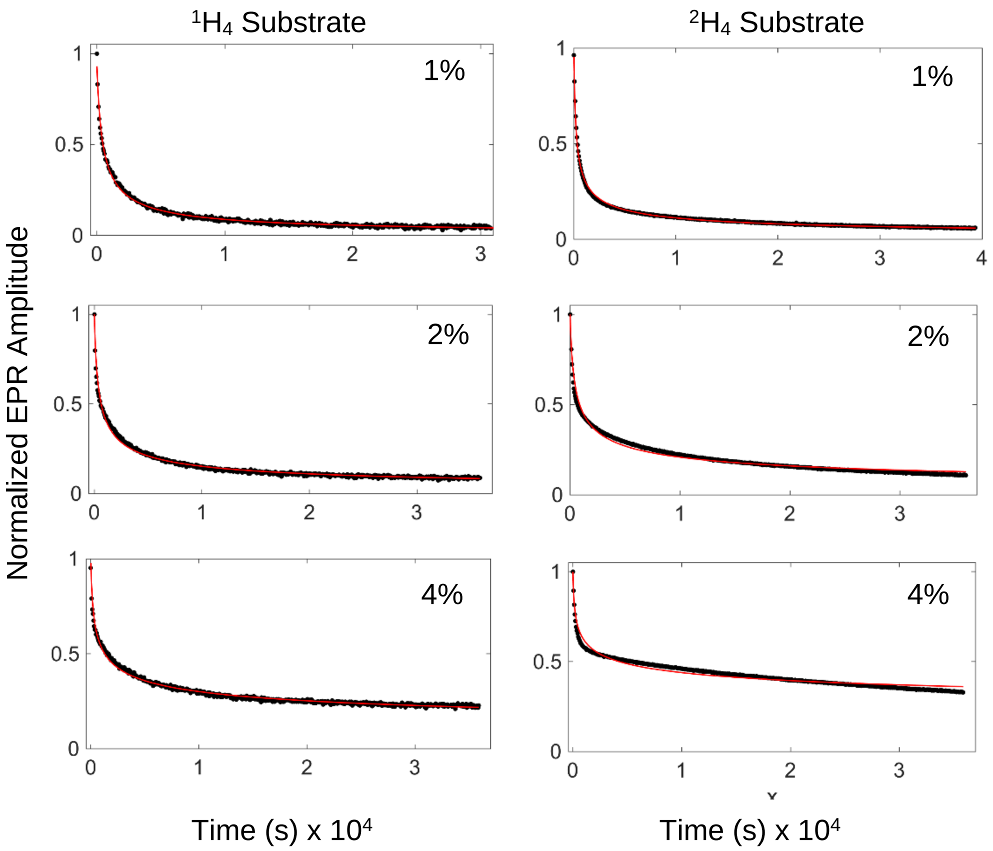

**Figure 4.3. Power law fits to substrate radical amplitude decay at 217 K** for $^1H_4$-aminoethanol and $^2H_4$-aminoethanol with varying sucrose concentrations.

Figure 4.4 shows the peak-to-trough amplitude decay for both $^1H_4$-aminoethanol (A) and $^2H_4$-aminoethanol (B) substrate samples with sucrose concentrations between 0 and 30% (w/v) fitted with either a biexponential (0% for $^1H_4$ and $^2H_4$), monoexponential + power law (1-4% for $^1H_4$ and 1-30 for $^2H_4$), or power law (5-30% for $^1H_4$).

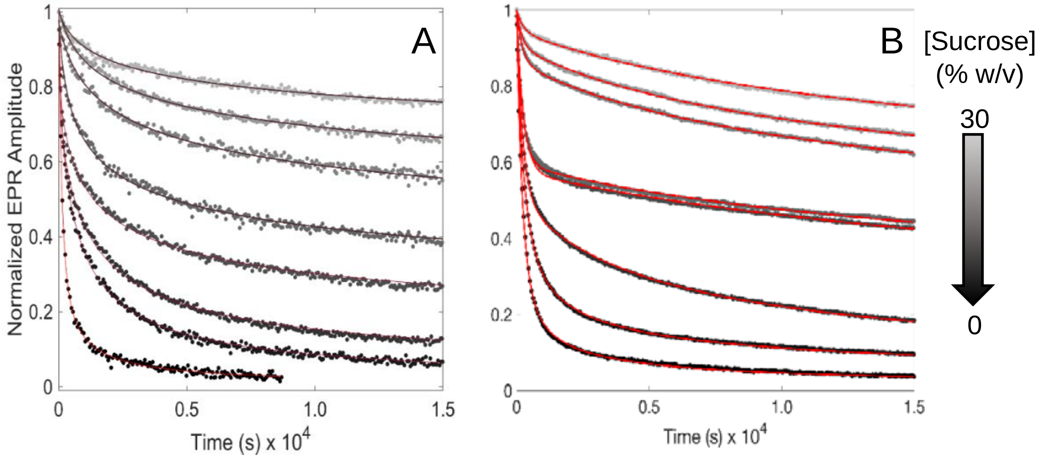

**Figure 4.4. Best fits for substrate radical amplitude decay at 217 K** for $^1H_4$-aminoethanol (A) and $^2H_4$-aminoethanol (B) with sucrose concentrations between 0 and 30% (w/v). Decays were fit to either a biexponential (0%), monoexponential + power law (1-4% for $^1H$ and 1-30% for $^2H$), or power law (5-30% $^1H$).

Table 4.1 shows the transient kinetic fits for $^1H_4$-aminoethanol substrate decays. The 0% (w/v) sucrose decay curves were fit to a biexponential. Sucrose concentrations of 1-4% (w/v) were also biphasic, the fast phase is described with a monoexponential and the slow phase is described by the power law (Equation 4.2). For sucrose concentrations of 5% and above, a single power law delineates the decay. The rate constant, $k_{peak,s}$, is the most probable rate constant in the power law distribution.

**Table 4.1. First-order rate constant and amplitude parameters** for the fit of the biexponential function (0%), monoexponential and power law (1-4%), and power law (5-30%) to the Co$^{II}$-substrate radical pair $^1H_4$-aminoethanol decay kinetics at 217 K. $A_{obs,s}$ (not shown) is 1- $A_{obs,f}$

| %(w/v) | $k_{obs,f}$ (s$^{-1}$) | $A_{obs,f}$ | $k_{peak,s}$ (s$^{-1}$) | $t_{0,obs,s}$ (s) | $n_{obs,s}$ | $R^{2\,a}$ |
|---|---|---|---|---|---|---|
| 0 | 1.2(±0.4) ×10$^{-2}$ | 0.63±0.09 | 3.8(±1.8) ×10$^{-3}$ | -- | -- | 0.9990 |
| 1 | 1.3(±0.1) ×10$^{-2}$ | 0.24±0.09 | 1.3(±0.3) ×10$^{-3}$ | 5.8(±0.3) ×10$^{2}$ | 7.5(±0.7) ×10$^{-1}$ | 0.9974 |
| 2 | 1.7(±0.1) ×10$^{-2}$ | 0.26±0.08 | 9.4(±2.0) ×10$^{-4}$ | 5.8(±0.2) ×10$^{2}$ | 5.4(±0.4) ×10$^{-1}$ | 0.9955 |
| 4 | 3.1(±0.5) ×10$^{-2}$ | 0.19±0.06 | 1.0(±0.1) ×10$^{-3}$ | 2.8(±0.2) ×10$^{2}$ | 2.7(±0.2) ×10$^{-1}$ | 0.9922 |
| 5 | -- | -- | 1.3(±0.1) ×10$^{-3}$ | 1.6(±0.1) ×10$^{2}$ | 2.0(±0.1) ×10$^{-1}$ | 0.9919 |
| 10 | -- | -- | 3.5(±0.5) ×10$^{-4}$ | 4.5(±0.2) ×10$^{2}$ | 1.6(±0.1) ×10$^{-1}$ | 0.9881 |
| 20 | -- | -- | 3.0(±0.4) ×10$^{-4}$ | 3.7(±0.2) ×10$^{2}$ | 1.1(±0.1) ×10$^{-1}$ | 0.9930 |
| 30 | -- | -- | 2.1(±0.3) ×10$^{-4}$ | 3.5(±0.3) ×10$^{2}$ | 7.3(±0.1) ×10$^{-2}$ | 0.9861 |

Table 4.2 shows the transient kinetic fits for $^2H_4$-aminoethanol substrate decays. The 0%(w/v) sucrose decay curves were fit to a biexponential. Sucrose concentrations of 1% (w/v)

and above were also biphasic, the fast phase is described with a monoexponential and the slow phase is described by the power law (Equation 4.2).

**Table 4.2. First-order rate constant and amplitude parameters** for the fit of the biexponential function (0%) and monoexponential and power law (1-30%) to the Co$^{\mathrm{II}}$-substrate radical pair $^{2}H_4$-aminoethanol decay kinetics at 217 K. $A_{\mathrm{obs,s}}$ (not shown) is 1- $A_{\mathrm{obs,f}}$

| %(*w/v*) | $k_{\mathrm{obs,f}}$ (s$^{-1}$) | $A_{\mathrm{obs,f}}$ | $k_{\mathrm{peak,s}}$ (s$^{-1}$) | $t_{0,\mathrm{obs,s}}$ (s) | $n_{\mathrm{obs,s}}$ | $R^2$ |
|---|---|---|---|---|---|---|
| 0 | $4.7(\pm0.5)\times10^{-3}$ | 0.80±0.04 | $1.6(\pm0.6)\times10^{-3}$ | -- | -- | 0.9992 |
| 1 | $3.7(\pm0.6)\times10^{-3}$ | 0.55±0.07 | $8.1(\pm0.4)\times10^{-4}$ | $5.8(\pm0.3)\times10^{2}$ | $4.7(\pm0.1)\times10^{-1}$ | 0.9981 |
| 2 | $4.5(\pm0.04)\times10^{-3}$ | 0.48±0.03 | $1.8(\pm0.6)\times10^{-4}$ | $3.4(\pm0.2)\times10^{3}$ | $6.2(\pm0.4)\times10^{-1}$ | 0.9993 |
| 4 | $4.0(\pm0.04)\times10^{-3}$ | 0.42±0.04 | $2.9(\pm1.6)\times10^{-5}$ | $1.7(\pm0.2)\times10^{4}$ | $4.7(\pm0.2)\times10^{-1}$ | 0.9981 |
| 5 | $4.5(\pm0.05)\times10^{-3}$ | 0.40±0.08 | $3.3(\pm1.5)\times10^{-5}$ | $9.8(\pm0.1)\times10^{3}$ | $3.2(\pm0.1)\times10^{-1}$ | 0.9974 |
| 10 | $4.8(\pm0.09)\times10^{-3}$ | 0.13±0.01 | $4.6(\pm1.6)\times10^{-5}$ | $5.3(\pm0.2)\times10^{3}$ | $2.4(\pm0.1)\times10^{-1}$ | 0.9995 |
| 20 | $5.0(\pm0.1)\times10^{-3}$ | 0.09±0.01 | $4.4(\pm1.5)\times10^{-5}$ | $4.9(\pm0.2)\times10^{3}$ | $2.1(\pm0.1)\times10^{-1}$ | 0.9994 |
| 30 | $4.2(\pm1.0)\times10^{-3}$ | 0.06±0.01 | $2.8(\pm1.2)\times10^{-5}$ | $7.6(\pm0.3)\times10^{3}$ | $2.2(\pm0.1)\times10^{-1}$ | 0.9612 |

## 4.4 Discussion

### 4.4.1 Decreased Amplitude of the Fast Phase

The fast phase rate is relatively constant from 0-4% sucrose concentration for $^{1}H_4$-aminoethanol substrate samples and throughout all the $^{2}H_4$-aminoethanol substrate samples. However, the fast phase amplitude decreases smoothly as sucrose concentration increases for both substrates. This decrease can be explained by a shift in the transition temperature region (described in Chapter 2) to higher temperatures for increasing sucrose concentrations. During rapid quench of the samples from (273 to 140 K) the sample temperature decreases at a rate of approximately 10 K/s. [51] The enzyme is actively forming diamagnetic products throughout the quench, leading to a loss of paramagnetic signal. The enzyme ensemble in each sample reacts at a rate $k_{obs,n}$ , that adheres to the Arrhenius reaction rate theory (Equation 2.6), from 295 K to the transition temperature region. The transition temperature region for samples with sucrose concentrations of 0% (w/v) occurs between 219-217 K, where the monotonic decay, characterized by a single reaction rate constant, bifurcates into two distinct rate constants: $k_{obs,f}$ and $k_{obs,s}$[103]. At this transition temperature region, these rate constants are temperature independent, at approximately 0.013 $s^{-1}$ ($^{1}H_4$) and 0.006 $s^{-1}$ ($^{2}H_4$) for the fast phase rate constant ($k_{obs,f}$). The slow phase rate constant ($k_{obs,s}$) is approximately 3-fold slower than the fast phase rate constant: 0.004 $s^{-1}$ ($^{1}H_4$) and 0.002 $s^{-1}$ ($^{2}H_4$). Each sample spends approximately 0.3 s in the transition region during quenching. For samples with sucrose concentrations of 0% (w/v) the amplitude loss at the transition temperature region is negligible for both $k_{obs,f}$ and $k_{obs,s}$.

According to previous TEMPOL spin probe experiments,[117] the dynamical transition shifts to higher temperatures for increasing sucrose concentrations. The rate constants: $k_{obs,f}$ and

$k_{\mathrm{obs,s}}$ , are faster than samples with sucrose concentrations of 0% (w/v). At higher temperatures, the amplitude loss becomes significant. Further, analysis of the transient kinetics for samples with various sucrose concentrations presented in this chapter (Figure 4.3, Tables 4.1-2) indicate that the slow phase rate constant $k_{\mathrm{obs,s}}$, slows with higher concentrations of sucrose, while the fast phase rate constant remains unchanged. This characteristic of the sucrose samples causes a greater amplitude loss in the fast phase than the slow phase. Specific temperature transitions for low sucrose concentrations are explored in the next chapter (Chapter 5).

### 4.4.2 Rate Distribution of the Slow Phase

The power law associated with the slow phase implies that the rate constant and activation energy are distributed. The rate distribution $g(k)$ can be calculated using a Laplace transform:

$$g(k) = \frac{(t_0 k)^n e^{-t_0 k}}{RT\Gamma(n)} \tag{4.5}$$

where $t_0$ and $n$ are the parameters from the power law fit, R and $T$ are the gas constant and temperature respectively and $\Gamma(n)$ is the gamma function. Full derivation of Equation 4.5 has been shown previously. [124] Figure 4.5-6 depicts the rate distribution for the $^1H_4$-aminoethanol substrate samples (Figure 4.5) and the $^2H_4$-aminoethanol substrate samples (Figure 4.6).

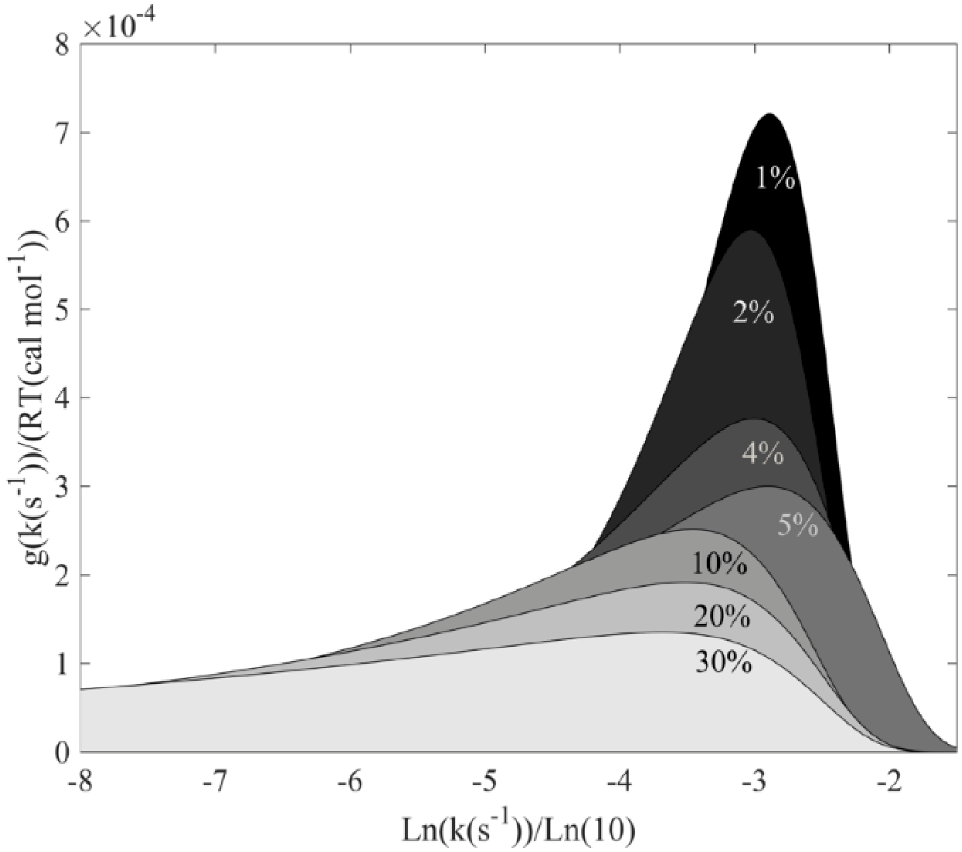

**Figure 4.5. Slow phase rate distribution for $^1H_4$-aminoethanol substrate samples at 217 K.** Distributions were calculated using Equation 4.5. The parameters $t_0$ and $n$ that were used to calculate the distribution are from the power law decay fits. Areas under the distributions are normalized.

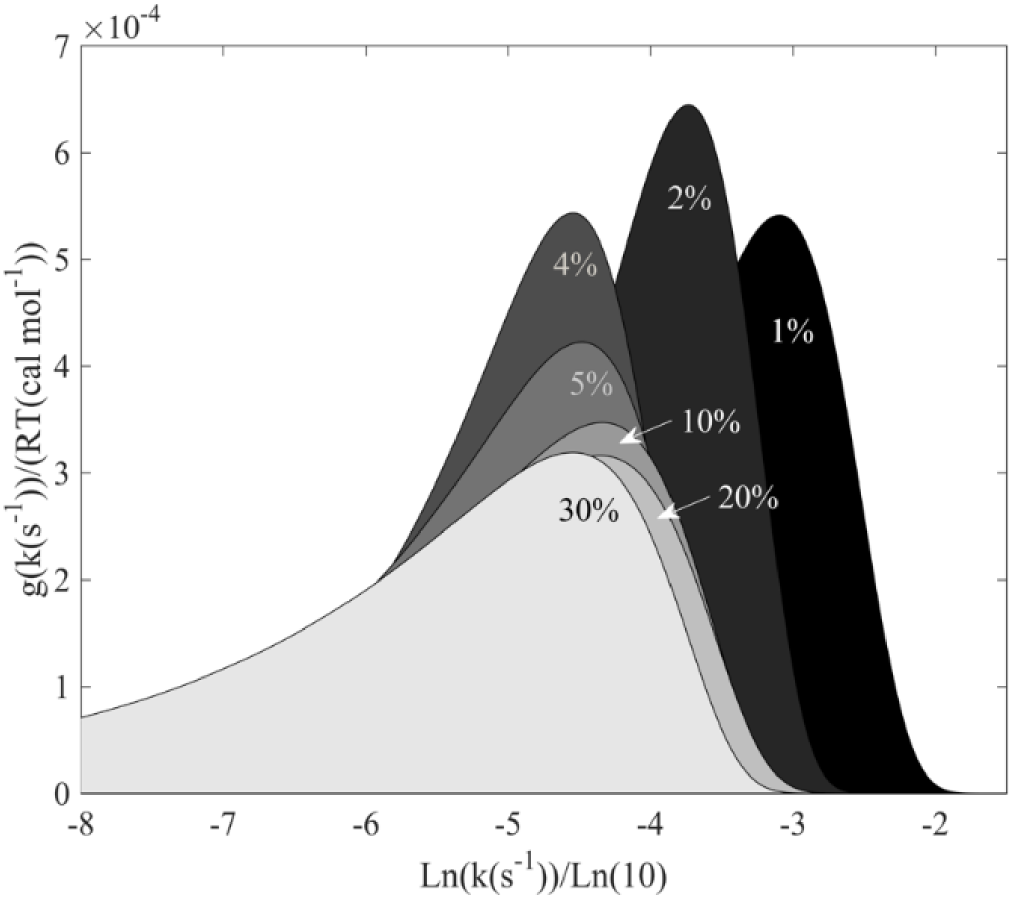

**Figure 4.6. Slow phase rate distribution for $^2H_4$-aminoethanol substrate samples at 217 K.** Distributions were calculated using Equation 4.5. The parameters $t_0$ and $n$ that were used to calculate the distribution are from the power law decay fits. Areas under the distributions are normalized.

Figure 4.7 shows the $^1H_4$-aminoethanol and $^2H_4$-aminoethanol substrate sample distributions compared directly. In general, the $^2H_4$-aminoethanol samples have narrower distributions and slower $k_{peak,s}$ values than the $^1H_4$-aminoethanol samples.

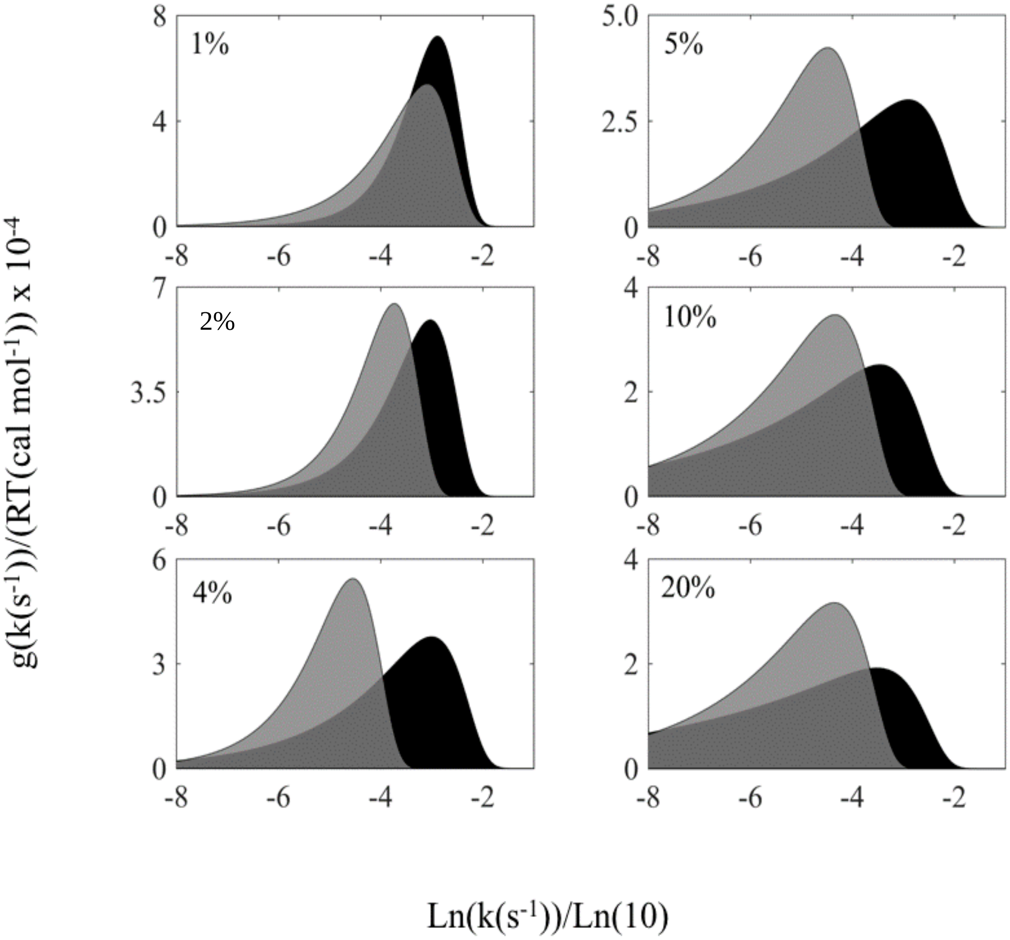

**Figure 4.7 Slow phase rate distributions at 217 K** for $^{1}H_4$-aminoethanol (black) and $^{2}H_4$-aminoethanol (gray) substrate samples for varying sucrose concentrations. Distributions were calculated using Equation 5. The parameters $t_0$ and $n$ that were used to calculate the distribution are from the power law decay fits. Areas under the distributions are normalized.

This could be due to the influence of the second hydrogen transfer step (HT2) on the $^{2}H_4$-aminoethanol samples. Based on the results of chapter 3, the rate constant associated with the HT2 step, $k_{HT}$, undergoes a dynamical temperature transition at 227 K for samples with sucrose concentrations of 0% (w/v). Increasing sucrose concentrations would shift the dynamical transition for $k_{HT}$ to higher temperatures with increased amounts of sucrose (similar to the transitions predicted in Table 4.3). This shift in transition temperature may change the $\frac{k_{HT}}{k_{PS}}$ fraction. The fraction would decrease compared to 0% sucrose concentrations because the Arrhenius slope for $k_{\mathrm{HT}}$ would increase in magnitude. Based on the low temperature IE vs $\frac{k_{HT}}{k_{PS}}$ plot (Figure 3.12) a decrease in $\frac{k_{HT}}{k_{PS}}$ fraction would cause an increase in the IE for $k_{\mathrm{obs,s}}$ which explains the shift of $k_{\mathrm{peak,s}}$ to slower rates (when comparing $^1$H and $^2$H samples with the same sucrose concentrations). The decrease in $\frac{k_{HT}}{k_{PS}}$ fraction would also increase IE for $k_{\mathrm{obs,f}}$ , however, the effect would be much less dramatic (Figure 3.12). than the IE on $k_{\mathrm{obs,s}}$ and could prove to be undetectable. Further high temperature, high sucrose studies for $^2H_4$-radical decay studies would be needed to determine the exact effect of the HT2 step on samples that include sucrose.

### 4.4.3 Sucrose Effect on Local, Incremental Fluctuations

The experimental temperature (217 K) is below the dynamic transition (assuming $\Delta T$ = 3 K) where local, incremental motions drive the reaction,[103] for sucrose concentrations > 0%. In this region, the kinetics are described using the three-state two-step model (Scheme 2.1). The incremental fluctuations associated with the slow phase are described using a power law (+1% sucrose concentration) instead of a single rate constant (0% sucrose concentration). This indicates that the energy barriers associated with the FEL become roughened, causing the protein to sample more configurations along the energy barriers as the sucrose concentration is increased.

## 4.5 Conclusions

The features ($k_{\mathrm{obs,f}}$ and $k_{\mathrm{obs,f}}$)of the first-order kinetic measurement for the substrate radical decays of varying concentrations of sucrose at 217 K reveal the dramatic effect protein dynamics have on the chemical reaction. Both populations (fast and slow) reveal different effects of sucrose on the protein dynamics. Both $^1H_4$-aminoethanol and $^2H_4$-aminoethanol substrate decay series reveal similar sucrose effects. Both decay series reveal a decrease in fast phase amplitude with increasing sucrose concentrations and no change in the rate of the observed fast phase ($k_{obs,f}$). Both slow phases for $^1H_4$-aminoethanol and $^2H_4$-aminoethanol substrate decay series exhibit power law behavior, however the $^1H_4$-aminoethanol substrate decays had a broader slow phase rate distribution.

The smooth decrease in fast phase amplitude ($A_{\mathrm{obs,f}}$) (with increased sucrose concentrations) reveal the shift of the dynamical transition, associated with the quenching of collective motions in the protein, to higher temperatures, which is consistent with previous TEMPOL studies of solvent dynamics.[117] The sucrose effect on local protein fluctuations manifests as an increase in protein configurational sampling along the reaction coordinate, demonstrated by the power law behavior of the slow phase (which is most closely associated with the $S_1^\bullet \leftrightarrow S_2^\bullet$ process).[103] However, the rate ($k_{\mathrm{obs,f}}$) associated with the fast phase remains constant with varying sucrose concentrations for both $^1H_4$-aminoethanol and $^2H_4$-aminoethanol substrates. This leads to the hypothesis that the local protein fluctuations driving the $S_2^\bullet \rightarrow P^\bullet$ process are different than the local protein fluctuations driving the $S_1^\bullet \leftrightarrow S_2^\bullet$ process. Application of the microscopic model is necessary, which is explored in the next chapter. Further, spectra collected at 120 K, prior to the decay of the samples at 217 K, for low concentrations of sucrose (0-4%) contain the Co(II)-substrate radical pair with the same features as 0% sucrose concentrations for both $^1H_4$-aminoethanol and $^2H_4$-aminoethanol substrate samples. This indicates that the kinetic features (changes in $k_{obs,s}$ and $k_{obs,f}$ relative to 0% sucrose concentrations) revealed by sucrose are dynamic in nature and do not originate from structural differences in the active site.

# Chapter 5

# Characterization of Contributions of Solvent-Coupled Protein Configurational Dynamics to the Rearrangement Reaction in $B_{12}$-Dependent Ethanolamine Ammonia-Lyase

## 5.1 Introduction

The dynamical temperature transitions present in $^1H_4$-aminoethanol and $^2H_4$-aminoethanol generated Co(II)- substrate radical pair decays in EAL[27, 57, 102, 125] demonstrate the effect of protein dynamics on the kinetics associated with the radical rearrangement step.[49, 58, 103] Within this dynamical transition (219 – 217 K), the fluctuations of the protein transition from collective to localized, incremental motions, that drive the chemical reaction from substrate to product.[1-3, 64-67] These motions define the native reaction coordinate for the radical rearrangement step.[69-70] Both $^1H_4$-aminoethanol and $^2H_4$-aminoethanol generated Co(II)- substrate radical pair decays[49, 78, 103] exhibit the same bifurcation and kinks in the Arrhenius plot of the rate constants within the transition temperature region (219-217 K). Therefore, this transition does not originate from a chemical process associated with primary or secondary hydrogen isotope effect or with any hydrogen transfer step. Rather, the bifurcation and kinks arise from a change in protein dynamics.[57-58, 95, 103, 107-110]

Protein dynamics are highly influenced by the solvent.[23, 114-118] Specifically, protein dynamics are affected by the formation of ice or glass in the bulk solvent as the solution freezes.[118] First-order kinetic measurements of the substrate radical pair decays reveal the dramatic effect of protein dynamics on the chemical reactions. Therefore, by introducing varying sucrose concentrations within a sample set (Chapter 4) the dynamical effects on the substrate radical step can be measured. Specifically, sucrose affects both collective and incremental protein fluctuations that define the reaction coordinate. (Figure 4.2, Tables 4.1-2) Results from the previous chapter, based on first-order kinetic measurements at 217 K, suggest a shift of the dynamical transition temperature region to higher temperatures upon addition of sucrose to the aqueous solution. This shift of the dynamical transition region is consistent with TEMPOL spin measurements.[117, 120-122]

The general effects sucrose concentrations have on the dynamics of the protein for both collective and incremental motions are established via the transient kinetics for the substrate radical step (Chapter 4). Low sucrose concentrations produce identical EPR substrate radical spectra to 0% sucrose spectra (Figure 4.1) (Co(II) to C1 distance of 11 ± 1 Å.[125-126] ). This suggests that any kinetic effects are a result of a change in the dynamics of the protein and not in an inherent structural change in the protein.

The most prevalent sucrose effect revealed in Chapter 4 was the distributive properties of the substrate radical decays. This non-exponential behavior suggests that EAL does not have a single structure but can assume many slightly different structures or configurational substates[127-128] with different reaction rates. According to the microscopic model previously presented,[103] there are two distinct states ($\mathbf{S}_1^\bullet$ and $\mathbf{S}_2^\bullet$) below the 217 K that describe the substrate radical. These two states are comprised of several configurational substates that provide the platform for protein motions.

In order to fully describe the effect of sucrose on the substrate radical the properties of enzyme motions need to be discussed in terms of the features of the free energy landscape (FEL). In this chapter we propose that sucrose restricts the motion of the enzyme, causing a rise in energy barrier height between the configurational substates. (Figure 5.13) These substates only reveal themselves at low temperatures, where each protein remains locked in a single configurational substate.[127] For samples without sucrose, the substrate radical decays become non-exponential at approximately 187 K.[129] For samples containing sucrose this non-exponential behavior occurs at much higher temperatures (Chapter 4). At these low temperatures the motion of the protein through the configurational substates becomes rate determining.

These motions can be classified as either a relaxation process, where the FEL is in flux, or equilibrium fluctuations, where the FEL is unchanging (on the timescale of the experiment).[127] In the EAL system, protein relaxation occurs at the transition temperature region (219-217 K) for samples without sucrose, where the protein is relaxing on the same timescale that chemical reaction occurs.[103] In this region, the kinetic behavior does not satisfy the Arrhenius relation and both the Arrhenius intercept and activation energy are changing with temperature. However, below this temperature region the FEL is unchanging and the kinetics follow the Arrhenius relation.[103]

Therefore, in order to determine whether the non-exponential behavior is caused by a relaxation process or equilibrium fluctuations, the substrate radical decays are fitted to the power law function (Equation 4.2) (slow phase). This power law assumes that the kinetics follow the Arrhenius behavior and the Arrhenius intercept and the activation energy distribution is constant with temperature.[97] Therefore, the activation energy distributions can be used as a metric for the type of motion that is influencing the kinetic behavior at a given temperature. This chapter identifies the types of motions and specific configurational substates that influence the kinetics of the reaction. Additionally, these kinetic studies fully characterize the transition temperature region and the sucrose effect on the two distinct sets of native protein collective configurational fluctuations for low sucrose concentration radical decays.[103]

## 5.2 Materials and Methods

### 5.2.1 Sucrose Sample Preparation

Sucrose solutions were prepared using the USDA Brix conversion tables[123] to calculate the weight per volume (w/v) percentage of sucrose in 10mM KPi solution. A 10%(w/v) stock solution was prepared and used to create 1% and 2% sucrose samples. Equation 4.1 was used to calculate the % (w/v) of the stock solution.

### 5.2.2 Enzyme Purification and Sample Preparation

Enzyme was purified from the *Escherichia coli* overexpression system incorporating the cloned S. typhimurium EAL coding sequence[89] as described,[90] with modifications.[37] The specific activity of purified EAL with aminoethanol as substrate was 20 μmol/min/mg (T = 298 K, *P* = 1 atm), as determined by using the coupled assay with alcohol dehydrogenase and NADH.[30]

Reactions were performed in aerobic buffer containing 10 mM potassium phosphate (pH 7.5). Manipulations were carried out on ice under dim red safe-lighting. No photodegradation of the coenzyme $B_{12}$ (adenosylcobalamin, AdoCbl) cofactor was detected under any of the conditions. An EAL-10 mM KPi solution was centrifuged (5000 rpm) with ~ 70% efficiency to isolate pure EAL for sample preparation. EAL was resuspended in 10mM KPi, varying %(w/v) sucrose, B12, and $^{1}H_{4}$-aminoethanol or $^{2}H_{4}$-aminoethanol substrate solutions. Final concentration of EAL was 15mg/mL which is equivalent to 20−30 μM for a holoenzyme molecular mass of 500 000 g/mol,[90] and an active site concentration of 120−180 μM, based on an active site/ holoenzyme stoichiometry of 6:1.[91-92] AdoCbl was added the sample at a ratio of 2:1 to EAL active site. $^{1}H_{4}$-aminoethanol substrate concentrations were 100mM. All samples were manually mixed and loaded into a 4 mm outer diameter EPR tube, and the tube was immersed in isopentane (T = 140 K; elapsed time, ∼10 s). The procedure for cryotrapping of the $Co^{2+}$-substrate radical pair samples has been described in detail.[51]

### 5.2.3 Time-Resolved, Full Spectrum EPR Measurements of Substrate Radical Decay

EPR spectra were collected by using a Bruker E500 ElexSys EPR spectrometer equipped with a Bruker ER4123 SHQE cavity. EPR samples were held at a staging temperature of 160−180 K and temperature was step-increased to decay measurement value of 203-232 K for samples with sucrose concentrations of 1 and 2% (w/v) for both $^1H_4$-aminoethanol substrates. The time from initiation of the temperature step to the start of acquisition of the first spectrum was 30−60 s.

### 5.2.4 Transient Kinetics Analysis

EPR spectra were collected every 5 seconds. For each EPR spectrum in the decay time series, the amplitude of the substrate radical signal was obtained from the difference between peak and trough amplitudes of the derivative feature around $g \approx 2.0$, with baseline correction. The decay curves were fit with a biexponential ($N$=2, equation (Equation 2.1) for $T > 220$ K (1% (w/v) sucrose samples) and $T > 223$ K (2% (w/v) sucrose samples) or a combination of a monoexponential ($N$=1, equation (Equation 2.1) (fast phase) and power law fit (Equation 4.2) (slow phase) for $T \leq 220$ K (1% (w/v) sucrose samples) and $T \leq 223$ K (2% (w/v) sucrose samples).[124]

### 5.2.5 Simulation of Substrate Radical Decay Based on the Distributed Rate Constant Model

Chapter 4 established the distributed rate constant model for the slow phase of the observed kinetics for sucrose concentrations 1-4 % (w/v) at 217 K:

$$A(t) = A_{obs,f}e^{-k_{obs,f}t} + (1 - A_f)(1 + \frac{t}{t_0})^{-n} \tag{5.1}$$

where the amplitude ($A$) is related to the parameters $k_{\mathrm{obs,f}}$, $t_0$ and $n$, where the most probable rate constant ($k_{\mathrm{peak,s}}$) is equal to $\frac{n}{t_0}$ [124] for the slow phase. The parameter $A_{\mathrm{obs,f}}$ is the proportion constant associated with the fast phase population that decays at a single rate, $k_{\mathrm{obs,f}}$. This model for the observed kinetics is used for samples with sucrose concentrations of both 1 and 2 % (w/v), for decays measured at $T \leq 220$ K (1% (w/v) sucrose samples) and $T \leq 223$ K (2% (w/v) sucrose samples).

Due to the slow phase rate distribution from the transient kinetic analysis for samples collected at 203-210 K with sucrose concentrations of 1% and 2% (w/v), (outside of the transition temperature region) the slow phase rate distribution from the transient kinetic analysis (Figure 5.3) was partitioned into 10 divisions (Figure 5.5) with equal areas for each sample decay. The average rate constant was calculated for each division (Figure 5.8, black squares) (Appendix 7.6). A set of 10 biexponential decays were generated for each sample using Equation 5.2:

$$A_i(t) = A_f e^{-k_f t} + (1 - A_f)e^{-k_{s,i}t} \tag{5.2}$$

where the amplitude for each biexponential is $A_i(t)$, $A_{\mathrm{f}}$ and $k_{\mathrm{f}}$ correspond first order decay parameters $A_{\mathrm{obs,f}}$ and $k_{\mathrm{obs,f}}$ from each experimental decay. The rate constant $k_{\mathrm{obs,s,i,}}$ is the average rate constant for the $i^{\mathrm{th}}$ division from each slow phase rate distribution from the transient kinetic analysis (Figure 5). The time ($t$) is the same time array used for the experimental decays (generated when the EPR spectra where collected). The decay curves were overlaid with the total normalized amplitude $\frac{\sum_{i=1}^{10} A_i(t)}{10}$ of the corresponding set of biexponential decays (Figure 6) and the R-squared were calculated.

### 5.2.6 Numerical simulation and fitting to the microscopic model

The set of biexponential decays generated for each substrate radical decay were fitted to the 3-state, 2-step microscopic kinetic model (Scheme 2.1), where $S_1^\bullet$ , $S_2^\bullet$ and $P$ are states, and $k_{12}$, $k_{21}$ and $k_P$ are first-order rate constants, for temperatures 203 and 210 K.

The set of ordinary differential equations (Equations 2.2-4) describe the time dependence of $S_1^\bullet$, $S_2^\bullet$ and P. The equations were solved explicitly, under the initial conditions, $S_1^\bullet = A_1$, $S_2^\bullet = 1-A_1$ and P = 0, where $A_1$ is the initial concentration of the S1 state. The substrate radical signal decays to zero and forms diamagnetic products. Therefore, the solution for P(t) was fit to the 1-normalized substrate radical decays by using the least squares regression analysis (Equation 2.5). The *lsqcurvefi*t function in Matlab was used to find the numerical solution for the product (P(t)) for each decay. Trust-region-reflective and Levenberg-Marquardt algorithms were used. Both algorithms were shown to have no significant difference between results, with the lower bounds of the step size and the function set to $10^{-10}$. Each fit of the microscopic model to the set of biexponential decays generated a corresponding array of values for the microscopic rate parameters, $k_{12}$, $k_{21}$, and $k_p$ associated with the microscopic model (Scheme 2.1).

## 5.3 Results

### 5.3.1 Time-Resolved, Full-Spectrum EPR Measurements of the $Co^{2+}$-Substrate Radical Pair Decay for 1% and 2% (w/v) Sucrose Concentrations

EPR spectra of the substrate radical component were acquired continuously as the decay of the $Co^{2+}$-substrate radical pair progressed, following $T$-step to temperatures of 203−232 K. The experimental decays were performed to a level of ≤10% of the initial amplitude, to identify the possible presence of multiple components and to obtain reliable rate constants and amplitudes from fits to theoretical decay functions The decay curves were well-fit by a biexponential function with the observed phase rates $k_{\mathrm{obs,n}}$ and $k_{\mathrm{obs,s*}}$ with corresponding amplitudes $A_{\mathrm{obs,n}}$ and $A_{\mathrm{obs,s*}}$ over the temperature range 223−232 K for 1% (w/v) sucrose samples and 225-232 K for 2% (w/v) sucrose samples (Table 1). The parameters $k_{\mathrm{obs,s*}}$ and $A_{\mathrm{obs,s*}}$, are associated with the small portion of the substrate radical decay that is several orders of magnitudes slower than the majority of the decay. This population does not appear to have a temperature dependence and does not follow any kinetic behaviors shown for 0% sucrose.

The decay curves collected at $T \leq 220$ K (1% sucrose) and at $T \leq 223$ K (2% sucrose) were fit to both a biexponential and a combination of monoexponential and power law (Equation 5.1). The biexponential fit failed to capture all the features of the substrate radical decays with $R^2 < 0.97$ (Figure 5.1 Top, Figure 4.2). However, the decay curves were well-fit by the monoexponential + power law equation. (Figure 5.1 Bottom, Figure 4.2). Figure 5.1 shows the fits of the radical decay with the monoexponential plus power law. A power law was also fit to the decays, which resulted in $R^2$ values similar to the biexponential fits and also failed to capture all the features of the decay (Figure 4.3).

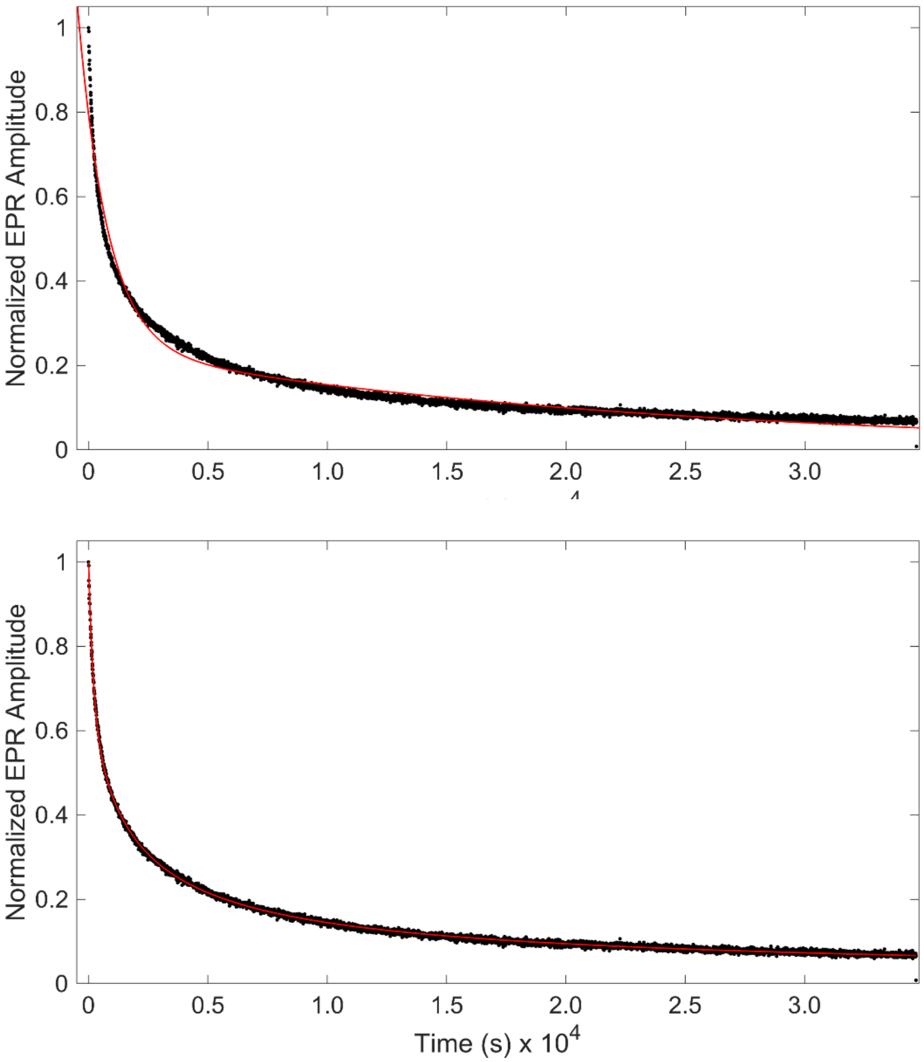

**Figure 5.1. Substrate radical amplitude decay with sucrose concentration of 1% (w/v) at 210 K** Samples were fit to a biexponential (top) and monoexponential + power law (bottom).

Therefore, Equation 5.1 was used to describe the transient kinetics for the decay curves collected at $T \leq 220$ K (1% sucrose) and at $T \leq 223$ K (2% sucrose). Figure 5.2 and Table 5.1 show the decay fits and their parameters respectively. The fast phase for each decay was described as a monoexponential decay with the rate constant $k_{\mathrm{obs,f}}$ ($T > 217$ K) or $k'_{\mathrm{obs,f}}$ ($220 \geq T \geq 217$ K and

223 ≥ $T$ ≥ 217 K, for 1% and 2% (w/v) sucrose concentrations respectively) and with the corresponding $A_{\mathrm{obs,f}}$ . The slow phase portion of each decay is distributed, and well-fit to a power law, with decay parameters $t_{0,\mathrm{obs,s}}$ and $n_{\mathrm{obs,s}}$, where the most probable decay rate is $k_{\mathrm{obs,s}}$ $\left(\frac{n_{obs,s}}{t_{0,obs,s}}\right)$ or $k'_{\mathrm{obs,s}}$ (220 ≥ $T$ ≥ 217 K and 223 ≥ $T$ ≥ 217 K, for 1% and 2% (w/v) sucrose concentrations, respectively). [124]

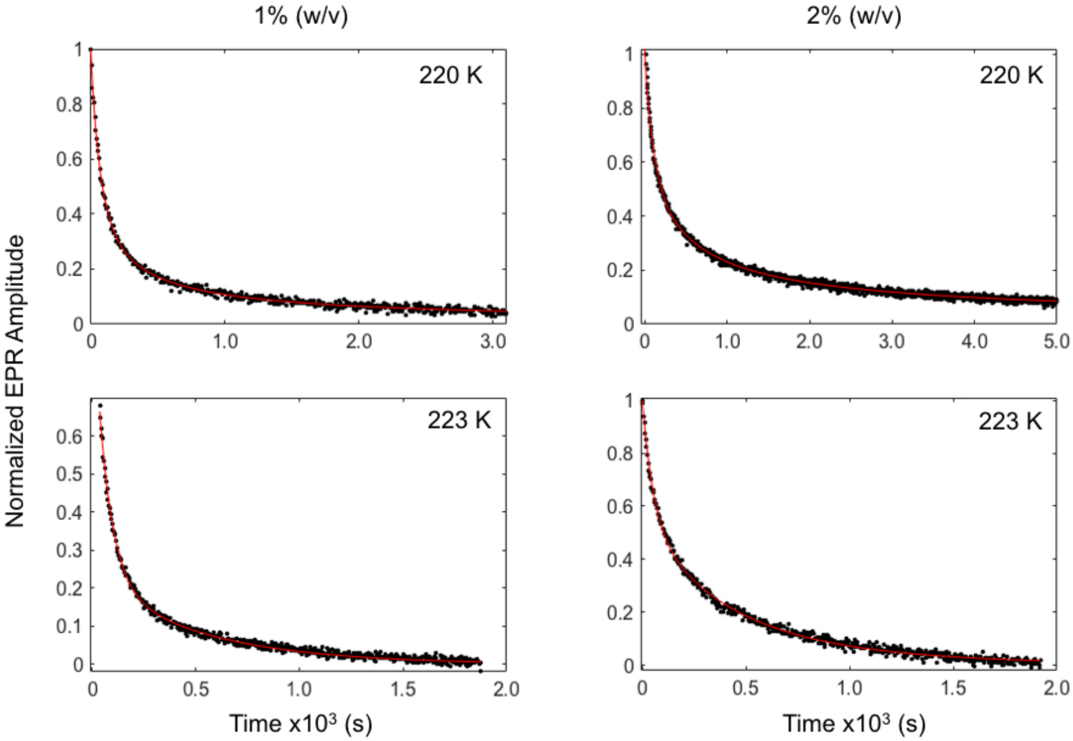

**Figure 5.2. Time-dependence of the EPR amplitude of the substrate radical. Decays** at $T$ = 220 and 223 K for 1 and 2% (w/v) values and overlaid best-fit biexponential (1% at 223 K) or monoexponential plus power law functions (2%, 1% at 220 K) (red line).

### 5.3.2 Temperature-Dependence of the Observed Rate Constants

Figure 5.3 shows the Arrhenius plot (ln $k_{\mathrm{obs}}$ versus $T^{-1}$) of the rate constants from the empirical fits to the decay of the $\mathrm{Co}^{2+}$- substrate radical pair state in EAL with 1-2% (w/v) sucrose concentrations from 203 to 232 K. They are characterized by three regions: (1) high-$T$

region, ($T \geq 223$ K for 1%, $T \geq 225$ K for 2% ) described by a dominant phase with the rate, $k_{\mathrm{obs,n}}$, which consists of ~ 90-80% of the sample decay. This phase represents the native reaction in this temperature region, both 1% and 2% sucrose decays adhere to the same linear relation as 0% sucrose decays.[103] The other rate constant, $k_{\mathrm{obs,s*}}$, is ~100x slower than the corresponding fast phase rate (Table 5.1). The Arrhneius dependence of this phase is unclear, due to the low signal-to-noise ratio at ≤ 10-20% of the initial decay amplitude. (2) The transition-$T$ region ($220 \geq T \geq 217$ K for 1%, $223 \geq T \geq 217$ K for 2%) includes a bifurcation of the native phase into fast and slow components with descending $T$ and the values of $k'_{\mathrm{obs,s}}$ and $k'_{\mathrm{obs,f}}$ remain $T$-independent. The slow phase rate, $k'_{\mathrm{obs,s}}$, for 1 and 2% sucrose is significantly slower than the 0% sucrose samples in this region.[103] There is no apparent transition of the other high-$T$ phase ($k_{\mathrm{obs,s*}}$) and appears to have been absorbed into the slow phase distribution. (3) In the low-$T$ region ($T < 217$ K), $k_{\mathrm{obs,s}}$ and $k_{\mathrm{obs,f}}$ display the same linear Arrhenius dependences as 0% sucrose samples[103] for both 1% and 2% sucrose samples (Table 5.2).

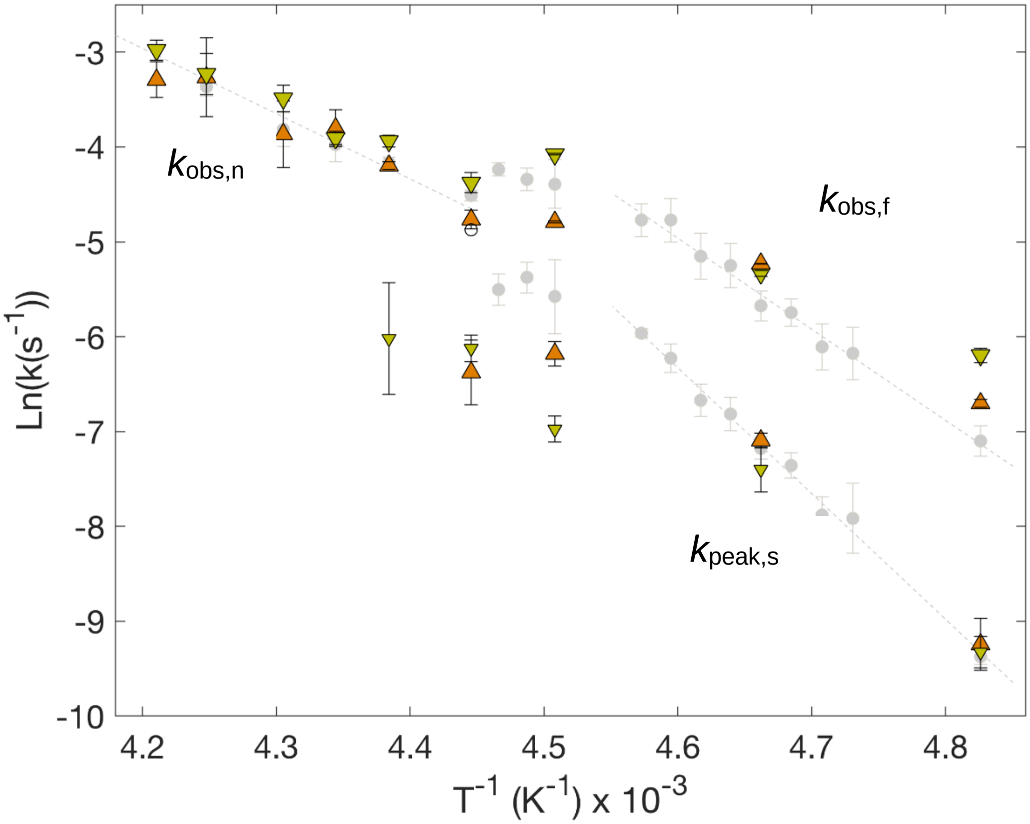

**Figure 5.3. Arrhenius plot of observed first-order rate constants for 1% (w/v) (orange triangles) and 2% (w/v) sucrose samples (yellow upside-down triangles)**. The mean $k_{obs}$ value for each temperature is shown, with associated standard deviations. The values for 0% (w/v) sucrose samples[103] are represented as light gray circles. The dashed lines represent the best fit to the data corresponding to the samples with sucrose concentrations of 0 % (w/v) for $k_{obs,n}$, $k_{obs,f}$ and $k_{obs,s}$. For samples containing 1-2 % (w/v) sucrose concentrations, the slow phase rate constant is represented by $k_{peak,s}$, which is the most probable rate constant in the power law distribution. The rate constant, $k_{obs,s*}$ is not depicted.

**Table 5.1. First-order rate constant and amplitude parameters with associated standard deviations, for the fit of the biexponential function for temperature range**: $232 \geq T \geq 223$ for 1% (w/v) sucrose concentrations and $232 \geq T \geq 225$ for 2% (w/v) sucrose concentrations to the CoII-substrate radical pair decay kinetics at 217 K. $A_{\mathrm{obs,s}}$ is 1- $A_{\mathrm{obs,f}}$.

| | $T\ (K^{-1})$ | $k_{\mathrm{obs,f}}$ ($\mathrm{s}^{-1}$) | $A_{\mathrm{obs,f}}$ | $k_{\mathrm{obs,s*}}$ ($\mathrm{s}^{-1}$) | $A_{\mathrm{obs,s*}}$ | $R^2$ |
|---|---|---|---|---|---|---|
| 1 % (w/v) Sucrose Samples | 223 | $1.5(\pm0.1)\times10^{-2}$ | 0.78±0.02 | $1.9(\pm1.0)\times10^{-4}$ | 0.22±0.02 | 0.9962 |
| | 225 | $2.2(\pm0.5)\times10^{-2}$ | 0.87±0.10 | $2.4(\pm1.0)\times10^{-4}$ | 0.13±0.10 | 0.9538 |
| | 227 | $2.1(\pm0.8)\times10^{-2}$ | 0.91±0.05 | $1.5(\pm1.2)\times10^{-4}$ | 0.09±0.05 | 0.9888 |
| | 230 | $3.8(\pm1.0)\times10^{-2}$ | 0.88±0.11 | $3.0(\pm1.9)\times10^{-4}$ | 0.12±0.11 | 0.9608 |
| | 232 | $3.7(\pm0.7)\times10^{-2}$ | 0.90±0.09 | $3.3(\pm0.4)\times10^{-4}$ | 0.10±0.09 | 0.9841 |
| 2% (w/v) Sucrose Samples | 225 | $2.0(\pm0.1)\times10^{-2}$ | 0.80±0.04 | $2.8(\pm0.1)\times10^{-4}$ | 0.20±0.04 | 0.9945 |
| | 227 | $1.5(\pm0.1)\times10^{-2}$ | 0.73±0.05 | $2.7(\pm0.1)\times10^{-4}$ | 0.27±0.05 | 0.9899 |
| | 230 | $4.0(\pm0.9)\times10^{-2}$ | 0.94±0.04 | $2.2(\pm0.5)\times10^{-4}$ | 0.06±0.04 | 0.9926 |
| | 232 | $5.1(\pm0.5)\times10^{-2}$ | 0.80±0.07 | $3.0(\pm1.0)\times10^{-4}$ | 0.20±0.07 | 0.9913 |

**Table 5.2. First-order rate constant and amplitude parameters for the fit of the mon-exponential and power law function for temperature range: 220 ≥ *T* ≥ 203** for 1% (w/v) sucrose concentrations and 223 ≥ *T* ≥ 203 for 2% (w/v) sucrose concentrations to the CoII-substrate radical pair decay kinetics with associated standard deviations. The fast phase is described with a monoexponential and the slow phase is described with the power law function where $k_{\mathrm{obs,s}} = \frac{n_{obs,s}}{t_{0,obs,s}}$ $A_{\mathrm{obs,s}}$ is 1- $A_{\mathrm{obs,f}}$.

| | $T$ ($K^{-1}$) | $k_{\mathrm{obs,f}}$ ($\mathrm{s}^{-1}$) | $A_{\mathrm{obs,f}}$ | $k_{\mathrm{obs,s}}$ ($\mathrm{s}^{-1}$) | $t_{0,\mathrm{obs,s}}$ (s) | $n_{\mathrm{obs,s}}$ | $R^{2\,\mathbf{a}}$ |
|---|---|---|---|---|---|---|---|
| 1 % (w/v) Sucrose Samples | 203 | $1.2(\pm0.5)\times10^{-3}$ | 0.34±0.10 | $1.9(\pm1.0)\times10^{-4}$ | $4.1(\pm0.5)\times10^{3}$ | $3.9(\pm0.1)\times10^{-1}$ | 0.9972 |
| | 210 | $5.3(\pm0.1)\times10^{-3}$ | 0.23±0.11 | $8.3(\pm0.6)\times10^{-4}$ | $7.7(\pm3.2)\times10^{2}$ | $6.4(\pm0.2)\times10^{-1}$ | 0.9975 |
| | 217 | $1.3(\pm0.1)\times10^{-2}$ | 0.24±0.09 | $1.3(\pm0.3)\times10^{-3}$ | $5.8(\pm0.3)\times10^{2}$ | $7.5(\pm0.7)\times10^{-1}$ | 0.9974 |
| | 220 | $1.1(\pm0.4)\times10^{-2}$ | 0.46±0.19 | $2.8(\pm0.7)\times10^{-3}$ | $3.1(\pm1.5)\times10^{2}$ | $8.5(\pm1.6)\times10^{-1}$ | 0.9940 |
| 2% (w/v) Sucrose Samples | 203 | $2.0(\pm0.1)\times10^{-3}$ | 0.18±0.05 | $8.9(\pm1.6)\times10^{-5}$ | $2.3(\pm0.3)\times10^{3}$ | $2.1(\pm0.4)\times10^{-1}$ | 0.9956 |
| | 210 | $4.8(\pm0.2)\times10^{-3}$ | 0.31±0.15 | $6.1(\pm1.6)\times10^{-4}$ | $8.1(\pm0.9)\times10^{2}$ | $5.0(\pm0.1)\times10^{-1}$ | 0.9976 |
| | 217 | $1.7(\pm0.1)\times10^{-2}$ | 0.26±0.08 | $9.4(\pm1.4)\times10^{-4}$ | $5.8(\pm0.2)\times10^{2}$ | $5.4(\pm0.4)\times10^{-1}$ | 0.9955 |
| | 220 | $1.3(\pm0.1)\times10^{-2}$ | 0.23±0.04 | $2.2(\pm0.3)\times10^{-3}$ | $2.2(\pm1.5)\times10^{2}$ | $7.2(\pm0.5)\times10^{-1}$ | 0.9947 |

| | | | | | | | |
|---|---|---|---|---|---|---|---|
| | 223 | 1.9(±0.1) $\times 10^{-2}$ | 0.44±0.07 | 2.4(±1.9) $\times 10^{-3}$ | 2.6(±0.8) $\times 10^{3}$ | 6.3(±1.6) $\times 10^{0}$ | 0.9953 |

## 5.4 Discussion

### 5.4.1 General Features of the Temperature-Dependent Free Energy Landscape Model

The piecewise-continuous Arrhenius dependences for the observed rate constants (Figure 2) for 1-2% (w/v) sucrose samples are described by a *T*-dependent FEL (Figure 2.6) with the same general features previously reported for $Co^{II}$-substrate radical pair $^{1}H_4$-aminoethanol decay kinetics for 0% (w/v) sucrose concentrations.[103] Both the bifurcation and kink features arise from *T*-dependent contributions of the protein to the FEL, as indicated by the abrupt changes in Arrhenius behavior. (Figure 2.2) The *T*-dependence of the FEL (Figure 2.6) is described with descending *T*, as follows:

Region 1, $T \geq 223$ K for 1% (w/v) and $T \geq 225$ K for 2% (w/v): Approximately 80-90% of the $^{1}H_4$-aminoethanol substrate radical decay is governed by the single rate constant, $k_{obs,n}$ to within one standard deviation of 0% (w/v) sucrose concentrations.[103] (Figure 5.3) The rate constants associated with 1% and 2% radical decays at $T = 232$ K (3.7(±0.7) $\times 10^{-2}$ s for 1% and 5.1(±0.5) $\times 10^{-2}$ s for 2%) are also consistent with the rate constant predicted from the 0% $k_{obs,n}$ Arrhenius dependence[103] ($5.3\times 10^{-2}$ s). This indicates that the native FEL (Figure 2.6 A) is unchanged for sucrose concentrations of 0-2%, where the $S^{\bullet}$ state encompasses a broad minimum, with many thermally accessible configurational states.[50, 96] The remaining 10-20% of the substrate radical signal decays at a much slower rate (~100-fold slower than $k_{obs,n}$ ), indicating an independent mechanism is driving this portion of the decay and does not involve the same sets of protein groups as those driving the majority of the decay. This population is not present in the 0% (w/v) sucrose concentration samples. When the decays are fitted to a biexponential, the 0% non-dominate phase is too small (< .01%) to be statistically relevant because the initial amplitude of the non-dominate phase is smaller than the noise level.

Region 2, $217 \leq T \leq 220$ K for 1% (w/v) and $217 \leq T \leq 223$ K for 2% (w/v): The bifurcation of $k_{\text{obs,n}}$, into $k'_{\text{obs,s}}$ and $k'_{\text{obs,f}}$, is a result of an abrupt transition in the FEL. The abrupt transition arises from an energy barrier (Figure 2.6 B) that partitions the broad $\mathbf{S}^{\bullet}$ minimum into two sequential microstates, $\mathbf{S}_1^{\bullet}$ and $\mathbf{S}_2^{\bullet}$, that differ in protein configuration. This leads to two components of decay: (1) The population in $\mathbf{S}_1^{\bullet}$ follows a sequential path from $\mathbf{S}_1^{\bullet}$ to $\mathbf{S}_2^{\bullet}$, and then $\mathbf{S}_2^{\bullet}$ to **P**. (2) The population in $\mathbf{S}_2^{\bullet}$ decays directly to **P** ($\mathbf{S}_2^{\bullet}$ can also convert to $\mathbf{S}_1^{\bullet}$ and return, prior to decay). These features are the same characteristics manifested in the 0% sucrose, $^1H_4$-aminoethanol substrate radical decays. Additionally, 1% sucrose decays display apparent $T$-independent $k'_{\text{obs,s}}$ and $k'_{\text{obs,f}}$ over a narrow range of $T$ values ($\Delta T \approx 4$ K), which is comparable to 0% sucrose decays ($\Delta T = 3$ K). The $T$-independent region for 2% sucrose decays is significantly larger ($\Delta T \approx 6\text{-}8$ K) than 0 and 1% sucrose decays, indicating that the protein configurational relaxation that occurs in parallel with the substrate radical decay in this temperature range occurs over a larger temperature range with increased sucrose concentrations.[22, 97-98, 103]

Region 3, $T < 217$ K: The observed rate constants $k_{\text{obs,f}}$ and $k_{\text{obs,s}}$ for 1 and 2% sucrose, substrate radical decays are in good agreement with the corresponding observed rate constants for 0% sucrose, substrate radical decays. $k_{\text{obs,s}}$ falls within one standard deviation of $k_{\text{obs,s}}$ from 0% radical decays for both 1 and 2%, while $k_{\text{obs,f}}$ fall within two standard deviations. This agreement with both $k_{obs,s}$ and $k_{obs,f}$ at $T < 217$ K indicates that the FEL is $T$-independent on the time scale of the substrate radical decay.

### 5.4.2 Rate Distribution of the Slow Phase

The power law fit associated with the slow phase implies a rate and activation energy barrier distribution.[97-98, 116] The continuous rate distribution $g(k)$ can be calculated using a Laplace transform (Equation 4.5). Figure 5.4 shows the rate distributions for 1 (A) and 2% (B) sucrose decays for $T < 223$ K.

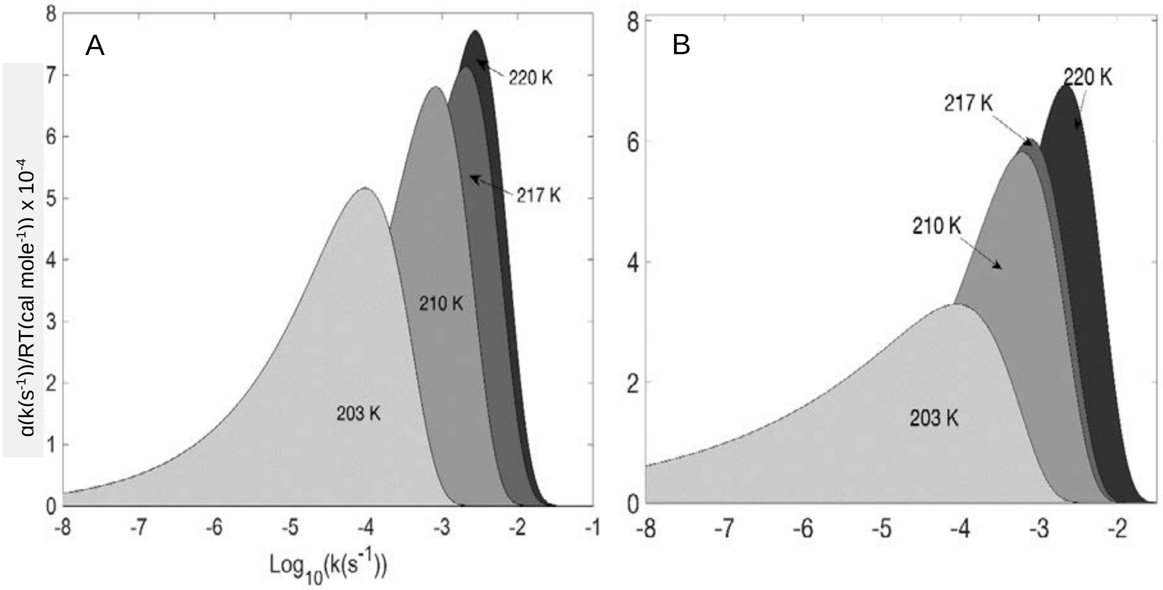

**Figure 5.4. Slow phase rate distribution for 1 (A) and 2% (B) sucrose concentrations.** Distributions were calculated using Equation 4.5. The parameters $t_0$ and $n$ were used to calculate the distribution are from the power law decay fits. The average values for $t_0$ and $n$ were used for each temperature. Areas under the distributions are normalized.

The values of *k* span a wide range from $10^{-8}$ to $10^{-2.5}$ $s^{-1}$ that encompassed ≥99% of the total distribution for all temperatures in and below the transition region for 1% (Figure 3A.) and 2% (Figure 3B.) sucrose decays. However, not all the rates are detectable under these experimental conditions. The decays were carried out until the samples decay to ≤ 10% of the initial amplitude. The cut-off value for the detectable rate constant would be the inverse of the time at which the experiment ended. Therefore, the slowest detectible rate can be estimated as one order of magnitude less than peak *k* value for the slow phase distributions. For example, the peak *k* value for 1% sucrose samples at 210 K is 6.1(±1.6) $\times 10^{-4}$ $s^{-1}$, therefore the slowest detectable rate constant is ~ 6 $\times 10^{-5}$ $s^{-1}$ in the distribution. Figure 5.5 shows the distribution widths for the slow phase widen with increasing sucrose concentrations and temperature. These results indicate that the increase of sucrose to the systems roughens the FEL, i.e. increases the energy barriers between the accessible configurational states along the reaction coordinate. Because decays in this temperature region are driven by *many* localized, incremental fluctuations,[103] the rate distribution for the slow phase is *continuous*. As temperature decreases, the width of the distributions expands, indicating that an increasing number of configurational states are contributing to the rate limiting step due to the increased energy barrier height between these configurational states and decrease in kinetic energy at low temperatures.[130] This phenomenon was also present in 0% sucrose radical decays, but at much lower temperatures ($T \leq$ 187 K).[129]

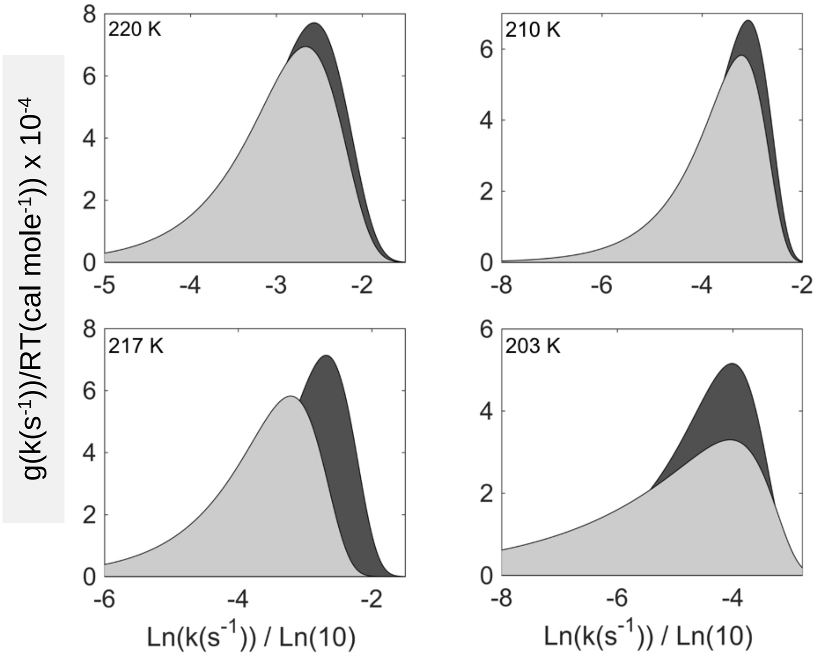

**Figure 5.5. Comparisons of the slow phase rate distributions for 1% (dark gray) and 2% (light gray) sucrose concentrations.** Distributions were calculated using Equation 4.5 in Ch 4. The parameters $t_0$ and $n$ were used to calculate the distribution are from the power law decay fits. The average values for $t_0$ and $n$ were used for each temperature. Areas under the distributions are normalized.

### 5.4.3 Activation Energy Distribution of the Slow Phase

The continuous activation energy distribution *g*(*E*) can be calculated using a Laplace transform (Equation 4.5) and the Arrhenius equation (Equation 2.6), derived from 0% $k_{12}$ Arrhenius dependence (Table 2.3). Figure 5.6 shows the activation energy distribution for temperatures between 220-203 K for samples with 1% (w/v) sucrose concentrations. Figure 5.7 shows the activation energy distributions for samples with 2% (w/v) sucrose concentrations.

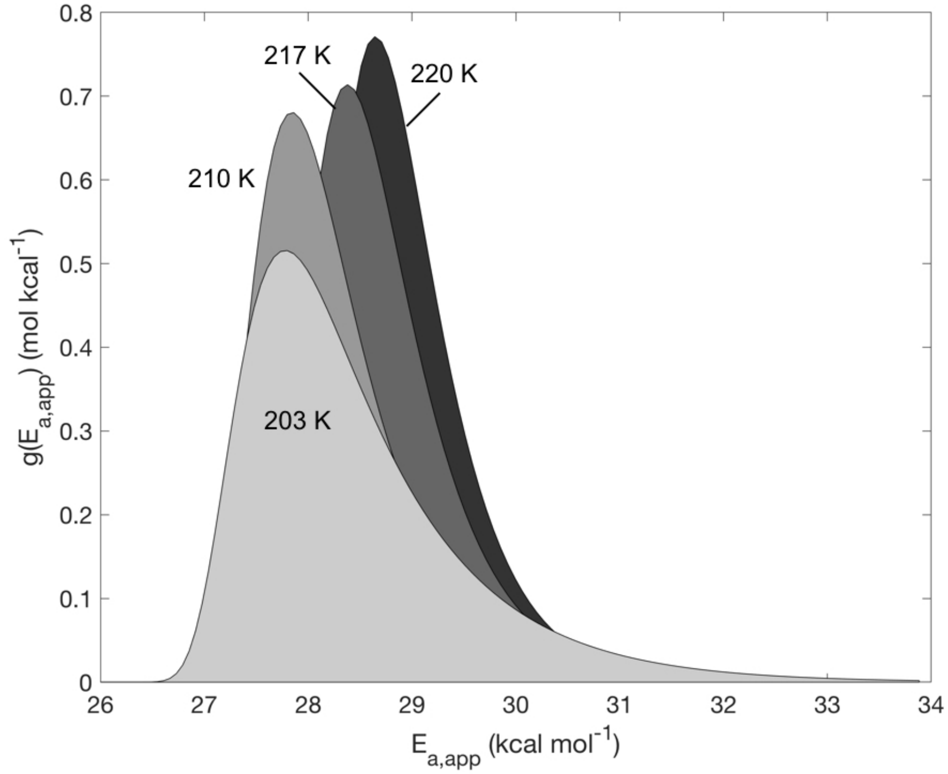

**Figure 5.6. The slow phase activation energy distributions for 1% (w/v) sucrose concentrations for *T* between 220-203 K.** Distributions were calculated using Equations 4.5 and 2.6. The parameters $t_0$ and *n* were used to calculate the distribution are from the power law decay fits. The Arrhenius *A* value was set to 5 x $10^{25}$ $s^{-1}$ that corresponds to the $k_{12}$ Arrhenius *A* value at 0% (w/v). The average values for $t_0$ and *n* were used for each temperature. Areas under the distributions are normalized.

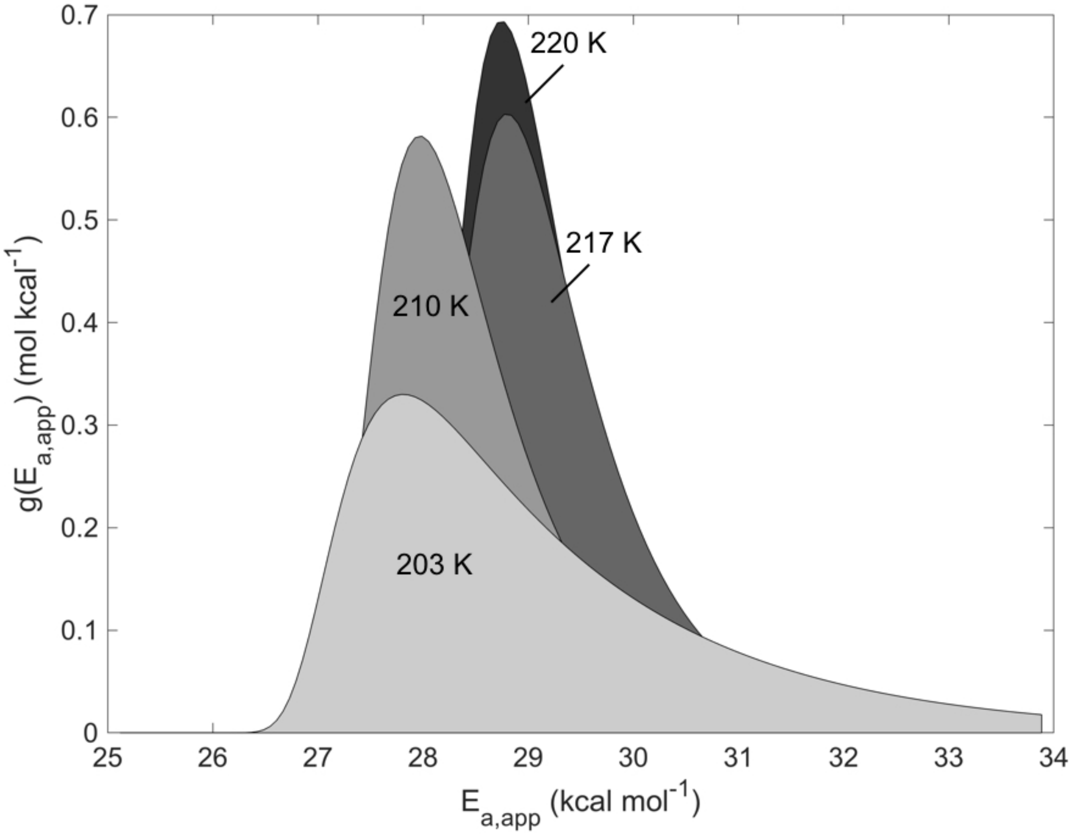

**Figure 5.7. The slow phase activation energy distributions for 2% (w/v) sucrose concentrations for *T* between 220-203 K.** Distributions were calculated using Equations 4.5 and 2.6. The parameters $t_0$ and $n$ were used to calculate the distribution are from the power law decay fits. The Arrhenius $A$ value was set to 5 x $10^{25}$ $s^{-1}$ that corresponds to the $k_{12}$ Arrhenius $A$ value at 0% (w/v). The average values for $t_0$ and $n$ were used for each temperature. Areas under the distributions are normalized.

The activation energy distributions show similar characteristics for both 1 and 2% (w/v) sucrose concentrations. The average peak activation energy for 220 and 217 K is 28.6 ± 0.3 kcal mol$^{-1}$ which is within one standard deviation of the activation energy calculated for $k_{12}$ (27.6 ± 1.4 kcal mol$^{-1}$) yet the average peak activation energies for $T$ = 210 and 203 K (27.8 ± 0.1 kcal mol$^{-1}$) is closer to the $k_{12}$ activation energy. This and the fact that the energy distributions for $T$ = 210 and 203 K show overlap of over 90%, leads to the conclusion that the energy distributions remain constant for $T \leq 210$ K for both 1 and 2% (w/v) sucrose concentrations. Although distributions for $T = 220$ and 217 K show similar overlap the Arrhenius plot of the peak rate constant values (Figure 2) show a non-linear Arrhenius relation, which suggests protein relaxation is occurring.[97] Therefore, the microscopic model is applied to substrate radical decays for $T = 210$ and 203 K, where the FEL is unchanging with temperature.

### 5.4.4. Reconciliation of the Fast Phase Amplitude Decrease with Increase Sucrose Concentrations

The transition temperature region, which is described by Region 2 (Section 5.3.2), is defined by the temperature independence of the radical decay. The transition temperature region shifts to higher temperatures for increasing sucrose concentrations ($220 \geq T \geq 217$ K for 1%, $223 \geq T \geq 217$ K for 2%). The transition temperature region also increases in width ($\Delta T$) with increasing sucrose, which explains the decrease in fast phase amplitude with increasing sucrose concentrations discussed in Ch. 4.4.1. Additionally, the high temperature decay experiments revealed a small portion (10-20%) of the decay does not adhere to the native reaction. Though unclear if this population undergoes a transition, it's assumed that this population is absorbed into the slow phase.

### 5.4.5 Transition Temperature Region Dependence on Sucrose Concentrations

The highest temperature in the transition region is defined by the bifurcation of $k_{\mathrm{obs,n}}$, into $k'_{\mathrm{obs,s}}$ and $k'_{\mathrm{obs,f}}$. The temperature at which the bifurcation occurs increases steadily with sucrose concentrations (219 K at 0%, 220 K at 1%, and 223 K at 2%) (Figure 2). This is consistent with the shift of the dynamical transition, associated with the quenching of collective motions in the protein, to higher temperatures.[117] The temperature span of the transition region also increases with sucrose ($\Delta T$ = 3 K at 0%, 4 K at 1%, and 6-8 K at 2%), indicating that the two distinct sets of specific collective configurational fluctuations that drive native rearrangement process[103] have varying sensitivity to sucrose.

The decays over the transition region for sucrose concentrations > 0% contain a power law component for the slow phase, which suggests a distribution in the decay rates.[22, 97-98] This can be attributed to an increase in heterogeneity of configurational states, caused by the increased energy barriers between configurational states that are contributing to the rate limiting step in EAL (Figure 5.13, B).

A feature present in 0% sucrose decays is that the bifurcation (boundary of the $k_{\mathrm{obs,n}}$ and $k'_{\mathrm{obs,s}}$, $k'_{\mathrm{obs,f}}$ ), and the kinks ($k'_{\mathrm{obs,s}}/k_{\mathrm{obs,s}}$, and $k'_{\mathrm{obs,f}}/k_{\mathrm{obs,f}}$ boundaries), occur without a significant discontinuity.[103] This smooth transition indicates that the molecular origin of the bifurcation and kinks is a transition from collective to localized, incremental motions, involving the same sets of protein groups that contribute to the radical rearrangement step. For 1 and 2% sucrose decays, the $k_{\mathrm{obs,n}}/k'_{\mathrm{obs,f}}$ and $k'_{\mathrm{obs,f}}/k_{\mathrm{obs,f}}$ boundaries also transition without a significant discontinuity, which is consistent with 0% sucrose decays. The slow phase consists of a distribution of rates, where $k'_{\mathrm{obs,s}}$ and $k_{\mathrm{obs,s}}$ are the most populated rates in the distribution. Approximately 30% of the distribution consists of rates that lie within one standard deviation of $k'_{\mathrm{obs,s}}$ for 0% sucrose decays, therefore the transition from $k_{\mathrm{obs,n}}$ to $k'_{\mathrm{obs,s}}$ is continuous. Assuming 1 and 2% sucrose decays adhere to the same Arrhenius relation as 0% sucrose decays,[103] the $k'_{\mathrm{obs,s}}/k_{\mathrm{obs,s}}$ boundary occurs without a significant discontinuity. Although there appears to be a discontinuity in Figure 5.3, the values for kobs,s are only the most populated rate, a significant amount of the population decays at a higher rate. Therefore, the transition occurs because of a change from collective motions to localized incremental motions involving the same sets of protein groups.

### 5.4.6 Partition of the Observed Slow Phase Distributions for $T < 217$ K

The $T$-dependent FEL model implies a minimal two-step/three-state kinetic mechanism for $T < 217$ K (Figure 2.7-8). Numerical simulations of the amplitude versus time data at the different $T$ values were based on the set of coupled differential equations for the time dependence of the $\mathbf{S}_1^\bullet$ , $\mathbf{S}_2^\bullet$ , and **P** populations (Equations 2.2-4). However, due to the distributive nature of the decays, the slow phase was partitioned into 10 divisions (Figure 5.5) and the average rate was determined ($k_{\mathrm{obs,s,i}}$) (Figure 5.8, black squares) in order to apply the microscopic model. Figure 5.8 shoes the power law-derived decay components of the slow phase were weighted equally in terms of area under the distribution curve for each decay, where each division includes a different $k$ range width (determined by the area). Another method would be to have equal $k$ ranges in each division and a scale factor for each slice, however this would require a scaling of the microscopic model simulations as well.

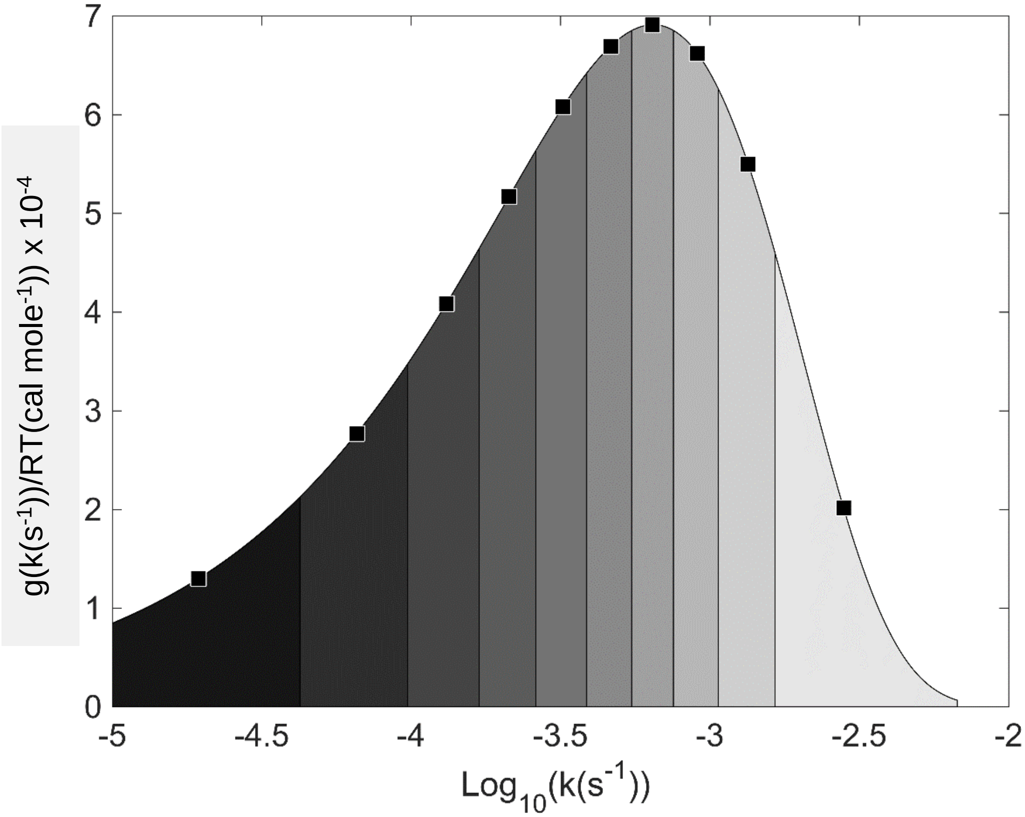

**Figure 5.8 Partitioned slow phase rate distribution for 1% sucrose decay at 210 K.** The black squares designate the average $k_{obs,s,i}$ value for each partition. The parameters $t_0$ and $n$ used to calculate the distribution are from the power law decay fits.

Figure 5.9A. shows the subsequently generated biexponential decays. Figure 5.9B shows the normalized generated biexponential decays overlaid with the experimental decay. The summation of the biexponential decays showed good agreement with the experimental decays with $R^2$ values > 0.995.

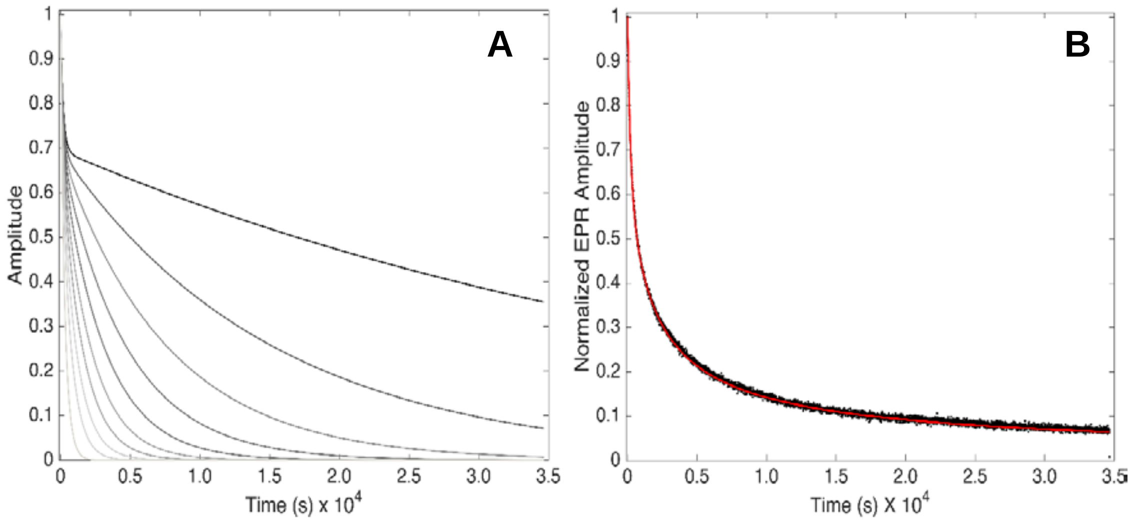

**Figure 5.9. The set of biexponential decays (A) generated from the rate parameters $k_{obs,f}$ and $k_{obs,s,i}$ derived from 1% sucrose decays at 210 K.** The biexponential decays were normalized and overlaid with the corresponding experimental decays.

### 5.4.7 Microscopic Kinetic Mechanism

Figures 5.10-11 show the numerical simulations that were applied to each set of biexponential decays associated with 1 and 2% sucrose decays at 203 and 210 K to determine the best-fit microscopic rate constants, ($k_{12}$, $k_{21}$, and $k_P$) and their corresponding distributions and peak rate values (Table 5.3). Figure 5.12 shows the 0% sucrose sample decays which were also fit to a monoexponential plus power law and numerical simulations were applied at 203 and 210 K for direct comparison. Amplitudes for the microscopic rate distributions correspond to the same amplitudes from the slow phase distribution fits. Therefore, the amplitudes for the microscopic rate distributions are not normalized.

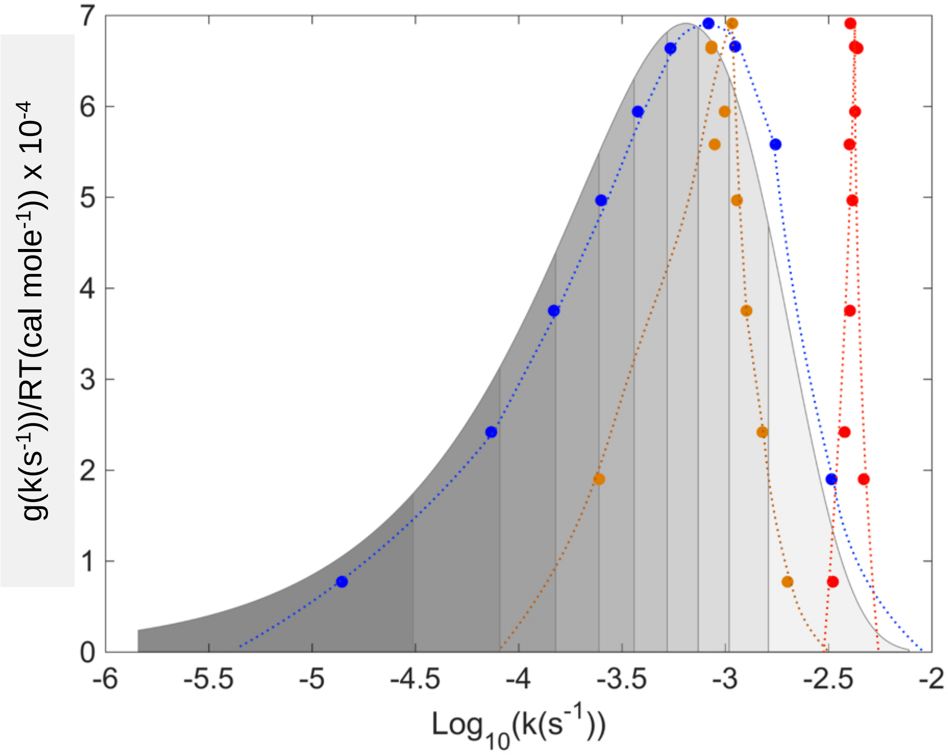

**Figure 5.10. Rate distributions for the microscopic rate parameters $k_{12}$ (blue), $k_{21}$ (orange), and $k_p$ (red) for 1% sucrose decay at 210 K.** The $k_{obs,s}$ rate distribution is depicted in faded gray.

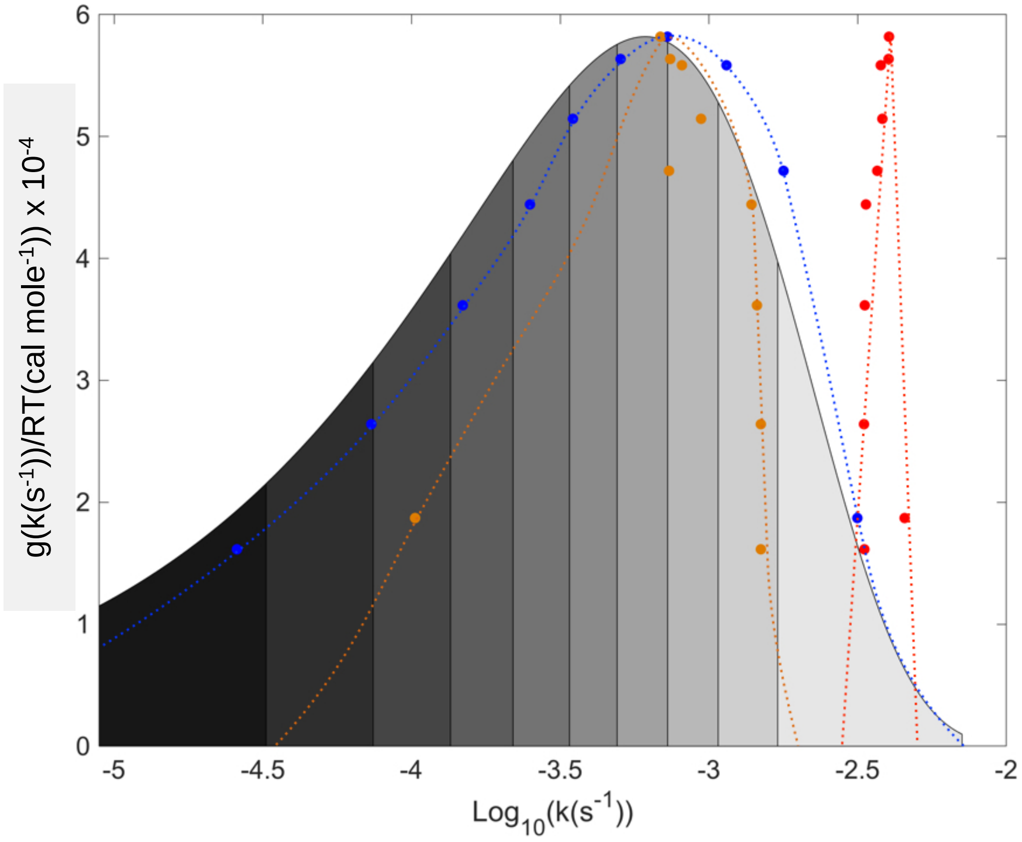

**Figure 5.11. Rate distributions for the microscopic rate parameters $k_{12}$ (blue), $k_{21}$ (orange), and $k_p$ (red) for 2% sucrose decay at 210 K.** The $k_{obs,s}$ rate distribution is depicted in faded gray.

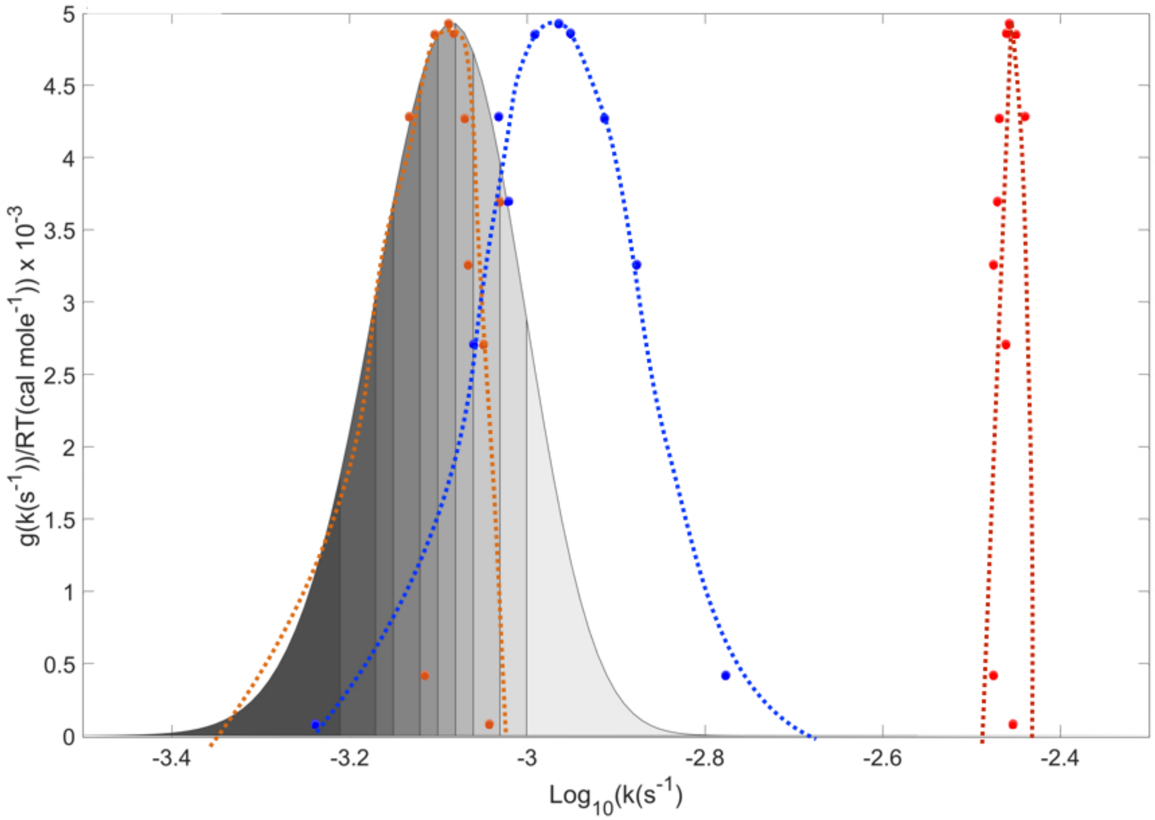

**Figure 5.12. Rate distributions for the microscopic rate parameters $k_{12}$ (blue), $k_{21}$ (orange), and $k_p$ (red) for 0% sucrose decay at 210 K.** The $k_{obs,s}$ rate distribution is depicted in faded gray.

**Table 5.3. Average peak values and standard deviations for the microscopic rate parameters $k_{12}$ , $k_{21}$ , and $k_p$ for 1 and 2 % sucrose decays at 203 and 210 K.** As well as the average initial concentration of the $S_1^{\bullet}$ state.

| | $T\ (K^{-1})$ | $[S_1^{\bullet}]_0$ | $k_{12,peak}$ ($s^{-1}$) | $k_{21,peak}$ ($s^{-1}$) | $k_{p,peak}$ ($s^{-1}$) |
|---|---|---|---|---|---|
| 0% (w/v) | 203 | 0.40(±0.05) | 3.3(±3.3) $\times 10^{-4}$ | 1.6(±1.3) $\times 10^{-4}$ | 1.2 (±0.3) $\times 10^{-3}$ |
| | 210 | 0.53(±0.05) | 2.1(±0.8) $\times 10^{-3}$ | 2.4(±1.5) $\times 10^{-3}$ | 4.2(±0.7) $\times 10^{-3}$ |

| | | | | | |
|---|---|---|---|---|---|
| 1% (w/v) | 203 | 0.50(±0.04) | 1.1(±0.6) ×10$^{-4}$ | 1.7(±1.0) ×10$^{-4}$ | 9.7 (±0.5) ×10$^{-4}$ |
| | 210 | 0.49(±0.02) | 1.1(±0.3) ×10$^{-3}$ | 1.3(±0.6) ×10$^{-3}$ | 4.1(±0.2) ×10$^{-3}$ |
| 2% (w/v) | 203 | 0.54(±0.06) | 1.6(±0.9) ×10$^{-4}$ | 8.4(±1.2) ×10$^{-4}$ | 1.1(±0.1) ×10$^{-3}$ |
| | 210 | 0.48(±0.02) | 7.3 (±0.8) ×10$^{-4}$ | 6.8(±1.0) ×10$^{-4}$ | 3.7(±0.2) ×10$^{-3}$ |

The fitting of the monoexponential plus power law equation to the 0% sucrose decays yielded similar $R^2$ values as the biexponential fits. Numerical simulations of the 0% sucrose decays reveal a very narrow distribution (less than half an order of magnitude), indicating that the biexponential fits are adequate in fully describing the observed decay kinetics at 0% sucrose concentrations.

The peak values for the microscopic rates for 1 and 2% sucrose radical decays show good agreement with 0% sucrose radical decays (within one standard deviations in most cases).[103] The initial amplitude of $S_1^{\bullet}$ state is higher in 1 and 2% sucrose decays, which is consistent with fast phase amplitude loss during sample quenching. The significant difference between the radical decays with sucrose and the radical decays without sucrose is caused by the distributions of the microscopic rate parameters (Table 5.4).

**Table 5.4. The Full Width Half Maximum (FWHM) of the rate distributions for the microscopic rate parameters $k_{12}$ , $k_{21}$ , and $k_p$ for 1 and 2 % sucrose decays at 203 and 210 K.**

| | *T (K$^{-1}$)* | FWHM of $k_{12}$ $\log_{10}(s^{-1})$ | FWHM of $k_{21}$ $\log_{10}$ $(s^{-1})$ | FWHM of $k_p$ $\log_{10}$ $(s^{-1})$ |
|---|---|---|---|---|
| 1% (w/v) | 203 | 1.6(±0.2) | 0.5(±0.3) | 0.1(±0.05) |
| | 210 | 0.9(±0.1) | 0.5(±0.2) | 0.1(±0.05) |
| 2% (w/v) | 203 | 2.0(±0.3) | 0.6(±0.4) | 0.2(±0.05) |
| | 210 | 1.1(±0.1) | 0.6(±0.2) | 0.1(±0.05) |

The distribution associated with the microscopic rate parameter $k_{12}$ mimics the slow phase distribution both in shape and width, while the $k_{21}$ distribution is significantly narrower than the slow phase distribution. The microscopic rate parameter, $k_p$ has effectively no distribution. This indicates that the $S_1^\bullet \rightarrow S_2^\bullet$ process of the FEL model [103] requires the most configurational changes the protein must execute in order to form the $S_2^\bullet$ state.[103, 131] Figure 5.13 shows a depiction of the free energy along the reaction coordinate (below 217 K) for 0% (A) and for 1-2% (B) (w/v) sucrose concentrations .

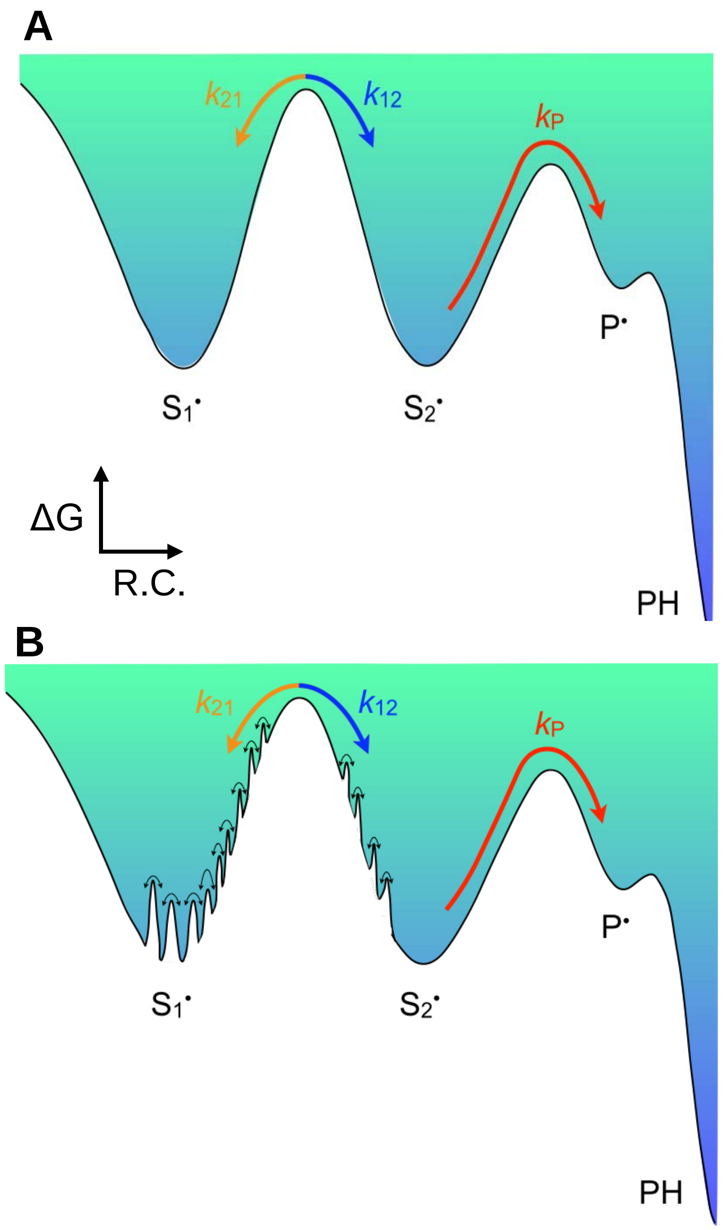

**Figure 5.13. Free Energy Diagram for 0% (A) and for 1-2% (B) (w/v).** The microscopic rates: $k_{12}$, $k_{21}$ and $k_P$ correspond to Scheme 2.1. The black arrows represent the motion of the protein as it samples the configurational substates of $S_1^{\bullet}$ and $S_2^{\bullet}$ that contribute to reaction.

## 5.5 Conclusion

Substrate radical pair decay kinetic measurements for low concentrations of sucrose identify enzyme features sensitive to dynamical changes in the protein relevant to a chemical step in EAL. Arrhenius dependencies reveal the same native reaction mechanism present in 0% sucrose samples ($T \geq 223$ K for 1% and $T \geq 225$ K for 2%). The bifurcation in the Arrhenius dependence for both 1 and 2% sucrose concentrations occur at different temperatures ($T \approx 220$ K for 1% and $T \approx 223$ K for 2%) from 0% sucrose samples, indicating that the set of collective motions associated with the bifurcation become effectively "quenched" at different temperatures. Remarkably, the kinks in the Arrhenius plot all occur at approximately the same temperature (217 K) for 0-2% sucrose concentrations. This further iterates that the bifurcation and kink are a result of two *distinct* sets of native collective protein configurational fluctuations and these two sets of fluctuations have different sensitivities to sucrose. The absence of significant discontinuities at the boundaries of the bifurcations and kinks indicate the same sets of protein groups and interactions mediate the rearrangement for all low sucrose concentrations (0-2%) for $232 \leq T \leq 203$ K. Below the transition region both 1 and 2% sucrose decays show good agreement with the 0% sucrose decays, indicating that the same local, incremental motions are driving the reaction.

The microscopic model revealed the distribution of the slow phase is most closely related to the rate $k_{12}$, associated with the $S_1^{\bullet} \rightarrow S_2^{\bullet}$ process. Implying that the formation of the $S_2^{\bullet}$ state requires the most configurational changes the protein must execute, which is consistent with the entropy difference between $S_1^{\cdot}$ and $S_2^{\cdot}$ arises from protein configurational entropy, where the enzyme utilizes the $S_1^{\bullet}$ state for stabilization of the radical pair.[103, 131] The utilization of sucrose as a vehicle for protein dynamic manipulation has revealed the dependence of specific fluctuations to the chemical steps of enzyme catalyzes.

# Chapter 6

# Conclusions

The results and analysis established in this dissertation reveal key insights in enzymology, specifically the role of configurational protein fluctuations in catalysis. The following paragraphs summarize the key insights from each chapter, which demonstrate a natural progression in the study of dynamical effects on EAL catalysis. This dissertation establishes the microscopic model, via the FEL, and identifies multiple distinct temperature transitions that correspond to the quenching of distinct sets of collective protein configurational fluctuations for two steps in the catalytic cycle of EAL (Chapters 2-3). Further, it establishes that these transitions can be tuned (shifted to higher temperatures) and explores the specific configurations in each specific microscopic state via the addition of a viscosogen (Chapters 4-5).

## 6.1 Chapter Two: Two Dynamical Regimes of the Substrate Radical Rearrangement Reaction in B12-Dependent Ethanolamine Ammonia-Lyase Resolve Contributions of Native Protein Configurations and Collective Configurational Fluctuations to Catalysis

The kinetics of the substrate radical rearrangement reaction step in B12-dependent ethanolamine ammonia-lyase (EAL) from Salmonella typhimurium are measured over a 92 K temperature range. The observed first-order rate constants display a piecewise-continuous Arrhenius dependence, with linear regions over 295 → 220 K (monoexponential) and 214→ 203 K (biexponential) that are delineated by a kinetic bifurcation and kinks at 219 and 217 K, respectively. The results are interpreted by using a free energy landscape model and derived microscopic kinetic mechanism. The bifurcation and kink transitions correspond to the effective quenching of two distinct sets of native collective protein configurational fluctuations that (1) reconfigure the protein within the substrate radical free energy minimum, in a reaction-enabling step, and (2) create the protein configurations associated with the chemical step. Below 217 K, the substrate radical decay reaction persists. Increases in activation enthalpy and entropy of both the microscopic enabling and reaction steps indicate that this non-native reaction coordinate is conducted by local, incremental fluctuations. Continuity in the Arrhenius relations indicates that the same sets of protein groups and interactions mediate the rearrangement over the 295 to 203 K range, but with a repertoire of configurations below 217 K that is restricted, relative to the native configurations accessible above 219 K. The experimental features of a culled reaction step, first-order kinetic measurements, and wide room-to-cryogenic temperature range, allow the direct demonstration and kinetic characterization of protein dynamical contributions to the core adiabatic, bond-making/bond-breaking reaction in EAL.

## 6.2. Chapter Three: Characterization of the Kinetic Isotope Effects on the Radical Rearrangement and Second Hydrogen Transfer Step

The $Co^{2+}$-substrate radical pair decay kinetics generated from $^{2}H_4$-aminoethanol were observed from 203- 230 K and the microscopic model proposed in chapter 2 was applied. These experiments similar a piecewise-continuous Arrhenius dependence, with linear regions over 295 → 220 K (monoexponential) and 214→ 203 K (biexponential) that are delineated by a kinetic bifurcation and kinks at 219 and 217 K, respectively. Experiments also reveal persistent isotope effect for both observed and microscopic rate constants.  These isotope effects are fully accounted for through the application of simulated decay curves that incorporate the second hydrogen transfer step (HT2) in the catalytic cycle of EAL. Results further support the Arrhenius characteristics radical rearrangement reaction (kink and bifurcation) are caused by the quenching of two distinct sets of specific collective motions in the protein. Additionally, ESEEM experiments revealed no significant structural difference between the microstates $S_1^\bullet$ and $S_2^\bullet$, indicating that the partitioning of the $S_1^\bullet$ and $S_2^\bullet$ states are dynamical in origin. Further, simulation results reveal three insights into the RR and HT2 steps. (1) The transient IEs are explained solely by HT2 or a combination of HT2 and a secondary IE on $k_{PN}$ and $k_P$. (2) The rate constant ($k_{HT}$) associated with HT2 undergoes a dynamical temperature transition at 227 K for either case (secondary IE or not). (3) This temperature transition is distinct from the temperature transitions associated with the RR step, indicating that the set collective motions associated with HT2 step are different than the set of collective motions associated with the RR.

### 6.3. Chapter Four: Protein and Coupled Solvent Dynamic Contributions to the Radical Rearrangement Step in a $B_{12}$-Dependent Enzyme Addressed by Sucrose Effects on Reaction Kinetics at 217 K

The radical rearrangement and HT2 step in the catalytic cycle of EAL[27, 57, 102] is influenced by fluctuations of the protein.[103] This is evident through the abrupt change in the temperature dependencies of the substrate radical decay, when studied over a large temperature range (92 K) for both $^1H_4$ and $^2H_4$-aminoethanol generated substrate radical pairs. Protein dynamics are highly influenced by the solvent[114] and have been studied intensively.[23, 115-117] Specifically, this chapter explores the unique effects of the solvent sucrose has on both observed phases associated with the decay of $^1H_4$-aminoethanol and $^2H_4$-aminoethanol generated Co(II)-substrate radical pair decays in EAL. These experiments reveal two characteristics: (1) the diminishing fast phase population with higher sucrose concentrations, caused by the shift of the dynamical transition temperature region to higher temperatures; (2) The distributive property associated with the slow phase rate(s), caused by the roughening of the FEL. Additionally, the different effects sucrose has on both the fast and slow phase indicate that the local protein fluctuations driving the $S_2^\bullet \rightarrow P^\bullet$ process are different than the local protein fluctuations driving the $S_1^\bullet \leftrightarrow S_2^\bullet$ process.

## 6.4. Chapter Five: Characterization of Contributions of Solvent-Coupled Protein Configurational Dynamics to the Rearrangement Reaction in B12-Dependent Ethanolamine Ammonia-Lyase

The general effects sucrose concentrations have on the dynamics of the protein for both collective and incremental motions are established in chapter 4 via the transient kinetics for the substrate radical step. Specific sucrose effects on $S_2^\bullet \rightarrow P^\bullet$ and $S_1^\bullet \leftrightarrow S_2^\bullet$ processes are revealed through $Co^{2+}$-substrate radical pair decay kinetics generated from $^1H_4$-aminoethanol from 203-232 K and the application microscopic model. Arrhenius dependencies reveal the same native reaction mechanism present in 0% sucrose samples ($T \geq 223$ K for 1% and $T \geq 225$ K for 2%) The bifurcation in the Arrhenius dependence for both 1 and 2% sucrose concentrations occur at different temperatures ($T \approx 220$ K for 1% and $T \approx 223$ K for 2%) from 0% sucrose samples, indicating that the set of collective motions associated with the bifurcation become effectively “quenched” at different higher temperatures for increasing sucrose concentrations. The kinks in the Arrhenius plot all occur at approximately the same temperature (217 K) for 0-2% sucrose concentrations. This indicates that the bifurcation and kink are a result of two *distinct* sets of native collective protein configurational fluctuations. The microscopic model revealed the distribution of the slow phase is most closely related to the rate $k_{12}$, associated with the $S_1^\bullet \rightarrow S_2^\bullet$

process. This implies that the formation of the $S_2^\bullet$ state requires the most configurational changes the protein must execute.

These experimental and analytical methods established here provide a significant step forward in the field of enzyme kinetics. The catalytic cycle of EAL is a unique system where a specific chemical step (radical rearrangement step) acts as a probe to explore the dynamical contributions to catalysis. EAL provide a general, direct approach to reveal the contributions of native protein configurations and specific fluctuations to the chemical steps of enzyme catalyzes.

# References

1. Nagel, Z. D.; Klinman, J. P., A 21(st) century revisionist's view at a turning point in enzymology (vol 5, pg 543, 2009). *Nat. Chem. Biol.* **2009,** *5* (9), 696-696.

2. Olsson, M. H. M.; Parson, W. W.; Warshel, A., Dynamical contributions to enzyme catalysis: Critical tests of a popular hypothesis. *Chemical Reviews* **2006,** *106* (5), 1737-1756.

3. Kraut, D. A.; Carroll, K. S.; Herschlag, D., Challenges in enzyme mechanism and energetics. *Annu. Rev. Biochem.* **2003,** *72*, 517-571.

4. Jackson, C. J.; Foo, J. L.; Tokuriki, N.; Afriat, L.; Carr, P. D.; Kim, H. K.; Schenk, G.; Tawfik, D. S.; Ollis, D. L., Conformational sampling, catalysis, and evolution of the bacterial phosphotriesterase. *Proc. Natl. Acad. Sci. U. S. A.* **2009,** *106* (51), 21631-21636.

5. Henzler-Wildman, K. A.; Lei, M.; Thai, V.; Kerns, S. J.; Karplus, M.; Kern, D., A hierarchy of timescales in protein dynamics is linked to enzyme catalysis. *Nature* **2007,** *450* (7171), 913-U27.

6. Boehr, D. D.; Dyson, H. J.; Wright, P. E., An NMR perspective on enzyme dynamics. *Chemical Reviews* **2006,** *106* (8), 3055-3079.

7. Ramanathan, A.; Savol, A.; Burger, V.; Chennubhotla, C. S.; Agarwal, P. K., Protein conformational populations and functionally relevant substates. *Accounts of Chemical Research* **2014,** *47* (1), 149-156.

8. Boehr, D. D.; McElheny, D.; Dyson, H. J.; Wright, P. E., The dynamic energy landscape of dihydrofolate reductase catalysis. *Science* **2006,** *313* (5793), 1638-1642.

9. Hammes-Schiffer, S., Catalytic efficiency of enzymes: a theoretical analysis. *Biochemistry* **2013,** *52* (12), 2012-2020.

10. Nashine, V. C.; Hammes-Schiffer, S.; Benkovic, S. J., Coupled motions in enzyme catalysis. *Curr. Opin. Chem. Biol.* **2010,** *14* (5), 644-651.

11. Henzler-Wildman, K. A.; Thai, V.; Lei, M.; Ott, M.; Wolf-Watz, M.; Fenn, T.; Pozharski, E.; Wilson, M. A.; Petsko, G. A.; Karplus, M.; Hubner, C. G.; Kern, D., Intrinsic motions along an enzymatic reaction trajectory. *Nature* **2007,** *450* (7171), 838-U13.

12. Rupley, J. A.; Careri, G., Protein hydration and function. *Advances in Protein Chemistry* **1991,** *41*, 37-172.

13. Helliwell, J. R.; Kornyshev, A.; Halle, B.; Engberts, J., Protein hydration dynamics in solution: a critical survey - discussion. *Philos. Trans. R. Soc. B-Biol. Sci.* **2004,** *359* (1448), 1223-1224.

14. Oleinikova, A.; Sasisanker, P.; Weingartner, H., What can really be learned from dielectric spectroscopy of protein solutions? A case study of ribonuclease A. *J. Phys. Chem. B* **2004,** *108* (24), 8467-8474.

15. Panagopoulou, A.; Kyritsis, A.; Shinyashiki, N.; Pissis, P., Protein and water dynamics in bovine serum albumin-water mixtures over wide ranges of composition. *J. Phys. Chem. B* **2012,** *116* (15), 4593-4602.

16. Ngai, K. L.; Lunkenheimer, P.; Leon, C.; Schneider, U.; Brand, R.; Loidl, A., Nature and properties of the Johari-Goldstein beta-relaxation in the equilibrium liquid state of a class of glass-formers. *Journal of Chemical Physics* **2001,** *115* (3), 1405-1413.

17. Goldstein, M., The past, present, and future of the Johari-Goldstein relaxation. *Journal of Non-Crystalline Solids* **2011,** *357* (2), 249-250.

18. Liu, Y. H.; Fujita, T.; Aji, D. P. B.; Matsuura, M.; Chen, M. W., Structural origins of Johari-Goldstein relaxation in a metallic glass. *Nature Communications* **2014,** *5*.

19. Angell, C. A.; Smith, D. L., Test of the entropy basis of the Vogel-Tammann-Fulcher equation. Dielectric relaxation of polyalcohols near Tg. *J. Phys. Chem.* **1982,** *86* (19), 3845-3852.

20. Angell, C. A., Formation of glasses from liquids and biopolymers. *Science* **1995,** *267*, 1924-1935.

21. Angell, C. A.; Ngai, K. L.; McKenna, G. B.; McMillan, P. F.; Martin, S. W., Relaxation in glassforming liquids and amorphous solids. *Journal of Applied Physics* **2000,** *88* (6), 3113-3157.

22. Frauenfelder, H.; Chen, G.; Berendzen, J.; Fenimore, P. W.; Jansson, H.; McMahon, B. H.; Stroe, I. R.; Swenson, J.; Young, R. D., A unified model of protein dynamics. *Proc. Natl. Acad. Sci.* **2009,** *106*, 5129-5134.

23. Fenimore, P. W.; Frauenfelder, H.; McMahon, B. H.; Young, R. D., Bulk-solvent and hydration-shell fluctuations, similar to alpha- and beta-fluctuations in glasses, control protein motions and functions. *Proc. Natl. Acad. Sci. U. S. A.* **2004,** *101* (40), 14408-14413.

24. Qin, Y. Z.; Wang, L. J.; Zhong, D. P., Dynamics and mechanism of ultrafast water-protein interactions. *Proc. Natl. Acad. Sci. U. S. A.* **2016,** *113* (30), 8424-8429.

25. Koshland, D. E., Application of a theory of enzyme specificity to protein synthesis. *Proc. Natl. Acad. Sci. U. S. A.* **1958,** *44* (2), 98-104.

26. Banerjee, R., *Chemistry and biochemistry of B12*. Wiley: New York, 1999.

27. Toraya, T., Radical catalysis in coenzyme B12-dependent isomerization (eliminating) reactions. *Chem. Rev.* **2003,** *103*, 2095-2127.

28. Bradbeer, C., Clostridial rermentations of choline and ethanolamine . Preparation and properties of cell-free extracts. *J Biol Chem* **1965,** *240* (12), 4669-4674.

29. Stojiljkovic, I.; Baumler, A. J.; Heffron, F., Ethanolamine utilization in Salmonella typhimurium: nucleotide sequence, protein expression, and mutational analysis of the cchA cchB eutE eutJ eutG eutH gene cluster. *Journal of bacteriology* **1995,** *177* (5), 1357-1366.

30. Kaplan, B. H.; Stadtman, E. R., Ethanolamine deaminase a cobamide coenzyme-dependent enzyme. Purification assay and properties of wnzyme. *Journal of Biological Chemistry* **1968,** *243* (8), 1787-&.

31. Hubbard, B. K.; Gulick, A. M.; Babbitt, P. C.; Rayment, I.; Gerlt, J. A., Evolution of enzymatic activities in the enolase superfamily: Mechanism, structure, and metabolic context of glucarate dehydratase from Escherichia coli. *Faseb Journal* **1999,** *13* (7), A1446-A1446.

32. Marsh, E. N. G., Coenzyme B-12 (cobalamin)-dependent enzymes. *Essays in Biochemistry, Vol 34, 1999* **1999,** *34*, 139-154.

33. Banerjee, R.; Ragsdale, S. W., The many faces of vitamin B-12: Catalysis by cobalamin-dependent enzymes. *Annu. Rev. Biochem.* **2003,** *72*, 209-247.

34. Kofoid, E.; Rappleye, C.; Stojiljkovic, I.; Roth, J., The 17-gene ethanolamine (eut) operon of Salmonella typhimurium encodes five homologues of carboxysome shell proteins. *Journal of bacteriology* **1999,** *181* (17), 5317-5329.

35. Huseby, D. L.; Roth, J. R., Evidence that a metabolic microcompartment contains and recycles private cofactor pools. *Journal of bacteriology* **2013,** *195* (12), 2864-2879.

36. Garsin, D. A., Ethanolamine utilization in bacterial pathogens: roles and regulation. *Nat. Rev. Microbiol.* **2010,** *8* (4), 290-295.

37. Bovell, A. M.; Warncke, K., The structural model of Salmonella typhimurium Ethanolamine Ammonia-Lyase directs a rational approach to the assembly of the functional [(EutB–EutC)2]3 oligomer from isolated subunits. *Biochemistry* **2013,** *52* (8), 1419-1428.

38. Shibata, N.; Tamagaki, H.; Hieda, N.; Akita, K.; Komori, H.; Shomura, Y.; Terawaki, S.; Mori, K.; Yasuoka, N.; Higuchi, Y.; Toraya, T., Crystal structures of Ethanolamine Ammonia-lyase complexed with coenzyme B-12 analogs and substrates. *J Biol Chem* **2010,** *285* (34), 26484-26493.

39. Warncke, K.; Schmidt, J. C.; Ke, S.-C., Identification of a rearranged-substrate, product radical intermediate and the contribution of a product radical trap in vitamin B12 coenzyme-dependent ethanolamine deaminase catalysis. *J. Am. Chem. Soc.* **1999,** *121* (45), 10522-10528 [Correction: J. Am. Chem. Soc. 130, 6055 (2008)].

40. Finke, R. G.; Hay, B. P., Thermolysis of Adenosylcobalamin - a product, kinetic, and CO-C5' bond-dissociation energy study. *Inorg. Chem.* **1984,** *23* (20), 3041-3043.

41. Bucher, D.; Sandala, G. M.; Durbeej, B.; Radom, L.; Smith, D. M., The elusive 5 '-Deoxyadenosyl radical in coenzyme-B-12-mediated reactions. *Journal of the American Chemical Society* **2012,** *134* (3), 1591-1599.

42. Bucher, D.; Sandala, G. M.; Durbeej, B.; Radom, L.; Smith, D. M., The elusive 5'-deoxyadenosyl radical in coenzyme-B12-mediated reactions. *J. Am. Chem. Soc.* **2012,** *134*, 1591-1599.

43. Babior, B. M.; Moss, T. H.; Ormejohn.Wh; Beinert, H., Mechanism of action of Ethanolamine Ammonia-Lyase, a B12-Dependent Enayme - participation of paramagnetic species in catalytic deamination of 2-aminopropanol. *Journal of Biological Chemistry* **1974,** *249* (14), 4537-4544.

44. Retey, J.; Suckling, C. J.; Arigoni, D.; Babior, B. M., Stereochemistry of reaction catalyzed by Ethanolamine Ammonia-Lyase, an Adenosylcobalamin-dependent enzyme -

example of racemization of accopanying substitution. *Journal of Biological Chemistry* **1974,** *249* (19), 6359-6360.

45. Atherton, N. M., *Principles of electron spin resonance*. Ellis Horwood : PTR Prentice Hall: New York, 1993; p ix, 585 p.

46. Bender, C. J. B., *Computational and instrumental methods in EPR*. Springer: New York, NY, 2006.

47. Wertz, J. E.; Bolton, J. R., *Electron spin resonance*. Chapman and Hall: New York, 1986.

48. Canfield, J. M.; Warncke, K., Geometry of reactant centers in the CoII-substrate radical pair state of coenzyme B12-dependent Ethanolamine Deaminase determined by using orientation-selection-ESEEM spectroscopy. *J. Phys. Chem. B* **2002,** *106,* 8831-8841.

49. Zhu, C.; Warncke, K., Reaction of the CoII-substrate radical pair catalytic intermediate in coenzyme B12-dependent Ethanolamine Ammonia-Lyase in frozen aqueous Solution from 190 to 217 Kelvin. *Biophys. J.* **2008,** *95,* 5890-5900.

50. Wang, M.; Warncke, K., Kinetic and thermodynamic characterization of CoII-substrate radical pair formation in coenzyme B12-dependent Ethanolamine Ammonia-Lyase in a cryosolvent system by using time-resolved, full-spectrum continuous-wave electron paramagnetic resonance spectroscopy. *J. Am. Chem. Soc.* **2008,** *130,* 4846-4858.

51. Wang, M.; Zhu, C.; Kohne, M.; Warncke, K., Resolution and characterization of chemical steps in enzyme catalytic sequences by using ow-Temperature and Time-Resolved, Full-Spectrum EPR Spectroscopy in Fluid Cryosolvent and Frozen Solution Systems. *Electron Paramagnetic Resonance Investigations of Biological Systems by Using Spin Labels, Spin Probes, and Intrinsic Metal Ions, Pt A* **2015,** *563*, 59-94.

52. Likhtenshtein, G. I., *Spin labeling methods in molecular biology*. John Wiley and Sons: New Your, 1976.

53. Wertz, J. E.; Bolton, J. R., *Electron spin resonance : elementary theory and practical applications*. Chapman and Hall: New York, 1986; p xiv, 481, 17 unnumbered pages.

54. Eaton, G. R.; Eaton, S. S.; Barr, D. P.; Weber, R. T.; SpringerLink (Online service), Quantitative EPR a practitioners guide. Springer-Verlag Vienna,: Vienna, 2010; p. 1 online resource. http://dx.doi.org/10.1007/978-3-211-92948-3.

55. Abragam, A.; Pryce, M. H. L., Theory of the nuclear hyperfine structure of paramagnetic resonance spectra in crystals. *Proceedings of the Royal Society of London Series a-Mathematical and Physical Sciences* **1951,** *205* (1080), 135-153.

56. Babior, B. M.; Moss, T. H.; Orme-Johnson, W. H.; Beinert, H., Mechanism of action of Ethanolamine Ammonia-Lyase, a B12-dependent enzyme - participation of paramagnetic species in catalytic deamination of 2-aminopropanol. *J Biol Chem* **1974,** *249* (14), 4537-4544.

57. Bandarian, V.; Reed, G. H., Ethanolamine Ammonia-Lyase. In *Chemistry and Biochemistry of B12*, Banerjee, R., Ed. John Wiley and Sons: New York, 1999; pp 811-833.

58. Zhu, C.; Warncke, K., Kinetic isolation and characterization of the radical rearrangement step in coenzyme B12-dependent Ethanolamine Ammonia-Lyase. *J. Am. Chem. Soc.* **2010,** *132* (28), 9610-9615.

59. Bender, G.; Poyner, R. R.; Reed, G. H., Identification of the substrate radical intermediate derived from ethanolamine during catalysis by Ethanolamine Ammonia-Lyase. *Biochemistry* **2008,** *47* (43), 11360-11366.

60. Ke, S. C., Spin-spin interaction in ethanolamine deaminase. *Biochim. Biophys. Acta* **2003,** *1620*, 267-272.

61. Canfield, J. M.; Warncke, K., Active site reactant center geometry in the CoII-product radical pair state of coenzyme B12-dependent Ethanolamine Deaminase determined by using orientation-selection-ESEEM spectroscopy. *J. Phys. Chem. B* **2005,** *109,* 3053-3064.

62. Pilbrow, J., EPR of B12-dependent enzyme reactions and related systems. In *B12*, Dolphin, D., Ed. Wiley: New York, 1982; pp 431-462.

63. Boas, J. F.; Hicks, P. R.; Pilbrow, J. R.; Smith, T. D., Interpretation of electron spin resonance spectra due to some B12-dependent enzyme reactions. *J. Chem. Soc. Faraday Trans. 2* **1978,** *74*, 417-431.

64. Kamerlin, S. C. L.; Warshel, A., At the dawn of the 21st century: Is dynamics the missing link for understanding enzyme catalysis? *Proteins* **2010,** *78* (6), 1339-1375.

65. Glowacki, D. R.; Harvey, J. N.; Mulholland, A. J., Taking Ockham's razor to enzyme dynamics and catalysis. *Nature Chemistry* **2012,** *4* (3), 169-176.

66. Fan, Y.; Cembran, A.; Ma, S.; Gao, J., Connecting protein conformational dynamics with catalytic function as illustrated in dihydrofolate reductase. *Biochemistry* **2013,** *52,* 2036-2049.

67. Kohen, A., Role of dynamics in enzyme catalysis: substantial versus semantic controversies. *Accounts of Chemical Research* **2015,** *48* (2), 466-473.

68. Boehr, D. D.; McElheny, D.; Dyson, H. J.; Wright, P. E., The dynamic energy landscape of dihydrofolate reductase catalysis. *Science* **2006,** *313*, 1638-1642.

69. Reed, G. H., Radical mechanisms in adenosylcobalamin-dependent enzymes. *Curr. Opin. Chem. Biol.* **2004,** *8* (5), 477-483.

70. Frey, P. A.; Hegeman, A. D., *Enzymatic reaction mechanisms*. Oxford University Press: New York, 2007.

71. Marcus, R. A.; Sutin, N., Electron transfers in chemistry and biology. *Biochimica Et Biophysica Acta* **1985,** *811* (3), 265-322.

72. Hammes-Schiffer, S.; Benkovic, S. J., Relating protein motion to catalysis. *Ann. Rev. Biochem.* **2006,** *75*, 519-541.

73. Klinman, J. P., Importance of protein dynamics during enzymatic C-H bond cleavage catalysis. *Biochemistry* **2013,** *52*, 2068-2077.

74. Wang, Z.; Singh, P.; Czekster, C. M.; Kohen, A.; Schramm, V. L., Protein mass-modulated effects in the catalytic mechanism of dihydrofolate reductase: beyond promoting vibrations. *Journal of the American Chemical Society* **2014,** *136* (23), 8333-8341.

75. Klinman, J. P., Dynamically achieved active site precision in enzyme catalysis. *Accounts of Chemical Research* **2015,** *48* (2), 449-456.

76. Hay, S.; Scrutton, N. S., Good vibrations in enzyme-catalysed reactions. *Nature Chemistry* **2012,** *4* (3), 161-168.

77. Nakanishi, M.; Sokolov, A. P., Protein dynamics in a broad frequency range: Dielectric spectroscopy studies. *Journal of Non-Crystalline Solids* **2015,** (407), 478-485.

78. Zhu, C.; Warncke, K., Kinetic isolation and characterization of the radical rearrangement step in coenzyme B-12-dependent Ethanolamine Ammonia-lyase. *Journal of the American Chemical Society* **2010,** *132* (28), 9610-9615.

79. Wetmore, S. D.; Smith, D. M.; Bennet, J. T.; Radom, L., Understanding the mechanism of action of B12-dependent Ethanolamine Ammonia-Lyase: synergistic interactions at play. *J. Am. Chem. Soc.* **2002,** *124*, 14054-14065.

80. Sandala, G. M.; Smith, D. M.; Radom, L., Divergent mechanisms of suicide inactivation for ethanolamine ammonia-lyase. *J. Am. Chem. Soc.* **2005,** *127*, 8856-8864.

81. Semialjac, M.; Schwarz, H., Computational study on mechanistic details of the aminoethanol rearrangement catalyzed by the vitamin B-12-dependent ethanolamine ammonia lyase: His and Asp/Glu acting simultaneously as catalytic auxiliaries. *Journal of Organic Chemistry* **2003,** *68* (18), 6967-6983.

82. Poyner, R. R.; Anderson, M. A.; Bandarian, V.; Cleland, W. W.; Reed, G. H., Probing nitrogen-sensitive steps in the free-radical-mediated deamination of amino alcohols by ethanolamine ammonia-lyase. *J. Am. Chem. Soc.* **2006,** *128* (22), 7120-7121.

83. Frey, P. A., Cobalamin coenzymes in enzymology. In *Comprehensive natural products II chemistry and biology*, Mander, L.; Lui, H.-W., Eds. Elsevier: Oxford UK, 2010; Vol. 7, pp 501-546.

84. Green, J. L.; Fan, J.; Angell, C. A., The protein-glass analogy: New insight from homopeptide comparisons. *J. Phys. Chem.* **1994,** *98* (51), 13780-13790.

85. Ngai, K. L.; Paluch, M., Classification of secondary relaxation in glass-formers based on dynamic properties. *Journal of Chemical Physics* **2004,** *120* (2), 857-873.

86. Lewandowski, J. R.; Halse, M. E.; Blackledge, M.; Emsley, L., Direct observation of hierarchical protein dynamics. *Science* **2015,** *348* (6234), 578-581.

87. Goldstein, M., Viscous liquids and the glass transition: A potential energy picture. *Journal of Chemical Physics* **1969,** *51* (9), 3728-+.

88. Stillinger, F. H., A topographic view of supercooled liquids and glass formation. *Science* **1995,** *267*, 1935-1939.

89. Faust, L. R. P.; Connor, J. A.; Roof, D. M.; Hoch, J. A.; Babior, B. M., Cloning, sequencing, and expression of the genes encoding the adenosylcobalamin-dependent

Ethanolamine Ammonia-Lyase of Salmonella-typhimurium. *J Biol Chem* **1990,** *265* (21), 12462-12466.

90. Faust, L. P.; Babior, B. M., Overexpression, purification, and some properties of the adocbl-dependent Ethanolamine Ammonia-Lyase from Salmonella-typhimurium. *Arch Biochem Biophys* **1992,** *294* (1), 50-54.

91. Hollaway, M. R.; Johnson, A. W.; Lappert, M. F.; Wallis, O. C., The number of functional sites per molecule of the adenosylcobalamin-dependent enzyme, ethanolamine deaminase, as determined by a kinetic method. *European Journal of Biochemistry* **1980,** *111* (1), 177-188.

92. Bandarian, V.; Reed, G. H., Hydrazine cation radical in the active site of ethanolamine ammonia-lyase: Mechanism-based inactivation by hydroxyethylhydrazine. *Biochemistry* **1999,** *38*, 12394-12402.

93. Moore, J. W.; Pearson, R. G., *Kinetics and mechanism*. Wiley and Sons: New York, 1981.

94. Hollaway, M. R.; White, H. A.; Joblin, K. N.; Johnson, A. W.; Lappert, M. F.; Wallis, O. C., A spectrophotometric rapid kinetic study of reactions catalyzed by coenzyme B12-dependent ethanolamine ammonia-lyase. *Eur. J. Biochem.* **1978,** *82*, 143-154.

95. Bandarian, V.; Reed, G. H., Isotope effects in the transient phases of the reaction catalyzed by ethanolamine ammonia-lyase: Determination of the number of exchangeable hydrogens in the enzyme-cofactor complex. *Biochemistry* **2000,** *39* (39), 12069-12075.

96. Schopf, P.; Mills, M. J. L.; Warshel, A., The entropic contributions in vitamin B-12 enzymes still reflect the electrostatic paradigm. *Proc. Natl. Acad. Sci. U. S. A.* **2015,** *112* (14), 4328-4333.

97. Austin, R. H.; Beeson, K. W.; Eisenstein, L.; Frauenfelder, H.; Gunsalus, I. C., Dynamics of ligand binding to myoglobin. *Biochemistry* **1975,** *14*, 5355-5373.

98. Agmon, N., Coupling of protein relaxation to ligand binding and migration in myoglobin. *Biophys. J.* **2004,** *87*, 1537-1543.

99. Ringe, D.; Petsko, G. A., The 'glass transition' in protein dynamics: what it is, why it occurs, and how to exploit it. *Biophys Chem* **2003,** *105* (2-3), 667-680.

100. Jansson, H.; Bergman, R.; Swenson, J., Role of solvent for the dynamics and the glass transition of proteins. *J. Phys. Chem. B* **2011,** *115*, 4099-4109.

101. Panagopoulou, A.; Kyritsis, A.; Serra, R. S. I.; Ribelles, J. L. G.; Shinyashiki, N.; Pissis, P., Glass transition and dynamics in BSA-water mixtures over wide ranges of composition studied by thermal and dielectric techniques. *BBA-Proteins Proteomics* **2011,** *1814* (12), 1984-1996.

102. Brown, K. L., Chemistry and enzymology of vitamin B12. *Chem. Rev.* **2005,** *105*, 2075-2149.

103. Kohne, M.; Zhu, C.; Warncke, K., Two dynamical regimes of the substrate radical rearrangement reaction in B-12-dependent Ethanolamine Ammonia-Lyase resolve contributions of native protein configurations and collective configurational fluctuations to catalysis. *Biochemistry* **2017,** *56* (25), 3257-3264.

104. Frey, P. A.; Hegeman, A. D.; Reed, G. H., Free radical mechanisms in biology. *Chem. Rev.* **2006,** *106*, 3302-3316.

105. Bandarian, V.; Reed, G. H., Analysis of the electron paramagnetic resonance spectrum of a radical intermediate in the coenzyme B12-dependent ethanolamine ammonia-lyase catalyzed reaction of S-2-aminopropanol. *Biochemistry* **2002,** *41*, 8580-8588.

106. Canfield, J. M.; Warncke, K., Geometry of reactant centers in the Co-II-substrate radical pair state of coenzyme B-12-dependent ethanolamine deaminase determined by using orientation-selection-ESEEM spectroscopy. *J. Phys. Chem. B* **2002,** *106* (34), 8831-8841.

107. Weisblat, D. A.; Babior, B. M., Mechanism of action of Ethanolamine Ammonia-Lyase a B12-dependent enzyme .8. Further studies with compounds labeled with isotopes of hydrogen - identification and some properites of rate-limiting step. *Journal of Biological Chemistry* **1971,** *246* (19), 6064-&.

108. Cook, P. F., Enzyme mechanisms from isotope effects. **1991**.

109. Cleland, W. W., The use of isotope effects to determine enzyme mechanisms. *Journal of Biological Chemistry* **2003,** (278), 51975-51984.

110. Anslyn, E. V.; Dougherty, D. A., *Modern physical organic chemistry*. University Science: Sausalito, Calif., 2006; p xxviii, 1095 p.

111. Sun, L.; Groover, O. A.; Canfield, J. M.; Warncke, K., Critical role of arginine 160 of the EutB protein subunit for active site structure and radical catalysis in coenzyme B12-dependent ethanolamine ammonia-lyase. *Biochemistry* **2008,** *47* (20), 5523-5535.

112. Sun, L.; Hernandez-Guzman, J.; Warncke, K., OPTESIM, a versatile toolbox for numerical simulation of electron spin echo envelope modulation (ESEEM) that features hybrid optimization and statistical assessment of parameters. *J. Magn. Reson.* **2009,** *200*, 21-28 (Cover Article).

113. Wang, M.; Warncke, K., Entropic origin of cobalt-carbon bond cleavage catalysis in adenosylcobalamin-dependent ethanolamine ammonia-lyase. *J. Am. Chem. Soc.* **2013,** *135*, 15077-15084.

114. Chaplin, M., Opinion - Do we underestimate the importance of water in cell biology? *Nat. Rev. Mol. Cell Biol.* **2006,** *7* (11), 861-866.

115. Fenimore, P. W.; Frauenfelder, H.; McMahon, B. H.; Parak, F. G., Slaving: Solvent fluctuations dominate protein dynamics and functions. *Proc. Natl. Acad. Sci. U. S. A.* **2002,** *99* (25), 16047-16051.

116. Frauenfelder, H.; Chen, G.; Berendzen, J.; Fenimore, P. W.; Jansson, H.; McMahon, B. H.; Stroe, I. R.; Swenson, J.; Young, R. D., A unified model of protein dynamics. *P Natl Acad Sci USA* **2009,** *106* (13), 5129-5134.

117. Chen, H.; Sun, L.; Warncke, K., Heterogeneous ordered-disordered structure of the mesodomain in frozen sucrose-water solutions revealed by multiple electron paramagnetic resonance spectroscopies. *Langmuir* **2013,** *29*, 4357-4365.

118. Siemer, A. B.; Huang, K. Y.; McDermott, A. E., Protein-ice interaction of an antifreeze protein observed with solid-state NMR. *Proc. Natl. Acad. Sci. U. S. A.* **2010,** *107* (41), 17580-17585.

119. Buldyrev, S. V.; Kumar, P.; Sastry, S.; Stanley, H. E.; Weiner, S., Hydrophobic collapse and cold denaturation in the Jagla model of water. *J. Phys.-Condes. Matter* **2010,** *22* (28), 12.

120. Bhat, S. N.; Sharma, A.; Bhat, S. V., Vitrification and glass transition of water: Insights from spin probe ESR. *Phys. Rev. Lett.* **2005,** *95*, 2357021-2357024.

121. Johari, G. P.; Hallbrucker, A.; Mayer, E., The glass liquid transition of hyperquenched water. *Nature* **1987,** *330*, 552-553.

122. Banerjee, D.; Bhat, S. N.; Bhat, S. V.; Leporini, D., ESR evidence for 2 coexisting liquid phases in deeply supercooled bulk water. *Proc. Natl. Acad. Sci.* **2009,** *106*, 11448-11453.

123. Sucrose Conversion Table, FILE CODE 135-A-50. *United States Department of Agriculture (USDA)* **1981**.

124. Austin, R. H.; Beeson, K. W.; Eisenstein, L.; Frauenfelder, H.; Gunsalus, I. C., Dynamics of ligand-binding to myoglobin. *Biochemistry* **1975,** *14* (24), 5355-5373.

125. Canfield, J.; Warncke, K., Active site reactant center geometry in the $Co^{II}$-product radical pair state of coenzyme $B_{12}$-dependent Ethanolamine Deaminase determined by using orientation-selection electron spin-echo envelope modulation spectroscopy. *J. Phys. Chem. B* **2005,** *109* (7), 3053-3064.

126. Canfield, J.; Warncke, K., Geometry of reactant centers in the $Co^{II}$-substrate radical pair state of coenzyme

$B_{12}$-dependent Ethanolamine Deaminase determined by using

orientation-selection-ESEEM spectroscopy. *J. Phys. Chem. B* **2002,** *106* (34), 8831-8841.

127. Frauenfelder, H.; Sligar, S.; Wolynes, P., The energy landscapes and motions of proteins. *Science* **1991,** *254* (5038), 1598-1603.

128. Frauenfelder, H.; Petsko, G. A.; Tsernoglou, D., Temperature-dependent x-ray diffraction as a probe of protein structural dynamics. *Nature* **1979,** *280*, 558-563.

129. Chen, H. Structure and dynamics of the mesodomain environment of coenzyme B12-dependent Ethanolamine Ammonia-Lyase in frozen aqueous solutions and kinetics of the radical rearrangement reaction 173-187 K. Emory University, Atlanta, GA, 2014.

130. Frost, W., Kinetics and mechanism. A study of homogeneous chemical reactions. *Journal of the American Chemical Society* **1961,** *83* (23), 4870.

131. Ucuncuoglu, N.; Warncke, K., Radical capture and rearrangement-enabling functions of the substrate radical macrostate are enacted by two sequential protein configurational microstates in B12-dependent ethanolamine ammonia-lyase. University, E., Ed. 2017.

# Appendix

**7.1 CWXepr2mat**: Converts .DTA, .DSC, and .YGF files to .mat files for substrate radical decays and background spectra using MATLAB.

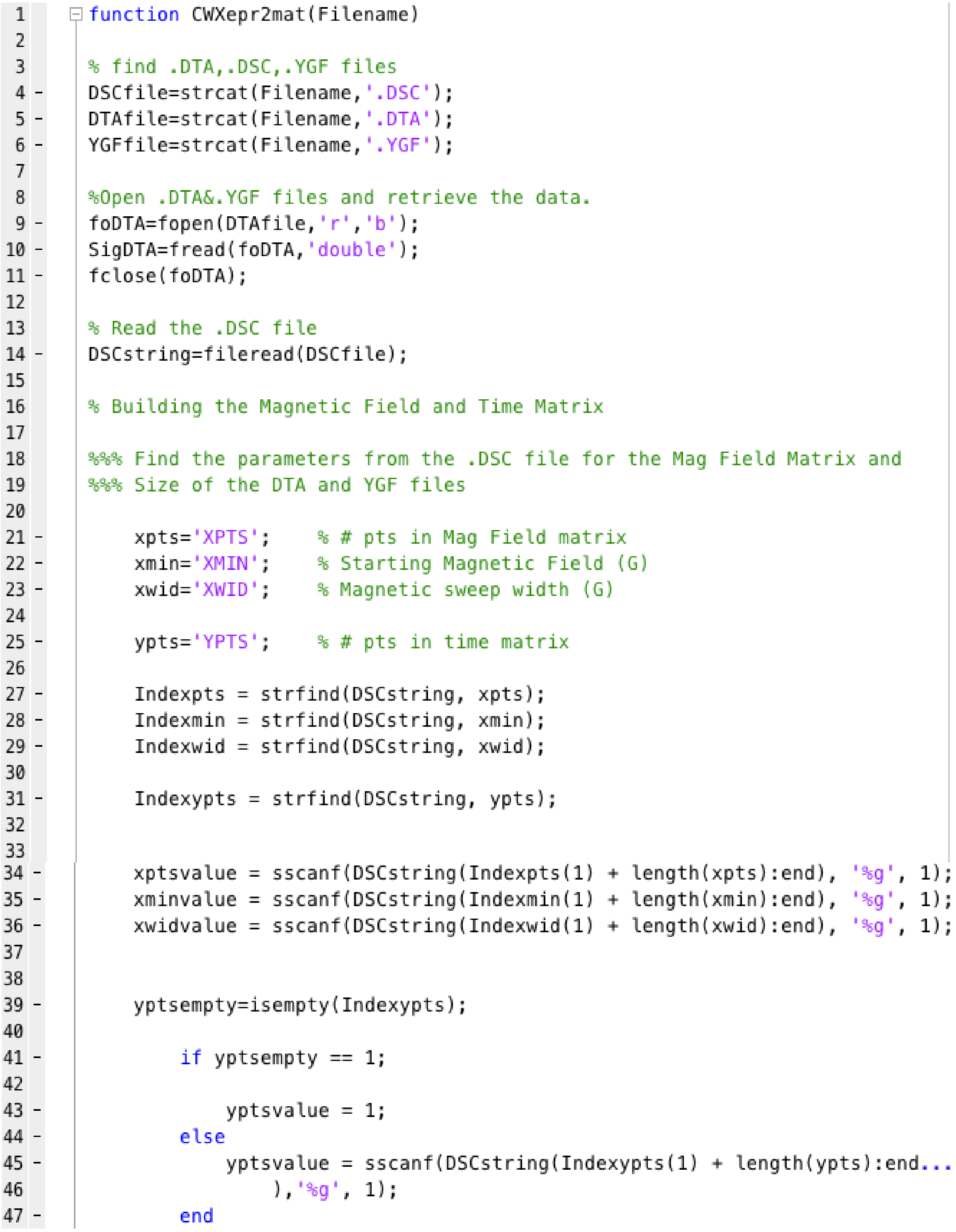

```
function CWXepr2mat(Filename)

% find .DTA,.DSC,.YGF files
DSCfile=strcat(Filename,'.DSC');
DTAfile=strcat(Filename,'.DTA');
YGFfile=strcat(Filename,'.YGF');

%Open .DTA&.YGF files and retrieve the data.
foDTA=fopen(DTAfile,'r','b');
SigDTA=fread(foDTA,'double');
fclose(foDTA);

% Read the .DSC file
DSCstring=fileread(DSCfile);

% Building the Magnetic Field and Time Matrix

%%% Find the parameters from the .DSC file for the Mag Field Matrix and
%%% Size of the DTA and YGF files

    xpts='XPTS';    % # pts in Mag Field matrix
    xmin='XMIN';    % Starting Magnetic Field (G)
    xwid='XWID';    % Magnetic sweep width (G)

    ypts='YPTS';    % # pts in time matrix

    Indexpts = strfind(DSCstring, xpts);
    Indexmin = strfind(DSCstring, xmin);
    Indexwid = strfind(DSCstring, xwid);

    Indexypts = strfind(DSCstring, ypts);


    xptsvalue = sscanf(DSCstring(Indexpts(1) + length(xpts):end), '%g', 1);
    xminvalue = sscanf(DSCstring(Indexmin(1) + length(xmin):end), '%g', 1);
    xwidvalue = sscanf(DSCstring(Indexwid(1) + length(xwid):end), '%g', 1);


    yptsempty=isempty(Indexypts);

        if yptsempty == 1;

            yptsvalue = 1;
        else
            yptsvalue = sscanf(DSCstring(Indexypts(1) + length(ypts):end...
                ),'%g', 1);
        end
```

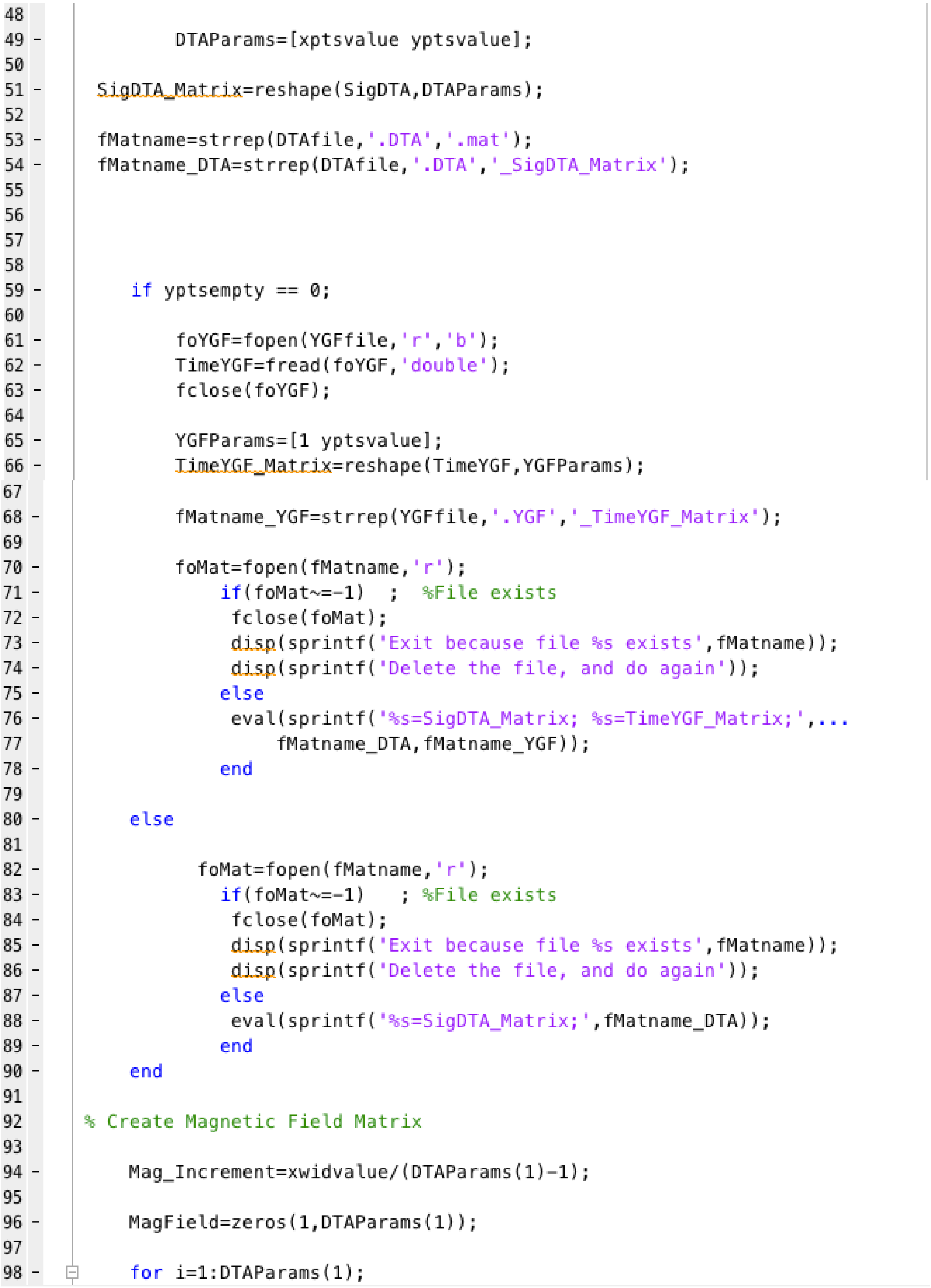

```

        DTAParams=[xptsvalue yptsvalue];

 SigDTA_Matrix=reshape(SigDTA,DTAParams);

 fMatname=strrep(DTAfile,'.DTA','.mat');
 fMatname_DTA=strrep(DTAfile,'.DTA','_SigDTA_Matrix');




    if yptsempty == 0;

        foYGF=fopen(YGFfile,'r','b');
        TimeYGF=fread(foYGF,'double');
        fclose(foYGF);

        YGFParams=[1 yptsvalue];
        TimeYGF_Matrix=reshape(TimeYGF,YGFParams);

        fMatname_YGF=strrep(YGFfile,'.YGF','_TimeYGF_Matrix');

        foMat=fopen(fMatname,'r');
            if(foMat~=-1)  ;  %File exists
             fclose(foMat);
             disp(sprintf('Exit because file %s exists',fMatname));
             disp(sprintf('Delete the file, and do again'));
            else
             eval(sprintf('%s=SigDTA_Matrix; %s=TimeYGF_Matrix;',...
                 fMatname_DTA,fMatname_YGF));
            end

    else

          foMat=fopen(fMatname,'r');
            if(foMat~=-1)   ; %File exists
             fclose(foMat);
             disp(sprintf('Exit because file %s exists',fMatname));
             disp(sprintf('Delete the file, and do again'));
            else
             eval(sprintf('%s=SigDTA_Matrix;',fMatname_DTA));
            end
    end

% Create Magnetic Field Matrix

    Mag_Increment=xwidvalue/(DTAParams(1)-1);

    MagField=zeros(1,DTAParams(1));

    for i=1:DTAParams(1);
```

```
    MagField(i)=xminvalue+(i-1)*Mag_Increment;
    end
    MagField=MagField';

    fMatname_Mag=strrep(DTAfile,'.DTA','_MagField');
    eval(sprintf('%s=MagField;',fMatname_Mag));

%
    if yptsempty == 0;

             %save the .mat file
          eval(sprintf('save %s %s %s %s -v6;',fMatname,fMatname_DTA,...
              fMatname_YGF,fMatname_Mag));


    else

          %save the .mat file
          eval(sprintf('save %s %s %s -v6;',fMatname,fMatname_DTA,...
              fMatname_Mag));
    end




end
```

**7.2 evalSraddecay2:** Converts .mat files of specral data (spectra, time matrix, background spectrum) into peak-to-trough amplitude and time matrices using MATLAB.

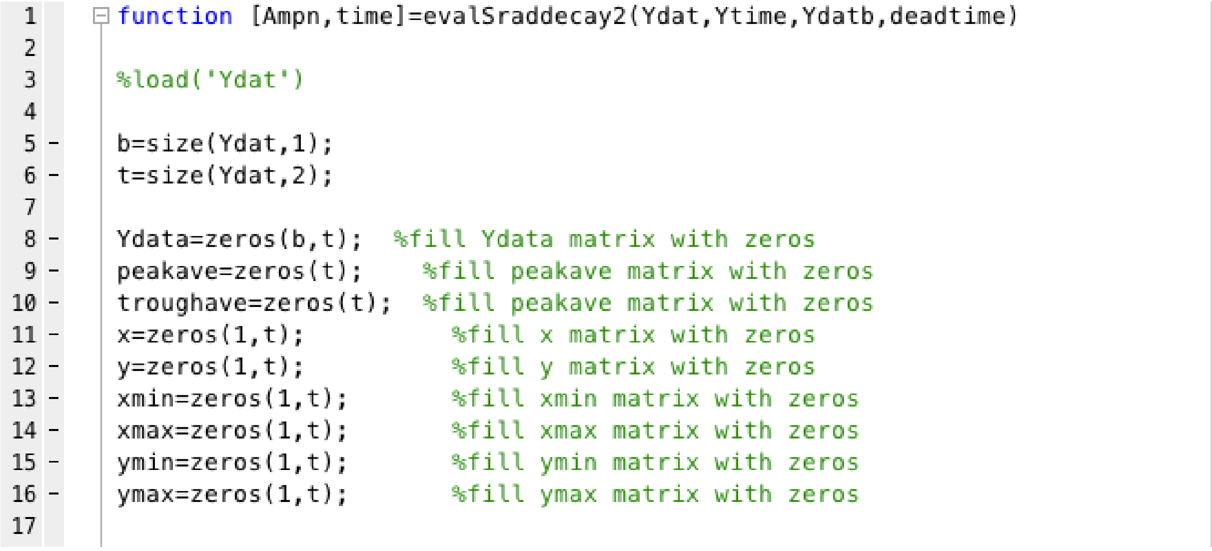

```
function [Ampn,time]=evalSraddecay2(Ydat,Ytime,Ydatb,deadtime)

%load('Ydat')

b=size(Ydat,1);
t=size(Ydat,2);

Ydata=zeros(b,t);  %fill Ydata matrix with zeros
peakave=zeros(t);    %fill peakave matrix with zeros
troughave=zeros(t);  %fill peakave matrix with zeros
x=zeros(1,t);          %fill x matrix with zeros
y=zeros(1,t);          %fill y matrix with zeros
xmin=zeros(1,t);       %fill xmin matrix with zeros
xmax=zeros(1,t);       %fill xmax matrix with zeros
ymin=zeros(1,t);       %fill ymin matrix with zeros
ymax=zeros(1,t);       %fill ymax matrix with zeros

```

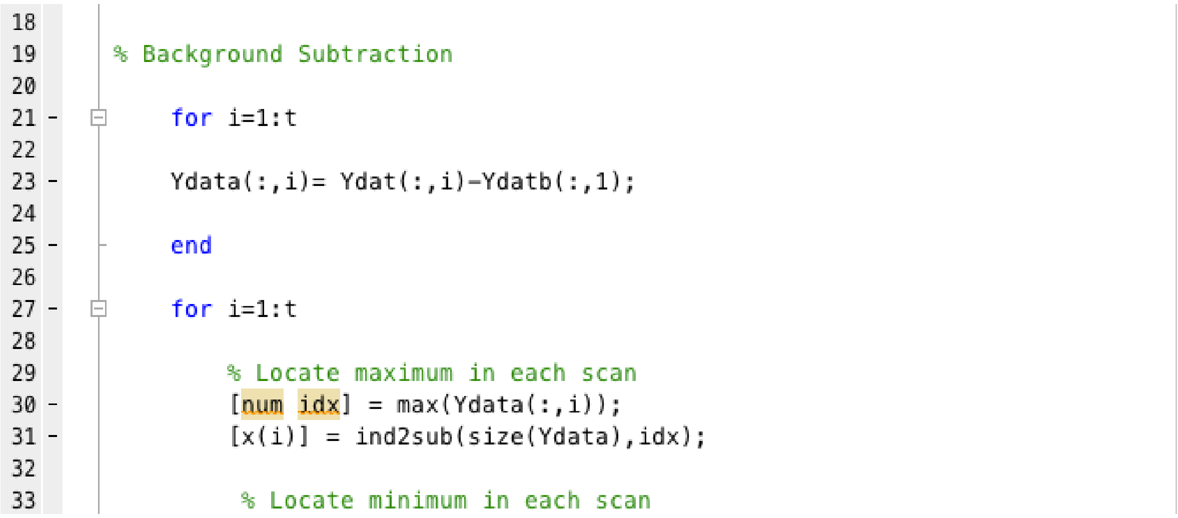

```

% Background Subtraction

    for i=1:t

    Ydata(:,i)= Ydat(:,i)-Ydatb(:,1);

    end

    for i=1:t

        % Locate maximum in each scan
        [num idx] = max(Ydata(:,i));
        [x(i)] = ind2sub(size(Ydata),idx);

         % Locate minimum in each scan
```

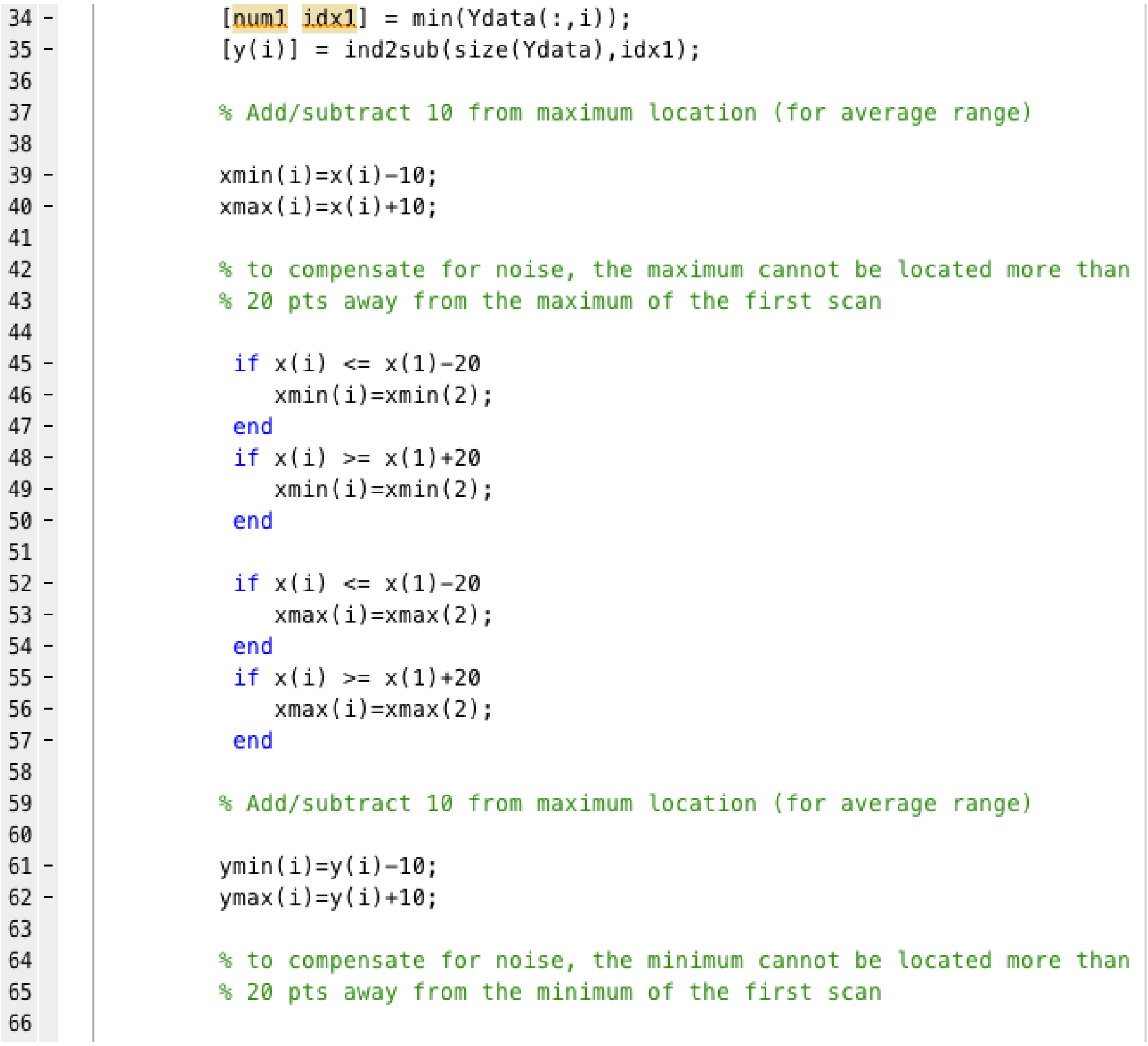

```
        [num1 idx1] = min(Ydata(:,i));
        [y(i)] = ind2sub(size(Ydata),idx1);

        % Add/subtract 10 from maximum location (for average range)

        xmin(i)=x(i)-10;
        xmax(i)=x(i)+10;

        % to compensate for noise, the maximum cannot be located more than
        % 20 pts away from the maximum of the first scan

         if x(i) <= x(1)-20
            xmin(i)=xmin(2);
         end
         if x(i) >= x(1)+20
            xmin(i)=xmin(2);
         end

         if x(i) <= x(1)-20
            xmax(i)=xmax(2);
         end
         if x(i) >= x(1)+20
            xmax(i)=xmax(2);
         end

        % Add/subtract 10 from maximum location (for average range)

        ymin(i)=y(i)-10;
        ymax(i)=y(i)+10;

        % to compensate for noise, the minimum cannot be located more than
        % 20 pts away from the minimum of the first scan

```

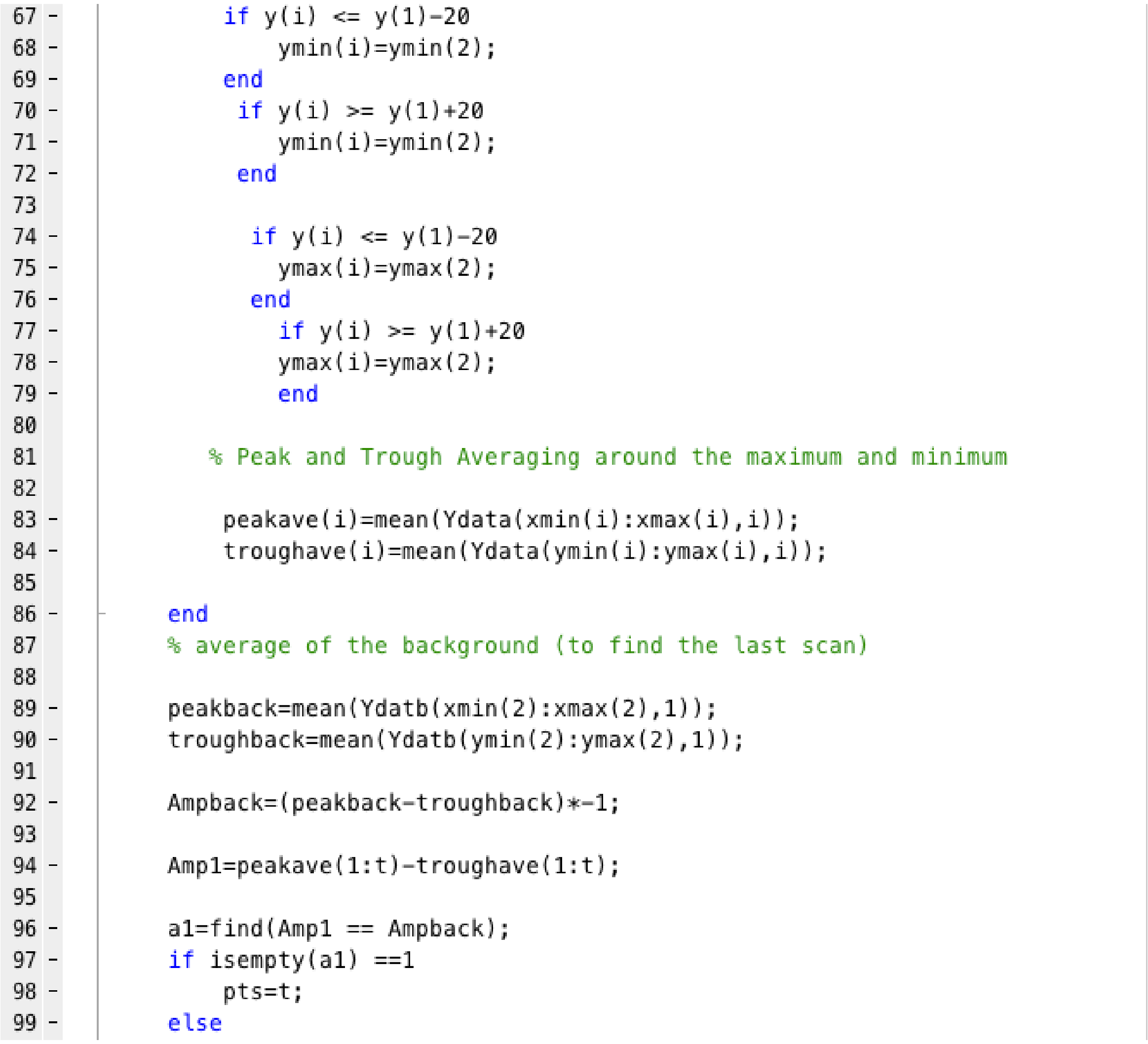

```
        if y(i) <= y(1)-20
            ymin(i)=ymin(2);
        end
         if y(i) >= y(1)+20
            ymin(i)=ymin(2);
         end

          if y(i) <= y(1)-20
            ymax(i)=ymax(2);
          end
            if y(i) >= y(1)+20
            ymax(i)=ymax(2);
            end

       % Peak and Trough Averaging around the maximum and minimum

        peakave(i)=mean(Ydata(xmin(i):xmax(i),i));
        troughave(i)=mean(Ydata(ymin(i):ymax(i),i));

    end
    % average of the background (to find the last scan)

    peakback=mean(Ydatb(xmin(2):xmax(2),1));
    troughback=mean(Ydatb(ymin(2):ymax(2),1));

    Ampback=(peakback-troughback)*-1;

    Amp1=peakave(1:t)-troughave(1:t);

    a1=find(Amp1 == Ampback);
    if isempty(a1) ==1
        pts=t;
    else
```

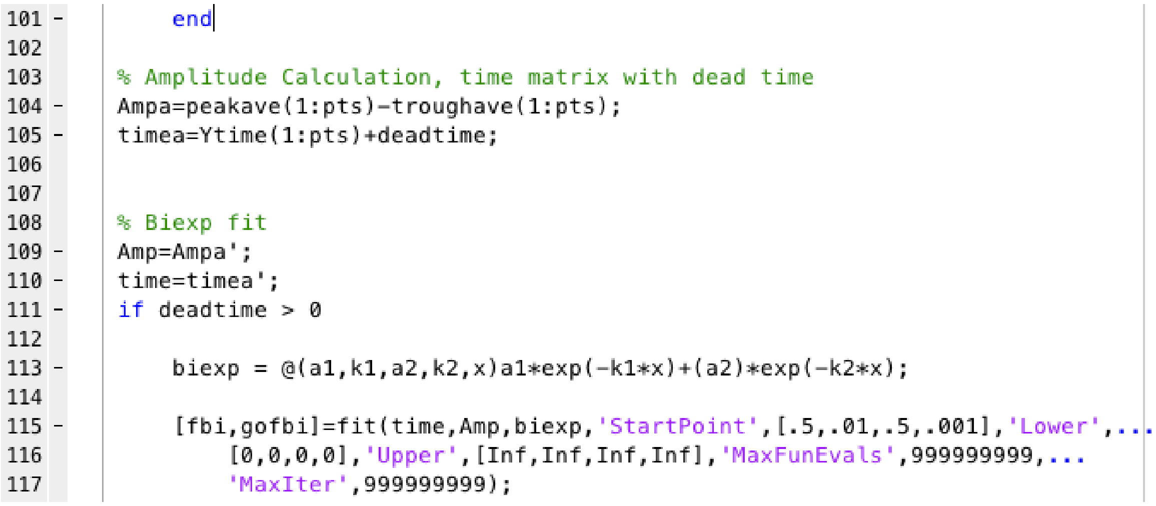

```
    end

% Amplitude Calculation, time matrix with dead time
Ampa=peakave(1:pts)-troughave(1:pts);
timea=Ytime(1:pts)+deadtime;


% Biexp fit
Amp=Ampa';
time=timea';
if deadtime > 0

    biexp = @(a1,k1,a2,k2,x)a1*exp(-k1*x)+(a2)*exp(-k2*x);

    [fbi,gofbi]=fit(time,Amp,biexp,'StartPoint',[.5,.01,.5,.001],'Lower',...
        [0,0,0,0],'Upper',[Inf,Inf,Inf,Inf],'MaxFunEvals',999999999,...
        'MaxIter',999999999);
```

```
        coefs=coeffvalues(fbi);
        gofbic=struct2cell(gofbi);
        gofbir=gofbic(2);
       % Mono-exponential fit
        if cell2mat(gofbir) < .99
            mep = @(a1,k1,a2,t0,n,x)a1*exp(-k1*x)+(a2)*(1+x/t0).^n;

            [fmep,~]=fit(time,Amp,mep,'StartPoint',[.5,.01,.5,100,-1],'Lower',...
                [0,0,0,0,-Inf],'Upper',[Inf,Inf,Inf,Inf,0],'MaxFunEvals',999999999,...
                'MaxIter',999999999);

            coefsmep=coeffvalues(fmep);

            nf=coefsmep(1)+coefsmep(3);

            Ampn=Amp./nf;
        else
            coefsbi=coeffvalues(fbi);
            nf1=coefsbi(1)+coefsbi(3);
            Ampn=Amp./nf1;
        end
    %       figure
    %      plot(fbi,time,Amp)
    else
        Ampn=Amp./Amp(1);

    end
```

**7.3 lsqcurvefitmod:** Fits the *P*(*t*) solution from the microscopic model to the peak-to-trough amplitude of the substrate radical decay using the built in MATLAB function *lsqcurvefit*.

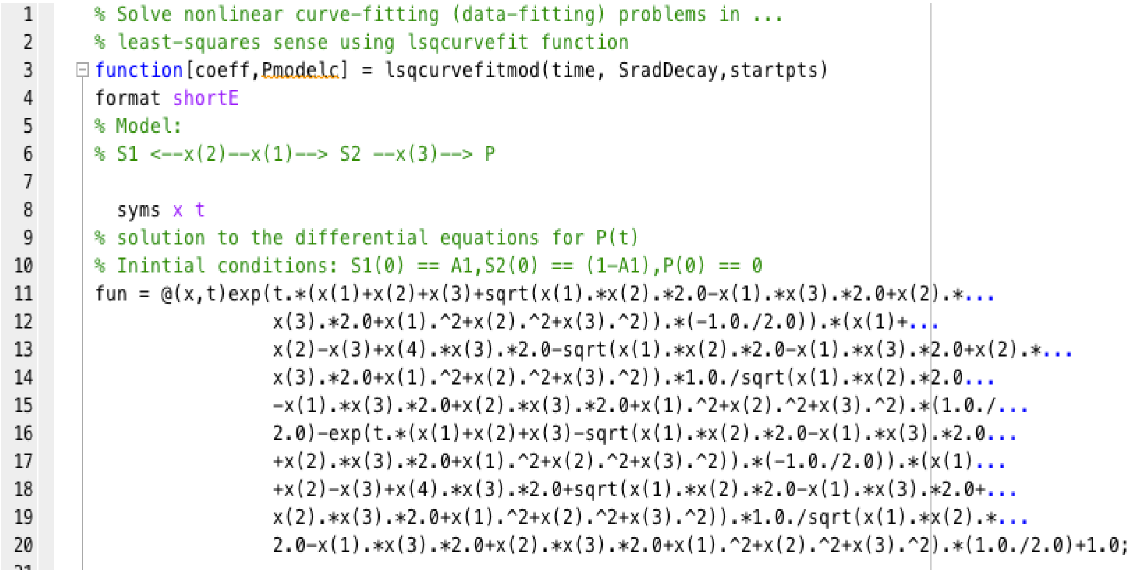

```
% Solve nonlinear curve-fitting (data-fitting) problems in ...
% least-squares sense using lsqcurvefit function
function[coeff,Pmodelc] = lsqcurvefitmod(time, SradDecay,startpts)
format shortE
% Model:
% S1 <--x(2)--x(1)--> S2 --x(3)--> P

  syms x t
% solution to the differential equations for P(t)
% Inintial conditions: S1(0) == A1,S2(0) == (1-A1),P(0) == 0
fun = @(x,t)exp(t.*(x(1)+x(2)+x(3)+sqrt(x(1).*x(2).*2.0-x(1).*x(3).*2.0+x(2).*...
                x(3).*2.0+x(1).^2+x(2).^2+x(3).^2)).*(-1.0./2.0)).*(x(1)+...
                x(2)-x(3)+x(4).*x(3).*2.0-sqrt(x(1).*x(2).*2.0-x(1).*x(3).*2.0+x(2).*...
                x(3).*2.0+x(1).^2+x(2).^2+x(3).^2)).*1.0./sqrt(x(1).*x(2).*2.0...
                -x(1).*x(3).*2.0+x(2).*x(3).*2.0+x(1).^2+x(2).^2+x(3).^2).*(1.0./...
                2.0)-exp(t.*(x(1)+x(2)+x(3)-sqrt(x(1).*x(2).*2.0-x(1).*x(3).*2.0...
                +x(2).*x(3).*2.0+x(1).^2+x(2).^2+x(3).^2)).*(-1.0./2.0)).*(x(1)...
                +x(2)-x(3)+x(4).*x(3).*2.0+sqrt(x(1).*x(2).*2.0-x(1).*x(3).*2.0+...
                x(2).*x(3).*2.0+x(1).^2+x(2).^2+x(3).^2)).*1.0./sqrt(x(1).*x(2).*...
                2.0-x(1).*x(3).*2.0+x(2).*x(3).*2.0+x(1).^2+x(2).^2+x(3).^2).*(1.0./2.0)+1.0;
```

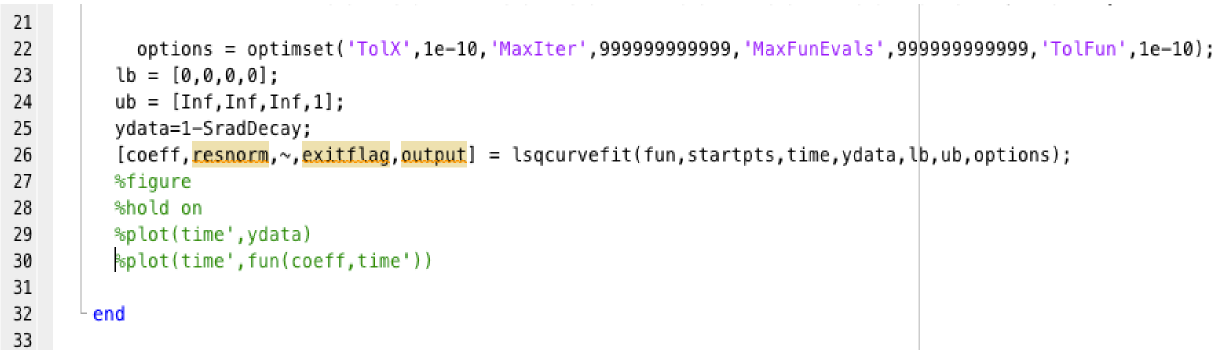

```
     options = optimset('TolX',1e-10,'MaxIter',999999999999,'MaxFunEvals',999999999999,'TolFun',1e-10);
   lb = [0,0,0,0];
   ub = [Inf,Inf,Inf,1];
   ydata=1-SradDecay;
   [coeff,resnorm,~,exitflag,output] = lsqcurvefit(fun,startpts,time,ydata,lb,ub,options);
   %figure
   %hold on
   %plot(time',ydata)
   %plot(time',fun(coeff,time'))

 end

```

**7.4 Incorporate HT2 Step into Microscopic Model:** Solves 4 state, 3 step model using MATLAB function *dsolve* . Also substitutes variables $k_p$, $k_{12}$, $S^{\bullet}_{1,0}$, and $k_{21}$ variables with the protiated values calculated in Ch 2.

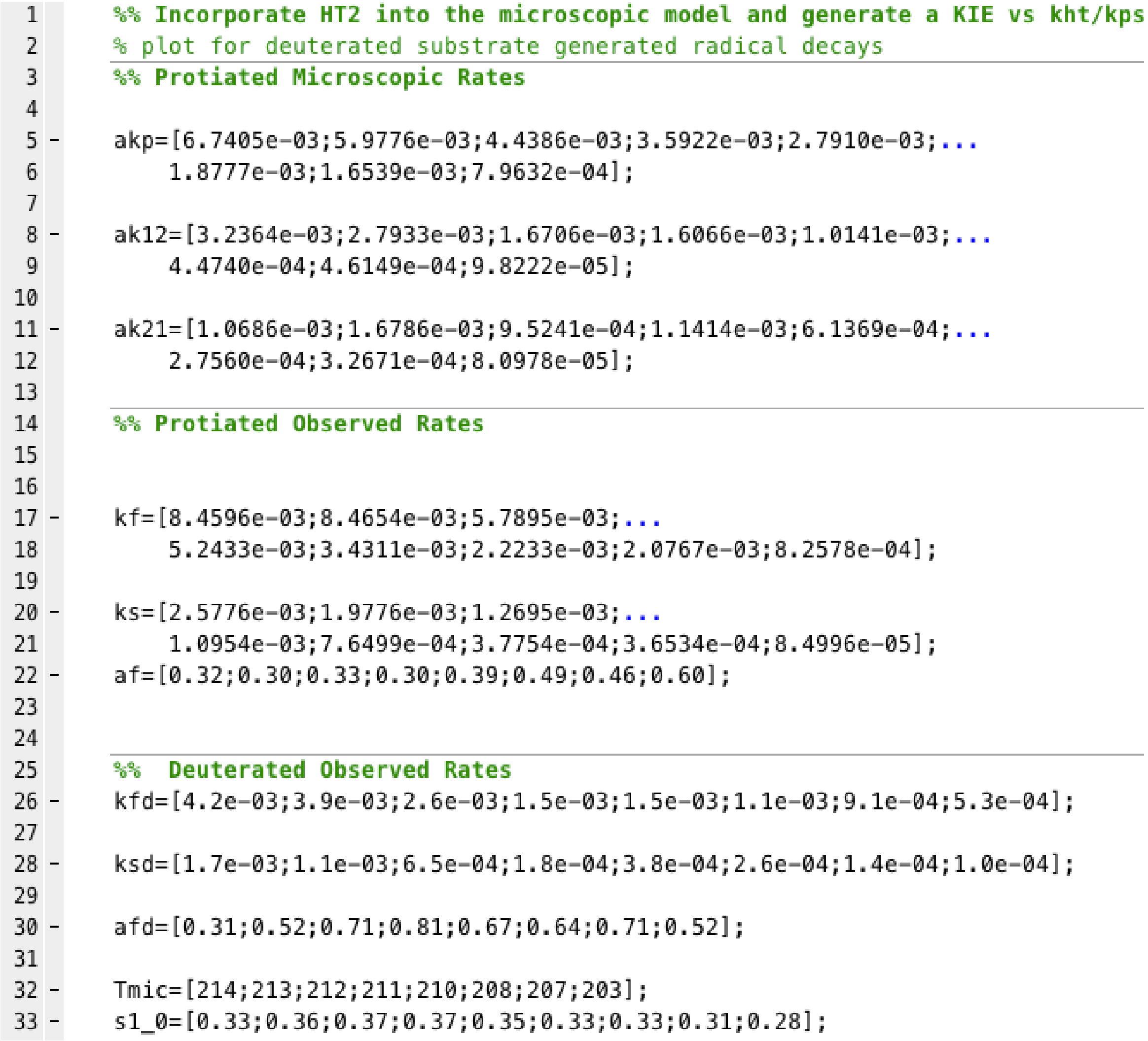

```
%% Incorporate HT2 into the microscopic model and generate a KIE vs kht/kps
% plot for deuterated substrate generated radical decays
%% Protiated Microscopic Rates

akp=[6.7405e-03;5.9776e-03;4.4386e-03;3.5922e-03;2.7910e-03;...
    1.8777e-03;1.6539e-03;7.9632e-04];

ak12=[3.2364e-03;2.7933e-03;1.6706e-03;1.6066e-03;1.0141e-03;...
    4.4740e-04;4.6149e-04;9.8222e-05];

ak21=[1.0686e-03;1.6786e-03;9.5241e-04;1.1414e-03;6.1369e-04;...
    2.7560e-04;3.2671e-04;8.0978e-05];

%% Protiated Observed Rates


kf=[8.4596e-03;8.4654e-03;5.7895e-03;...
    5.2433e-03;3.4311e-03;2.2233e-03;2.0767e-03;8.2578e-04];

ks=[2.5776e-03;1.9776e-03;1.2695e-03;...
    1.0954e-03;7.6499e-04;3.7754e-04;3.6534e-04;8.4996e-05];
af=[0.32;0.30;0.33;0.30;0.39;0.49;0.46;0.60];


%%  Deuterated Observed Rates
kfd=[4.2e-03;3.9e-03;2.6e-03;1.5e-03;1.5e-03;1.1e-03;9.1e-04;5.3e-04];

ksd=[1.7e-03;1.1e-03;6.5e-04;1.8e-04;3.8e-04;2.6e-04;1.4e-04;1.0e-04];

afd=[0.31;0.52;0.71;0.81;0.67;0.64;0.71;0.52];

Tmic=[214;213;212;211;210;208;207;203];
s1_0=[0.33;0.36;0.37;0.37;0.35;0.33;0.33;0.31;0.28];
```

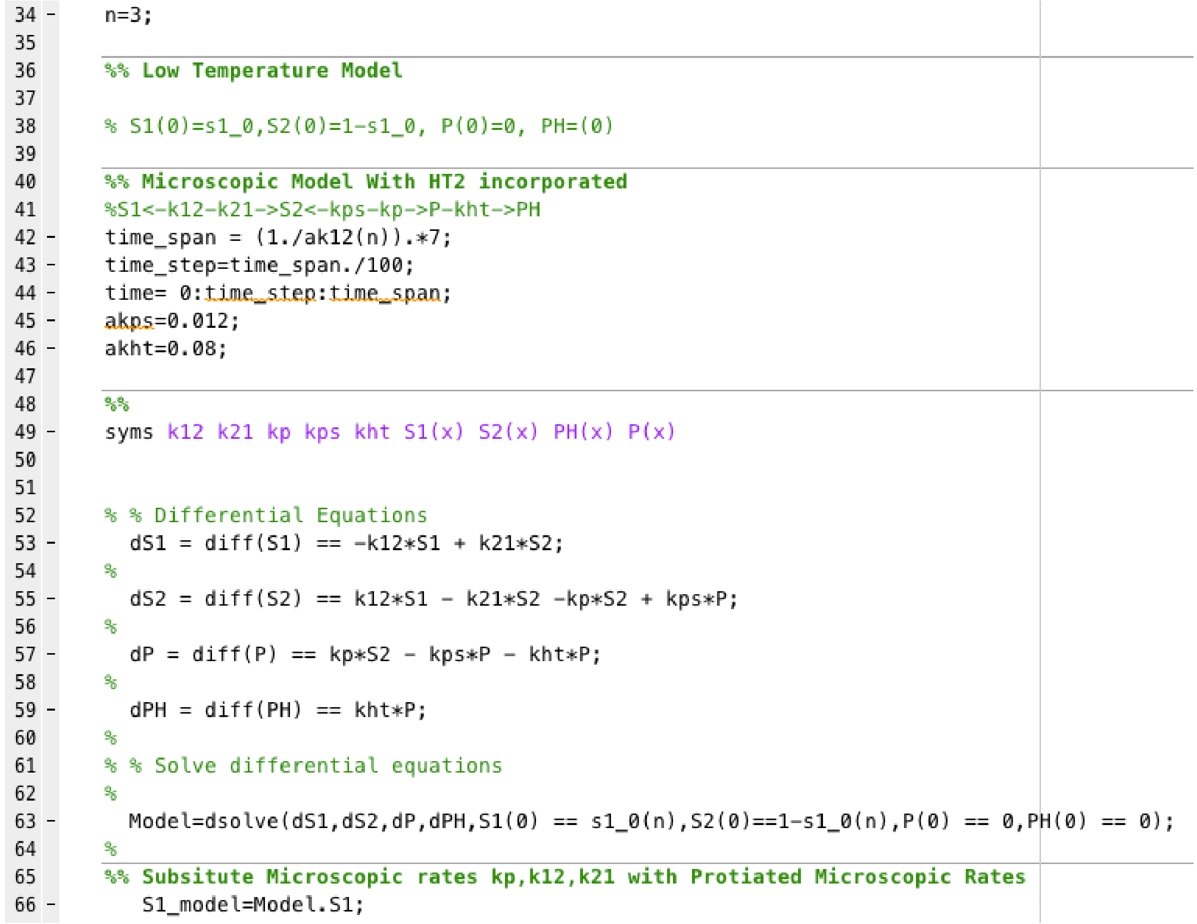

```
n=3;

%% Low Temperature Model

% S1(0)=s1_0,S2(0)=1-s1_0, P(0)=0, PH=(0)

%% Microscopic Model With HT2 incorporated
%S1<-k12-k21->S2<-kps-kp->P-kht->PH
time_span = (1./ak12(n)).*7;
time_step=time_span./100;
time= 0:time_step:time_span;
akps=0.012;
akht=0.08;

%%
syms k12 k21 kp kps kht S1(x) S2(x) PH(x) P(x)


% % Differential Equations
  dS1 = diff(S1) == -k12*S1 + k21*S2;
%
  dS2 = diff(S2) == k12*S1 - k21*S2 -kp*S2 + kps*P;
%
  dP = diff(P) == kp*S2 - kps*P - kht*P;
%
  dPH = diff(PH) == kht*P;
%
% % Solve differential equations
%
  Model=dsolve(dS1,dS2,dP,dPH,S1(0) == s1_0(n),S2(0)==1-s1_0(n),P(0) == 0,PH(0) == 0);
%
%% Subsitute Microscopic rates kp,k12,k21 with Protiated Microscopic Rates
   S1_model=Model.S1;
```

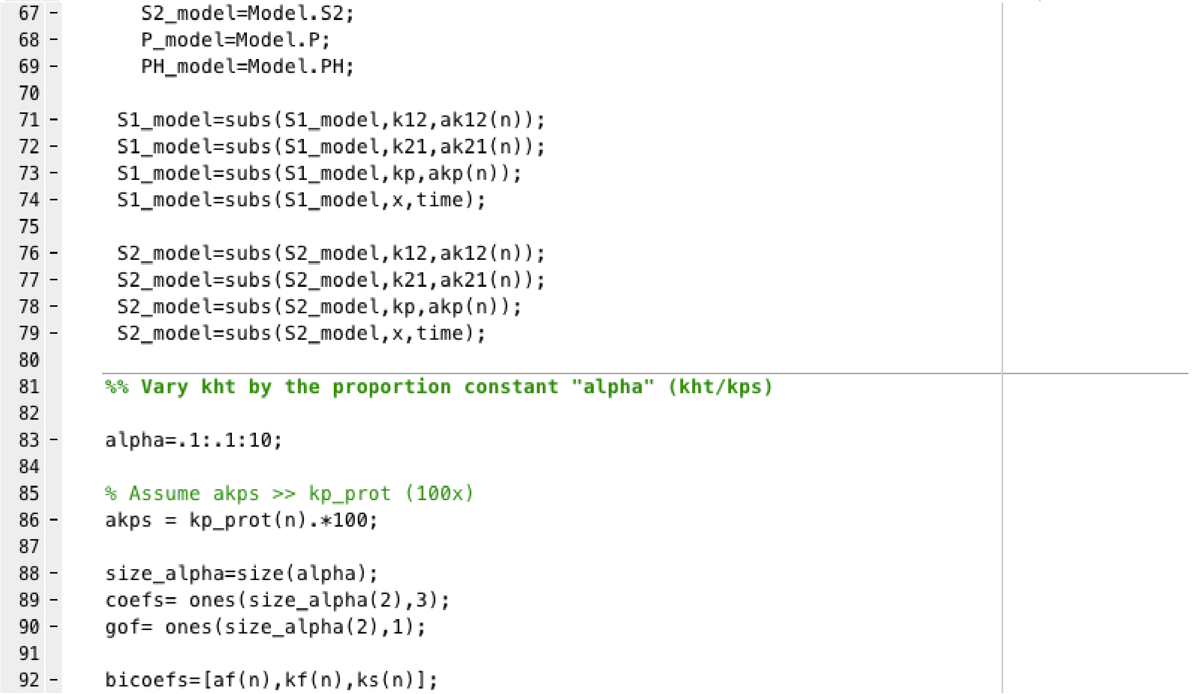

```
   S2_model=Model.S2;
   P_model=Model.P;
   PH_model=Model.PH;

 S1_model=subs(S1_model,k12,ak12(n));
 S1_model=subs(S1_model,k21,ak21(n));
 S1_model=subs(S1_model,kp,akp(n));
 S1_model=subs(S1_model,x,time);

 S2_model=subs(S2_model,k12,ak12(n));
 S2_model=subs(S2_model,k21,ak21(n));
 S2_model=subs(S2_model,kp,akp(n));
 S2_model=subs(S2_model,x,time);

%% Vary kht by the proportion constant "alpha" (kht/kps)

alpha=.1:.1:10;

% Assume akps >> kp_prot (100x)
akps = kp_prot(n).*100;

size_alpha=size(alpha);
coefs= ones(size_alpha(2),3);
gof= ones(size_alpha(2),1);

bicoefs=[af(n),kf(n),ks(n)];
```

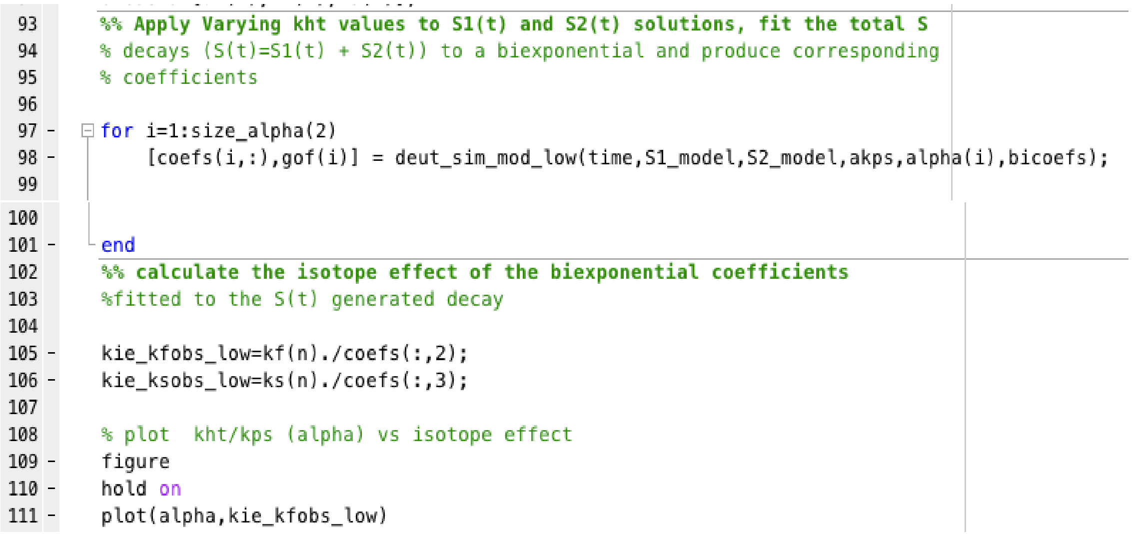

```
%% Apply Varying kht values to S1(t) and S2(t) solutions, fit the total S
% decays (S(t)=S1(t) + S2(t)) to a biexponential and produce corresponding
% coefficients

for i=1:size_alpha(2)
    [coefs(i,:),gof(i)] = deut_sim_mod_low(time,S1_model,S2_model,akps,alpha(i),bicoefs);


end
%% calculate the isotope effect of the biexponential coefficients
%fitted to the S(t) generated decay

kie_kfobs_low=kf(n)./coefs(:,2);
kie_ksobs_low=ks(n)./coefs(:,3);

% plot  kht/kps (alpha) vs isotope effect
figure
hold on
plot(alpha,kie_kfobs_low)
```

**7.5 deut_sim_mod_low:** substitutes variables $k_{ps}$, and $k_{HT}$ variables with the numerical values and fit Smodel to biexp function.

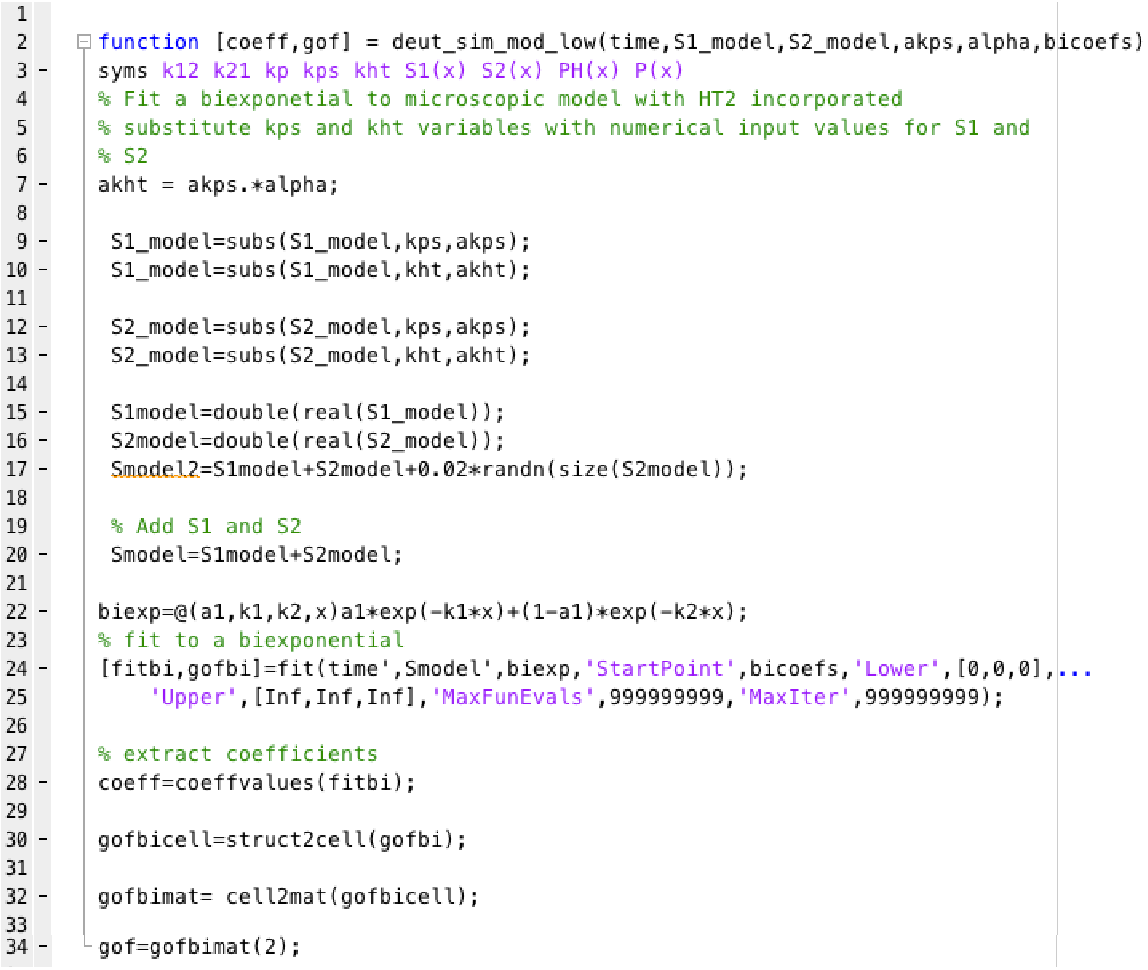

```

function [coeff,gof] = deut_sim_mod_low(time,S1_model,S2_model,akps,alpha,bicoefs)
syms k12 k21 kp kps kht S1(x) S2(x) PH(x) P(x)
% Fit a biexponetial to microscopic model with HT2 incorporated
% substitute kps and kht variables with numerical input values for S1 and
% S2
akht = akps.*alpha;

 S1_model=subs(S1_model,kps,akps);
 S1_model=subs(S1_model,kht,akht);

 S2_model=subs(S2_model,kps,akps);
 S2_model=subs(S2_model,kht,akht);

 S1model=double(real(S1_model));
 S2model=double(real(S2_model));
 Smodel2=S1model+S2model+0.02*randn(size(S2model));

 % Add S1 and S2
 Smodel=S1model+S2model;

biexp=@(a1,k1,k2,x)a1*exp(-k1*x)+(1-a1)*exp(-k2*x);
% fit to a biexponential
[fitbi,gofbi]=fit(time',Smodel',biexp,'StartPoint',bicoefs,'Lower',[0,0,0],...
    'Upper',[Inf,Inf,Inf],'MaxFunEvals',999999999,'MaxIter',999999999);

% extract coefficients
coeff=coeffvalues(fitbi);

gofbicell=struct2cell(gofbi);

gofbimat= cell2mat(gofbicell);

gof=gofbimat(2);
```

**7.6 distmod_090717:** Incorporates distributive properties of slow phase into microscopic model for substrate radical decays with varying sucrose concentrations.

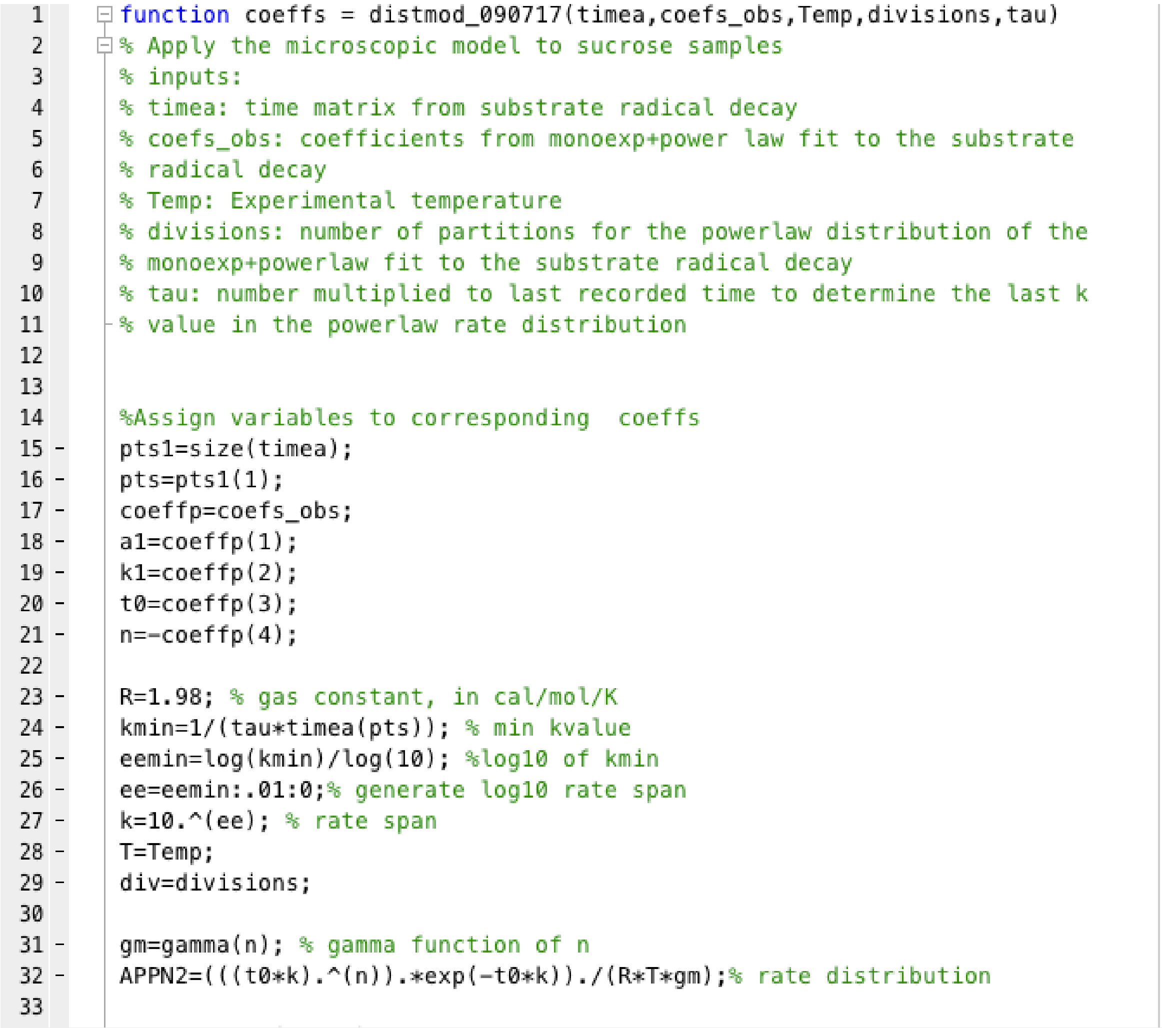

```
function coeffs = distmod_090717(timea,coefs_obs,Temp,divisions,tau)
% Apply the microscopic model to sucrose samples
% inputs:
% timea: time matrix from substrate radical decay
% coefs_obs: coefficients from monoexp+power law fit to the substrate
% radical decay
% Temp: Experimental temperature
% divisions: number of partitions for the powerlaw distribution of the
% monoexp+powerlaw fit to the substrate radical decay
% tau: number multiplied to last recorded time to determine the last k
% value in the powerlaw rate distribution


%Assign variables to corresponding  coeffs
pts1=size(timea);
pts=pts1(1);
coeffp=coefs_obs;
a1=coeffp(1);
k1=coeffp(2);
t0=coeffp(3);
n=-coeffp(4);

R=1.98; % gas constant, in cal/mol/K
kmin=1/(tau*timea(pts)); % min kvalue
eemin=log(kmin)/log(10); %log10 of kmin
ee=eemin:.01:0;% generate log10 rate span
k=10.^(ee); % rate span
T=Temp;
div=divisions;

gm=gamma(n); % gamma function of n
APPN2=(((t0*k).^(n)).*exp(-t0*k))./(R*T*gm);% rate distribution

```

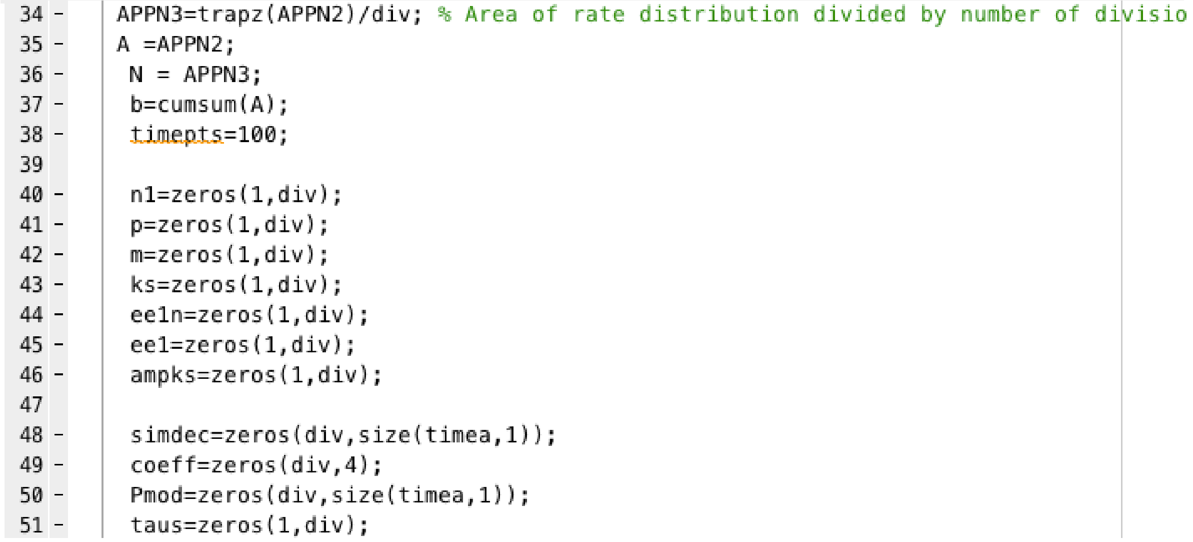

```
APPN3=trapz(APPN2)/div; % Area of rate distribution divided by number of divisio
A =APPN2;
 N = APPN3;
 b=cumsum(A);
 timepts=100;

 n1=zeros(1,div);
 p=zeros(1,div);
 m=zeros(1,div);
 ks=zeros(1,div);
 ee1n=zeros(1,div);
 ee1=zeros(1,div);
 ampks=zeros(1,div);

 simdec=zeros(div,size(timea,1));
 coeff=zeros(div,4);
 Pmod=zeros(div,size(timea,1));
 taus=zeros(1,div);
```

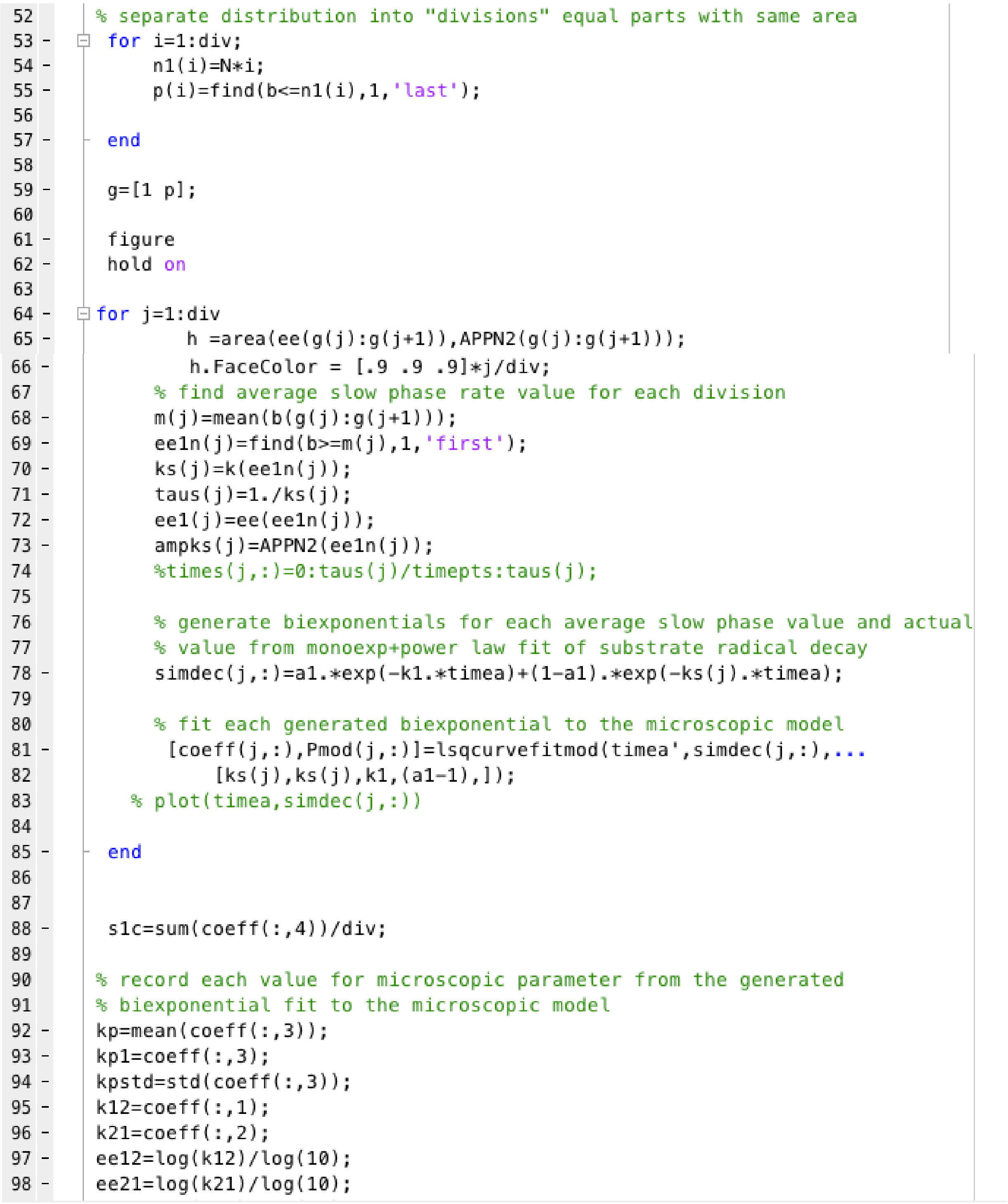

```
% separate distribution into "divisions" equal parts with same area
 for i=1:div;
     n1(i)=N*i;
     p(i)=find(b<=n1(i),1,'last');

 end

 g=[1 p];

 figure
 hold on

for j=1:div
        h =area(ee(g(j):g(j+1)),APPN2(g(j):g(j+1)));
        h.FaceColor = [.9 .9 .9]*j/div;
     % find average slow phase rate value for each division
     m(j)=mean(b(g(j):g(j+1)));
     ee1n(j)=find(b>=m(j),1,'first');
     ks(j)=k(ee1n(j));
     taus(j)=1./ks(j);
     ee1(j)=ee(ee1n(j));
     ampks(j)=APPN2(ee1n(j));
     %times(j,:)=0:taus(j)/timepts:taus(j);

     % generate biexponentials for each average slow phase value and actual
     % value from monoexp+power law fit of substrate radical decay
     simdec(j,:)=a1.*exp(-k1.*timea)+(1-a1).*exp(-ks(j).*timea);

     % fit each generated biexponential to the microscopic model
      [coeff(j,:),Pmod(j,:)]=lsqcurvefitmod(timea',simdec(j,:),...
          [ks(j),ks(j),k1,(a1-1),]);
   % plot(timea,simdec(j,:))

 end


 s1c=sum(coeff(:,4))/div;

% record each value for microscopic parameter from the generated
% biexponential fit to the microscopic model
kp=mean(coeff(:,3));
kp1=coeff(:,3);
kpstd=std(coeff(:,3));
k12=coeff(:,1);
k21=coeff(:,2);
ee12=log(k12)/log(10);
ee21=log(k21)/log(10);
```

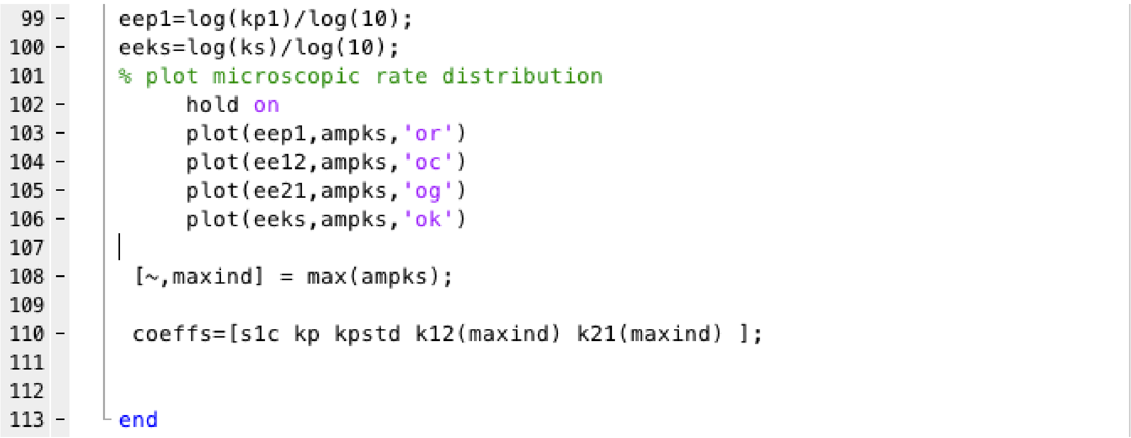

```
eep1=log(kp1)/log(10);
eeks=log(ks)/log(10);
% plot microscopic rate distribution
    hold on
    plot(eep1,ampks,'or')
    plot(ee12,ampks,'oc')
    plot(ee21,ampks,'og')
    plot(eeks,ampks,'ok')

 [~,maxind] = max(ampks);

 coeffs=[s1c kp kpstd k12(maxind) k21(maxind) ];


end
```